Sedimentology, Stratigraphy and Geochronology of Deep-Water Upper Slope Deposits, Neoproterozoic Windermere Supergroup of Western Canada

Richard Smith

A thesis submitted to the University of Ottawa in partial fulfillment of the requirements for the Master's degree in Earth Sciences

Department of Earth and Environment Sciences
Faculty of Science

University of Ottawa

Abstract

The stratigraphic architecture and depositional character of upper-slope channel–levee systems in the Neoproterozoic Isaac Formation is investigated. Detailed section measuring, mapping on high-resolution aerial drone images, and comparison with documented lower-slope channel complexes reveal that upper-slope channels are markedly thinner yet substantially coarser grained, exhibit deeper incision and more extensive cannibalization with pervasive mudstone-clast breccia. In contrast, levee deposits are comparatively finer-grained and dominated by upper-division turbidites. These patterns suggest that turbidity currents were typically undercapacity over the steep upper slope, resulting in prolonged erosion and confinement before transitioning to overcapacity, and therefore depositional conditions downslope. Despite these differences, detrital zircon assemblages, reflecting sediment provenance, and the evolution of channel complex architecture resemble those documented farther downslope, suggesting that temporal and spatial changes in these attributes are related to granolumetric changes along the source to sink profile and to flow hydraulics controlled by position along the continental slope**.**

Résumé

L'architecture stratigraphique et les caractéristiques sédimentaires des systèmes de chenaux et de levées situés dans la partie supérieure du versant de la formation néoprotérozoïque Isaac ont été étudiées. Des mesures détaillées, une cartographie à partir d'images aériennes haute résolution prises par drone et une comparaison avec les complexes de chenaux documentés du versant inférieur révèlent que les chenaux du versant supérieur sont nettement plus minces mais à grain beaucoup plus grossier, présentent une incision plus profonde et une cannibalisation plus étendue avec une brèche de clastes de mudstone omniprésente. En revanche, les dépôts des levées sont comparativement plus fins et dominés par des turbidites de division supérieure. Ces observations suggèrent que les courants de turbidité étaient généralement sous-capacité sur le versant supérieur escarpé, ce qui a entraîné une érosion et un confinement prolongés avant de passer à une surcapacité, et donc à des conditions de dépôt en aval. Malgré ces différences, les assemblages de zircons détritiques, qui reflètent la provenance des sédiments, et l'évolution de l'architecture complexe des chenaux ressemblent à ceux documentés plus en aval, ce qui suggère que les changements temporels et spatiaux de ces attributs sont liés aux changements granulométriques le long du profil source-puits et à l'hydraulique des écoulements contrôlée par la position le long du talus continental.

Acknowledgements

I would first like to express my sincere gratitude to my supervisor, Dr. Bill Arnott, for giving me the opportunity to do a Masters along with his guidance, insight, and steady support throughout this project. Our many discussions about the WSG consistently pushed me to think more critically and refine my ideas. I am especially thankful for his encouragement and for securing funding that made it possible for me to complete my master's degree. I am also deeply grateful to my co-supervisor, Dr. Celeste Cunningham, for her thoughtful feedback especially on levee deposits, and willingness to provide direction and support whenever it was needed. Her perspective strengthened this work in meaningful ways.

I would like to thank my examiners, Dr. Don Cummings and Dr. Quentin Gail, for taking the time to review my thesis and for their careful evaluation and constructive feedback.

This work would not have been possible without the technical support of several individuals. I am appreciative to Dr. Dave Schneider for his assistance with processing my samples for geochronology, and to Dr. Glenn Poirier for his help with imaging my zircon grains in the Electron Microprobe Lab in the Advanced Research Complex. I am also thankful for Sam Morfin for his support in the Laser Ablation Lab. Their expertise and patience were greatly appreciated. I am grateful for the financial support provided by the Earth Science Department at the University of Ottawa, which made this research possible. To my fellow graduate students (Ishmael, Jack, Matt L.) thank you for the encouragement, shared struggles, and the many after-school beers at FnS that helped keep things in perspective.

Finally, I would like to thank my family back home in Belize, especially my mom, Michelle Augustine, for her unwavering belief in me. Her constant positive reinforcement carried me through the moments when I felt like giving up. This accomplishment is as much hers as it is mine.

Table of Contents

List of Figures

List of Tables

Chapter 1: Introduction

1.1 Windermere Supergroup Overview

The Neoproterozoic Windemere Supergroup (WSG) is a regionally extensive, unconformity bounded metasedimentary sequence exposed throughout western North America that provides a window into the breakup of the supercontinent Rodinia (750–560 Ma) along its northwestern margin (Young et al., 1973). Local exposures of the WSG crop out from northwestern Mexico to the western United States, then continuously through most of the southern Canadian Cordillera and further northward to the Yukon-Alaska border region (Fig. 1.1A) (Ross et al., 1995; Ross and Arnott, 2007).

Rocks of the WSG represent syn-rift to post-rift magmatism and sedimentation along the northwestern incipient passive margin of Laurentia (ancestral North America) and the developing proto-Pacific Ocean (Young et al., 1979; Ross, 1991). The spatial and temporal variability of the passive margin that formed following rifting is reflected in the varying sedimentological characteristics of the WSG on the regional scale. Strata in northern Mexico and the western United States are interpreted to be deposited in shallow-marine to continental sedimentary environments (Link et al., 2003; Young, 1979). Northward, localities in the southern Canadian Cordillera represent deposition in deep-marine shallowing upward to shallow-marine environments with excellent exposures of basin floor to upper slope strata in the Cariboo Mountains of east-central British Columbia (Hadlari et al., 2021; Ross and Arnott, 2007). Further northward in the Yukon-Alaska region strata are interpreted to represent upper continental slope to shallow-marine deposits (Fig. 1.1B) (Rainbird et al., 1997; Young, 1984).

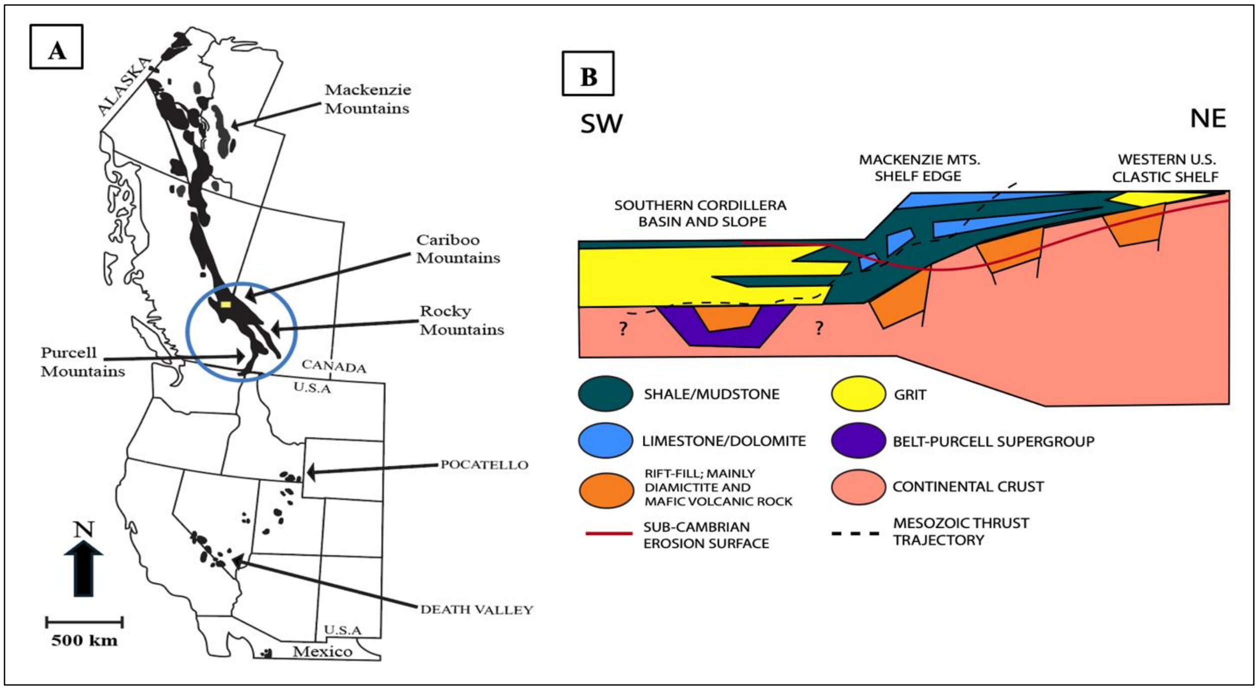

Fig. 1.1: *A) Map showing the regional distribution of exposed Windermere Supergroup (WSG) rocks from northern Mexico to northern Canada. Deep marine strata is highlighted by the blue circle with the yellow rectangle indicating the study area. B) Schematic cross-section of western North America at approximately 600 Ma, illustrating lateral facies variations within t the WSG. In the western U.S., strata are dominated by shallow-marine shelf deposits whereas in the Mackenzie Mountains (northern Canadian Cordillera) they transition from upper slope to shelf-edge settings. In contrast, strata in the southern Canadian Cordillera consist mostly of deep-marine facies, including basin-floor shoaling upward to upper slope deposits. The red line indicates the sub-Cambrian unconformity that truncates portions of the stratigraphy in the eastern part of the Windermere Basin (redrawn from Ross and Arnott, 2007).*

1.2 Tectonic History

The placement of the Windermere Supergroup (WSG) within Neoproterozoic Laurentia is pivotal for unraveling the enigmatic, late-stage continental rifting events of Rodinia and the evolution of the ancestral North America craton. The formation of Laurentia was initiated during the Paleoproterozoic (2.0–1.6 Ga) with a series of orogenic events that continued until the early Neoproterozoic as the supercontinent Rodinia amalgamated (Hoffman, 1988). The Precambrian tectonic elements that form much of Laurentia are generally subdivided into two main segments: Archean and Proterozoic terranes. Prominent Archean provinces that accreted to form Laurentia included the Slave, Rae-Hearne, Superior, and smaller continental fragments including the Wyoming, Medicine Hat, Sask, Marshfield, and Nain terranes (Whitmeyer and Karlstrom, 2007). These collisions led to the closure of extensive oceans, marking key tectonic events in the Precambrian evolution of the northern North American continent, including the assembly of Archean provinces, Thelon Orogen, Wopmay Orogen, Hearne/Rae collision, Wyoming/Superior collision (Hoffman, 1988).

The southern part of the North American continent, including much of the continental United State, underwent assembly between 1.8–1.0 Ga through the accretion of juvenile volcanic arcs and ocean terranes (Whitmeyer and Karlstrom, 2007). This assembly gave rise to accretionary provinces, including the Yavapai province, Mazatzal province, Granite-Rhyolite province, and the Llano-Grenville, province (Whitmeyer and Karlstrom, 2007).

By the late Neoproterozoic (1000–560 Ma) Laurentia, along with most other global continental landmasses, coalesced to form the supercontinent Rodinia that extended from the northern polar region to the equator (Hoffman, 1988). The spatial configuration of the plates (Laurentia, East Antarctic, North China, Australia etc.) that made up Rodinia is still much debated, with different models of interconnection supported by geological correlations and paleomagnetic constraints (Li et al., 2008; Rainbird et al., 1997). Notably, since the geological record of Laurentia suggests the craton being bounded on all sides by Neoproterozoic passive continental margins, it is typically regarded to have laid at the center of the supercontinent (Hoffman, 1991; Li et al., 2008).

The break-up of Rodinia started at ~ 780 Ma (Fig. 1.2) and formed an extensive passive continental margin along the margin of the expanding paleo-Pacific Ocean between Gondwana and western Laurentia (Ross, 1991; Young, 1984). This marked the beginning of the WSG in western North America and consists of syn-rift to passive margin sequences, including the progradation of the Laurentian passive margin into the proto-Pacific miogeocline (Bond and Kominz, 1984; Ross et al., 1995; Hadlari et al., 2021).

Later, during the mostly Mesozoic (late Jurassic to Late Paleocene) Cordilleran Orogeny, the WSG underwent alterations in its present-day position, geometry, and thickness. Accretion of allochthonous terranes and orogenesis formed five morphogeological belts that make up the Canadian Cordillera: Insular Belt, Coast Belt, Intermontane Belt, Omineca Belt, and Foreland Belt. These belts, distinguished by unique deformational styles and metamorphic grades, align sub-parallel to the north-northwestern trend of the Cordillera (Stewart, 1972). In the southern Canadian Cordillera rocks of the WSG are well exposed in the Foreland Fold and Thrust Belt and the Omineca Belt. The mostly siliciclastic succession of sedimentary rocks experienced upper amphibolite metamorphic conditions in the southern Cariboo and western Purcell Mountains but in the northern Cariboo Mountains only sub-greenschist metamorphism with the preservation of primary sedimentary textures and structures, and therein the invaluable opportunity for detailed sedimentological investigation (Ross and Arnott, 2007).

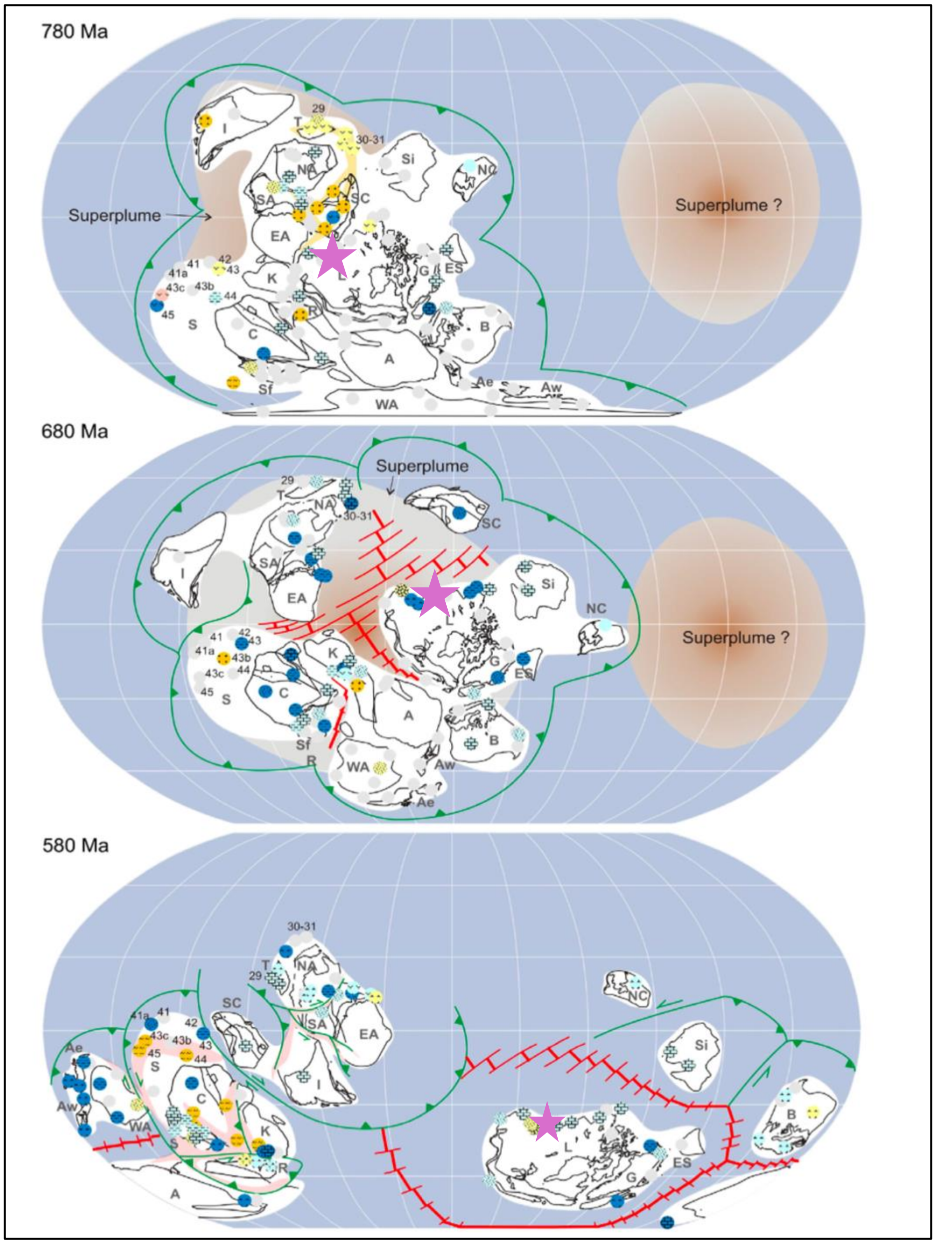

Fig. 1.2: *Global paleogeographic reconstruction of supercontinent Rodinia showing the dispersal of continental landmasses as rifting began at three discrete time intervals by Li et al., (2008). Approximate location of the Windermere turbidite system in the southern Canadian Cordillera indicated by purple star.*

1.3 Regional Stratigraphy

Mesoproterozoic metamorphic basement rocks in the Canadian Cordillera and the northwestern US record orogenic events associated with the assembly and evolution of supercontinents Columbia/Nuna (1.7–1.3 Ma) and Rodinia (1.1–0.75 Ma) (Box et al., 2020). These rocks are then overlain unconformably by sedimentary sequences that represent intracratonic basins or passive continental margins formed during the breakup of the supercontinents (Rainbird et al., 1997; Young et al., 1979). The Windermere Supergroup (WSG) in the southern Canadian Cordillera (Fig. 1.3) and northwestern US unconformably overlies metamorphic rocks of the Belt-Purcell Supergroup (1.5–1.4 Ga), or high-grade metamorphic rocks varying in age from Archean to late Proterozoic (Crowley, 1999; Ross and Arnott, 2007).

The basal part (~ 2.5 km) of the WSG consists of syn-rift sedimentary and mafic volcanic rocks, which in southeast B.C. comprise the Toby and Irene formations, respectively, and record the initial rifting of Laurentia from the Rodinia supercontinent. The Toby Formation consists of glaciogenic diamictites interbedded with mudstone, sandstone, limestone, and conglomerate. The Irene Formation includes andesitic greenstones, tuff, and volcanic conglomerates (Li et al., 2013), and in its uppermost part has recently been dated with a U-Pb SHRIMP (zircon) at 669.6 ±6.7 Ma (Hadlari et al., 2024).

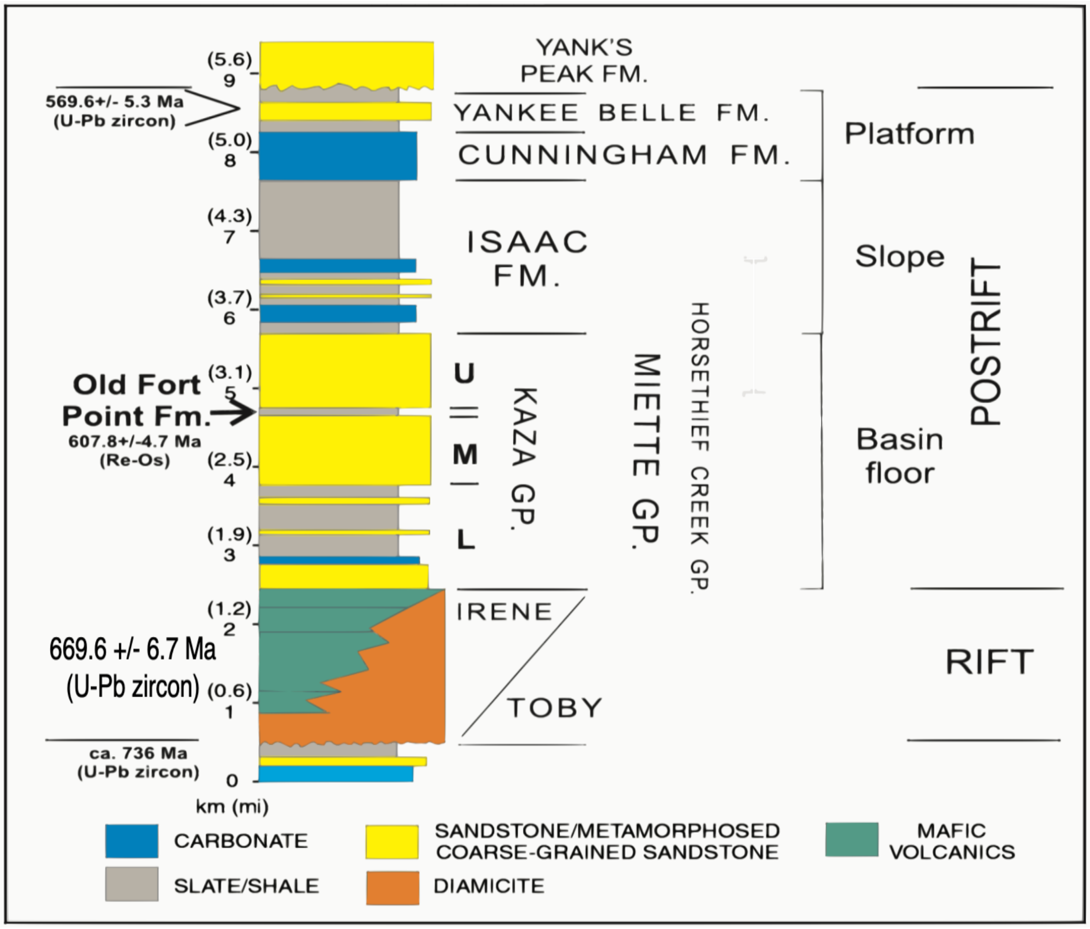

***Fig. 1.3**: Regional stratigraphic column of the Windermere Supergroup in the southern Canadian Cordillera from Ross and Arnott (2007).*

Post-rift strata conformably overlie the Toby-Irene succession and form a 5–7 km-thick basin-floor to slope to platform sequence comprising coarse-grained, sandstone-rich turbidites interbedded with mudstone and minor carbonate (Ross and Arnott, 2007). This succession is informally termed the Windermere turbidite system and represents the largest of its kind in the ancient geological record, covering an area of at least 80,000 km^2, making it dimensionally similar to the modern Mississippi, Amazon and Congo turbidite systems (Ross et al., 1991; Ross and Arnott, 2007).

In the Cariboo Mountains of east-central British Columbia, post-rift strata are made up of the Kaza and Cariboo groups and correlate with the Miette Group to the east in the Rocky Mountains and the Horsethief Group to the south in the Purcell and Selkirk mountains (Ross and Arnott, 2007; Smith et al., 2014). The Kaza Group (2–4 km-thick) is subdivided into lower, middle, and upper parts and represents basin-floor sedimentation along the passive margin of Neoproterozoic Laurentia (Ross and Arnott, 2007). The lower Kaza Group consists of distal basin floor calc-schists, marble, and meta-sandstones that transition upward into the middle and upper Kaza characterized by metamorphosed sub-feldspathic sandstone representing depositional lobe deposits on the medial to proximal parts of the basin floor (Terlaky et al., 2015).

The Old Fort Point Formation (OFP), marked by thin-bedded siliciclastic and carbonate turbidites, serves as a distinctive and regionally extensive marker unit within the WSG, and in the Cariboo Mountains separates the upper and middle Kaza groups (Ross and Arnott, 2007; Smith et al., 2014). The OFP's unique geological and chemical characteristics suggest a major transgression that reduced deep-water siliciclastic sedimentation but increased mudstone and carbonate deposition under anoxic conditions (Ross and Murphy, 1988).

The Kaza Group is overlain by the 5 km-thick Cariboo Group (Fig. 1.4), which in its lower part is divided into the Isaac, Cunningham, and Yankee Belle formations (Ross and Arnott, 2007). The Isaac Formation is made up primarily of mudstone (i.e. fine-grained thin-bedded turbidites) with laterally discontinuous but decameter to >100 m-thick sandstone units representing base-of-slope leveed-channel complexes. Additionally, the Isaac Formation consists of common slump, slide and debris flow deposits indicative of gravitational (slope) instability (Ross et al., 1995; Ross and Arnott, 2007). The Cunningham Formation is over 550 m thick and consists predominantly of limestone and dolostone with minor mudstone, siltstone, and shale (Ross et al., 1995). The Yankee

Belle is up to 900 m thick and comprises alternating limestone, sandstone, siltstone, and shale (Rowe, 2003). Respectively, the Cunningham and Yankee Belle formations represent deposition on the upper continental slope and high-energy continental shelf (Ross et al., 1995). Together the Kaza and Cariboo groups form a several km-thick, upward-shallowing succession interpreted to represent progradation of the western continental margin of Laurentia into the proto-Pacific Ocean (Ross and Arnott, 2007; Ross et al., 1995; Hadlari et al., 2021).

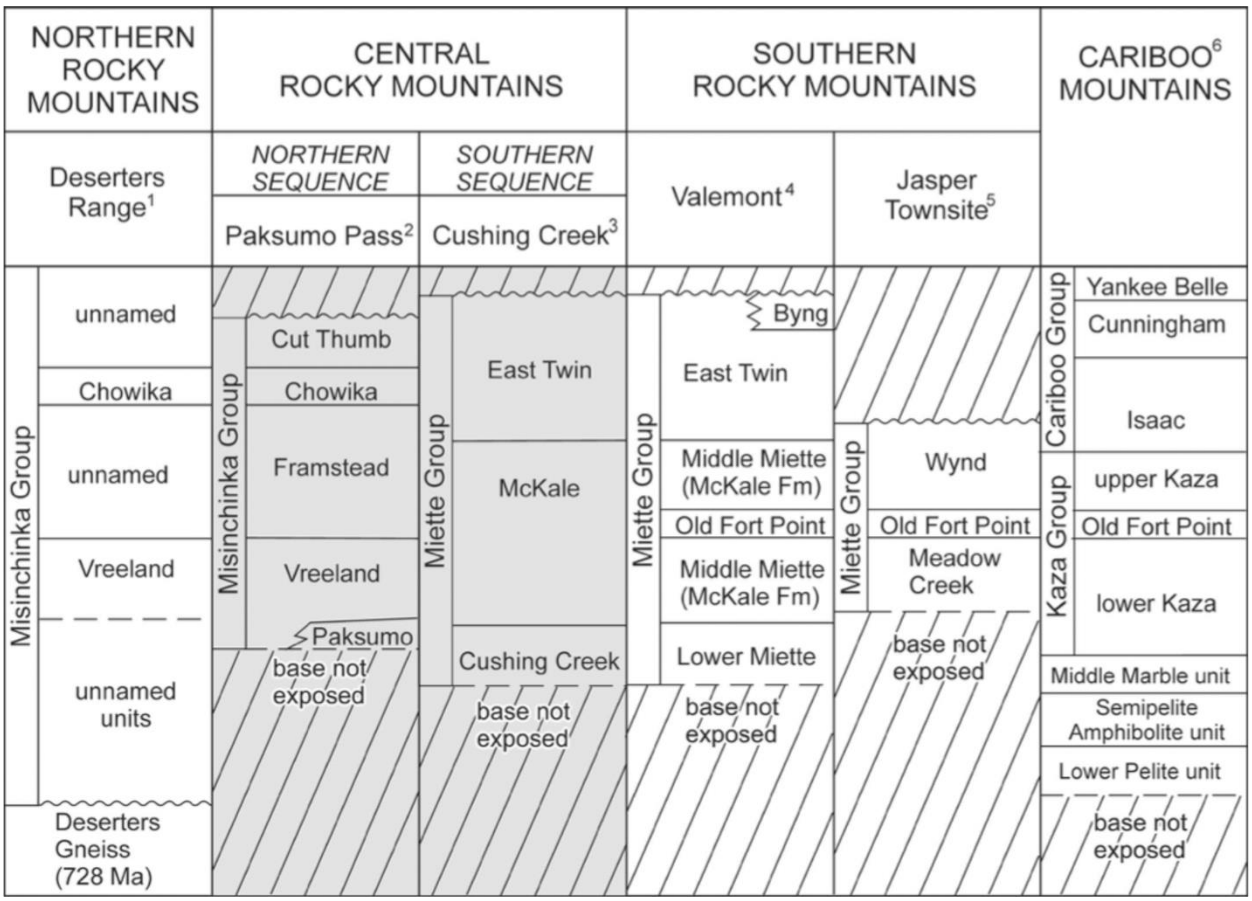

Fig. 1.4: *Stratigraphic nomenclature of Neoproterozoic strata in the southern Canadian Cordillera (from McMechan et al., 2015).*

The top of the Windermere Supergroup is marked by a rift-related unconformity (Aitken, 1969), which in the Cariboo Mountains separates the WSG from the lower Cambrian Yanks Peak Formation. This second rift event led to substantial uplift and erosion of Windermere-aged shallow-marine and continental facies in the eastern part of the basin (Ross et al., 1995). In the northern Canadian Cordillera, the transition to post-rift passive margin sedimentation was originally interpreted to have occurred by ca. 550 Ma, but recent data indicate it did not take place until after ca. 500 Ma, based on a regional unconformity beneath upper Cambrian carbonates that truncates the uppermost Ediacaran Rackla Group, which includes formations such as the Nadaleen, Gametrail, and Blueflower (Moynihan et al., 2019). This revision suggests that rifting and tectonic activity persisted into the early to middle Cambrian. Affected units of the Rackla Group preserve key global signals including the Shuram–Wonoka $\delta^{13}C$ excursion and Ediacaran macrofossils reflecting the final stages of syn- to early post-rift deposition. Overlying Cambrian successions vary across structural domains, reflecting ongoing tectonism and differential subsidence (Gordey and Anderson, 1993; Moynihan et al., 2019).

1.4 Castle Creek Study Area

The Castle Creek study area is located in the northern Cariboo Mountains of east-central British Columbia, where Neoproterozoic strata of the Windermere Supergroup form a worldclass example of an ancient passive-margin turbidite succession recording the transition from basin-floor to slope deposits (Fig. 1.5A; Ross and Arnott, 2007). At Castle Creek, an over 4.0-km-thick perpendicular to bedding and 7–8 km along depositional strike succession of the upper Kaza Group and overlying Isaac Formation is exposed (Fig. 1.5B). Strata dip steeply (~ 89°) and have been largely stripped of surficial debris and vegetation by recent deglaciation (<100 years). Collectively these conditions allow sedimentological documentation from millimetre to kilometre scale.

The lower ~ 800 m of the section comprises the upper Kaza Group, consisting mainly of laterally continuous, decametre-thick units of mostly coarse-grained sandstone interbedded with thin-bedded turbidites interpreted to represent depositional lobes and terminal splays formed by poorly confined turbidity currents on the basin floor (Terlaky et al., 2015). These strata are conformably overlain by the more than 3.5 km-thick Isaac Formation consisting of mudstone-dominated deposits interbedded with discontinuous, several-decametre-thick sandstone and conglomerate units interpreted as slope leveed-channel deposits (Ross and Arnott, 2007; Fraino et al., 2022). Collectively, these strata record an upward-shallowing transition from basin-floor to slope settings within the Windermere deep-marine system (Ross and Parrish, 1991; Arnott, 2007; Ross and Arnott, 2007).

Structurally, the Castle Creek section lies on the steep limb of a southwest-verging anticline within the Isaac Lake Synclinorium, a structural depression developed through multiple deformation events (Reid et al., 2002). Regional studies identify four major deformation phases (D1–D4) and two low-grade metamorphic events (M1–M2) related to the mid-Jurassic to Tertiary accretion of terranes along the western margin of North America (Murphy and Rees, 1983; Murphy, 1987a, b; Reid et al., 2002). Strata in the study area have been most affected by the second deformational event (D2) that formed a northwestward plunging asymmetric anticline with the Castle Creek outcrop being exposed on its ~ vertical-dipping limb. Despite deformation and metamorphism, primary sedimentary textures and structures remain exceptionally well preserved, making Castle Creek an outstanding natural laboratory for the investigation of Neoproterozoic deep-marine depositional systems and their post-depositional modification.

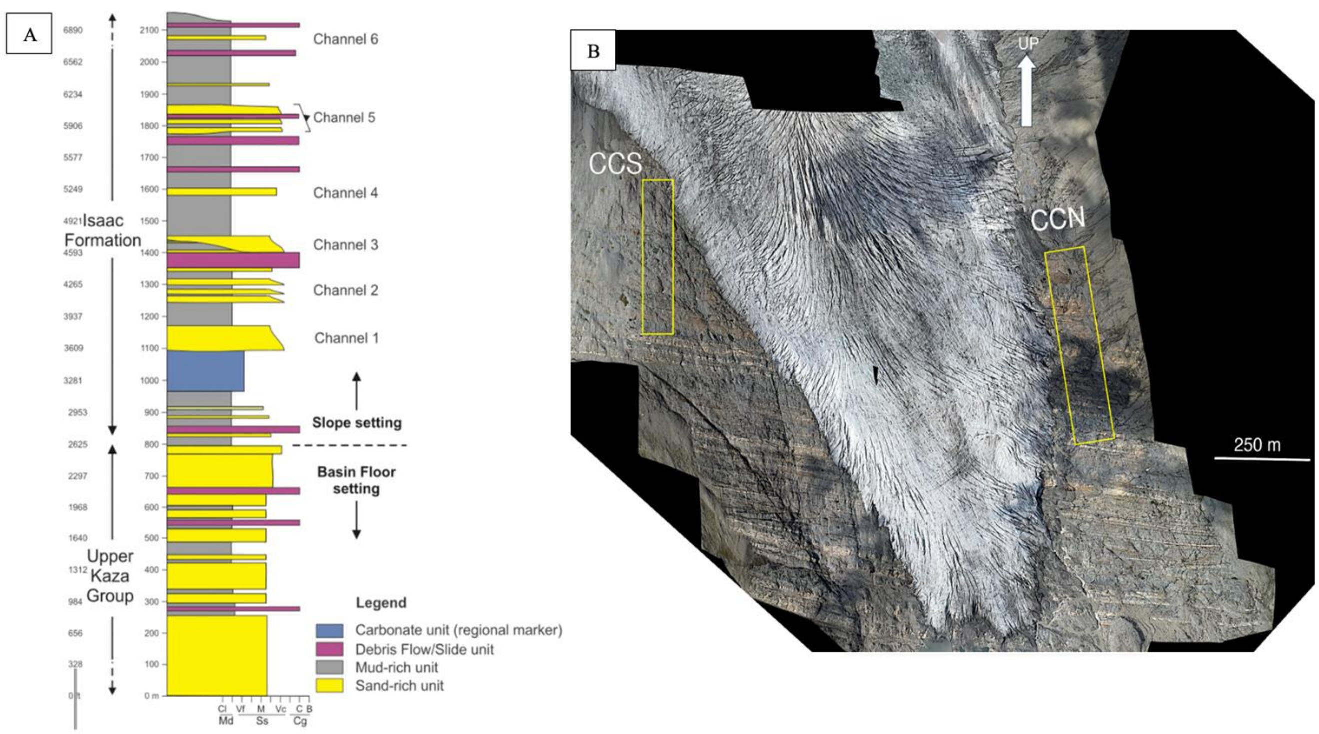

Fig. 1.5: *A.) Composite stratigraphic column of the Castle Creek study area showing its major stratal components (Ross and Arnott, 2007). B.) Aerial photomosaic showing slope deposits of the Isaac Formation at the Castle Creek outcrop. Study areas CCN and CCS, respectively Castle Creek north and south, are highlighted by yellow boxes.*

1.5 Thesis objective and Structure

The primary objective of this thesis is to investigate and interpret the stratigraphic and sedimentological architecture of newly exposed deep-marine channel–levee deposits on the upper continental slope, with the goal of reconstructing the temporal and spatial evolution of strata in the study interval and to compare the results with previous studies that investigated strata deposited lower on the slope. A secondary objective is to examine sediment provenance through detrital zircon U–Pb geochronology. These results are used to compare age signatures and possible changes in sediment sourcing compared to leveed-channel systems deposited farther downslope in the Isaac Formation.

This thesis follows a traditional structure: Chapter 1 provides an overview of the tectonic history, regional and local geology of the Windermere Supergroup along with a literature review of sediment-gravity flows and the architecture of deep-marine channel and levee systems. Chapter 2 presents a detailed lithological and petrographic description of all identified facies. Chapter 3 outlines the vertical distribution of stratal elements that comprise the study interval. Chapter 4 analyzes the spatial and temporal evolution of channel complexes in the study area within a sequence-stratigraphic framework, emphasizing the factors that governed their development. This chapter also compares the stratal elements described in the study area with strata deposited lower on the continental slope. Chapter 5 summarizes the main conclusions of this work and identifies key avenues for future research.

1.6 Methodology

1.6.1 Fieldwork and Detailed Stratigraphy

Fieldwork was conducted at the Castle Creek north and south study area over a period of ~ 5 weeks that included measuring stratigraphic sections and mapping major contacts and internal features to identify stratal elements and map them on high-resolution aerial drone images. A total of 13 stratigraphic logs (ranging from ~ 10–500 m thick) were measured in bed-by-bed detail (i.e. centimeter scale). Basal contacts, lithology, grain size, bed thickness, clast characteristics, primary and secondary sedimentary structures, and paleocurrent measurements were recorded. Petrographic analysis of 8 thin sections was carried out to characterize textural attributes including grain size and sorting, grain composition, cement and matrix content and the effects of diagenesis and tectonism to better constrain depositional and post-depositional processes. Thin-section petrography was conducted using an Olympus BX-41 trinocular microscope under plane-polarized, cross-polarized and reflected light.

1.6.2 Detrital Zircon U-Pb Geochronology

Detrital zircon U-Pb geochronology was used to constrain sediment provenance. Sandstone samples, each weighing about ~ 1–2 kg, were collected from the Castle Creek North study areas. Zircon grains were separated using standard mineral separation procedures, including, crushing, sieving, and heavy liquid separation. Zircon grains ranging from 53–300 µm were hand-picked using an Olympus BX51 zoom stereo microscope. Selected zircons were then mounted in a ~ 30 mm circular plastic mould and embedded in epoxy.

High-resolution imaging of grains internal structures and morphologies was performed using a Gemini500 Scanning Electron Microscope (SEM). U-Pb isotopic analyses were conducted with a Photon Machines Analyte Excite 193 nm excimer laser coupled to an Agilent 7700x inductively coupled plasma mass spectrometer (ICP–MS) following the analytical procedures outlined in Matthews et al., (2016). Instrumental mass bias was corrected using reference standards 91500, Plešovice, and NIST612 (Wiedenbeck et al., 1995). Data reduction was performed using the software Iolite and analyses were filtered by removing data points with >10% discordance. For grains younger than ca. 1000 Ma $^{238}U/^{206}Pb$ ages were used whereas for grains older than ca. 1000 Ma $^{207}Pb/^{206}Pb$ ages were applied (Gehrels, 2011). Detrital zircon age data are presented as kernel density estimation (KDE) plots to interpret sediment provenance. Major age populations were identified and correlated with potential source terranes. All stages of U–Pb zircon geochronological sample preparation and data processing—including mineral separation, hand-picking, epoxy mounting, imaging, and subsequent data reduction—were carried out by the author. These procedures were performed in-house at the University of Ottawa in the Electron Microprobe Laboratory and the Laser Ablation Laboratory in the Advanced Research Complex.

1.7 Terminology

Bed thickness terminology used in this study is based on the classification scheme of Ingram (1954), where very thin-bedded refers to beds 1–3 cm thick, thin-bedded to 3–10 cm, medium-bedded to 10–30 cm, thick-bedded to 30–100 cm, and very thick-bedded to beds exceeding 100 cm. Grain size descriptions follow the Udden-Wentworth scale (Udden, 1914; Wentworth, 1922).

Turbidites are described using the Bouma (1962) framework, which divides a typical turbidite into five divisions:

- T_a: Massive or structureless sandstone, often with a scoured base, reflecting deposition from high-density turbulent flow with minimal tractional influence.
- T_b: Planar-laminated sandstone, usually finer-grained than Ta
- T_c: Ripple cross-laminated sandstone, typically fine-grained sand
- T_d: Planar-laminated siltstone-mudstone.
- T_e: Fine-grained mud, typically of hemipelagic or pelagic origin.

It is important to note that complete Bouma sequences are uncommon, and partial sequences are more typical. For this study, lower division turbidites refer to beds containing T_a and/or T_b divisions, whereas upper division turbidites comprise only the upper two or three divisions (T_c, T_d, and T_e). Due to the inability to differentiate T_d from T_e in the field, these are grouped here as a single $T_{d/e}$ division.

In the context of this study, 'amalgamated' refers to stratal successions comprising strata deposited by multiple flow events but where intervening finer-grained strata, possibly with traction transport structures, and/or mud-rich partings are absent.

1.8 Deep-Marine Sedimentary Processes

1.8.1 Introduction to sediment gravity flows in deep-marine environments

Physical mechanisms involved in the transport and deposition of sediment in deep-marine settings are poorly constrained despite their capacity to move, over very short periods of time, substantial amounts (>100 km^3) of detrital material over extensive areas (100s to 1000s of kilometers) from the continental shelf to the distal basin floor (Kneller and Buckee, 2000; Talling et al., 2012; Talling, 2014). Among the most influential agents shaping the geologic record of these deep-water environments are sediment gravity flows. Sediment gravity flows are formed by suspended sediment that creates a density difference between the flow and the ambient fluid that maintains the flow (Middleton and Hampton, 1973). In contrast, fluid gravity flows involve the movement of fluid, generally air or water, under the influence of gravity, which in turn creates forces that moves the sediment as bed, suspended and wash loads.

A comprehensive physical mechanistic understanding of sediment gravity flows remains underdeveloped, due in large part to their powerful, destructive nature compounded with their infrequent occurrence in modern natural systems (Talling et al., 2013). Thus, our current understanding is largely based on interpretations from the ancient geological record and meticulously controlled laboratory experiments. Initiation points of sediment gravity flows have been identified in areas near the continental shelf-slope break and lower positions on the slope with varying triggering mechanisms, including hyperpycnal river outflows, slope failure, storm-induced re-suspension near the shelf edge and seismic activity (Piper and Normark, 2001; Mutti and Normark, 1987). The evolution of sediment gravity flows downslope is influenced by changes in gradient, fluid entrainment, erosion, deposition, and flow expansion, rendering the characteristics of the final deposit largely independent of the initiation process (Mulder and Alexander, 2001; Shanmugam, 2006; Normandeau et al., 2020).

Sediment gravity flows encompass a spectrum of gravity-driven processes, each contributing to the formation of unique deposits in the rock record. Because of their complex nature, deciphering the original flow conditions from observation in the rock record is inherently challenging due to the diverse range of depositional processes and added complexities introduced by diagenesis and deformation (Mulder and Alexander, 2001). There have been numerous attempts to classify sediment gravity flows based on different parameters such as sediment concentration, sediment-support mechanisms, flow rheology and a combination of rheology and sediment-support mechanisms (Table 1.1). While there is a general acceptance that sediment gravity flows can be broadly categorized into turbidity currents and debris flows, there exists a spectrum of intermediate flow types. The classification scheme of Mulder and Alexander (2001) is an attempt to encapsulate key variations among flow types grounded in flow behaviour, grain size distribution, and grain support mechanism. This scheme introduces two end-member categories: cohesive flows and non-cohesive frictional flows, providing a nuanced framework to better understand the diverse behaviours exhibited by sediment gravity flows in deep water settings.

Name	**Sediment support mechanism**
Fluid Turbulence	Coherent movement of fluid masses at an angle to the main axis of the flow in order to minimize a momentum gradient. Turbulence intensity increases with the velocity gradient and is capable of suspending sediment if the strength of the upward component of turbulence motion equals or exceeds the downward settling (gravity) velocity of the particle (Middleton and Hampton, 1973).
Hindered Settling	Reduced particle settling velocity due to increased drag imposed by upward moving fluid/sediment mixture that increases with sediment concentration (Davies, 1968).
Buoyancy	Displacement of fluid by a particle generates an upward force on the particle that is equal to the mass of the displaced fluid volume (Lowe, 1979).
Dispersive Pressure	Collision between solid particles generates a dispersive force that helps maintain the particles in suspension but also causes the flow to dilate. Grain-to-grain interactions become increasingly important as sediment concentration increases (Bagnold, 1962).
Matrix Strength (cohesive strength)	Ionic surface charges and large surface area:volume ratio of clay size particles causes them to become aggregated into larger masses by weak van der Waals forces. At sufficiently high concentration the aggregated clay minerals form a sufficiently strong particle network capable of supporting the weight of larger grains (Mulder and Alexander, 2001)

Table 1.1: *List of particle support mechanisms that individually, or in combination, are active in sediment gravity flows (adapted from Dumouchel, 2015).*

1.8.2 Cohesive Flows

Cohesive flows, known as mud flows or debris flows, represent a category of sediment gravity flow characterized by non-Newtonian behaviour and a laminar flow state (Shanmugam, 2021; Mulder and Alexander, 2001). Clay mineral particles, which in most cases make up most of the clay size fraction, are weakly charged on their surfaces and under appropriate conditions form a larger-scale network of aggregated clay particles– a process termed flocculation or more generally aggregation. This network of flocculated clay particles leads to the development of mechanical strength in the flow, known as matrix strength, and increases effective flow viscosity (Mulder and Alexander, 2001). Although the dominant particle support mechanism in cohesive flow is matrix strength, a host of other physical mechanisms collectively contribute to the suspension of particles such as particle-particle interaction, buoyancy effects, hindered settling, and elevated pore pressure (Arnott, 2010).

Modern systems demonstrate that debris flows can extend over considerable distances (several 100s of kilometers), depositing sediment that is often poorly sorted and massive (Gardner and Kidd, 1983). Notably, these deposits frequently exhibit flat (non-erosional) basal contacts, attributed to turbulence dampening by the fine-grained, cohesive matrix. The occurrence of these features has been ascribed to hydroplaning, a phenomenon where a layer of ambient fluid accumulates between the bed and the base of the flow, causing a significant reduction in basal drag (Mohrig and Marr, 2003). Partial or complete transformation of debris flows may take place over time as mixing or dilution of the flow occurs at the head or along the upper surface of the body (Hampton, 1975; Fisher, 1983). Such transformations can prompt a reduction in flow strength, causing the flow to transition into another type of sediment gravity flow, such as a hyperconcentrated density or concentrated density flow, especially if coarser sized sediment is abundant in the flow (Hampton, 1975).

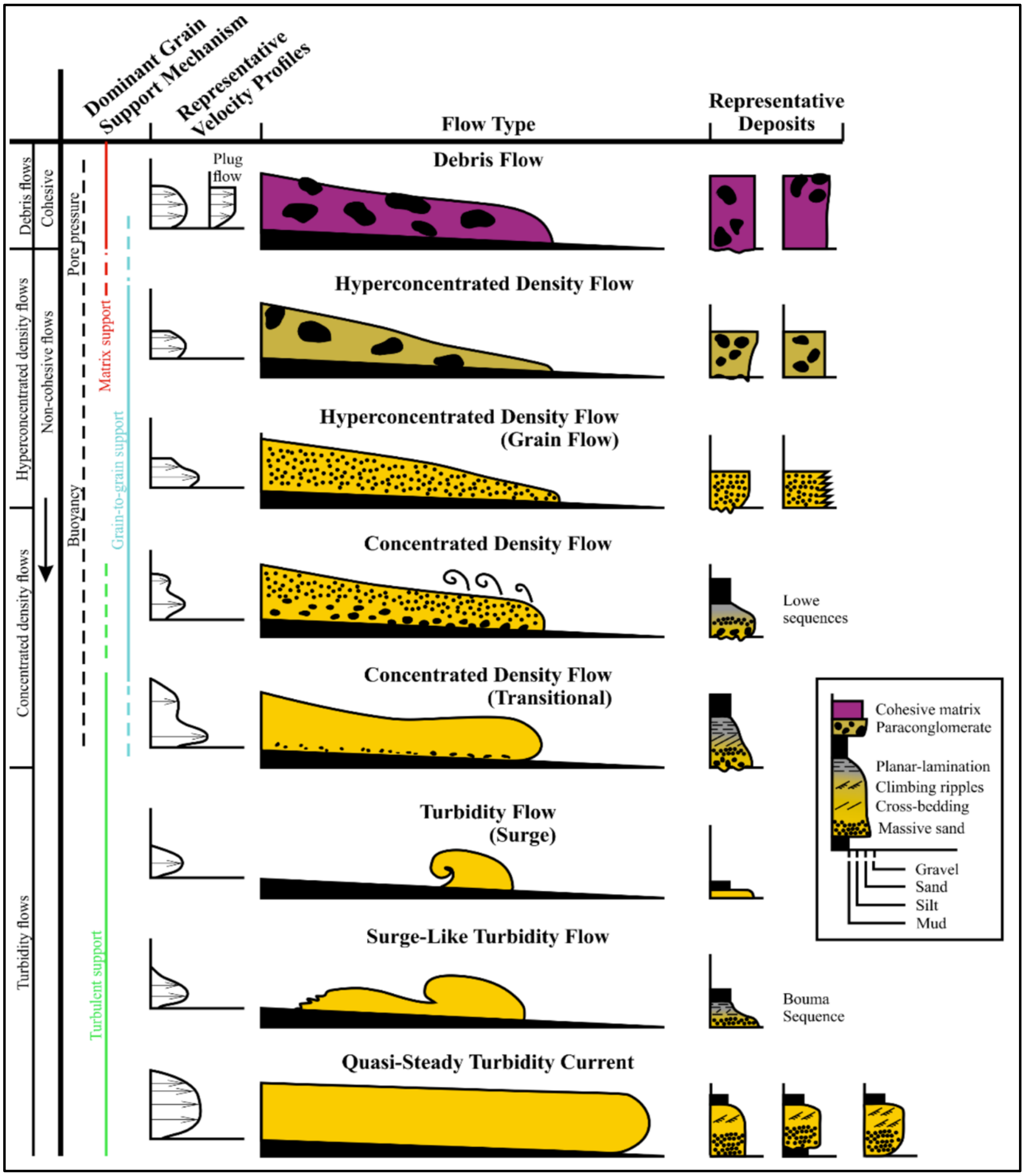

Fig. 1.6: *Conceptual diagram illustrating the classification of subaqueous sediment-gravity flows. The framework distinguishes between cohesive and non-cohesive (frictional) flows, with the latter further categorized into hyperconcentrated flows, concentrated flows, and turbidity currents. The diagram also depicts typical grain-support mechanisms, velocity profile, flow geometries, and representative deposits (Redrawn by Billington, 2019 from Mulder and Alexander, 2001).*

1.8.3 Non-cohesive Flows

Non-cohesive, or frictional flows, are generally Newtonian fluids that lack yield strength and exhibit limited cohesive strength. This is primarily due to the absence of significant electrostatic interactions between unconsolidated sediment particles, in contrast to cohesive flows (Mulder and Alexander, 2001). These flows are primarily influenced by frictional interactions between particles and in the classification of Mulder and Alexander (2001) are subdivided into three categories. Subdivisions are delineated by the principal sediment-support mechanisms, which include grain-to-grain interactions, buoyancy, fluid turbulence, hindered settling, pore pressure, and bed support. The dominant sediment-support mechanism is controlled by parameters like sediment concentration, flow conditions, sediment type, and grain size distribution. Mulder and Alexander (2001) identified three categories of frictional flows: hyperconcentrated density flows, concentrated density flows, and turbidity currents (Fig. 1.7).

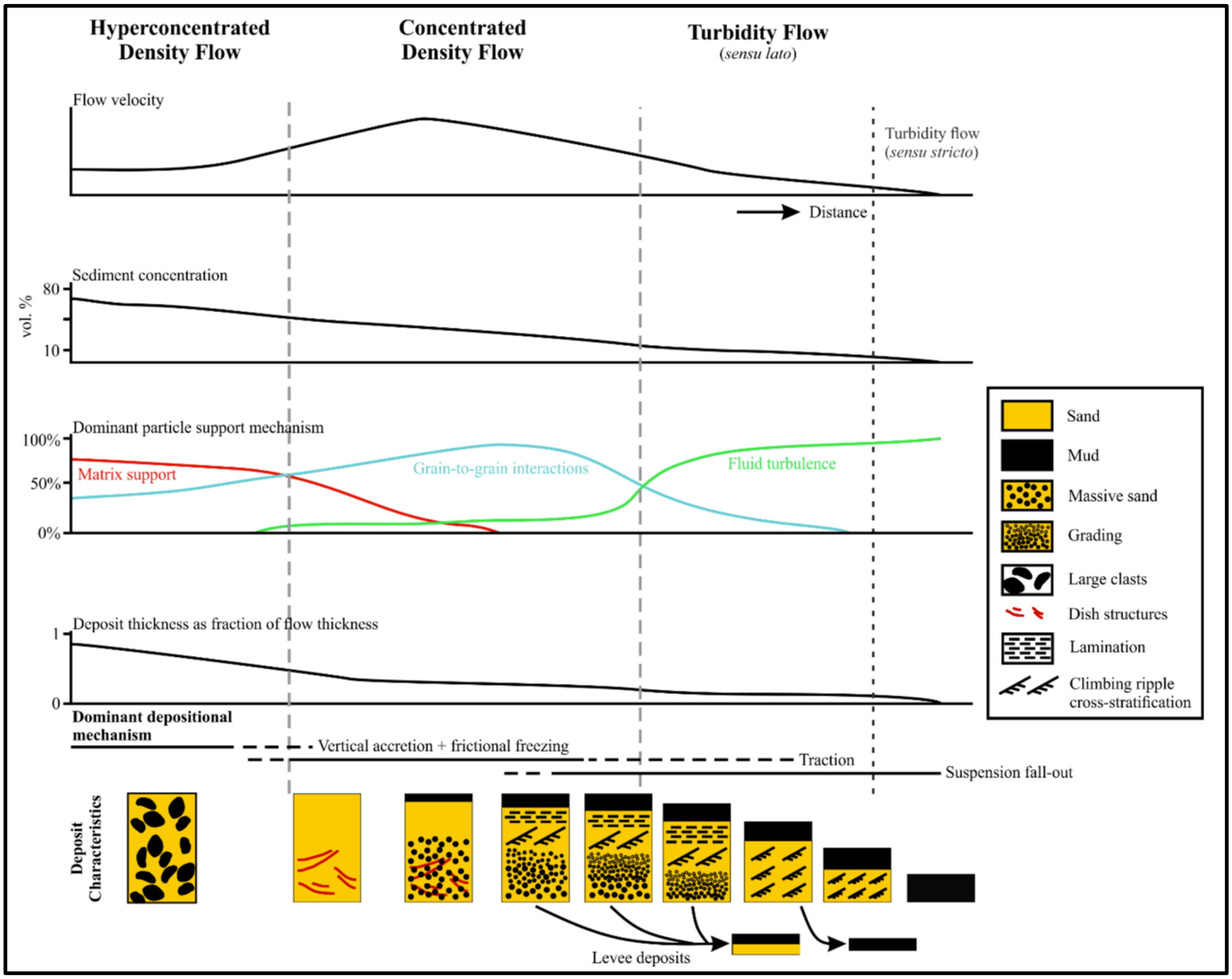

Fig. 1.7: *Schematic diagram showing the progression of frictional flow characteristics across a mechanical continuum, with flow types distinguished by varying sediment concentration. These concentration differences influence both flow dynamics and resulting depositional features. (Adapted from Mulder and Alexander, 2001; redrawn by Billington, 2019).*

1.8.4 Hyperconcentrated Density Flows

Hyperconcentrated density flows, or grain flows, are defined as flows in which sediment volume concentration exceeds 25%. This compares with sediment concentration in cohesive flows but differs in the main particle support mechanism (Mulder and Alexander, 2001). In hyperconcentrated density flows grain-to-grain interaction is the main particle support mechanism (Mulder and Alexander, 2001). If under (transport) capacity flows can erode the bed and may transform downslope into concentrated flows if sufficiently diluted by fluid entrainment. The primary depositional mechanism in these flows is frictional freezing resulting from grain-to-grain interaction, leading to deposits characterized by massive silt, sand, or gravel, occasionally displaying local inverse grading (Mulder and Alexander, 2001).

1.8.5 Concentrated Density Flows

Concentrated density flows are differentiated from hyperconcentrated density flows based on sediment volume concentration but entail the same principal grain support mechanism. The sediment concentration of concentrated density flows ranges from 10–25%, and grain-to-grain interaction causing dispersive pressure is the primary particle support mechanism (Mulder and Alexander, 2001). In addition, buoyancy, fluid turbulence, pore pressure, hindered settling, and bed support collectively contribute to the sediment-support mechanisms within these flows with fluid turbulence becoming the main support mechanism if dilution by fluid entrainment becomes sufficient (Mulder and Alexander, 2001).

Lowe sequences were introduced by Lowe (1982) and provides insight into the depositional architecture of these flows. Lowe sequences typically display a characteristic upward-fining pattern due to differential particle settling, where coarser sediments are deposited initially, followed by a gradual transition to finer-grained deposits as the flow wanes. Lowe (1982) introduced a comprehensive six-part classification of concentrated density flow deposits, divided into two main categories: gravel-rich deposits (R1, R2, R3) and sand-rich deposits (S1, S2, S3) (Fig. 1.8). The gravel-rich facies are deposited first and include: R1 – structureless gravel; R2 – inverse grading resulting from traction carpet deposition; and R3 – normally graded gravel deposited from suspension. In contrast, sand-rich deposits include: S1 – bed load transport manifest as either planar- and/or cross-stratified sandstone; S2 – reverse graded fine- to coarse-grained sandstone and is the product of traction carpet deposition as sedimentation rate increases; and S3 – massive or normally graded sandstone deposited by suspension fallout (Lowe, 1982).

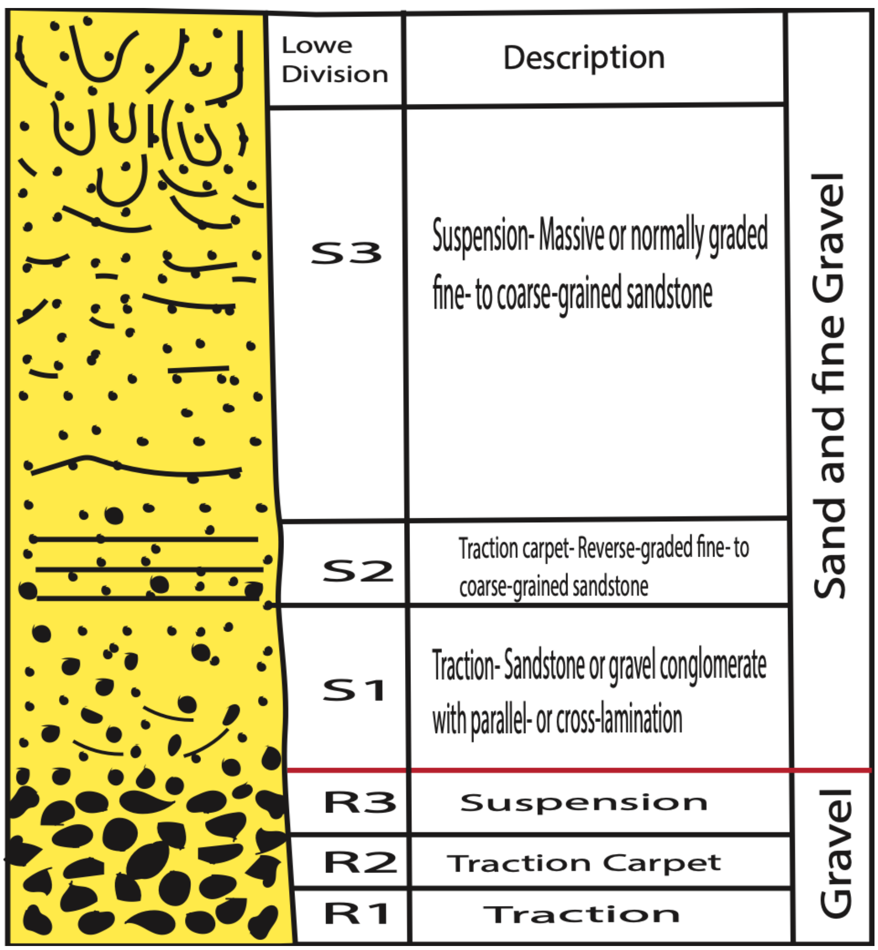

Fig. 1.8: *Idealized Lowe sequence for concentrated density flows showing typical grain size profile and sedimentary structures along with primary sedimentation type. (redrawn from Lowe, 1982).*

1.8.6 Turbidity Currents

Turbidity currents are the most common frictional flow and are considered the primary mechanism for transporting clastic sediment into the deep oceans (Arnott, 2010). Functioning as Newtonian fluids, turbidity currents exhibit sediment concentrations < 9 vol%, a threshold defined by Bagnold (1962) and known as the Bagnold limit (at 9 vol% spacing between adjacent particles is of the order of particle diameter). At this sediment volume concentration the main particle support mechanism is fluid turbulence, diminishing the effect of grain-to-grain interactions and pore pressure due to ambient fluid entrainment and consequent flow dilution (Mulder and Alexander, 2001; Arnott, 2010).

An idealized turbidity current exhibits a longitudinal structure comprising three interconnected sections: the head, body, and tail (Fig. 1.9). The head features an overhanging nose formed through basal friction and mixing with the surrounding fluid, transporting sediment-rich fluid back toward the body (Kneller and Buckee, 2000; Arnott, 2010). To sustain the flow, the body must continuously supply sediment to the head, which moves at a velocity 30–40% faster than the head. Additionally, the three segments of a turbidity current host distinct sediment populations, causing longitudinal differentiation by grain size. Coarser sediment concentrates in the lower part of the head, displacing fine sediment upward and backward into the body. This process eventually forms a dilute dispersion of fine-grained, low-density sediment, constituting the tail of the flow (Kneller and Buckee, 2000; Arnott, 2010).

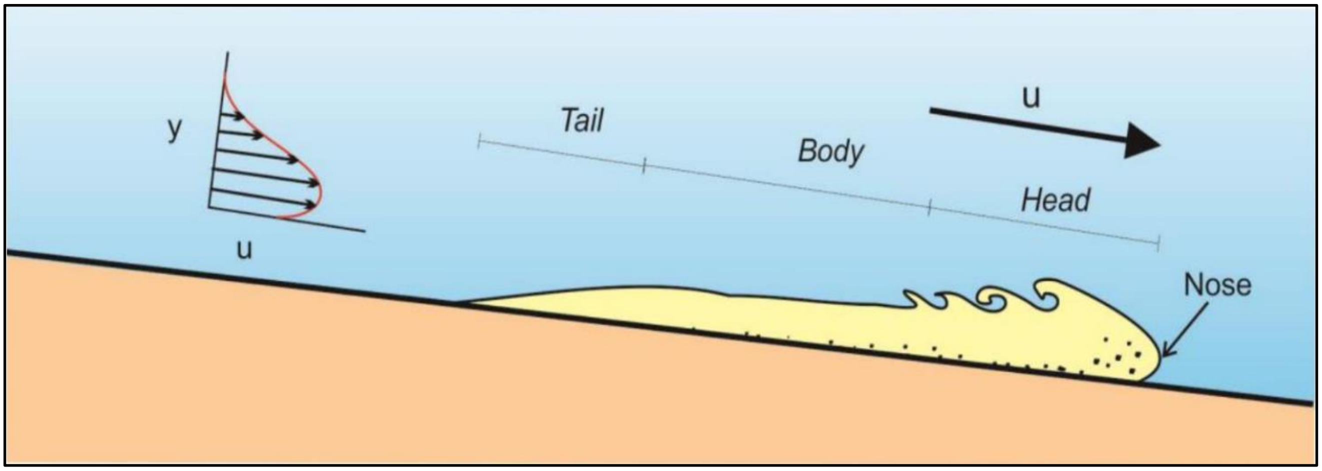

Fig. 1.9: *Schematic diagram of the longitudinal structure of a turbidity current showing a distinct head, body, and tail. The head features an overhanging 'nose' caused by friction at both the upper and lower flow boundaries (Kneller and Buckee, 2000). The velocity profile to the left indicates that flow velocity increases from the bed, peaks at around 20–30% of the total flow thickness and then declines toward the top (Mulder and Alexander, 2001). Diagram adapted from Navarro, 2016).*

The sedimentary deposit formed by a turbidity current is commonly termed a turbidite. Bouma (1962) was the first to detail the vertical succession, now recognized as the classical turbidite or Bouma sequence, and believed to be formed by a decelerating low-density turbidity current with a volume sediment concentration less than the Bagnold limit. The Bouma sequence is characterized by five divisions, T_a to T_e (Fig. 1.10). The T_a division consists of massive or graded, coarse- to medium-grained sand deposited directly from suspension. The absence of traction sedimentary structures like planar lamination or cross-stratification is attributed to the high rates of suspension fallout that hinder the development of tractional features (Arnott and Hand, 1989), or alternatively, insufficient near-bed density stratification that negates the development of bed-surface defects that would then evolve into raised bed forms like ripples and dunes (Tilston et al., 2015). Overlying the T_a division, the T_b division is composed of planar-laminated, medium- to fine-grained sand, indicating reduced rates of sediment fallout with recent studies suggesting that planar lamination forms through traction transport on an aggrading bed surface that lacks the necessary bed defects for angular bedform development, such as ripples and dunes (Tilston et al., 2015). The T_b division is succeeded by cross-stratified fine- to very fine-grained sand (T_c), interpreted to be formed by migrating current ripples (Stow and Bowen, 1980; Khan, 2012). The T_d division comprises alternating siltstone and claystone laminae related to alternating rheological states in a near-bed zone of elevated sediment concentration and effective viscosity, and laminar flow conditions (Al-Mufti and Arnott, 2024). Finally, the T_d is capped by the T_e division, consisting of mudstone deposited through fine-grained suspension fallout (Lowe, 1982).

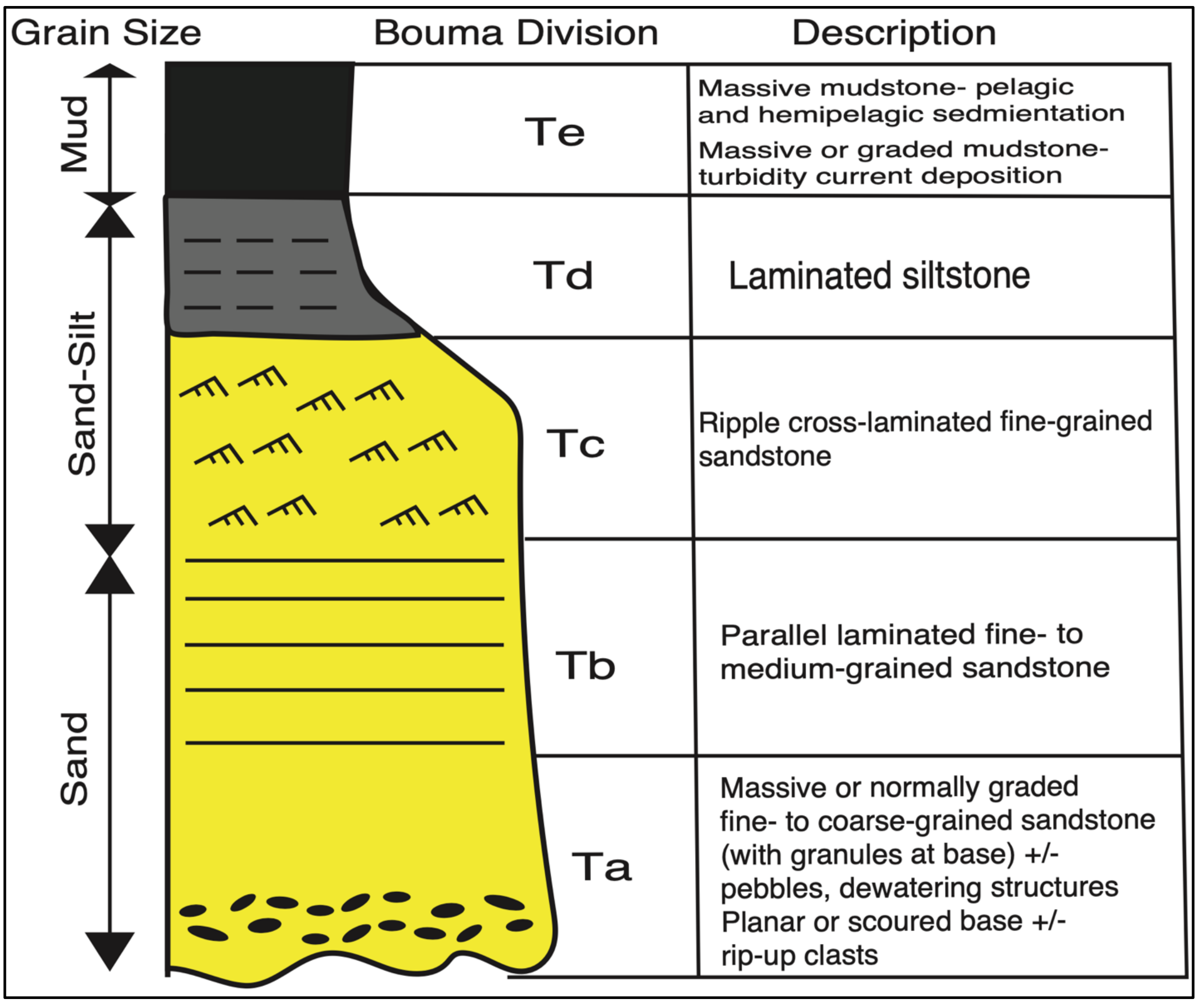

Fig. 1.10: *Complete Bouma sequence showing grain size and sedimentary structures observed in each division (redrawn and modified from Bouma, 1962).*

1.8.7 Mass Movement Deposits

Mass movement or mass wasting deposits represent masses of sediment, induced by gravity, moving coherently downslope along distinct failure planes (Shanmugam, 2006; Arnott, 2010). Mass movements can occur suddenly or gradually and are initiated when the force of gravity exceeds basal friction and tensile strength in the sedimentary mass (Stow, 1985). This downslope movement persists until the resisting forces, primarily friction along the base, overcome the gravitational force, leading to en-masse deposition (Shanmugam and Moiola, 1997). There are several types of mass movement deposits, each characterized by the material involved, the mechanism of movement, the velocity, and the scale of the event (Shanmugam, 2006). In deep marine settings the most common mass movement deposits are slides and slumps.

A slide or rockslide is a type of landslide that can be triggered by various factors, including gravitational oversteepening, earthquakes, volcanic activity, or storms. Slides occur when a mass of rock or consolidated sediment detaches from a slope and moves rapidly downward, often along a planar surface such as a bedding plane, joint, or fault (Pickering et al., 1986). The eventual slide deposit often consists of large, angular rock fragments separated by listric faults and/or pulverized sediment (Shanmugam, 2021). In contrast, slumps are characterized by mass wasting that involves the downward and outward movement of coherent sediments over a concave-upward or spoon-shaped failure surface (Shanmugam, 2021). Slumps are typically associated with the instability of sedimentary layers, often occurring in areas with weakened or water-saturated sediments and are typically slower than slides (Campbell, 2005). The key characteristics of slump deposits include features indicating more ductile rather than brittle (slide) deformation, and include rotated blocks that have rotated backward relative to the direction of movement due to the rotational nature of the slump, folding of lamination in discrete blocks, and a head scarp that marks the detachment zone of the slump mass, which commonly is a steep or vertical face (Campbell, 2005). The surface of slump deposits are usually irregular, with a series of mounds and depressions caused by the disintegration of the moving mass and the rotation of blocks.

During downslope movement, a slide may transform into a slump, characterized by the mass moving along an upward-concave basal detachment surface, giving rise to a variety of internal deformational structures marked by evident contortion and rotation (Stow, 1985). In some cases, the entrainment of ambient fluid into the slide or slump causes them to expand, and eventually, particles to become suspended in the fluid and a frictional flow is formed (Fig. 1.11) (Shanmugam et al., 1994).

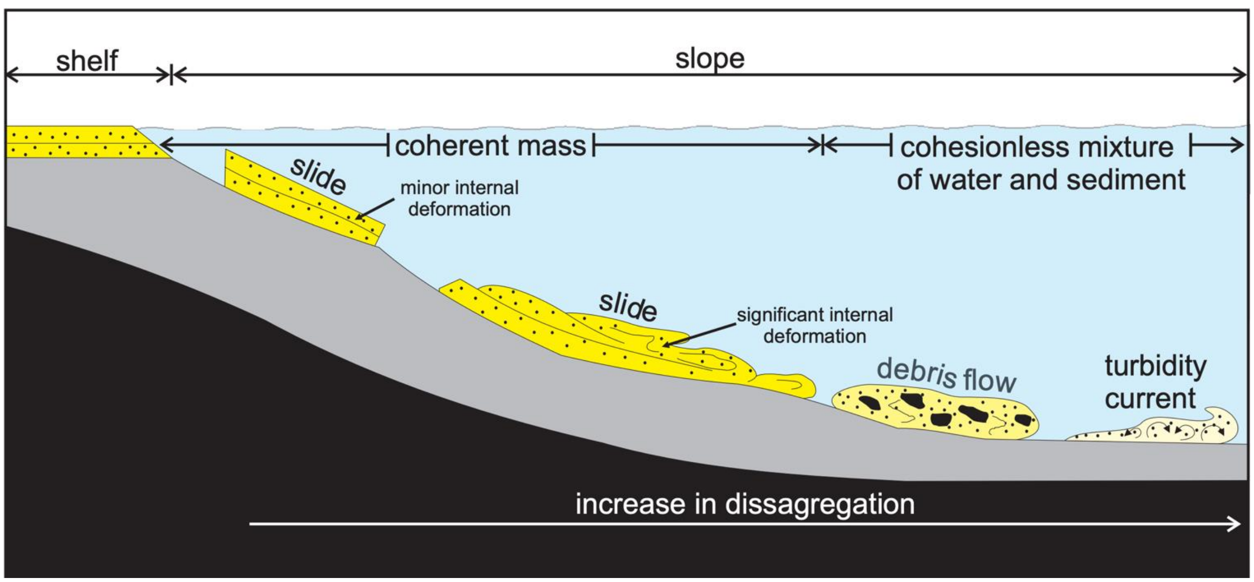

Fig. 1.11: *Schematic diagram depicting the spectrum of sediment gravity flows and their general downslope progression from coherent slides to fully fluidized, non-cohesive flows. Slides originate from failure of a gravitational unstable sediment mass and are characterized by limited, mostly brittle, internal deformation, which idealistically intensifies (i.e. more ductile deformation) downslope as slides transition into slumps. With continued entrainment of ambient fluid slumps transform into debris flows, and ultimately into turbidity currents. (adapted from Khan, 2012; after Shanmugam et al., 1994).*

1.9 Deep-Marine Channels and Levees

1.9.1 Submarine Channels and Levees Overview

Deep-water channels are prominent geomorphological features on modern continental slopes and serve as the primary pathways for transporting sediment basinward via sediment gravity flows (Mutti and Normark, 1987; Covault et al., 2014). The study of the sedimentological and stratigraphic characteristics of deep-marine channels has advanced recently with the application of high-resolution 3D seismic data from modern and ancient turbidite systems (Mississippi fan, Bengal fan etc.), along with detailed outcrop and core studies (Arnott, 2010).

The structure and sedimentary patterns of deep-marine channels are partly controlled by base level, which is linked to the equilibrium profile. In deep marine environments, base level, also termed gravity base, defines the maximum basinward extent a turbidity current can travel (Kneller, 2003). When the base level remains constant and the channel is in equilibrium, sediments bypass the area and are deposited further downslope (Fig. 1.12A). Under these conditions, channels are limited to migrating within a plane that is parallel to the equilibrium profile, similar to the behaviour of meandering belts in sinuous, continental river systems. This results in minimal aggradation, leading to a stratigraphic record characterized by one or more laterally migrating channel bodies with rare lateral accretion deposits (Arnott, 2010; Kneller, 2003). Disequilibrium causes compensatory adjustments in channel behaviour: base-level fall steepens the gradient, enhancing incision (erosion) and sediment bypass, whereas base-level rise flattens the profile, promoting aggradation and vertical stacking of channels (Fig. 1.13).

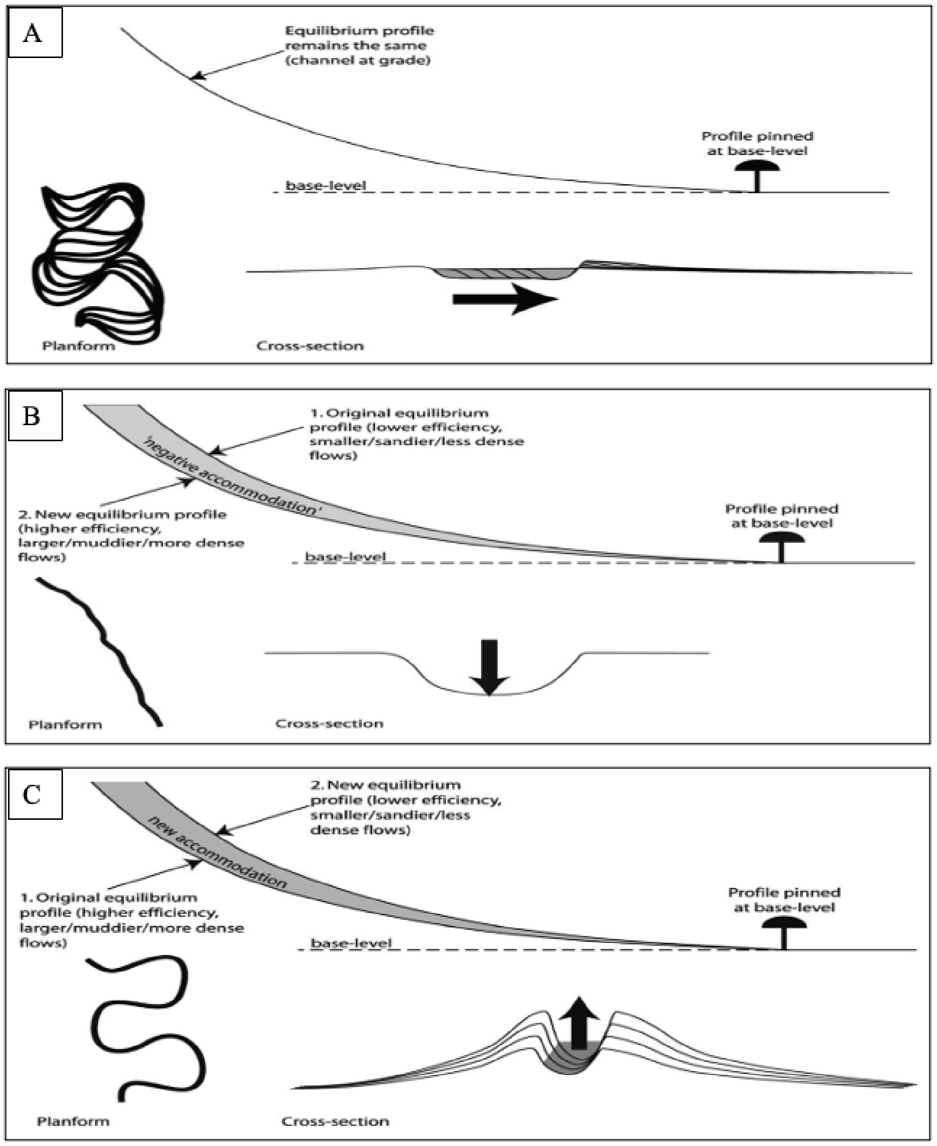

Fig. 1.12: *A) Schematic illustration of a channel profile at grade, showing generalized planform and cross-sectional view. Flow conditions remain constant and most sediment is bypassed downslope closer to the base level. B) Schematic illustration of erosional channel, the equilibrium profile lies below the slope profile resulting in erosion. C) The equilibrium profile lies above the slope profile resulting in aggradation of the channel (Kneller, 2003).*

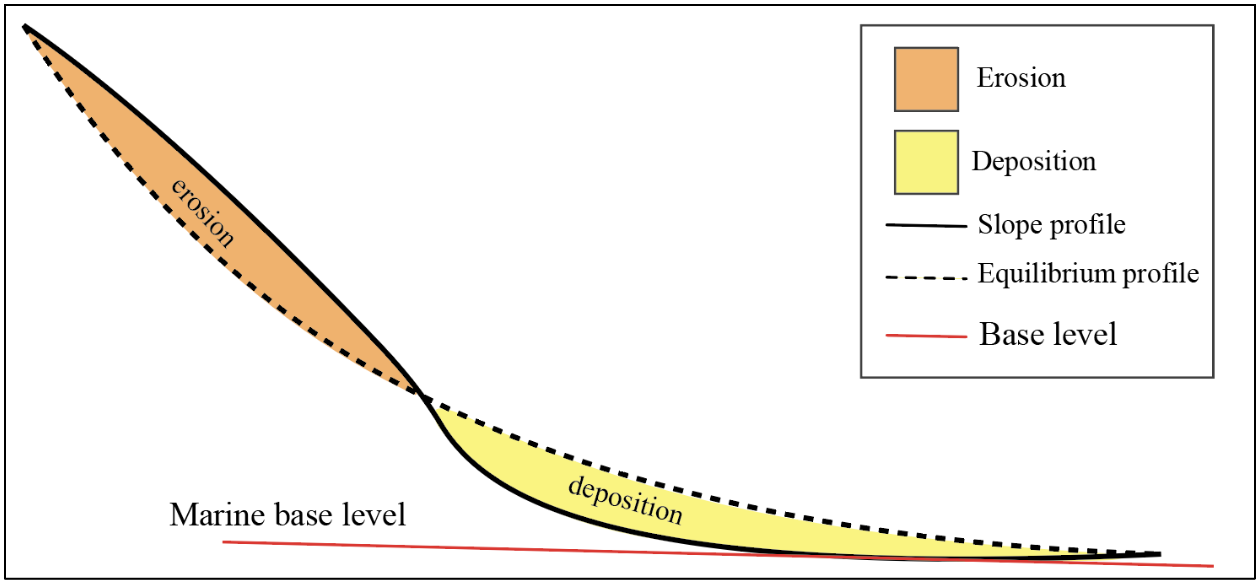

Fig. 1.13: *Schematic illustration of equilibrium profile in relation to actual slope profile (modified from Samuel et al., 2003).*

In both ancient and modern turbidite systems, three main types of channels have been identified: erosional, depositional, and mixed erosional-depositional (Mutti and Normark, 1987; Pickering et al., 1995; Clark and Pickering, 1996). Erosional channels develop when flow conditions change, causing the channel profile to rise above the graded profile. This results in substrate erosion and a decrease in channel slope. These channels generally have low sinuosity, occur on steep slopes, and are often linked with frequent channel avulsion (Kneller, 2003; Clark and Pickering, 1996). Conversely, aggradational or depositional channels are flanked by depositional levees, which over time, increasingly confine the channel. In these channels the equilibrium profile lies below the graded profile, leading to aggradation, and accordingly, increase in channel slope.

1.9.2 Evolution of Deep-Marine Channels

Submarine channels typically evolve through four distinct phases: inception, bypass, filling, and abandonment (Mutti and Normark, 1987; Clark and Pickering, 1996). During the inception phase channels experience net erosion as multiple high-efficiency sediment gravity flows scour a prominent, sharp-based topographical low that facilitates sediment transport further into the basin (Clark and Pickering, 1996; Arnott, 2010; McHargue et al., 2011). The bypass phase follows, characterized by flows that neither significantly erode nor deposit sediment except for laminated mudstone and some clast-rich lags from partially bypassing flows (Clark and Pickering, 1996; McHargue et al., 2011). As flow efficiency decreases over time sediment begins to accumulate in the channel, beginning the backfilling process (Gardner and Borer, 2000). During filling, channels typically show a progression of lithofacies that indicate different positions in the channel, ranging from channel axis, to off-axis, to channel margins. Axial deposits are usually composed of thick, coarse-grained sandstone beds whereas channel-margin facies consist of interbedded fine-grained sandstone and mudstone; off-axis strata have an intermediate composition (Clark and Pickering, 1996; McHargue et al., 2011). The final phase of submarine channel evolution is channel abandonment when an upstream avulsion redirects the flow along a new path within the broader channel belt or more regional turbidite system (Posamentier and Kolla, 2003).

In their evolution, deep-sea channels often show an initial phase of lateral migration of successive channels followed by aggradation with minimal lateral movement (Peakall et al., 2000; McHargue et al., 2011). According to McHargue et al., 2011, the degree of channel organization is influenced by the relief of unfilled channel elements at the time of abandonment. Early channels, which exhibit limited relief and are poorly confined, lead to the accumulation of sand-rich deposits that create positive topography. This leads to younger channels forming in adjacent bathymetrically lower areas forming a disorganized channel stacking pattern (Fig. 1.14A) with poor preservation of overbank/levee deposits due to frequent avulsion and erosion (McHargue et al., 2011). In contrast, channels with greater confinement are typically underfilled resulting in unfilled topography that captures and directs later flows leading to a more organized channel stacking pattern (Fig. 1.14B). This organized pattern is more common in the later stages of channel belt evolution and is associated with flows enriched in fine-grained sediment, which then reduces flow efficiency and promotes channel and levee aggradation (McHargue et al., 2011; Sylvester et al., 2011).

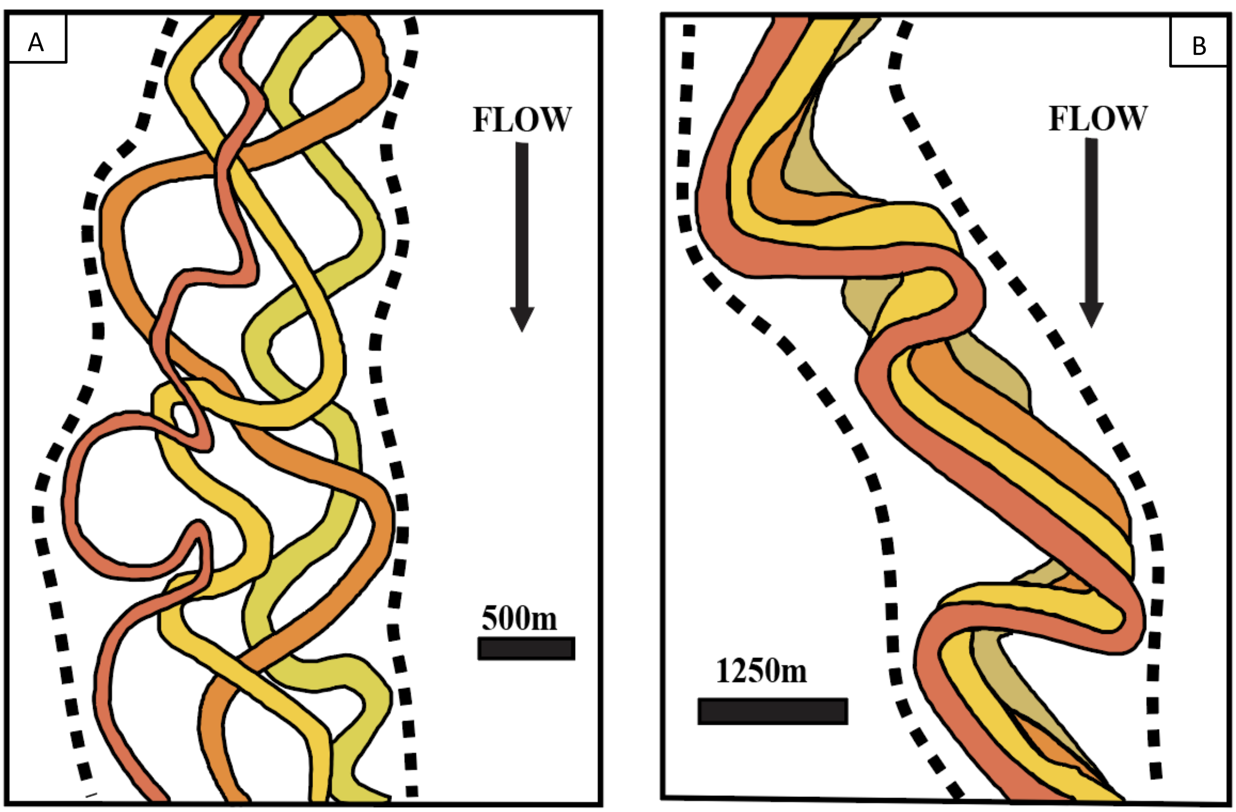

Fig. 1.14: *Plan-view schematic of channel units showing contrasting stacking arrangements of four channel elements. Dashed lined indicate outer confinement of the channel belt. Arrows show downstream direction. A) Disorganized stacking pattern of channel elements with position and architecture of elements varying with little spatial coherence. B) Organized stacking pattern with each channel element closely mirroring the location and geometry of the preceding one (redrawn from McHargue et al., 2011).*

1.9.3 Comparing Submarine Channels to Their Continental Fluvial Counterparts

Channels in fluvial systems are commonly about 200 m wide, less than 20 m deep and have slopes ranging from 0.00001 to 0.05 whereas their deep-marine counterparts are an order of magnitude wider (100 meters to several kilometers), deeper (~ 200 meters) and steeper (0.0001 to 0.02). These differences result from reduced gravity due to buoyancy effects in addition to increased friction at the interface between the sediment laden flow and ambient fluid (Konsoer et al., 2013). However, despite these dimensional differences, deep-marine channels commonly exhibit a sinuous planform geometry resembling that in meandering fluvial channels (Jobe et al., 2016; Wynn et al., 2007).

The differences in depositional records between deep-marine slope channels and fluvial systems can be attributed to fundamental differences in sediment transport mechanisms. In subaerial fluvial systems sand and coarser sediment is typically transported as bedload with finer-grained sediment carried in suspension. Accordingly, traction-transport sedimentary structures, like dune and ripple cross-stratification, make-up most of the sand-rich part of the fluvial channel sedimentary record. In contrast, most of the detrital sediment flux through deep-marine channels is transported in suspension as sediment gravity flows. Deposition is dominated, although not excusive to, by direct suspension fallout forming structureless, typically normally graded strata.

These fundamental differences in flow behavior also influence channel morphology. For instance, sinuous fluvial channels tend to migrate laterally over time with minimal vertical accretion, whereas deep-marine channels typically exhibit more limited lateral migration and instead aggrade steeply while translating downstream (Jobe et al., 2016; Wynn et al., 2007; Sprague et al., 2002). Additionally, in submarine environments, the small density contrast between the flow and ambient water promotes buoyancy-driven superelevation at channel bends, which enhances overspill and facilitates the development of extensive levees—much higher and wider than in fluvial systems (Khan and Arnott, 2011; Wynn et al., 2007; Sprague et al., 2002).

1.9.4 Deep-Marine Levees

Overbanking processes are much more pronounced in deep-water environments compared to fluvial settings. Turbidity currents act as the main transport mechanism in deep-marine channels and their upper boundary is marked by a much smaller density difference between the flow and ambient fluid (Navarro et al., 2007; Khan et al., 2011). This reduced contrast allows the upper part of the flow to expand vertically and overtop channel margins, aided by buoyant support from the ambient water. As a result, sediment is typically transferred long distances beyond the margin of the channel and into the overbank region (Hiscott et al., 1997; Khan et al., 2011). Submarine channels are flanked by levees (Fig. 1.15) formed through three main overbanking processes: flow stripping, inertial overspill and continuous overspill (Piper and Normark, 1983; Clark and Pickering, 1996; Khan et al., 2011).

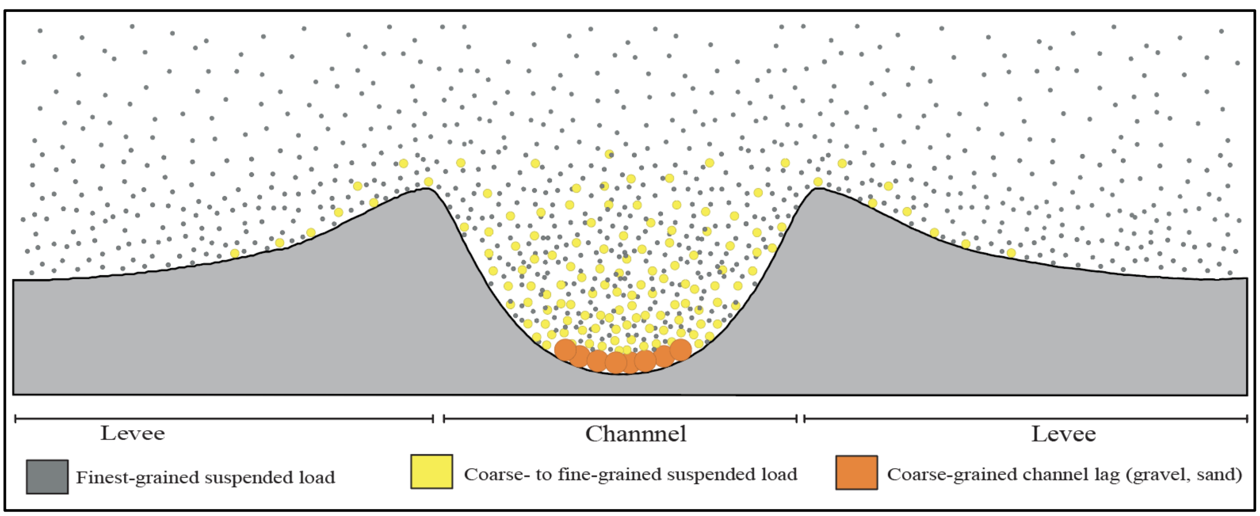

Fig. 1.15: *Cross-section illustration of a leveed channel. Coarse-grained, dense basal portion of the flow remains confined within the channel whereas the finer-grained portion of the flow is concentrated in the upper part of the flow allowing it to be more prone to overspill onto the channel margin and accumulate on the levees (redrawn from Cunningham and Arnott, 2021).*

Flow stripping occurs along the outer bends of submarine channels where the momentum of stratified turbidity currents causes the upper, fine-grained part of the flow to separate from the lower, denser part (Piper and Normark, 1983; Arnott, 2010). This less dense, upper layer then escapes the channel confines and spreads laterally over the channel margin, while the denser, sand-rich, basal part continues its confined path downslope. The phenomenon is accentuated by superelevation (inertial overspill), where flow inertia causes flow thickness to increase along the outer bend thereby accentuating overspill – a process that in submarine systems compared to their subaerial counterparts is markedly greater due to the reduced density difference between the flow and the ambient fluid (Khan and Arnott, 2011; Posamentier and Kolla, 2003). Inertial overspill also involves the momentum of the entire flow not just its dilute upper portion overriding the channel margin (Hay et al., 1983). Both processes preferentially deposit sediment on the outer bend of the channel, leading to asymmetrical levee development with thicker, more sand-rich levee deposits along the outer bend compared to the inner bend.

In contrast, continuous overspill occurs when the thickness of the throughgoing turbidity current exceeds the height of the levee crest, allowing the upper part of the flow to spill uniformly over both sides (Peakall et al., 2000; Kane et al., 2007; Arnott, 2010). As this upper, finer-grained part separates from the main body of the flow it wanes rapidly, resulting in a sharp decline in transport capacity. Consequently, the proximal parts of levees (closest to the channel margin) tend to accumulate coarser-grained, thick-bedded deposits often containing complete or nearly complete Bouma sequences (T_{abcde})(Hiscott et al., 1997; Beaubouef, 2004; Khan and Arnott, 2011; Bergen et al., 2022). As levees aggrade and channel relief increases, only the upper, most dilute parts of the flow overtop the channel margins and deposit thinner, finer-grained turbidites dominated by upper Bouma divisions (T_{cde}) (Hiscott et al., 1997; Kane et al., 2007; Khan and Arnott, 2011;

Bergen et al., 2022). Laterally, most levee deposits fine and thin away from the channel margin – changes that can occur over distances of several hundred meters or more gradually over several kilometers (Clemenceau et al., 1999; Kane et al., 2007; Khan and Arnott, 2011; Bergen et al., 2022). Additionally, inner-bend levees, being thinner and finer-grained, tend to exhibit more gradual thinning and fining trends compared to outer-bend levees (Khan and Arnott, 2011).

Chapter 2: Results

2.1 Facies Description and Interpretation

2.1.1 Facies 1 (F1) Normally Graded and Massive Conglomerate and Sandstone

2.1.1.1. F1 Description

Facies 1 (F1) comprises thick to very thick-bedded (0.3–3 m), normally graded or massive conglomerate and sandstone. Normally graded beds, which make up approximately 60% of the facies, consist primarily of fine granule conglomerate or upper very coarse-grained sandstone grading upward to coarse- or medium-grained sandstone. Massive beds (Fig. 2.1C) make up the remainder of the facies, varying from fine granule conglomerate or very coarse-grained sandstone, with some beds being medium- or upper coarse-grained sandstone. Basal contacts are usually amalgamated (40-60% of beds) where the base of the bed is interpreted to be marked by a sharp increase in grain size (Fig. 2.1A), which commonly coincides with the appearance of mud intraclasts. Soft sediment deformation structures are present locally at the base of some beds, specifically load and flame structures and rare sandstone injections. Load structures reach lengths of 5–30 cm and widths of 5–25 cm, whereas flame structures range from 2–20 cm long and 5–25 cm wide. Sharply bounded, sub-horizontal sandstone injections up to 30 cm long and 15 cm wide are common along the base of channel units where they extend from the base of sandstone beds into adjacent mud-rich, thin-bedded turbidites. These features reach lengths of up to 30 cm and widths of approximately 15 cm. Less frequently, similar injections occur between amalgamated sandstone beds within a channel fill.

Another notable feature of F1 strata are matrix-supported ‘breccia zones’ in the lower part of most beds that vary from 0.3–2.5 m thick with intraclasts concentrated in a matrix of upper very coarse-grained sandstone or fine granule conglomerate (Fig. 2.1, B and D). Clasts are subangular to rounded and consist of a variety of lithologies including mudstone, carbonate-cemented mudstone, or interstratified sandstone-mudstone. Clasts range from 2–60 cm in length and 5–40 cm in width and are oriented with their apparent long-axis subparallel to the base of the bed.

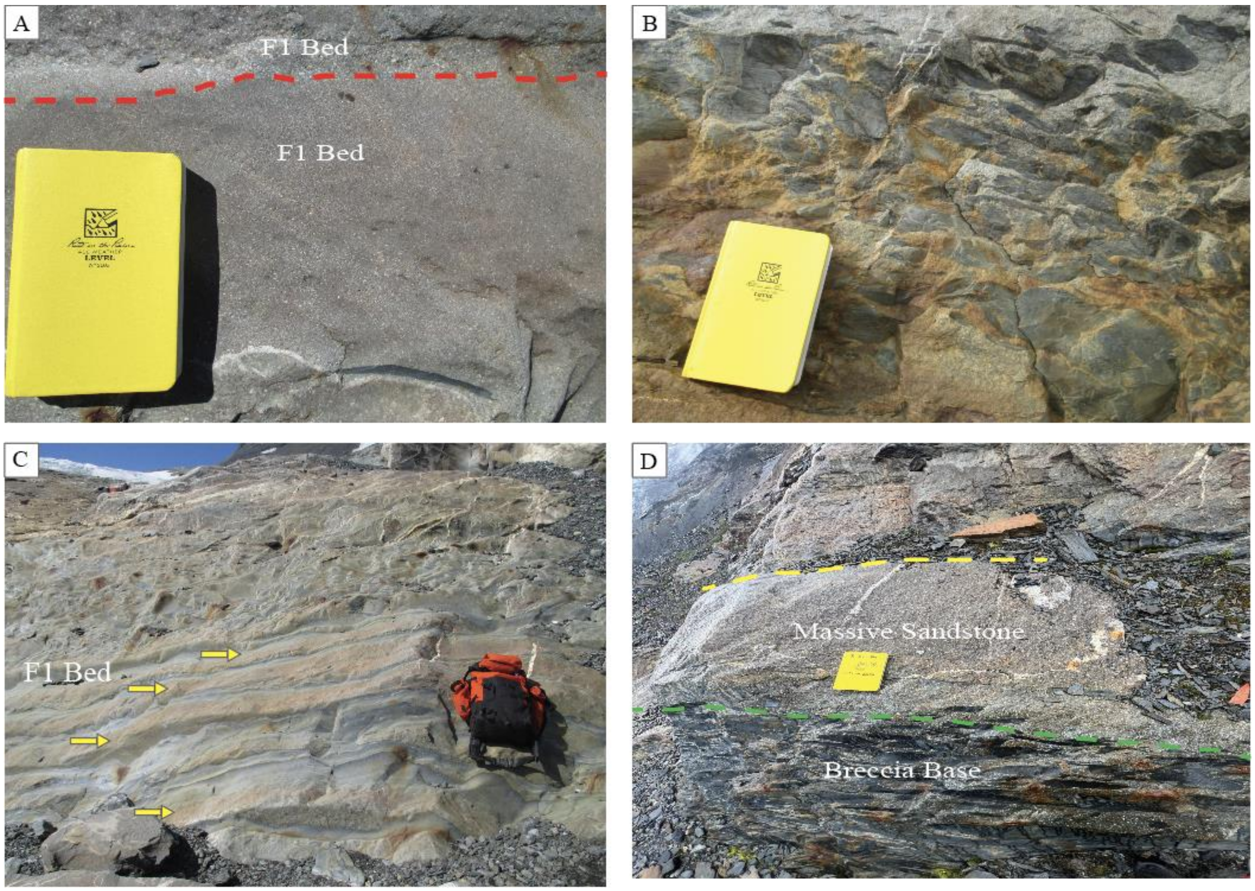

Fig. 2.1: *Outcrop photographs of Facies F1. Field notebook is 20 cm long. A) Two stacked, amalgamated F1 beds. The lower bed is very coarse-grained sandstone with dispersed mud intraclasts grading upward to medium-grained sandstone overlain sharply (red dash line) by upper very coarse-grained sandstone at the base of the upper bed. Field notebook for scale. B) Abundant, subrounded mud intraclasts dispersed in a matrix of upper very coarse-grained at the base of an F1 bed. Field notebook for scale. C) Stack of massive, medium-bedded, medium-grained F1 sandstone beds (highlighted by yellow arrows). Field sack for scale. D) Example of a mud intraclast layer at the base of an F1 bed. Green dash line delineates the top of the brecciate zone, yellow dash line marks the top of the bed. Field notebook for scale.*

In thin section, F1 displays a very poorly sorted, framework-supported fabric composed of approximately 90% framework grains, 5–10% recrystallized matrix, and minor calcite cement (<2%) (Fig. 2.2A). Framework grains are subangular to subrounded and range in size from medium sand to granules. Monocrystalline quartz comprises approximately 80% of the framework grains. Quartz grain boundaries commonly show features like bulging recrystallization, subgrain rotation, and less frequently, sutured boundaries (Fig. 2.2, A and B). Feldspar (including plagioclase and orthoclase) makes up 10–15% of the framework and occurs as finer grains relative to quartz. Feldspar grains are commonly partially or fully altered to sericite (Fig. 2.2D). Lithic fragments are rare (<2%) (Fig. 2.2C), typically siliciclastic, and are often partially altered to muscovite. No internal structures or identifiable textures are observed in these fragments. The matrix occupies intergranular space and is composed of recrystallized clay, occurring as a mixture of muscovite, sericite, and chlorite, in addition to dispersed silt- to very fine-grained quartz and feldspar. Minor pyrite are present, and sparry calcite occurs locally as interstitial cement and as a replacement of feldspar and lithic grains.

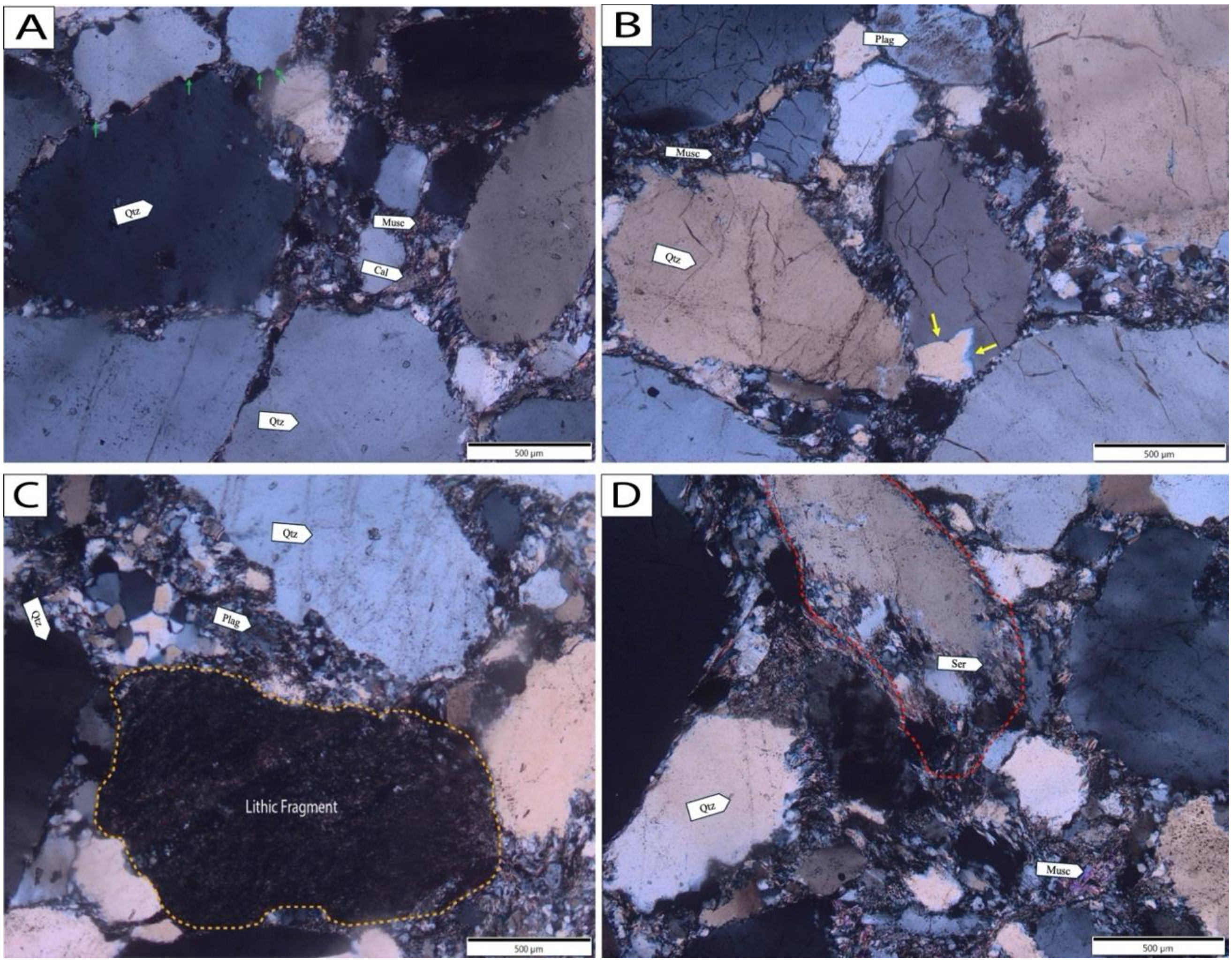

Fig. 2.2: *Thin section photomicrographs of Facies F1 (cross-polarized light, XPL). A) Very coarse-grained, poorly sorted sandstone composed of subrounded quartz (Qtz) grains with a matrix of quartz silt and muscovite (Mus), and minor sparry calcite (Cal). Green arrows indicate quartz grain bulging along grain boundaries. B) Very coarse-grained, poorly sorted sandstone. Yellow arrows highlight subgrain rotation within a quartz (Qtz) grain. C) Coarse-grained sandstone with a lithic, most probably mud fragment (outlined by orange polygon). D) Very poorly sorted, very coarse-grained sandstone containing a plagioclase grain (outlined by red polygon) partly replaced by sericite (Ser).*

2.1.1.2. F1 Interpretation

F1 strata represent the T_a division described by Bouma (1962) or S_3 division of Lowe (1982) and are interpretated to represent deposition from concentrated or hyper-concentrated flows (Mulder and Alexander, 2001). The deposition of F1 strata occurs either rapidly from highly depletive flows (Arnott and Hand, 1989), or incrementally from quasi-steady flows (Kneller and Branney, 1995), and is attributed to the settling of suspended particles (Alexander and Mulder, 2001). The absence of parallel- or cross-stratification (i.e. structureless) is most likely related to the inhibition of the inception and amplification of bed-surface defects due to a thick, plug-like high sediment concentration region at the base of the flow (Arnott and Hand, 1989; Arnott, 2012, Tilston et al., 2015). Uncommonly, beds of F1 are capped by a thin-bedded (2–5 cm) siltstone-mudstone beds (F3) indicating deposition during the final flow stages as the dilute tail of the flow deposited mud by suspension settling (Lowe, 1982) or later hemipelagic fallout (Meyer, 2004). Soft sediment deformation structures, such as flame and load structures, suggest gravitational loading of sand-rich sediment over lower density, fluid saturated, typically mud-rich substrate. This also suggests a short time interval between successive turbidity currents and consequently minimal compaction and maintenance of water-saturated conditions in the seabed.

Erosive basal contacts and 'breccia zones' at the base of some F1 beds are interpreted as the product of hyperconcentrated or concentrated flows with sufficient turbulent stress and flow capacity to scour and entrain previously deposited fine-grained strata (Mutti and Normark, 1987; Talling et al., 2012). The presence of mud-clast breccia zones at or near the base of beds is interpreted as evidence of substrate erosion and incorporation of clasts into the basal part of the flow (Amy and Talling, 2006; Prélat et al., 2009). This process suggests localized substrate failure or fragmentation, potentially enhanced by elevated pore fluid pressures in mud-rich layers in the substrate (Kane et al., 2007).

2.1.2 Facies 2 (F2): Tractional Transport Sandstone

2.1.2.1. F2 Description

Facies 2 (F2) is subdivided into three subfacies. F2.1 (~ 30% of the facies) comprises thin- to medium bedded (3–25 cm), planar-laminated coarse- to medium-grained sandstone that is normally graded to fine-grained sandstone (T_b Bouma division) (Fig. 2.3A). Facies F2.2 comprises the majority of F2 facies (~ 70% of the facies) and is characterized by small-scale, cross-laminated (Fig. 2.3B), very fine- or fine-grained sandstone capped by silty mudstone (T_{cde}). Cross-laminated sandstone comprises a single or 2–4 non-climbing ripple formsets (Fig. 2.3C) with basal contacts being typically planar-abrupt and less commonly erosional with subtle scours 0.5–1 cm deep. Single sets are 0.5–1 cm thick and typically overlain by massive, very thin- to thin-bedded mudstone (1–5 cm). Cosets consisting of 2–4 non-climbing ripple sets are 2–10 cm thick and overlain sharply by a structureless mudstone cap.

F2.3 is uncommon (≤1% of the facies) and consists of thick-bedded (40–80 cm), large-scale cross-stratified sandstone (Fig. 2.3D). Basal contacts are generally erosive and marked locally by scours 10–15 cm deep. Beds consist of high-angle, planar-tabular cross-stratified set of lower very coarse-grained sandstone that range from 10–15 cm thick. Beds pinch out laterally over a few meters and are commonly bounded above and below by upper coarse-grained, massive sandstone. Paleocurrent measurements from F2.2 strata indicate general sediment transport toward the northwest (330°).

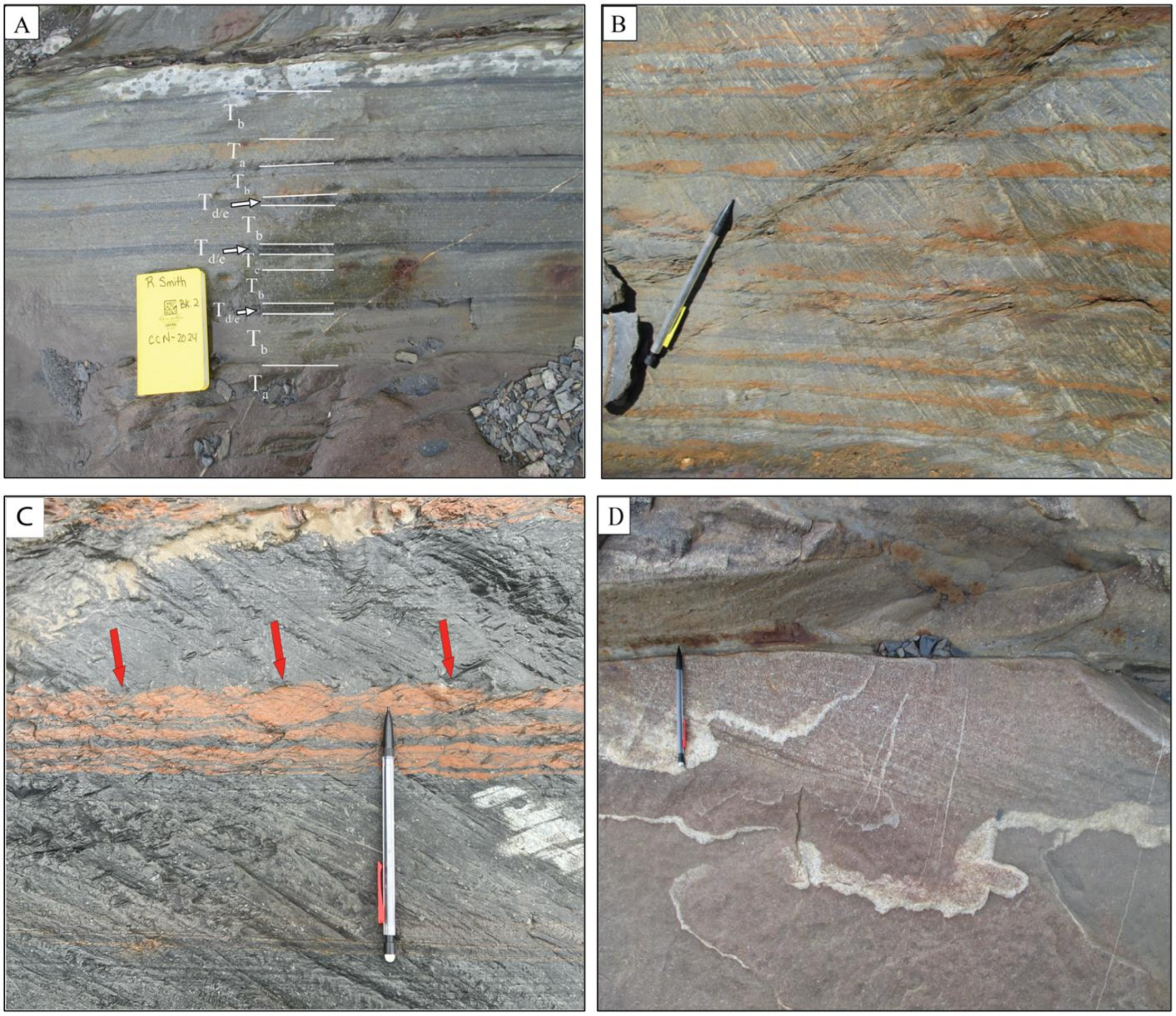

Fig. 2.3: *Outcrop photographs of Facies F2. A) Medium- to thin-bedded, medium-grained lower division turbidites (T_{abde}, T_{bde} or T_{bcde}). T_b divisions consist of plane-parallel laminations of upper medium- to upper fine-grained sandstone. Field notebook for scale. B) Thin-bedded, upper division (T_{cde}) turbidites. The T_c (F2.1) division consists of very fine- to fine-grained sandstone with well-developed single ripple cross-stratified formset overlain by massive silty mudstone (T_{de}). Note the distinctive orange colour of the sandstone beds caused by oxidation of iron-rich calcite cement. Pencil for scale. C) Medium-bedded, upper division (T_{cde}) turbidites. The T_c (F2.1) division (highlighted by red arrows) consists of multiple stacked ripple sets (up to 4 cm thick) capped by a massive silty mudstone (T_{de}). Field notebook for scale. D) Thick-bedded, coarse-grained, high-angle cross-stratified sandstone (F2.2). Pencil for scale.*

In thin section, Facies F2 displays alternating, inclined laminae of very fine- or fine-grained sandstone that appear as dark and light bands under cross-polarized light (XPL). The lighter laminae are relatively coarser grained and moderately to well-sorted, whereas the darker laminae are finer grained with a higher proportion of matrix (Fig. 2.4A). Laminae are inclined approximately 5–10° relative to the thin section edge, with subtle grain alignment parallel to the lamination. Framework grains make up approximately 60% of the sample and are dominated by quartz (90%) with minor feldspar. Intergranular spaces are filled with a matrix of recrystallized calcite and minor clay minerals altered to muscovite and sericite. Additionally, a pervasive sparry calcite cement (Fig. 2.4B) is present in some thin sections of F2, locally comprising up to ~ 25–30% of the sample volume.

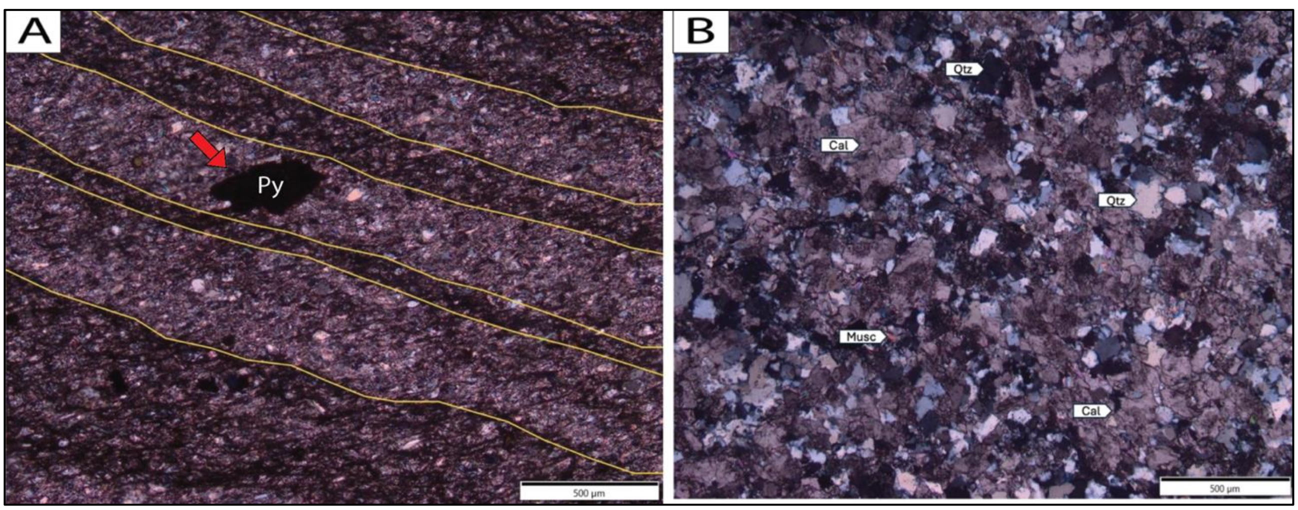

Fig. 2.4: *Thin section photomicrographs of Facies F2 (cross-polarized light, XPL). A) Ripple cross-laminated, fine-grained sandstone showing alternating laminae defined by subtle variations in grain size and clay content (laminae highlighted by yellow lines). Framework grains are dominated by quartz (Qtz) in a matrix of recrystallized calcite. Red arrow points to medium-grained, opaque, authigenic pyrite (Py) grain. B) Cross-laminated, fine-grained sandstone composed of moderately sorted, fine-grained quartz (Qtz) dispersed in a matrix of quartz silt, muscovite (Ms), and sericite (Ser). Note the presence of extensive patches of iron-rich calcite (Cal) cement (~ 25%).*

2.1.2.2. F2 Interpretation

F2.1 beds are interpreted to represent the T_b division of the classical Bouma sequence, deposited from turbidity currents with relatively low rates of sediment fallout and, by inference, lower sediment concentrations than those responsible for the T_a division of F1 strata (Arnott and Hand, 1989). The development of planar lamination within these beds implies near-bed flow conditions that were not conducive for the initiation or amplification of angular bedforms. Such conditions may reflect initially high flow velocities and/or elevated sediment concentrations that suppressed the formation of the small bed irregularities required for ripple or dune growth (Arnott, 2012; Tilston et al., 2015).

Small-scale, cross-laminated beds of F2.2 are interpreted as the T_c division of the classical Bouma sequence (Bouma, 1962). Ripple cross-stratification forms when small topographic irregularities, or "bed defects" change the pattern of fluid flow in the near-bed region that then leads to flow separation, defect amplification, and the growth of angular bed forms (Venditti et al., 2005). These defects originate from hydrodynamic instabilities that develop at the boundary of the slower-moving, sediment-rich bed-load layer and the overlying, faster and less dense near-bed flow (Venditti et al., 2005; Venditti et al., 2006). The instability manifests as a waveform feature that imparts a repeating pattern of erosion and deposition on the bed, namely erosion and sediment transport under the wave trough and flow expansion and sediment deposition forming a bed defect under the wave crest. Eventually, upward growth of the bed defect causes flow separation and rapid amplification of the original bed irregularity, driving the transition from small-scale perturbations to fully developed ripples through a process Venditti et al. (2005) term "defect initiation."

The large-scale, high-angle cross-stratified sandstones of F2.3 are interpretated as the product of downflow-migrating subaqueous dunes. Suspended sediment concentration near the base of the flow created hydrodynamic instabilities similar to those required for the formation of current ripples (F2.2). Under conditions of higher flow velocity, however, these small-scale bed defects expanded into larger dune forms. Dune cross-stratification is relatively rare in deep-marine deposits, which Arnott (2012) attributes to near-bed sediment conditions that suppress bed defect initiation and amplification in turbidity currents moving at velocities otherwise suited for dune growth.

2.1.3 Facies 3 (F3): Planar-Laminated Siltstone, Structureless Mudstone

2.1.3.1. F3 Description

Facies 3 (F3) is characterized by thin-bedded (1–5 cm), planar-laminated siltstone (T_d) overlain sharply by thin-bedded (1–10 cm) mudstone (T_e), consistent with the upper divisions (T_{de}) of the Bouma turbidite sequence. These beds abruptly overlie beds of F1 and F2 strata (Fig. 2.5A), either forming the upper part of more complete turbidites, or occurring as isolated, stacked packages up to 5–10 beds thick (Fig. 2.5B). Basal contacts are exclusively abrupt-planar. The distinct dark blue to grey color of F3 makes it easy to recognize in the field where it contrasts the typical brown or light grey color of F1 and F2 interbeds.

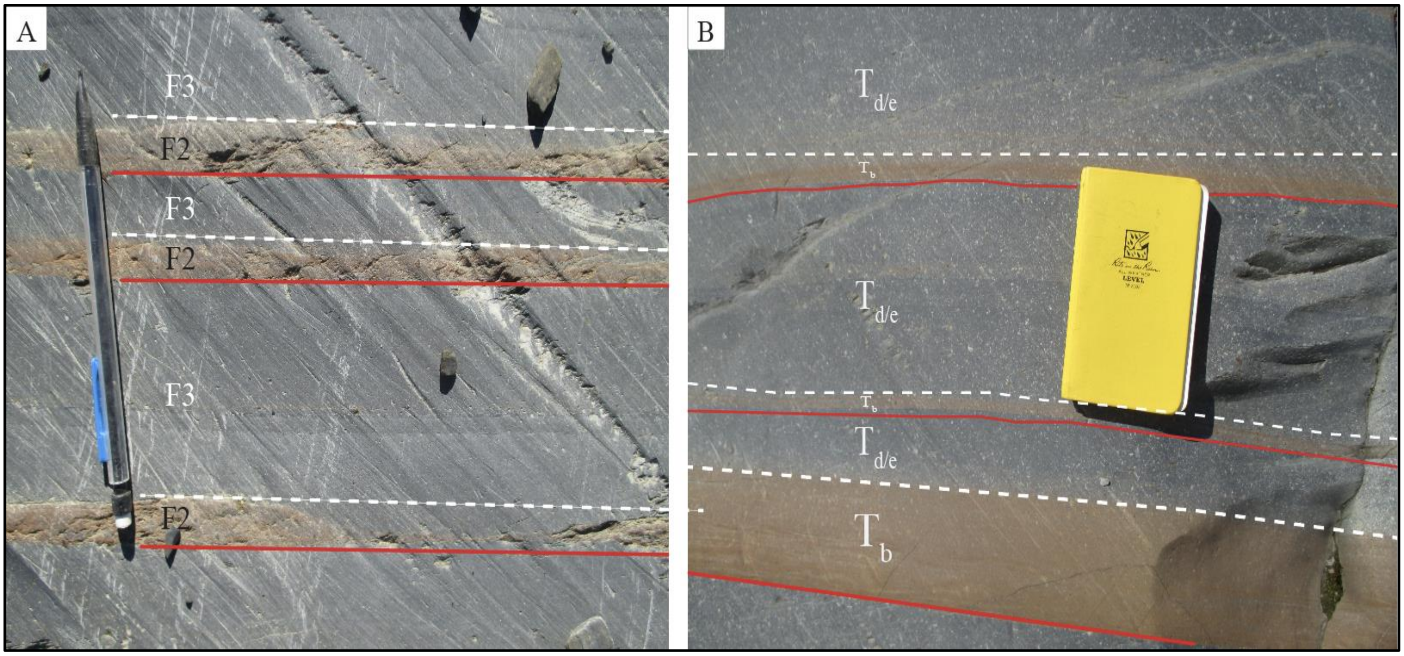

Fig. 2.5: *Outcrop photographs of Facies F3. A) Thin- to medium-bedded, fine-grained, upper division (T_{cde}) turbidites displaying alternating light (F2) and dark (F3) defined by grain size contrasts. Pencil for scale. B) Thin- to medium-bedded lower-division calciturbidites (T_{bde}) consisting of a basal planar-laminated part (T_b) overlain abruptly by planar-laminated siltstone overlain by massive mudstone (T_{de}) (dark blue/grey). Field notebook for scale.*

In thin section, Facies F3 consists of approximately 20% grains and 80% matrix. The grains are mostly very fine-grained, subangular to subrounded quartz and minor feldspar sand grains (Fig. 2.6B). The matrix is composed of muscovite, sericite, and silt-sized quartz grains and is present throughout both siltstone and mudstone intervals. F3 includes planar-laminated siltstone intervals that are overlain by sharp-based, poorly sorted, massive mudstone with dispersed silt-sized quartz grains (Fig. 2.6C). Where observed the contacts between siltstone and mudstone layers occur as sharply alternating light and dark bands. The light bands consist of moderately sorted, very fine-grained to silt-sized quartz, whereas the dark bands contain higher proportion of recrystallized clay minerals and fewer quartz grains.

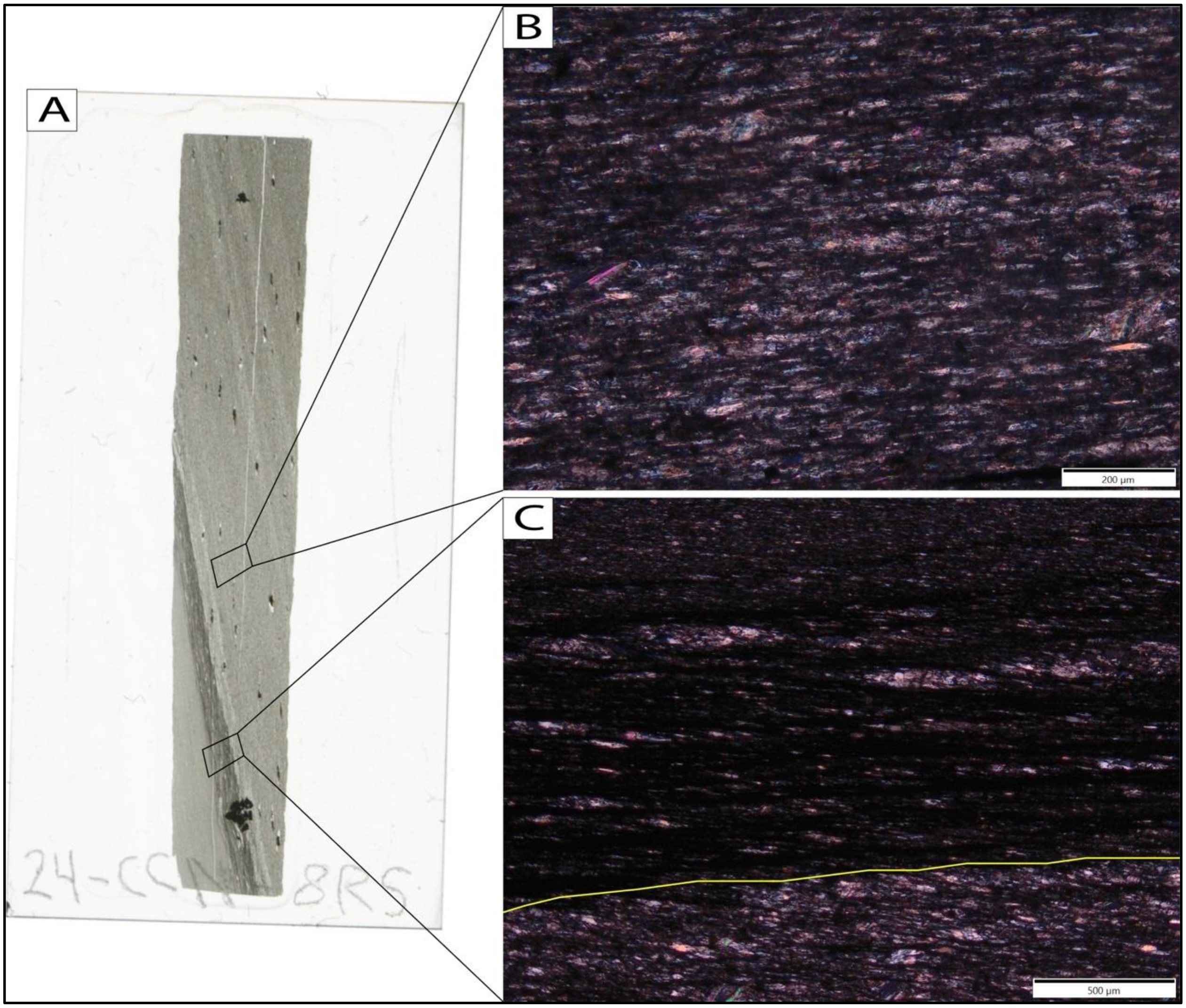

Fig. 2.6: *Thin section photomicrographs of Facies F3. A) Thin section cut through planar-laminated siltstone and structureless mudstone. Arrow indicates way-up. B) Cross-polarized (XPL) photomicrograph showing structureless mudstone with dispersed silt-sized quartz grains and recrystallized matrix composed of muscovite and sericite (T_e division). C) XPL photomicrograph showing structureless mudstone (T_e) overlain sharply (yellow line) by alternating thinly laminated silt-rich and clay-rich layers (T_d).*

2.1.3.2. F3 Interpretation

F3 strata are interpreted to represent the T_{de} division described by Bouma (1962), deposited by fine-grained, low-energy turbidity currents. The depositional model proposed by Al-Mufti and Arnott (2024) explains the origin of planar lamination in fine-grained sediment gravity flow deposits as a product of alternating rheological states in the very-near-bed zone of a thicker, most probably turbulent low-energy turbidity current. Within this submillimeter to millimeter-thick very-near-bed zone (viscous sublayer), high sediment concentration, possibly approaching several tens of percent volume sediment concentration, results in laminar flow conditions and non-Newtonian fluid behaviour. The emplacement of well-sorted silt laminae reflects shear thinning to pseudo-Newtonian conditions and the preferential settling of medium to coarse silt. As silt becomes depleted and the local concentration of clay-size particles increases, lubrication forces, but more significantly, frictional particle interactions increase, resulting in an increase in effective viscosity, and accordingly energy dissipation, causing the flow to shear thicken. This condition is inherently unstable and any external stress perturbation, such as a turbulent burst from the overlying buffer layer or outer flow region, can cause particles to abruptly arrange into transient, tightly packed aggregates termed 'hydroclusters' (Brady and Bossis, 1985). These structures intensify frictional interactions leading to an abrupt and dramatic increase in effective viscosity marked by discontinuous shear thickening and ultimately shear jamming and the rapid en masse deposition of a poorly sorted, clay-rich layer.

Following shear jamming the newly immobilized poorly sorted, clay-rich layer forms the upper surface of the static bed and the cycle repeats with the deposition of the next silt-rich overlain by clay-rich layer. Repetition of this process builds up the rhythmic alternation of planar-laminated siltstone and massive mudstone laminae observed in in the T_d part of a T_{de} turbidite (F3). The capping T_e part of F3 strata represents pure suspension settling of hemipelagic or pelagic sediment with no bed-surface sediment transport.

2.1.4 Facies 4 (F4): Matrix-Supported Conglomerate

2.1.4.1. F4 Description

Facies 4 (F4) consists of subangular to subrounded pebble or granule quartz grains (0.2–1 cm) and lithic clasts dispersed in a silty mudstone matrix (Fig. 2.7A). Strata range from 0.6–13 m thick with lithic clasts that are principally carbonate-cemented mudstone ranging from 10–70 cm long and 2–30 cm wide (Fig. 2.7B), and mudstone clasts that are 2–15 cm long and 2–10 cm wide. Clasts composed of interstratified sandstone-mudstone, which are 50–200 cm long and 20–50 cm wide, are rare and where present are concentrated near the base of the conglomerate unit, whereas other clast types are more generally dispersed throughout the deposit. Bed bases are commonly erosional with relief as much as 50 cm, with clasts, irrespective of kind, oriented with their apparent long-axis parallel to the base of the bed.

In thin section, F4 exhibits a matrix-supported, very poorly sorted fabric and consists of approximately 75–80% matrix and 20–25% dispersed grains. The matrix is primarily clay that has been recrystallized to muscovite and sericite with uncommon fine-grained chlorite porphyroblasts. Silt-sized quartz and feldspar grains are scattered throughout the matrix along with minor calcite cement (<1%) present as pore-filling sparite and partial grain replacements, specifically around altered feldspar grains.

The dispersed grains are mostly fine- to coarse-grained sand in addition to subangular to subrounded granule-sized clasts (Fig. 2.7C). Monocrystalline quartz dominates the dispersed grains (~ 70%), though uncommon polycrystalline quartz is observed. Rarely quartz grains show evidence of bulging recrystallization while feldspar grains make up 5–10% of the dispersed grains and are typically partly to completely altered to sericite (Fig. 2.7D). Lithic fragments comprise 10–15% of dispersed grains and include coarse-grained carbonate clasts and siliciclastic rock fragments. Siliciclastic lithics are primarily fine-grained sandstone-siltstone fragments, some exhibiting internal lamination.

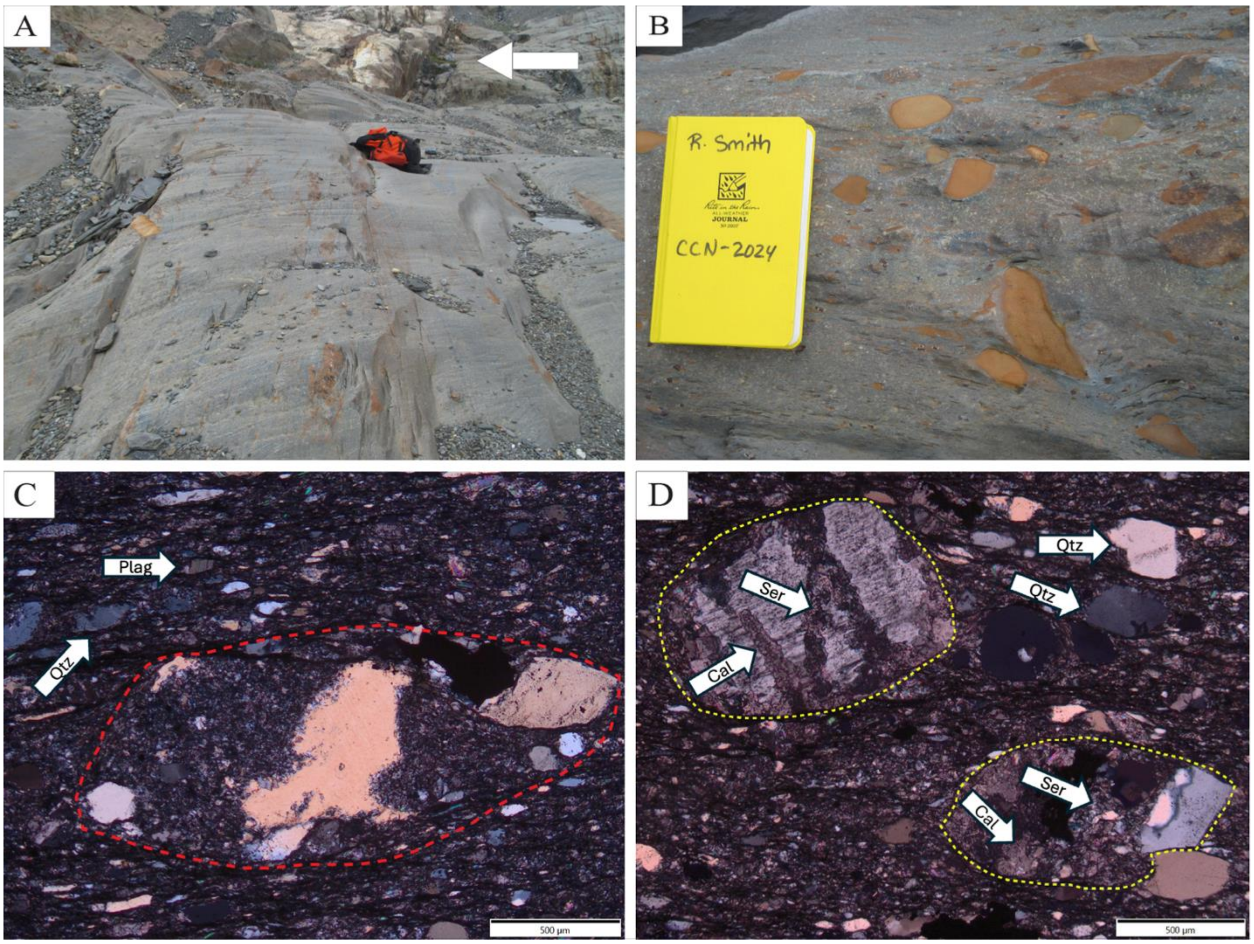

***Fig. 2.7**: Outcrop and thin section photomicrographs of Facies F4. A) Outcrop view of massive, matrix-supported conglomerate. B) Granule- to pebble-sized, subrounded to rounded carbonate-cemented mudstone intraclasts dispersed in a matrix of silty mudstone. Field notebook for scale. C) Thin section photomicrograph (XPL) of Facies F4 containing a granule-sized lithic fragment (outlined by red dash line) set in a matrix of silt-sized quartz (Qtz) and plagioclase (Plag) grains and muscovite (Musc). D) Thin section photomicrograph (XPL) of Facies F4 showing multiple plagioclase (Plag) grains (outlined by yellow dashed lines) partly to fully altered to calcite (Cal) and sericite (Ser). Matrix consist of dispersed quartz (Qtz), feldspar (Plag), and sericite/muscovite (recrystallized detrital clay).*

2.1.4.2. F4 Interpretation

With their sharp upper and lower contacts, lack of internal stratification, and lithic clasts and very coarse sand grains dispersed in a mud-rich matrix, strata of Facies 4 are interpreted to be deposited by cohesive gravity flows, specifically debris flows (Alexander and Mulder, 2001). Dispersed coarse sand grains and larger clasts were principally supported by (cohesive) matrix strength (Rodine and Johnson, 1976; Alexander and Mulder, 2001) aided by buoyancy effects and elevated pore pressure (Alexander and Mulder, 2001; Arnott, 2010). F4 strata deposited en masse when downward growth of the rigid plug extended to the bed casuing basal friction to equal or exceed the gravitational force driving the flow downslope (Iverson, 1997; Mulder and Alexander, 2001). The thickness of F4 deposits corresponds closely to the thickness of the parent flow, as post-depositional cohesive matrix strength helps preserve the original dimensions of the flow (Iverson, 1997).

2.2 Channel Unit and Mud-rich Unit Descriptions

2.2.1 Hierarchical Classification of Channel Elements in Deep-Marine Settings

Deep-marine channels are complex physiographic and stratigraphic features that evolve through erosion, sediment bypass, and deposition. Their stratal organization follows a hierarchal structure, with distinct architectural elements recording the history of channel evolution. This classification (Fig. 2.8) includes channel fills, channel units, and channel complexes (and channel complex sets), each representing different scales of stratal architecture (Mutti and Normark, 1987; Deptuck et al., 2003; Bain and Hubbard, 2016).

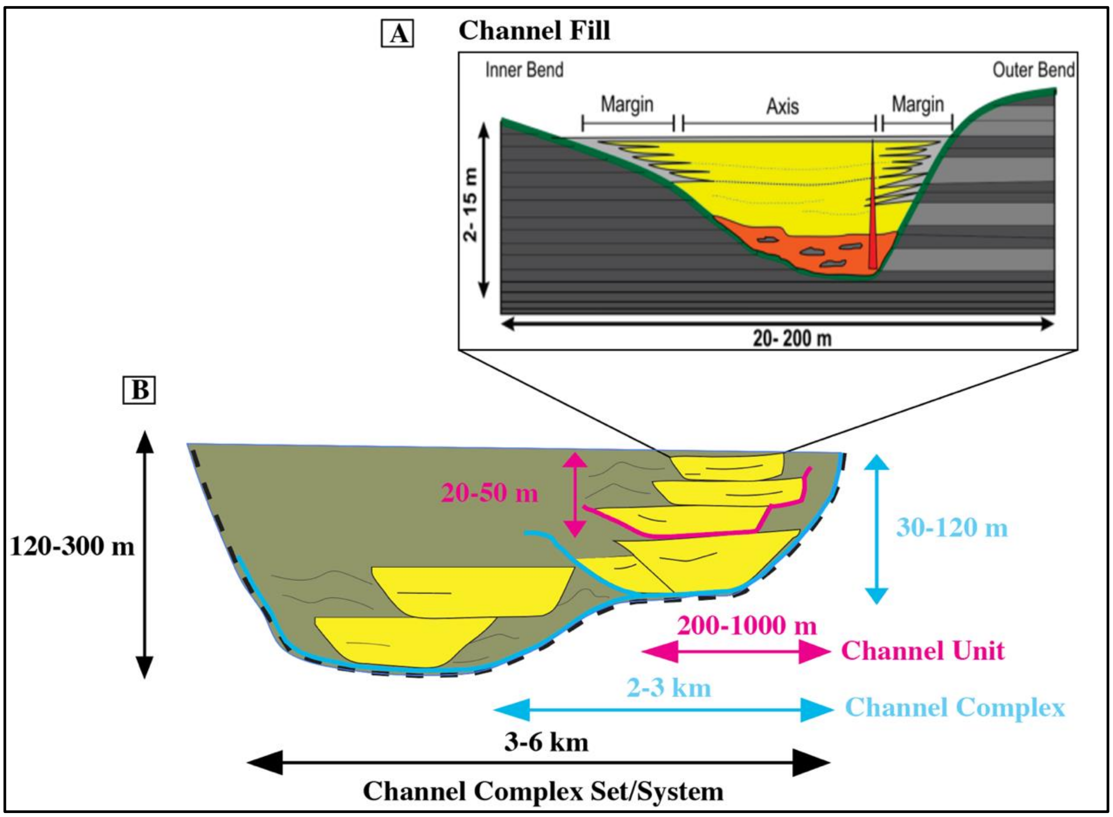

Fig. 2.8: *Conceptual diagram illustrating the hierarchical organization of deep-marine sedimentary channels (modified from Navarro (2005)). (A) Cross-section of a single leveed-channel fill showing lateral facies transitions from coarse-grained, thick-bedded axial deposits to finer-grained margin deposits. (B) Larger-scale schematic showing multiple channel fills forming a channel unit, which then stack to build a channel complex. Dimensional ranges reflect typical observations from outcrop and subsurface datasets.*

2.2.1.1. Channel Fill

A channel fill represents the sedimentary infill of a single channel following erosional inception. Channel fills typically range from 2–20 m thick, are tens to hundreds of meters wide and develop through sediment accumulation during low-energy phases when reduced flow capacity limits transport and promotes gradual infill—or be reworked by later, high-energy flows that remobilize and redistribute earlier deposits. The facies organization of a channel fill typically consists of an erosional base overlain by massive or graded sandstone or conglomerate, commonly with abundant mud intraclasts (Peakall et al., 2000; Jobe et al., 2011). Stratigraphically upward, channel fills often exhibit fining and thinning trends reflecting a decrease in flow capacity and depositional energy as channels in-fill and transition toward abandonment. Laterally, channel fills transition from thick-bedded sandstone in axial regions to finer-grained, thin-bedded turbidites along the margins, reflecting lateral energy dissipation and reduced sediment transport in the flow centered in the channel axis (Hubbard et al., 2014).

2.2.1.2. Channel Unit

A channel unit consists of one or more genetically related channel fills and is typically bounded by erosional surfaces that mark major phases of channel activity, abandonment, or re-incision. While individual channel fills are also bounded by erosion surfaces, these tend to be more localized and associated with individual flow events or single episodes of scour and fill. In contrast, the bounding surfaces of channel units usually correspond to more substantial stratigraphic discontinuities, such as composite scours, abrupt changes in architecture, or a shift in fill style, indicating a new phase of channel re-establishment within the larger depositional system (Clark and Pickering, 1996; McHargue et al., 2011). Channel units generally range from 10–50 m thick and 100–500 m wide.

2.2.1.3. Channel Complex

A channel complex represents the amalgamation of two or more channel units, typically forming in response to fundamental changes in long-lived sediment routing pathways. These complexes develop through successive cycles of erosion, avulsion, and sediment deposition, creating extensive stratigraphic bodies (Clark and Pickering, 1996; McHargue et al., 2011). Channel complexes commonly display scoured basal surfaces with large-scale scours, mud intraclasts conglomerate, and high-relief truncation surfaces suggesting periods of intense sediment bypass followed by backfilling (Jobe et al., 2011; Bain and Hubbard, 2016). These complexes can span extensive stratigraphic thicknesses (50–200+ m) and widths exceeding several kilometers.

2.2.2 Channel Unit Description

In this study nine channel units (SR-1 to SR-7) were identified (Fig. 2.9). Due to time constraints and project objective limitations, only SR-1, which in outcrop is the widest and best exposed channel unit in the study area, was measured in bed-by-bed detail at multiple locations along strike and mapped and analyzed in detail using aerial imagery to capture both vertical and lateral stratal and architectural variation (see Fig. 2.9). In contrast, the other channel units were studied along a single vertical measured transect (Fig. 2.10) where the unit was best exposed. As a result, lateral facies changes were not captured and could be the focus of future work to better characterize architectural stacking patterns and stratigraphic relationships across the broader slope system.

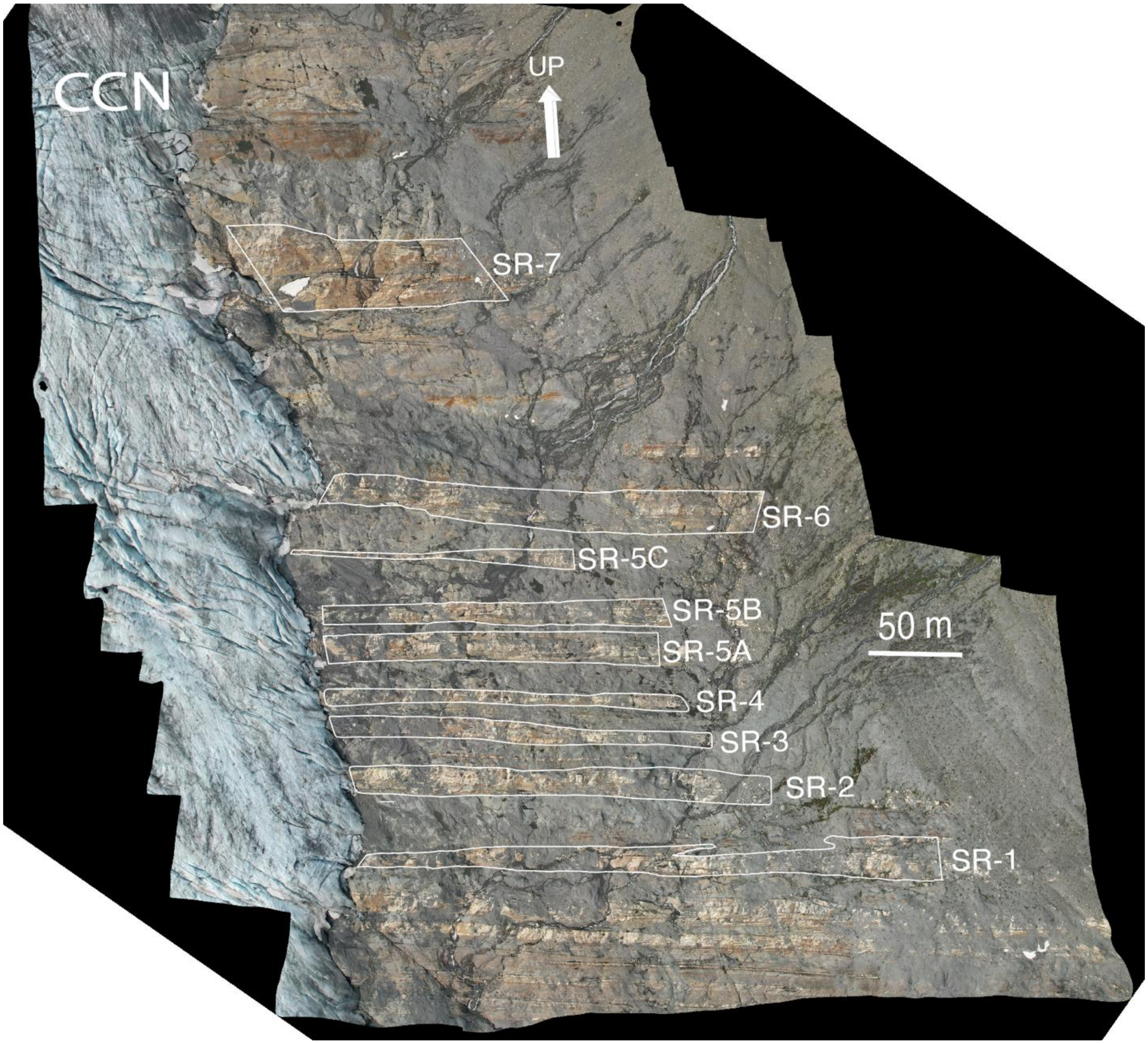

Fig. 2.9: *Drone photomosaic from the Castle Creek North outcrop with channel units outlined.*

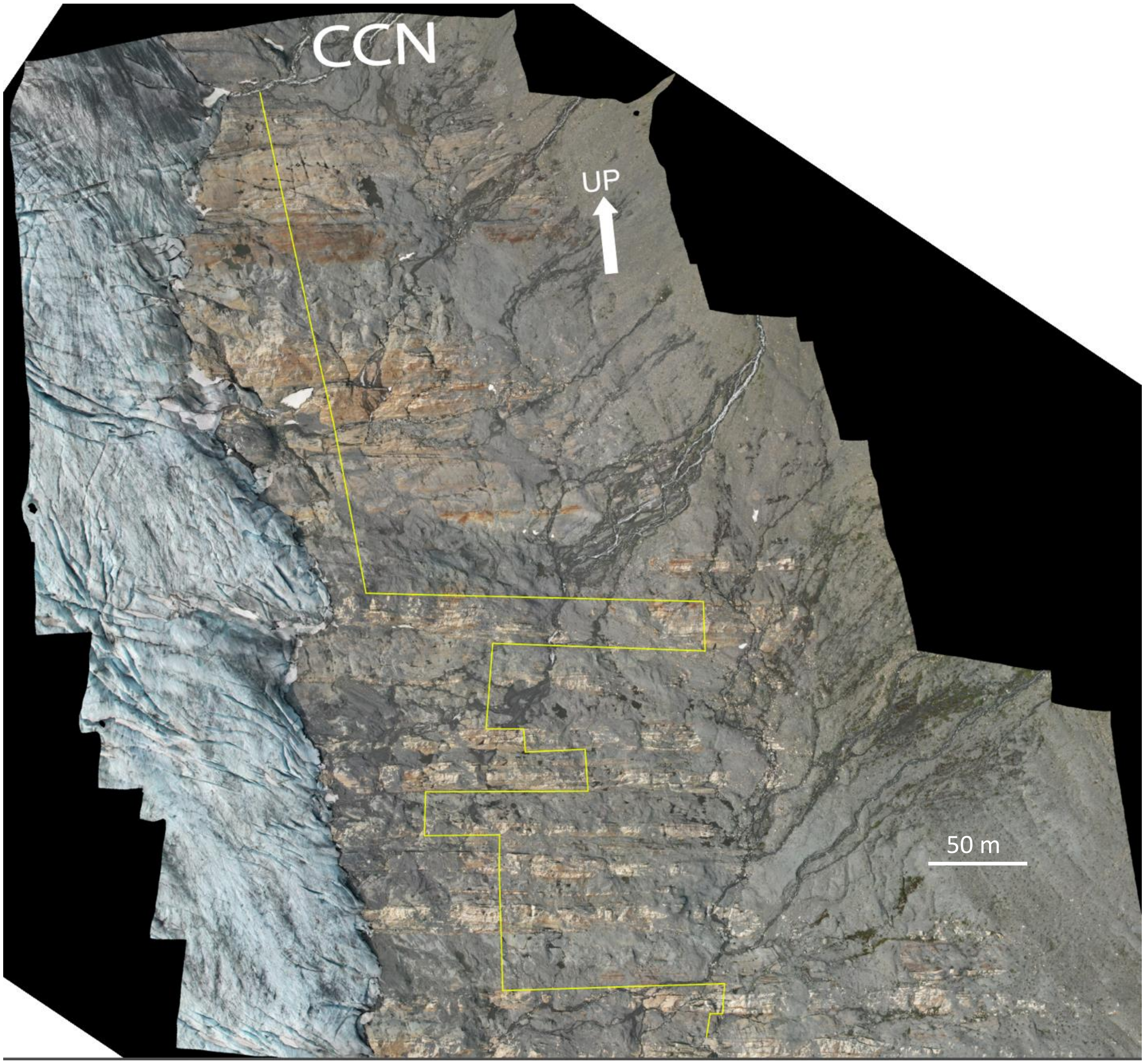

Fig. 2.10: *Drone photomosaic of the Castle Creek North outcrop showing vertical transect where detailed sections were measured.*

2.2.2.1. SR-1

Channel unit SR-1 is approximately 18 m thick and extends laterally for ~ 250 m across the Castle Creek northwest outcrop (Fig. 2.11A) before being obscured by glacial cover to the southeast and gravel to the northwest. Also, parts of the outcrop are locally covered by water and gravel, limiting comprehensive documentation of lateral and vertical variations across the entire unit. However, the most continuous exposure (Fig. 2.11, B and C) reveals three discrete, vertically stacked channel fills—CF-1, CF-2, and CF-3—bounded within a broader composite erosional surface scoured into the underlying debrite (DF-1) (Fig. 2.12). This basal erosional surface exhibits relief of up to 70 cm, locally marked by an abrupt increase in grain size to fine granule conglomerate and occurrence of abundant mud intraclasts.

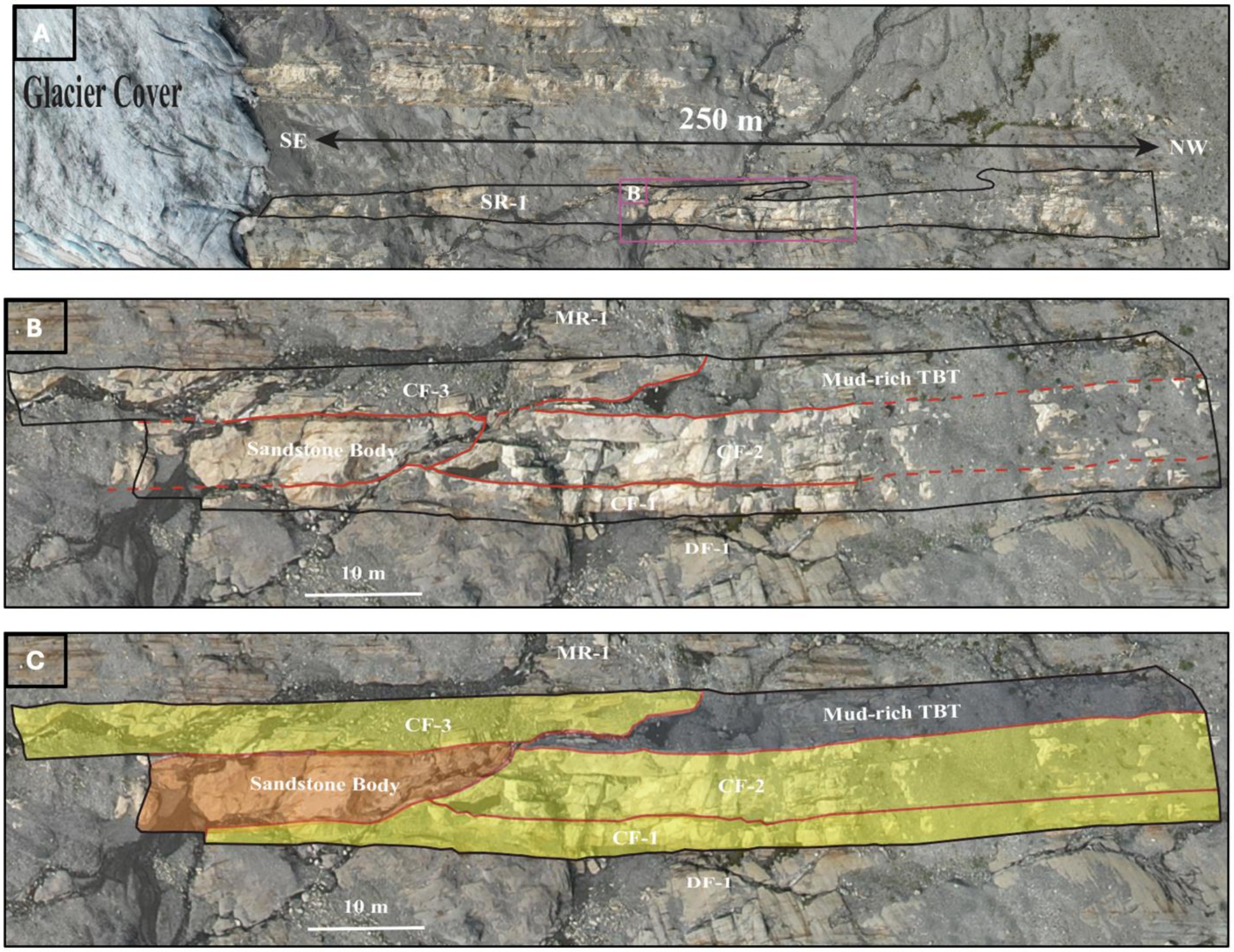

Fig. 2.11: *(A) Interpreted drone photomosaic showing the laterally extent of channel unit SR-1 in the Castle Creek north outcrop. The channel unit is outline by the black polygon; purple rectangle indicates area shown in parts B and C. Interpretated drone photomosaic of SR-1 comprising three channel fills and a deformed sandstone body outlined by solid and dashed red lines. SR-1 sharply and erosionally overlies DF-1 and is conformably overlain by MR-1.*

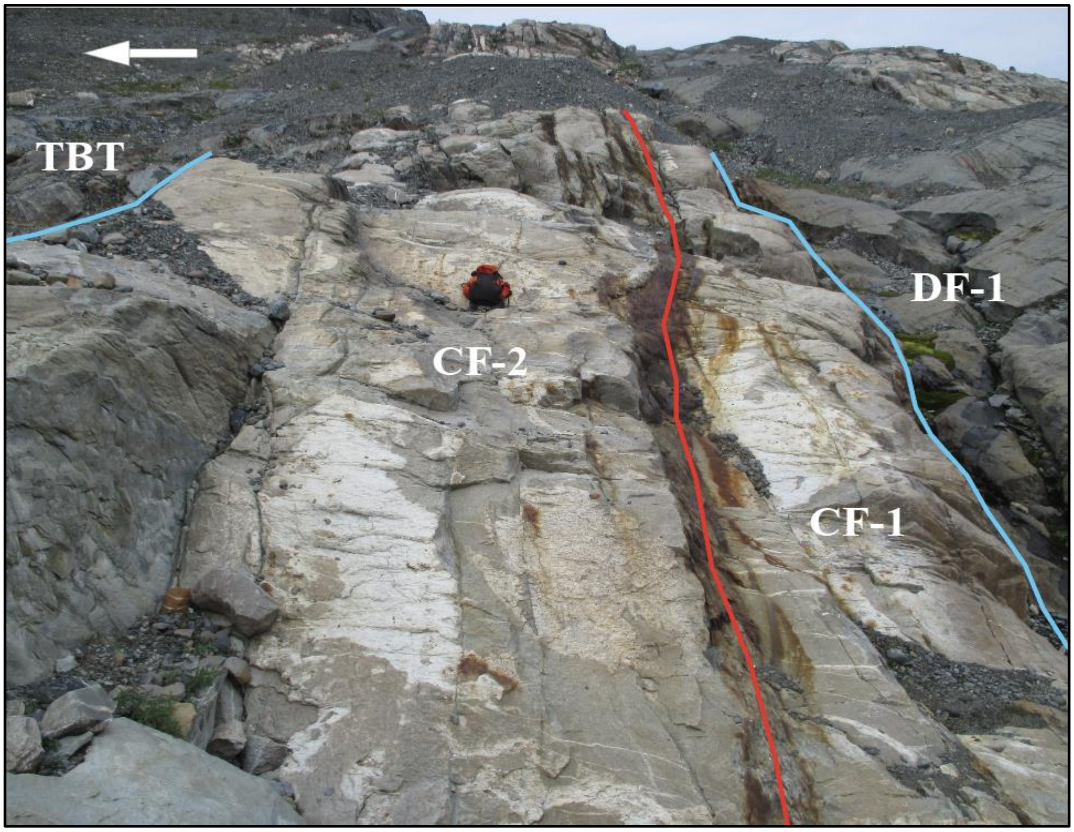

Fig. 2.12: *Field photo highlighting CF-1 and CF-2 channel fills. Red line corresponds to the contact between the channel fills whereas the blue line highlights the upper and lower boundaries of channel unit SR-1. Well-developed mudclast breccia is developed at the base of channel fills overlain by amalgamated, very coarse-grained sandstone and fine granule conglomerate. Stratigraphic up indicated by white arrow. Field backpack for scale.*

CF-1, the basal fill, is ~ 6 m thick and dominated by vertically stacked, thick to very thickly bedded (0.6–2 m, avg. ~ 1 m), fine granule conglomerate or upper very coarse-grained sandstone (F1). Beds are primarily massive or normally graded to coarse-grained sandstone. Load structures are common in the lower portion of the fill but decrease in abundance stratigraphically upward. Well-developed mudclast breccia occurs at the base of most beds, comprising concentrated subangular to subrounded intraclasts (2–50 cm in length) with their apparent long axis aligned parallel to bedding. Beds are amalgamated (i.e. no intervening fine-grained strata) with individual beds contacts interpreted to coincide with an abrupt increase in grain size or subtle erosional surface. Bed thickness and grain size changes little laterally or vertically.

CF-2 is ~ 10 m thick and dominated similarly by thick- to very thickly-bedded (0.8–3 m) massive or normally graded fine granule conglomerate or upper very coarse-grained sandstone (F1). Beds are amalgamated and commonly exhibit local scours with 5–10 cm of relief. At the base of the fill, beds contain mudclast breccia with clasts 5–25 cm long (Fig. 2.13A), with their apparent long-axis aligned parallel to bedding and decrease in size and abundance upward. Very coarse-grained sandstone injections that are 10–20 cm long and 5–10 cm thick, cross-cut adjacent finer-grained strata near the base of CF-2. Stratigraphically upwards, beds thin becoming mainly medium- or thick-bedded (average bed thickness: 0.3–0.6 m), with no significant change in grain size, and locally are interbedded with very thin-bedded, upper-division turbidites (T_{cde}) (F2.2 and F3).

CF-2 is capped in the northwest by a wedge of very thin to thin-bedded mud-rich turbidites. Laterally, CF-2 extends ~ 100 m northwest, where bed thickness subtly decreases becoming mostly thick-bedded and locally interbedded with very thin-bedded upper division turbidites. In the southeast, CF-2 is truncated by a thickly developed zone consisting of coarse- to very coarse-grained sandstone (Fig. 2.13B) that crosscuts surrounding strata at a high angle. The sandstone body is ~ 10–15 m thick and extends ~ 30 m laterally before being obscured by debris cover with irregular margins that interfinger with very thin-bedded, mud-rich turbidites (Fig. 2.13C). The sandstone is massive to subtly stratified and where present, bed contacts within this zone are faint and often marked by a shift in grain size and dispersed mud intraclast.

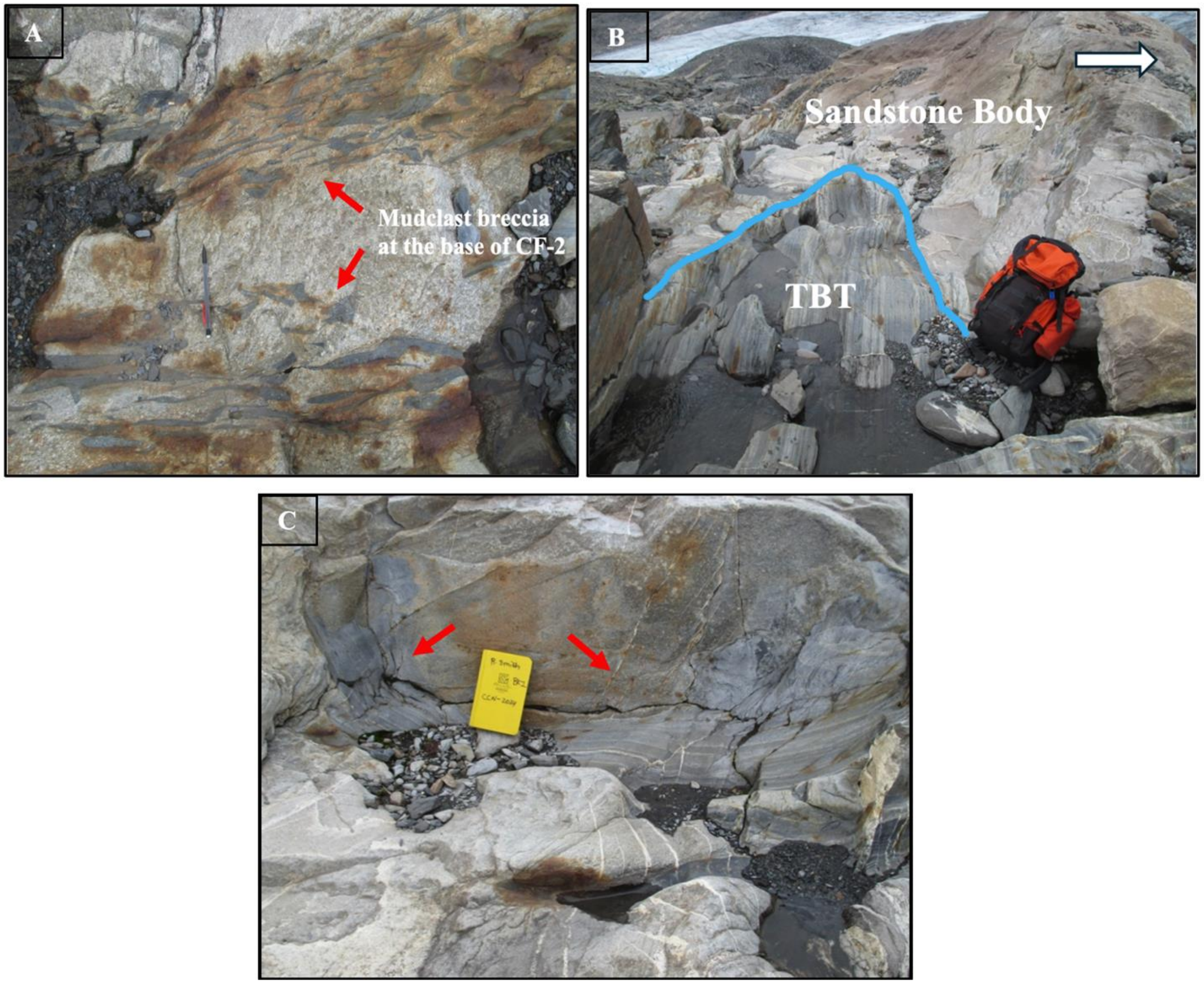

Fig. 2.13: *(A) Field photograph of well-developed mudclast breccia at the base of CF-2 with subrounded mud intraclasts (red arrows) oriented with their apparent long-axis parallel to base of beds. Pencil for scale. (B) Field photograph showing the irregular contact of the sandstone body with thin-bedded, upper division turbidites (outlined in blue) exhibiting distortion and interfingering on the margins with adjacent sandstone. Bedding within the sandstone body is massive to faintly bedded. Field backpack for scale. Stratigraphic up indicated by white arrow. (C) Field photograph showing a sharply defined, irregular contact (indicated by red arrows) between a very coarse- to coarse-grained sandstone body (above) and underlying thin-bedded, fine-grained strata (below). The contact is discordant and marked by abrupt truncation of fine-grained strata. Field notebook for scale.*

CF-3 is the uppermost fill, and its exposure is limited due to water and gravel cover. The fill is ~ 5 m thick and laterally offset to the southeast in sharp contact with a wedge of upper division very thin-bedded turbidites in the northwest and deformed strata in the southeast, forming an irregular basal contact marked by an increase in grain size to fine granule conglomerate with abundant quartz pebbles. Beds at the base of CF-3 are typically medium- to thick-bedded (average bed thickness: 0.2–0.6 m), although locally very thickly-bedded, but then become exclusively medium-bedded upward. Strata consist of massive or normally graded fine granule conglomerate or upper very coarse-grained sandstone (F1) that shows negligible lateral or vertical change. In the upper 2 m of the northwest exposure uncommon medium-bedded, upper coarse-grained sandstone exhibit large-scale cross-stratification in sets 10–13 cm thick that over a few meters laterally pinch out. CF-3 is then capped by mud-rich interval MR-1.

2.2.2.2. SR-2:

Channel unit SR-2 is approximately 10 m thick and bounded at its base by an irregular erosion surface that scours up to 10–20 cm deep into the underlying mud-rich deposit, MR-1. The unit comprises a single channel fill that at its base consists of a ~ 3 m-thick interval of upper very coarse-grained sandstone and fine granule conglomerate (F1). Well-developed mudclast breccia occurs throughout SR-2. Strata are very thickly bedded (1–2.5 m thick, average thickness ~ 1 m), massive, upper very coarse-grained sandstone or fine granule conglomerate (F1). Beds show a distinctive cross-cutting geometry with erosional contacts between individual bed as much as 0.8–1 m deep, with average relief ~ 50 cm (Fig. 2.14). Clasts, composed of massive mud or interstratified sand and mud, are 5–40 cm long subrounded to rounded with their apparent long-axis oriented subparallel to the base of the bed. Mudclast breccia is well developed in the lower part of SR-2 but becomes less common upward. No consistent upward-fining or -coarsening trend is noted in SR-2 but beds thin progressively from the base to a height of approximately 6.8 m where they reach a minimum thickness of 0.4–0.75 m where additionally, sandstone beds are capped by thin (≤ 2 cm) silty mudstone layers (F3).

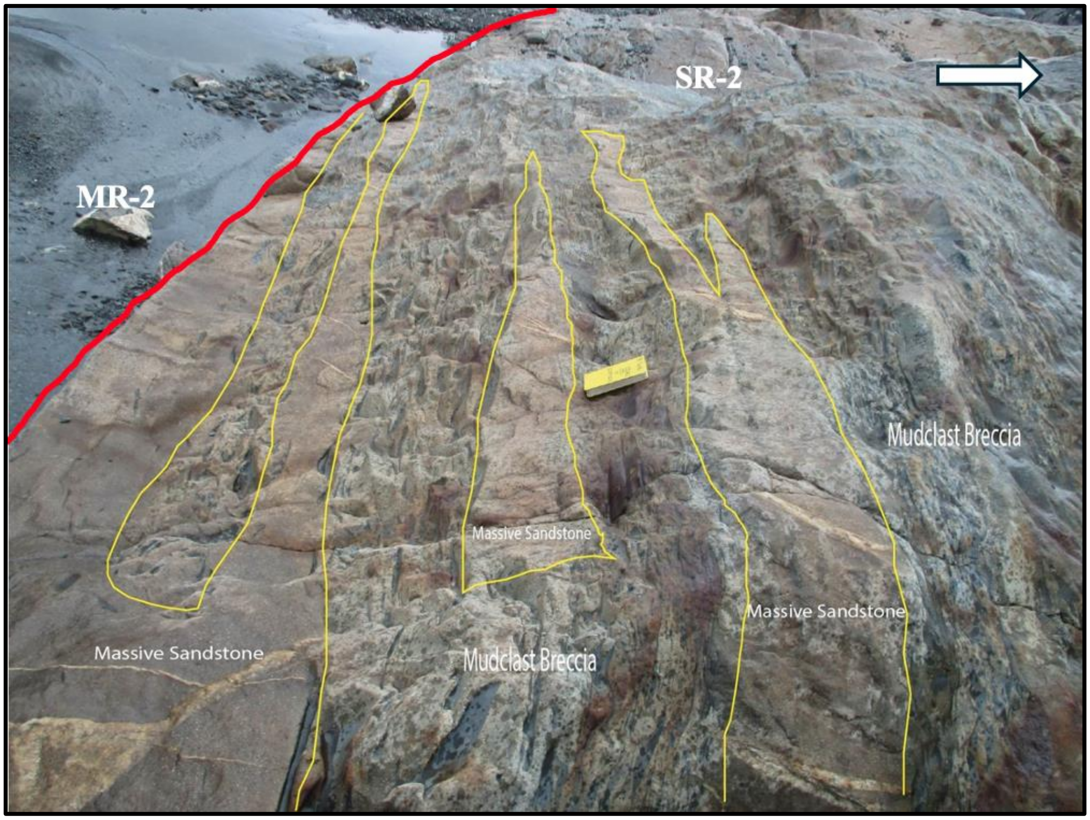

Fig. 2.14: *Outcrop photograph illustrating the cross-cutting and irregular geometry of massive sandstone and mudclast breccia layers at the base of channel unit SR-2. Yellow lines bound distinct sandstone lenses that pinch out against adjacent breccia intervals. The breccia consists predominantly of subrounded mud clasts supported in a very coarse-grained sandstone matrix. A similar architecture is observed in the basal part of channel units SR-5, SR-6. Stratigraphic up indicated by white arrow. Notebook for scale.*

2.2.2.3. SR-3:

Channel unit SR-3 is approximately 13 m thick and is bounded at its base by an undulating erosional surface that incises DF-2 with scours up to 40 cm deep. The unit contains three distinct channel fills. The first channel fill is 3.45 m thick with mudclast breccia in the basal sandstone bed containing subangular to subrounded mud intraclasts that are 2–30 cm long and aligned parallel to the base. This basal fill consists of two very thickly bedded sandstone beds (2.1 and 1.35 m, respectively) composed of upper very coarse-grained grading upward to coarse-grained sandstone (F1). Beds show negligible upward fining or thinning. The second channel fill is 5.6 m thick and is marked by an abrupt increase in grain size to fine granule conglomerate and a well-developed mudclast breccia in the basalmost bed. Beds at the base of the fill are composed of a succession of amalgamated beds of thickly to very thickly bedded (0.8–3 m) fine granule conglomerate or upper very coarse-grained sandstone (F1) grading upward to medium-grained sandstone. Beds thin upward to an average thickness of 0.6 m and become interbedded with very thin-bedded (1–2 cm) upper division turbidites (T_{cde}) (F2.2 and F3); grain size changes little. The third and uppermost fill is approximately 3 m thick and marked at its base by an increase in grain size and dispersed mud intraclasts (1–10 cm long). Beds are amalgamated and consist of thick-bedded (avg. bed thickness: 0.7–0.9 m) fine granule conglomerate that typically grades upward to medium-grained sandstone (F1). The succession of sandstone beds within this fill shows no significant variation in grain size or bed thickness upward and is capped by very thin- to thin-bedded turbidites of unit MR-3.

2.2.2.4. SR-4:

Channel unit SR-4 is approximately 7.5 m thick (Fig. 2.15A) and overlies an erosional surface incised into MR-3. The basal contact is marked by subtle ~ 10–20 cm deep scours that can be traced laterally for ~ 1 m. The unit contains two channel fills. The first channel fill is ~ 2 m thick and distinctively contains abundant quartz pebbles (0.3–0.5 cm) concentrated only at the base of beds. Beds at the base of this fill consist of a succession of thick-bedded (avg. bed thickness: 0.5–0.8 m) very coarse- or coarse-grained sandstone beds that grade upward to medium-grained sandstone (F1). Above this, grain size shows a reverse grading trend, coarsening from coarse- to upper very coarse-grained sandstone with no significant changes in bed thickness.

The second fill is ~ 4.5 m thick and marked by an increase in grain size to fine granule conglomerate and presence of abundant mudclasts at the base of the beds. Beds of this fill are thick to very thickly bedded (0.5–1.5 m, average ~ 0.8 m), consisting of fine granule conglomerate that grades upward to medium- or coarse-grained sandstone (F1). Bed contacts are identified by abrupt changes in grain size and/or abundance of mudclasts (5–20 cm long) and less common interstratified sand and mudclasts (20–40 cm long) (Fig. 2.15B). Clasts are subangular to subrounded with their long-axis aligned parallel to bedding – mudclasts becoming dominant upward as interstratified clasts become absent. Beds show a subtle upward thinning trend (average bed thickness: 0.5–0.6 m) and a slight decrease in grain size from granule conglomerate to upper coarse-grained sandstone.

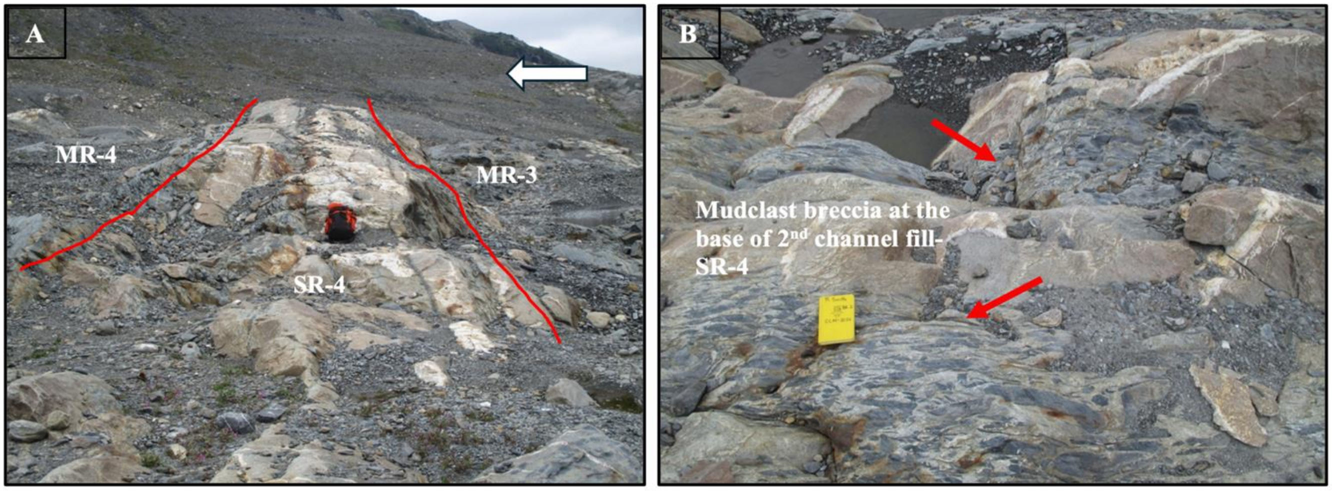

Fig. 2.15: *(A) Outcrop photograph showing SR-4, which is bounded at is base by thin-bedded turbidites of MR-3 and sharply overlain by thin-bedded turbidites of MR-4. Stratigraphic up indicated by white arrow. (B) Field photograph of well-developed mudclast breccia in the lower part of the second channel fill in SR-4 with subrounded mudclasts oriented with their apparent long-axis parallel to base of beds. Notebook for scale.*

2.2.2.5. SR-5A:

Channel unit SR-5A is approximately ~ 18 m thick and bounded at its base by an irregular contact with MR-4 and marked by an abrupt grain size increase. The unit contains two channel fills. The first fill is ~ 6 m thick and comprises medium to very thickly bedded (0.3–1.2 m, average 0.6 m) granule conglomerate or upper very coarse-grained sandstone (F1). Bed bases are erosional forming a cross-cutting geometry with relief of up to 90 cm, averaging ~ 30 cm. Locally, beds at the base of this fill consist of clast-supported conglomerate that are 0.7–1m thick and characterized by clast-supported, subrounded to rounded mudclasts ranging from 2–30 cm in length (Fig. 2.16A). The entire first fill contains abundant mudclasts (10–30 cm), quartz pebbles (0.5–1 cm), and minor interstratified sandstone-mudstone intraclasts (25–40 cm) along with carbonate-cemented sandstone clasts (Fig. 2.16B) . Quartz pebbles, interstratified clasts and carbonate clasts decrease in abundance upward whereas mudclast abundance changes little. Clasts are subangular to subrounded and with their apparent long-axis aligned parallel to bedding. This fill is capped by a ~ 50 cm interval of mud-rich, thin-bedded upper division turbidites (F2.2 and F3).

The second fill is ~ 12 m thick, sharply overlying the first and marked by a grain size increase to fine granule conglomerate with load and flame structures at the base. Basal beds are amalgamated and consist of thick- to very thick-bedded (0.6–1.1 m), fine granule conglomerate (F1) that are either ungraded or grade upward to medium-grained sandstone. Intraclast breccia is common at the base of beds and made up of mud intraclasts (5–40 cm long) and rare interstratified mud-sand intraclasts (30–50 cm long), both decreasing in abundance upward. This fill shows a clear thinning- and fining- upward trend marked by a gradational change from thick-bedded, amalgamated conglomerate to medium- and thin-bedded, complete, fine- or medium-grained sandstone turbidites.

Fig. 2.16: *(A) Outcrop photograph of clast-supported conglomerate at the base of the first channel fill of SR-5A with abundant subrounded to rounded mud, elongate mudclasts. Hammer for scale. (B) Carbonate-cemented sandstone clast (red arrow) at the base of SR-5A in a quartz pebble conglomerate bed. Pencil for scale.*

2.2.2.6. SR-5B:

Channel unit SR-5B is ~ 12 m thick (Fig. 2.17), separated from SR-5A by an erosional surface with scours up to 2 m deep. The base is marked by a grain size increase to fine granule conglomerate or very coarse-grained sandstone with abundant mudclasts. The lower ~ 4 m contains thick- to very thick-bedded (0.4–1 m, avg. 0.4 m) massive, fine granule conglomerate or very coarse-grained sandstone (F1) beds with abundant subrounded, 10–30 cm-long mudclasts aligned with their apparent long-axis aligned parallel to bedding. Overlying strata thin and fine upward to amalgamated coarse- or medium-grained sandstone (0.3–0.6 m). This interval transitions gradationally to a ~ 1 m-thick succession of medium-bedded (10–15 cm), medium-grained, upper-division turbidites (T_{cde}) (F2.2 and F3) overlain by 3 m-thick succession of very thin- to thin-bedded (2–6 cm) fine-grained, upper-division turbidites marking the top of the channel fill.

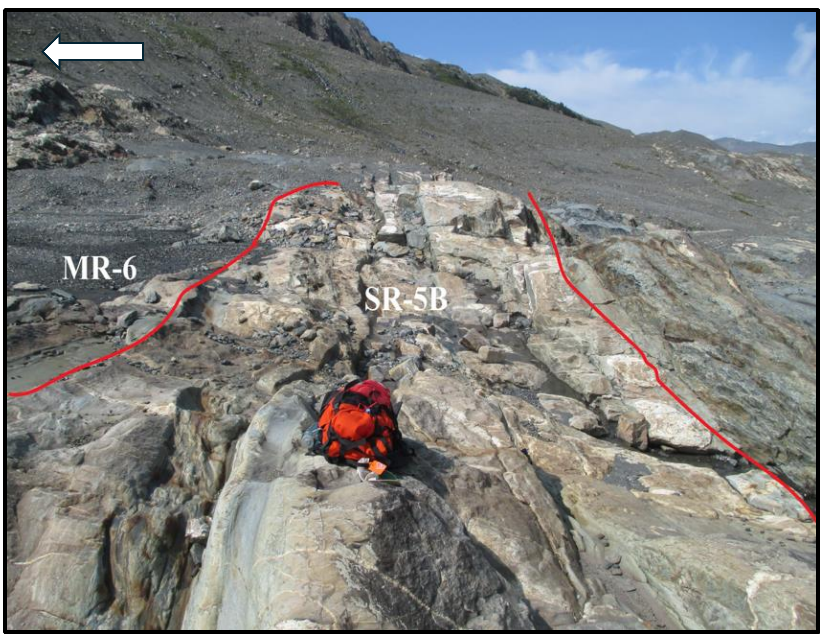

Fig. 2.17: *Outcrop photograph showing the thickness of channel unit SR-5. Stratigraphic up indicated by white arrow. Red lines mark the bounding surfaces of SR-5B. Field backpack for scale.*

2.2.2.7. SR-5C:

Channel unit SR-5C is ~ 7 m thick bounded at its base by an erosional contact with MR-5 with relief up to 40 cm. The unit contains a single channel fill composed of thick to very thickly bedded (0.4–1.5 m) upper very coarse-grained and coarse-grained sandstone beds (F1). Beds are massive and amalgamated with minimal changes in grain size and bed thickness vertically. Mudclast breccia occurs in the basal portion of the fill decreasing in abundance stratigraphically upward. Near the top of the fill, sandstone beds become interbedded with fine-grained, very thin- to thin-bedded (2–8 cm), upper-division turbidites (F2.2 and F3) before abruptly transitioning to complete very thin- and thin-bedded mud-rich turbidites.

2.2.2.8. SR-6:

Channel unit SR-6 is approximately 29 m thick (Fig. 2.18A) and overlies a sharp, erosional surface incised into MR-6. The basal contact is marked by an ~ 2 m-deep scour that can be traced laterally for ~ 20 m. The channel unit comprises two channel fills. The first fill is ~ 17 m thick and comprises amalgamated beds of massive pebble conglomerate (F1) (Fig. 2.18C). Beds are thick- to very thickly bedded (0.5–2 m, average thickness 0.8 m) and characterized by a distinctive cross-cutting geometry of adjacent beds, like that observed at the base of channel units SR-5, SR-4 and SR-2. Mudclast breccia are well-developed throughout the entire fill; clasts that are 5–80 cm long in addition to uncommon carbonate clasts that are 10–25 cm long (Fig. 2.18B). Carbonate clasts are most abundant near the base of the fill and decrease upward. Both clast types are subangular to subrounded with their apparent long-axis aligned parallel to the base of beds – mudclasts decrease in size upwards to ~ 5–20 cm. The fill shows an upward-thinning and -fining trend, transitioning gradually from thick- to very thickly bedded pebble conglomerate to a succession of medium- or thickly bedded (0.4–0.6 m), coarse-grained sandstone capped abruptly by a ~ 20 cm interval of thin-bedded, upper-division turbidites (F2.2 and F3). The second fill is ~ 12.6 m thick and erosionally overlies the first fill scouring the thin-bedded turbidite cap with subtle relief of 5–10 cm and also is marked by an increase in grain size to fine granule conglomerate. Beds in the basal part of the fill are amalgamated and composed of thick- to very thickly bedded (0.6–1.2 m), fine granule conglomerate (F1) that is massive or grades upward to medium-grained sandstone at the top of beds. Locally at the base of the channel fill, mudclast breccia is observed and composed of subrounded to rounded, 5–10 cm-long clasts. Stratigraphically upward, beds thin to medium-bedded (0.3–0.5 m) massive, medium- or coarse-grained sandstone interbedded with very thin- to thin-bedded, upper-division turbidites (F2.2 and F3). Upward in the channel fill, the abundance and thickness of upper-division turbidites increases, eventually culminating in a 2 m-thick interval composed entirely of very thin- to thin-bedded turbidites.

Fig. 2.18: *(A) Outcrop photograph of SR-6 composed of amalgamated, very coarse-grained sandstone or conglomerate beds sharply overlain by thin-bedded turbidites of MR-7. Stratigraphic up indicated by white arrow. Red line delineates the upper contact of SR-6. Backpack for scale (red circle). (B) Carbonate-cemented mudstone clast (red arrow) at the base of SR-6 in a quartz pebble conglomerate bed. Pencil for scale. (C) Well-developed mudclast breccia at the base of SR-6 in a quartz pebble conglomerate bed. Field book for scale.*

2.2.2.9. SR-7:

Channel unit SR-7 is approximately 42 m thick and erosionally overlies MR-7. Strata overlie an irregular basal surface with scours ranging from 20–60 cm deep. The base is also marked by an increase in grain size to very coarse-grained sandstone with abundant mud intraclasts. The channel unit comprises four channel fills. The first fill is ~ 17 m thick and is composed of thick- to very thickly bedded (0.5–1 m), massive or normally graded, lower very coarse- or coarse- sandstone beds (F1) with well-developed mudclast breccia in the lower half of the fill. In this lowermost part of the fill, sandstone beds are amalgamated with abundant subrounded to rounded mudclasts (5–20 cm in length) that are either concentrated near the base of the bed or present throughout its full thickness. Above this lower part of the fill sandstone beds gradationally thin and fine upward to medium-bedded (0.1–0.2 m), fine- or medium-grained sandstone that become interbedded with very thin- to thin-bedded, upper-division turbidites (F2.2 and F3). Towards the top of the fill strata consist primarily of very thin- to thin-bedded, upper-division turbidites interbedded locally with medium-bedded, medium-grained, lower-division turbidites (F1 and F2.1).

The second fill is ~ 12.4 m thick, its base marked by an abrupt increase in grain size and bed thickness. The fill is dominated by medium- to thick-bedded, complete Bouma turbidites interbedded with very thin- to thin-bedded, upper-division sandstone turbidites. Grain size varies between individual beds and ranges from coarse or upper fine sand with no obvious fining- or thinning-upward trend. The third fill is ~ 15.5 m thick and erosionally based with subtle scours ~ 5 cm deep. The base is marked by an increase in grain size to fine granule conglomerate and occurrence of mudclasts. The base of this fill is composed of amalgamated, sharp-based, thick-bedded (0.5–0.8 m) conglomerate (F1). Mudclast breccia is well-developed throughout this interval and consists of subangular to subrounded clasts ranging from 2–20 cm in length with their apparent long-axis oriented sub-parallel to the base of the bed. Stratigraphically upward mudclast abundance decreases and individual beds become separated by interbeds of very thin- to thin-bedded, upper-division turbidites (F2.2 and F3). The fill shows a thinning- and fining-upward trend to medium-bedded (15–20 cm), coarse- or medium-grained sandstone capped my thin-bedded, silty mudstone (2–5 cm) (F3). Near the top of the fill, sandstone beds become intercalated with thin-bedded fine-grained, upper-division turbidites before transitioning completely to very thin- and thin-bedded turbidites of MR-8.

2.2.3 Mud-rich Unit Description

Nine mud rich units (MR-1 to MR-9) were identified (Fig. 2.19) within the study area. Due to time constraints and project objective limitations the very fine-grained units were studied along a single vertical measured section. As a result, lateral facies changes were not captured and could be the focus of future work to better characterize architectural stacking patterns and facies changes along strike.

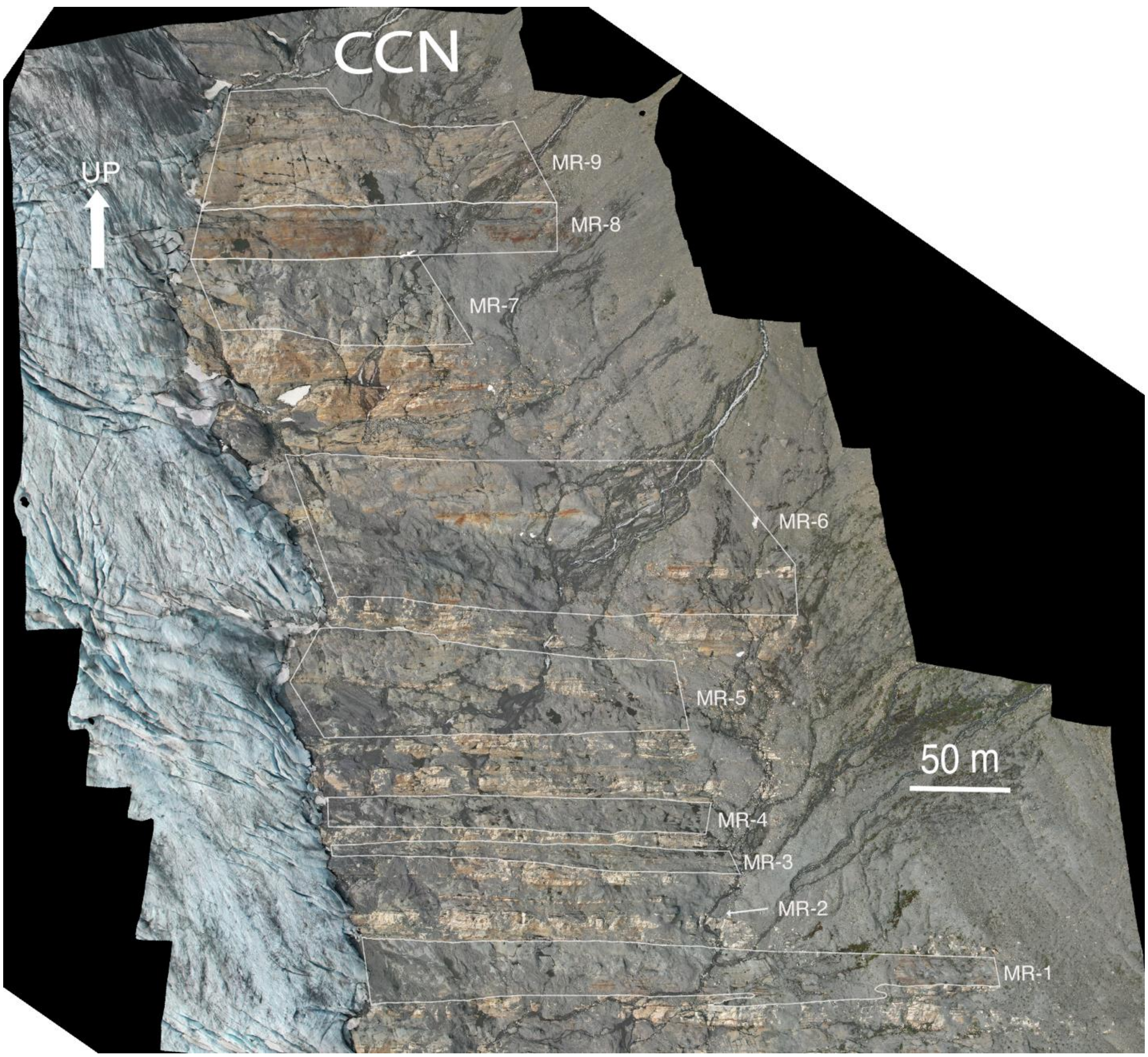

Fig. 2.19: *Drone photomosaic from the Castle Creek North outcrop with mud-rich units outlined.*

2.2.3.1. MR-1:

MR-1 is approximately 30.5 m thick and sharply overlies SR-1 channel unit along a planar contact. MR-1 is generally characterized by laterally continuous (>100 m), very thin- or thin-bedded turbidites that range from 3–8 cm thick, commonly representing lower- and upper-division Bouma sequences ($T_{abd/e}$, $T_{bd/e}$ or $T_{cd/e}$). These are uncommonly interbedded with medium-bedded (10–20 cm thick) typically $T_{bd/e}$ turbidites. Bed contacts are usually planar, although local erosive and loaded bases are observed. The basal 5–6 m of MR-1 has a relatively high sand-to-mud ratio (~ 70:30) and consists of coarse-grained, medium- to thick-bedded (12–35 cm), lower-division turbidites (F1 and F2.1). This basal package fines and thins gradationally upward to thin-bedded, fine-grained lower division turbidites ($T_{bd/e}$). The upper ~ 25 m of MR-1 is marked by an abrupt decrease in sand-to-mud ratio (~ 20:80) and is dominated by very fine- to fine-grained, very thin- to thin-bedded (2–8 cm), upper-division turbidites (F2.2 and F3) that are locally interbedded with medium-bedded (10–12 cm), fine-grained, lower-division Bouma sequences ($T_{ad/e}$ or $T_{bd/e}$) (F1 and F2.1). T_c beds are dominant in the upper interval of MR-1, comprising fine- to medium-grained sandstone with single set ripple cross-stratification, with individual ripple sets ranging from 1–2 cm thick.

2.2.3.2. MR-2:

MR-2 is approximately 4.5 m thick and sharply overlies an irregular surface at the top of SR-2. Strata are primarily thin- to medium-bedded (4–20 cm), sand-rich, lower-division turbidites (T_{ab} or $T_{bd/e}$) (F1 and F2.1) that fine and thin upward. The lower 3.5 m of the unit is dominated by medium- to thick-bedded (20–60 cm), medium- or coarse-grained, lower-division turbidites interstratified with very thin- to thin-bedded (3–5 cm) turbidites with an overall sand-to-mud ratio of approximately 60:40. Bedding contacts are mostly planar but erosional surfaces and load structures are observed locally. Above this lower interval the unit becomes increasingly dominated by medium-grained, very thin- to thin-bedded (2–8 cm) upper division turbidites (T_{cde}) (F2.2 and F3) with rare intercalated medium-bedded (10–20 cm), upper division turbidites. Sand-to-mud ratio in the upper interval is about 30:70.

2.2.3.3. MR-3:

MR-3 is ~ 10.5 m thick and has an irregular basal contact with the underlying SR-3 channel unit. Strata are composed primarily of medium- or fine-grained, thin-bedded (4–8 cm), lower division (T_{bde}) (F1 and F2.1) and upper division (T_{cde}) turbidites (F2.2 and F3) interbedded with medium- and thick-bedded turbidites ranging from 25–60 cm thick. The lower ~ 5.5 m of the unit is comparatively more sand rich with a sand-to-mud ratio of 70:30, comprising coarse- or medium-grained, very thin- to thin-bedded (3–8 cm), lower-division turbidites intercalated locally with medium-bedded (15–20 cm) turbidites. The top of this lower interval is marked by an abrupt decrease in bed thickness, grain size and sand content. The upper interval is ~ 4.5 m thick with a sand-to-mud ratio of approximately 20:80. Strata are composed almost exclusively of very thin to thin-bedded (2–6 cm), very-fine to fine-grained, upper-division turbidites (T_{cde}) intercalated with uncommon medium-grained, medium-bedded, upper-division turbidites (T_{cde}).

2.2.3.4. MR-4:

MR-4 is approximately 18 m thick and overlies a planar contact with channel unit SR-4. The succession is characterized by medium-grained, very thin- to thin-bedded (2–6 cm), lower-division ($T_{bd/e}$) and upper-division (T_{cde}) turbidites intercalated with medium-grained, medium-bedded turbidites ranging from 10–25 cm thick. The lower ~ 5.6 m of the unit has a sand-to-mud ratio of 60:40, dominated by medium-grained, very thin- to thin-bedded turbidites (3–7 cm), composed mostly of lower-division turbidites ($T_{abd/e}$ or $T_{bcd/e}$) (F1 and F2.1) with local medium-bedded turbidites. Bed contacts are normally planar but local erosional surfaces were observed. The overlying ~ 9.5-m interval consists also of medium-grained, very thin- to medium-bedded, lower-division turbidites but exhibits a higher sand-to-mud ratio (~ 80:20). The uppermost ~ 3.8 m of MR-4 records a dramatic increase in mud content, marked by a reduced sand-to-mud ratio (~ 30:70) and consisting entirely of fine-grained, very thin- to thin-bedded turbidites (2–7 cm). Strata are dominated by upper-division turbidites ($T_{cd/e}$) (F2.2 and F3), with uncommon T_a interbeds (F1).

2.2.3.5. MR-5:

MR-5 is approximately 40 m thick and has an irregular basal contact with the underlying channel unit. The unit is characterized by medium- to fine-grained, very thin to medium-bedded, lower- and upper-division turbidites, with a significant sand-rich interval near the middle of the unit. Average bed thickness is about 2–6 cm, with maximum thickness reaching 40 cm. Bed contacts are typically planar-abrupt, with local erosive and loaded bases. The lower ~ 7 m interval is composed primarily of coarse- to medium-grained, very thin to thin-bedded (2–8 cm), lower-division turbidites (T_{ab} or $T_{bd/e}$) (F1 and F2.1) with a sand-to-mud ratio of ~ 30:70, uncommonly interbedded with medium-bedded sequences ranging from 10 –15 cm.

The overlying ~ 17 m interval is dominated by medium- to fine-grained, medium-bedded (12–25 cm), lower-division turbidites (T_{bde} or T_{bcde}) (F1 and F2.1). This section shows an increase in mud content and overall turbidite thickness relative to the underlying interval with a sand-to-mud ratio of ~ 50:50. The remainder of MR-5 transitions abruptly to exclusively medium- to fine-grained, very thin to thin-bedded (1–6 cm, lower- and upper-division turbidites (T_{abde} or T_{cde}) (F2.2 and F3) that locally are interbedded with medium-bedded turbidites.

2.2.3.6. MR-6:

MR-6 is approximately 107 m thick and sharply overlies SR-6 channel unit along a planar contact. The deep red to orange hue of sandstone beds (Fig. 2.20A and B) is unique to MR-6. The basal 5 m consists of sand-rich (sand-to-mud ratio of 60:40), upper-division (T_{cde}) (F2.2 and F3) and lower-division (T_{bcde}) turbidites (F1 and F2.1). Beds are very thin to thin-bedded (3–8 cm, rarely up to 12 cm), medium-grained sandstone. Above this, the unit gradationally transitions to a ~ 25-m-thick interval of mud-rich (sand-to-mud ratio ~ 20:80), upper-division turbidites. Strata consist of fine-grained, very thin to thin-bedded turbidites (2–7 cm) uncommonly interbedded with medium-grained, medium-bedded (10–20 cm), upper-division turbidites (F2.2 and F3). Bed contacts are generally sharp and planar with local load structures. Upward, the next ~ 63 m has a similar sand-to-mud ratio (~ 40:60) but is dominated primarily by fine-grained, medium-bedded (15–25 cm up to 40 cm), upper-division turbidites with uncommon lower-division turbidite interbeds. The T_c division displays different styles including single set ripple, multiset ripple and starved ripple cross-stratification. This is followed by a ~ 12-m-thick interval marked by an increase in sand content (sand-to-mud ratio ~ 70:30) and consisting mostly of medium-grained, very thin- to thin-bedded (2–6 cm), upper-division turbidites intercalated with local medium-bedded turbidites (12–25 cm).

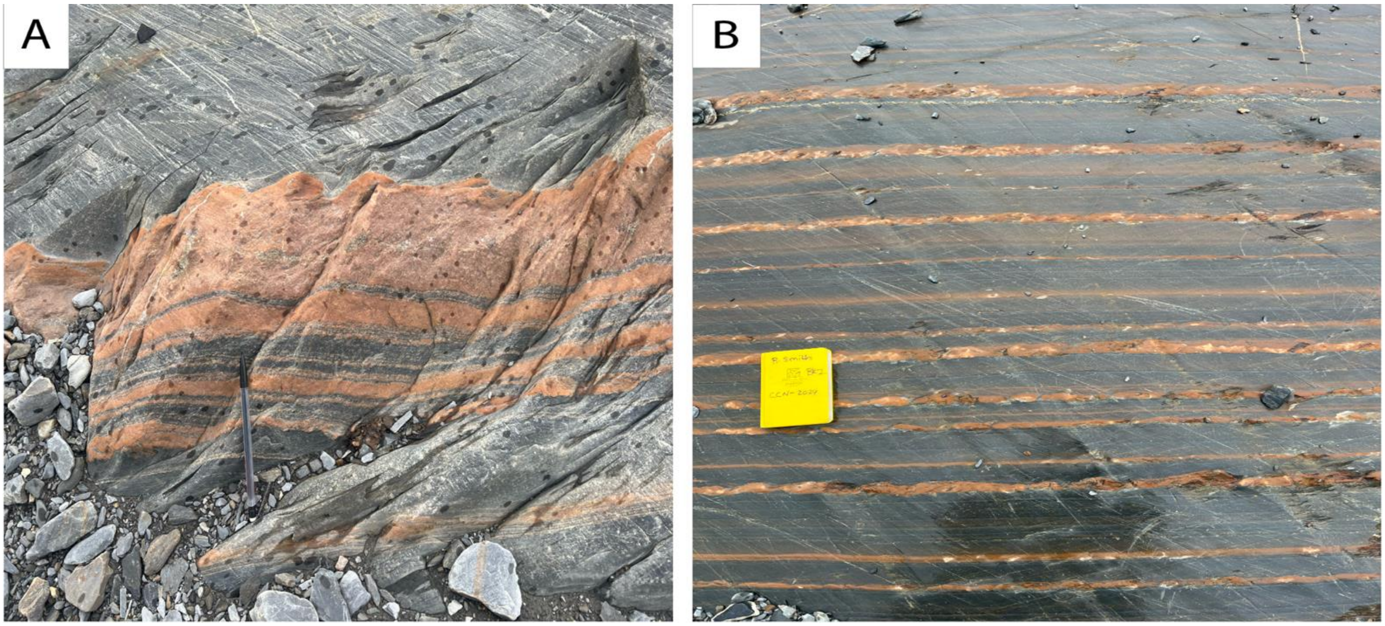

Fig. 2.20: *Outcrop photographs of MR-6. (A-B) medium- to thin-bedded, medium- to very fine-grained lower-division (T_{bde}) and and upper-division (T_{cde}) turbidites. Sandstone beds have a distinctive orange color caused by oxidation of iron-rich calcite cement. Pencil for scale (A) and notebook (B).*

2.2.3.7. MR-7:

MR-7 unit is ~ 52 m thick and sharply overlies a planar contact with channel unit SR-7. The unit is dominated by fine-grained, medium-bedded (10–25 cm thick), lower- and upper-division turbidites interbedded with very thin- to thin-bedded (1–6 cm) turbidites with a sand-to-mud ratio of approximately 30:70. Bedding contacts are mostly planar-abrupt. The basal 15 m of MR-7 consists exclusively of medium- or fine-grained, very thin- to thin-bedded, lower-division turbidites ($T_{abd/e}$ or $T_{bd/e}$) (F1 and F2.1). In this interval, T_c divisions are comparatively thicker, ranging from 1–15 cm, and are composed of fine- to medium-grained, multiset ripple cross-stratified sandstone. This interval is overlain by an ~ 37 m succession of mostly fine-grained, medium-bedded, upper-division turbidites (T_{cde}) (F2.2 and F3) interbedded locally with thin-bedded upper-division turbidites.

2.2.3.8. MR-8:

MR-8 is approximately 30 m thick and is bounded at its base by a planar contact with MR-7. The unit is distinctively organic-rich (Fig. 2.21A) with a diverse range of colors including: black, rusty red to orange, dark grey, and purple/pink in addition to abundant, dispersed pyrite (Fig. 2.21B). In addition, total organic carbon (TOC) ranges from 0.2 to 0.3 %, which is notably higher than other finer-grained strata in the Isaac Formation at Castle Creek, which generally is $\leq$ 0.1 % (Bergen, 2017; Cunningham and Arnott, 2021). Due to intense weathering internal sedimentary fabrics and primary structures are largely obscured. Despite this, the unit is composed primarily of very fine- to fine-grained, very thin- to thin-bedded (1–8 cm), lower-division turbidites ($T_{bd/e}$) (F1 and F2.1) or upper-division turbidites (T_{cde}) (Fig. 2.21C) intercalated with uncommon medium-bedded, fine-grained upper-division turbidites ranging from 10–12 cm thick. Grain size, turbidite thicknesses, and sand content change little upward.

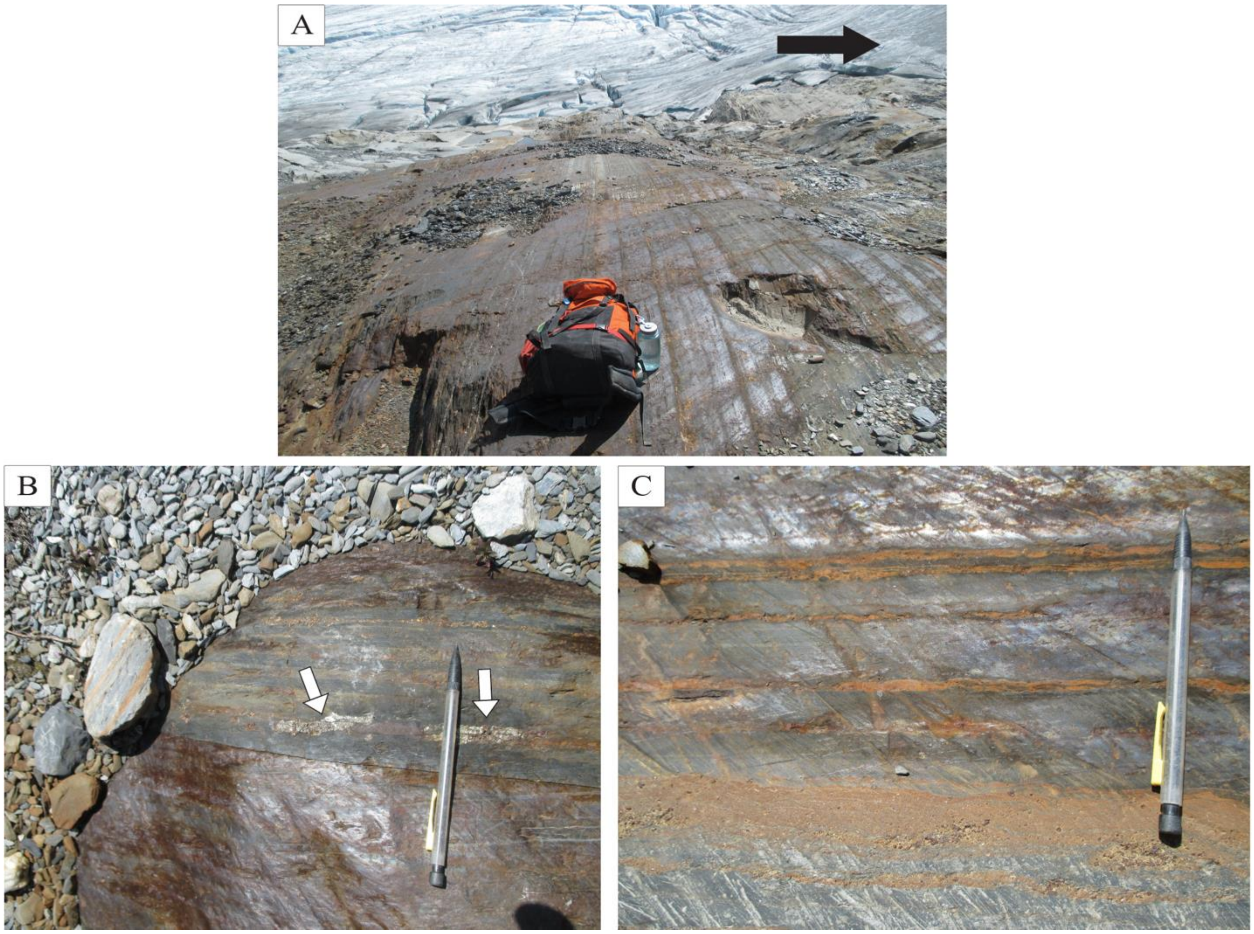

Fig. 2.21*: Outcrop photographs of MR-8. A) Laterally continuous, flat based, thin-bedded upper-division turbidites (T_{cde}) of MR-8. Field backpack for scale. Note dark colours of strata due to intense weathering. Stratigraphic up indicated by black arrow. B) Very thin bedded, stacked T_{de} beds with white arrows highlighting pyrite crystals. Pencil for scale. C) Very thin- to thin-bedded, upper-division turbidites (T_{cde}). Note dark orange color of sandstone beds (T_c) and black to dark grey colour of siltstone and sandstone beds (T_{de}). Pencil for scale.*

2.2.3.9. MR-9:

MR-9 is ~ 65 m thick with an erosional contact with MR-8, with relief up to 50 cm. Sandstone beds in this unit have a distinctive beige to light orange color that distinguishes them from sandstones in underlying mud-rich units (Fig. 2.22B). The basal 5 m is sand-rich with a sand-to-mud ratio of approximately 80:20 and consists of coarse-grained, medium- to thick-bedded (12–35 cm), lower-division (T_{ab} or uncommon T_{ade}) (F1 and F2.1) calciturbidites that fine and thin upward to fine- to medium-grained, very thin- to thin-bedded (2–4 cm), upper-division turbidites (T_{cde}) (F2.2 and F3) (Fig. 2.22A). T_a beds are 5–30 cm thick, massive or normally graded medium- to upper coarse-grained sandstone with dispersed mudclasts at their bases.

This, then, is overlain by a 5-m-thick, sand-rich (60:40 sand-to-mud ratio) interval consisting of medium-grained, very thin- to thin-bedded upper-division (F2.2 and F3) calciturbidites with uncommon T_a beds. Next is an ~ 20 m-thick, mud-rich (sand-to-mud ratio 30:70) interval composed mostly of very fine- to fine-grained, very thin- to thin-bedded (1–5 cm), upper-division (F2.2 and F3) calciturbidites. This is followed by an ~ 18-meter-thick sand-rich section (60:40 sand-to-mud ratio) composed of medium-grained, very thin- to thin-bedded (1–6 cm) lower-division ($T_{bcd/e}$ or $T_{bd/e}$) calciturbidites. The final ~ 12-m interval of MR-9 is mud-rich (30:70 sand-to-mud ratio), and composed exclusively of fine-grained, very thin- to thin-bedded (1–5 cm), upper-division (F2.2 and F3) calciturbidites.

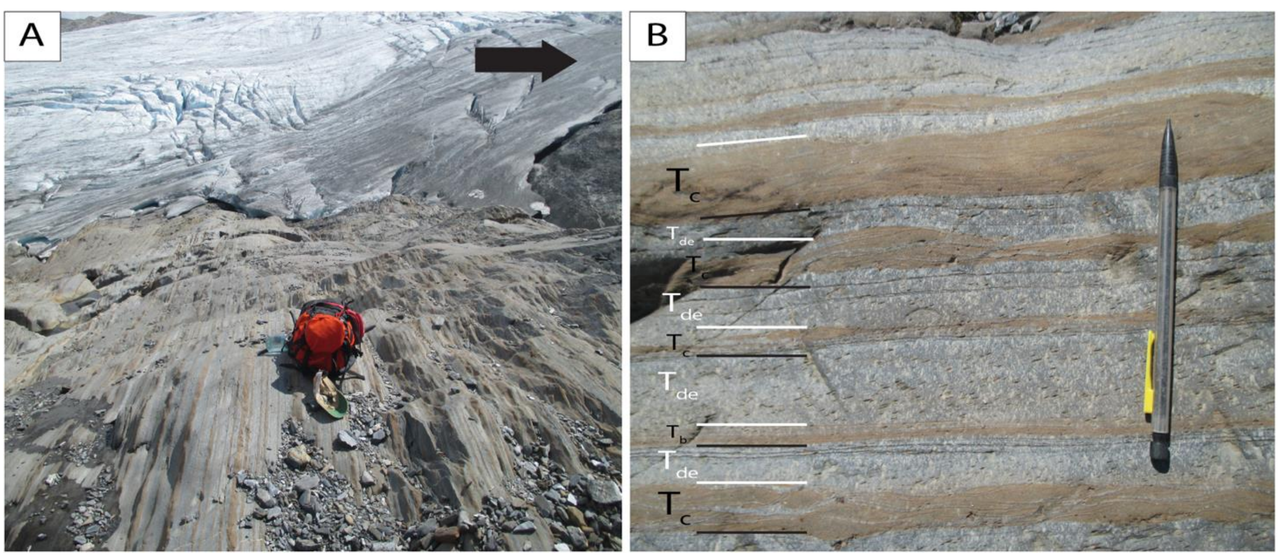

Fig. 2.22: *Outcrop photographs of MR-9. A) Laterally continuous, flat-based, thin-bedded, upper-division turbidites (T_{cde}) of MR-9. Field backpack for scale. Stratigraphic up indicated by black arrow. B) Very thin- to thin-fine-grained, cross-laminated sandstone intercalated with thin-bedded siltstone to mudstone (T_{cde}). Note the distinctive dark brown/beige colour of the sandstone beds. Pencil for scale.*

2.3 Detrital Zircon U-Pb Age Spectrum

Since > 90% of grains from the four samples (Fig. 2.23) had ages >1000Ma (see Appendix Table A. 1 to A. 4), Pb^{207}/Pb^{206} ages were used to construct kernel density estimate (KDE) plots of concordant ages. Zircon grains varied in morphology and grain size, ranging from 40-120 µm in length and 20-60 µm in width (aspect ratios of 3:1 to 1:1). Grains are predominantly subangular to subrounded with most exhibiting internal concentric zoning whereas others lacked internal structure (see Appendix Figure A. 1 and A. 2). KDE plots generated for each sample used measurements with <10% disconcordant ages after filtering. In the KDE plots shown below, the x-axis represents zircon ages in millions of years, while the y-axis shows the probability density, providing a smoothed estimate of the relative abundance of grains through time.

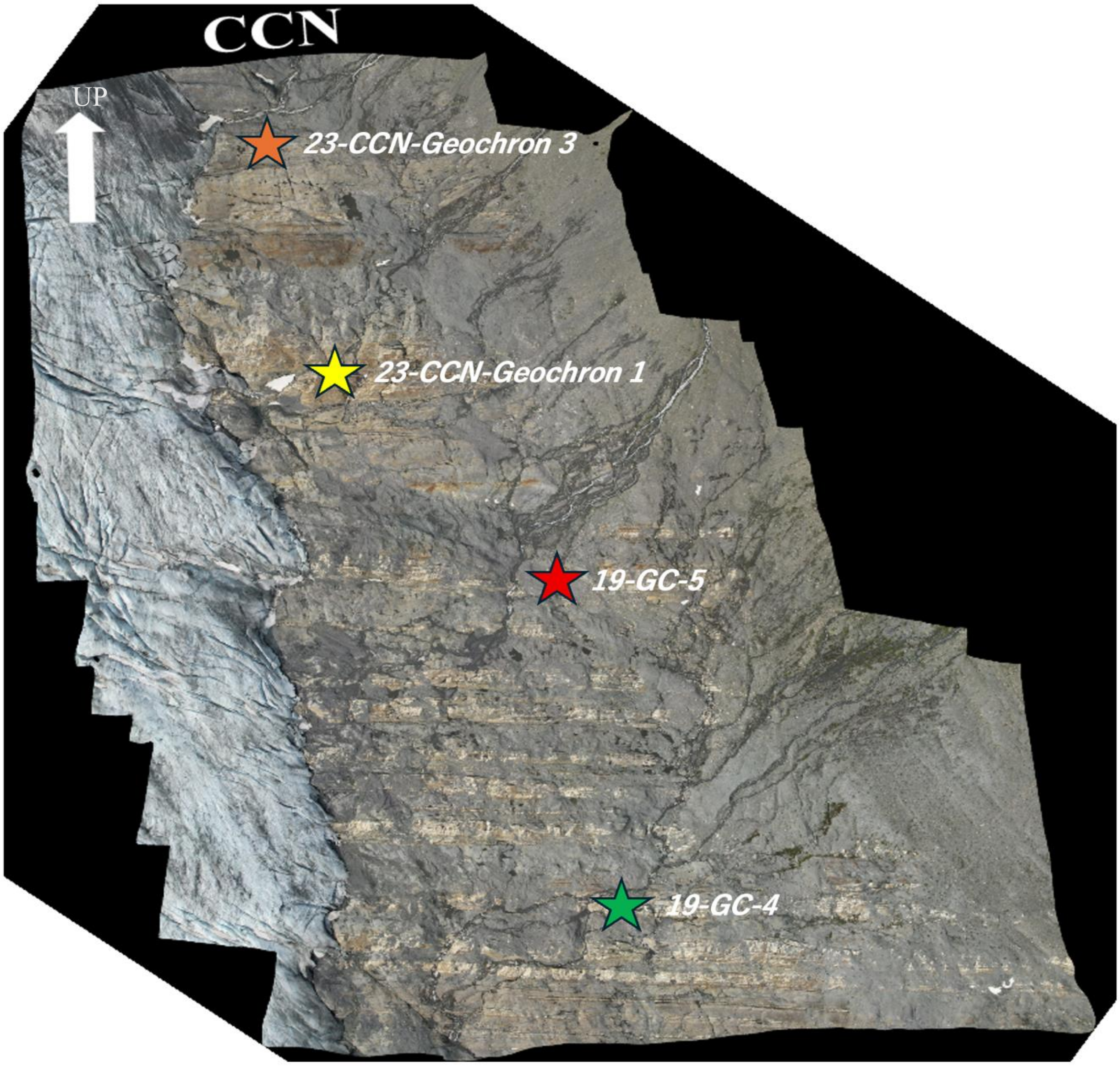

Fig. 2.23: *Photomosaic of the Castle Creek North study interval showing the locations of samples collected for detrital zircon U-Pb geochronology. Sample positions are marked by different coloured stars (19-GC-4, 19-GC-5, 23-CCN-Geochron 1 and 23-CCN-Geochron 3).*

2.3.1 19-GC-4:

The detrital zircon age distribution for this sample is bimodal but also includes a unique Neoproterozoic peak (Fig. 2.24). The dominant age population comprises Paleoproterozoic zircons ranging from 1.67 to 1.9 Ga, representing 56% of the total analyses. Archean ages account for 30%, with ages between 2.5 and 3.3 Ga. A smaller Mesoproterozoic population (~ 4%) consists of ages between 1.4 and 1.5 Ga. Most notably is a Neoproterozoic age cluster of grains from ~ 620 to 718 Ma and representing ~ 5% of the grains analyzed. This is a distinct age signature was previously reported by Pipe (2023) and shown to be confined to the interval between Isaac channel complex 3 and Isaac channel complex 6 at Castle Creek.

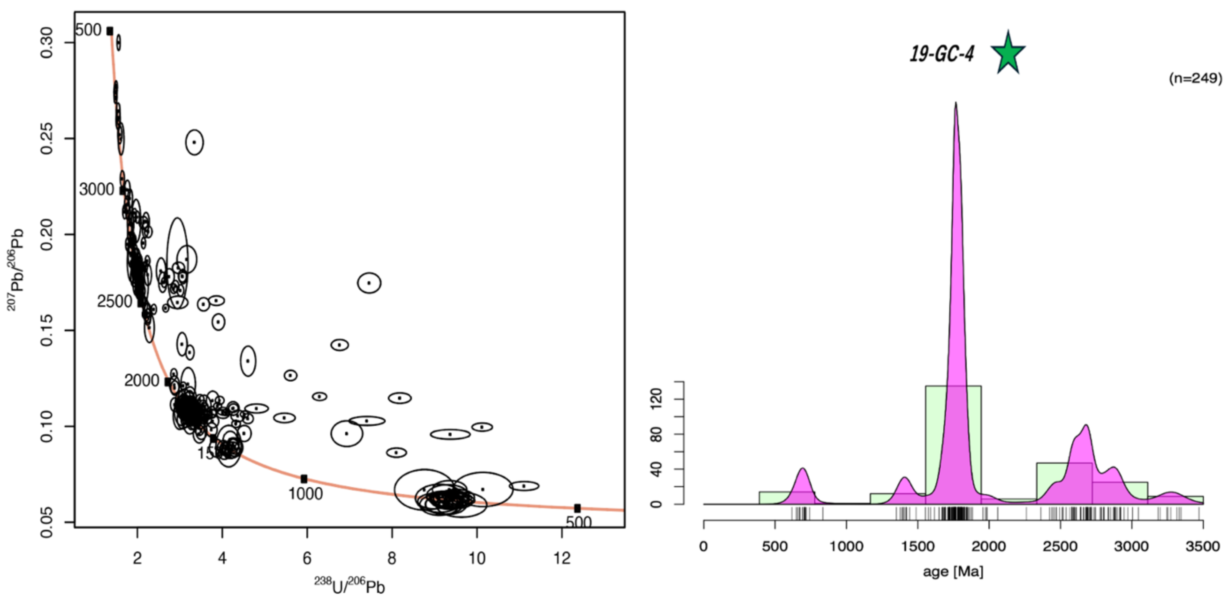

***Fig. 2.24**: Tera-Wasserburg diagram (left side) and Kernel Density Estimation (KDE) plot (right side) for sample 19-GC-4, illustrating detrital zircon age distributions. For the Tera-Wasserburg diagram each ellipse represents a single spot analysis and its 2σ standard error. KDE plots show the main age clusters. The spectrum is dominated by Paleoproterozoic and Archean age populations with a minor but distinct Neoproterozoic peak centered on ~ 650 Ma. This Neoproterozoic signal has previously been reported to be confined to strata between Isaac Channel Complex 3 and 6 at Castle Creek (Pipe, 2023).*

2.3.2 19-GC-5:

The detrital zircon age signature for this sample is characterized by a dominant Paleoproterozoic peak at ~ 1.8 Ga, with subordinate Mesoproterozoic and Archean age populations (Fig. 2.25). Of the total grains analyzed, 72% (186 grains) yield Paleoproterozoic ages between 1.62 and 2.1 Ga, forming the principal age cluster. ~ 5% of grains record Mesoproterozoic ages scattered between 1.1 and 1.46 Ga, while the remaining grains are Archean in age, ranging from 2.52 to 3.3 Ga. Like sample 19-GC-4, this sample has a unique Neoproterozoic age cluster between 632 and 748 Ma representing ~ 1% of the grains.

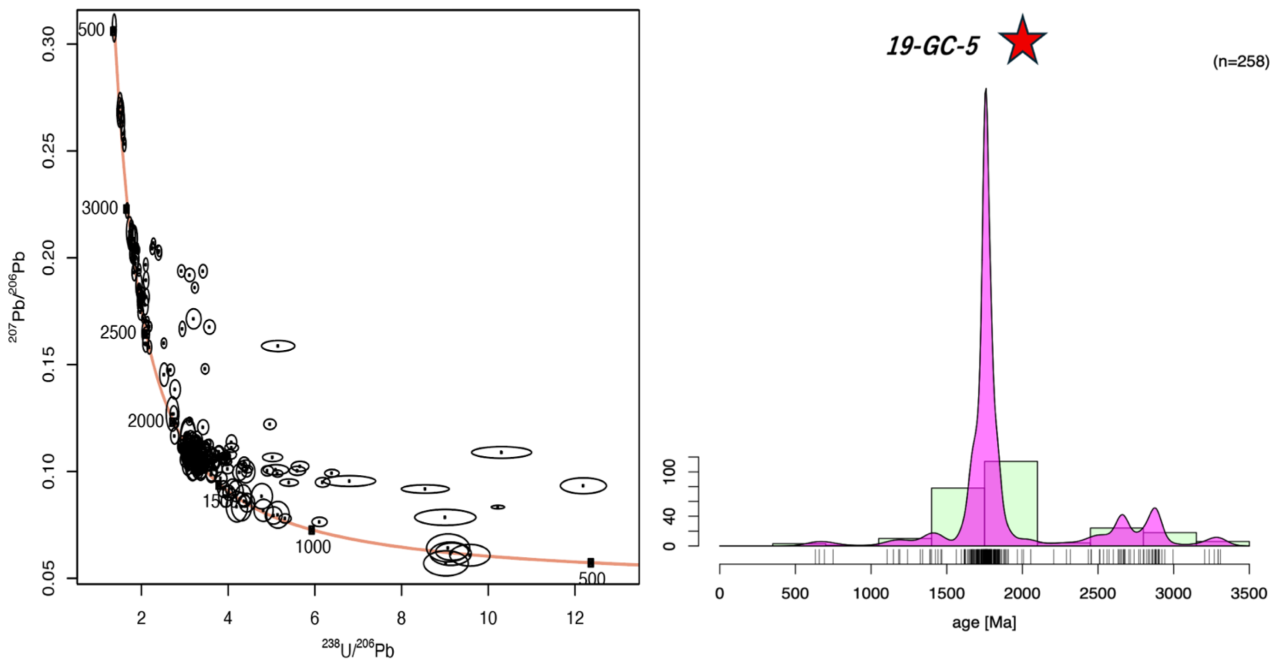

Fig. 2.25: *Tera-Wasserburg diagram (left side) and Kernel Density Estimation (KDE) plot (right side) for sample 19-GC-5, showing a bimodal detrital zircon age distribution. The spectrum is dominated by a Paleoproterozoic peak, with subordinate Mesoproterozoic and Archean age clusters, and includes a minor Neoproterozoic peak.*

2.3.3 23-CCN-Geochron 1:

The detrital zircon age distribution for this sample is bimodal, with a dominant Paleoproterozoic peak at ~ 1.8 Ga and subordinate peaks dispersed across the Neoarchean to Mesoarchean (Fig. 2.26). Of the 50 grains analyzed, 60% (30 grains) yield Paleoproterozoic ages ranging from 1.7 to 2.4 Ga whereas 30% (15 grains) fall within the Neoarchean to Mesoarchean interval (2.55–3.1 Ga). The remaining ages include two Mesoproterozoic grains (1.4–1.57 Ga) and three Paleoarchean grains at ~ 3.3 Ga.

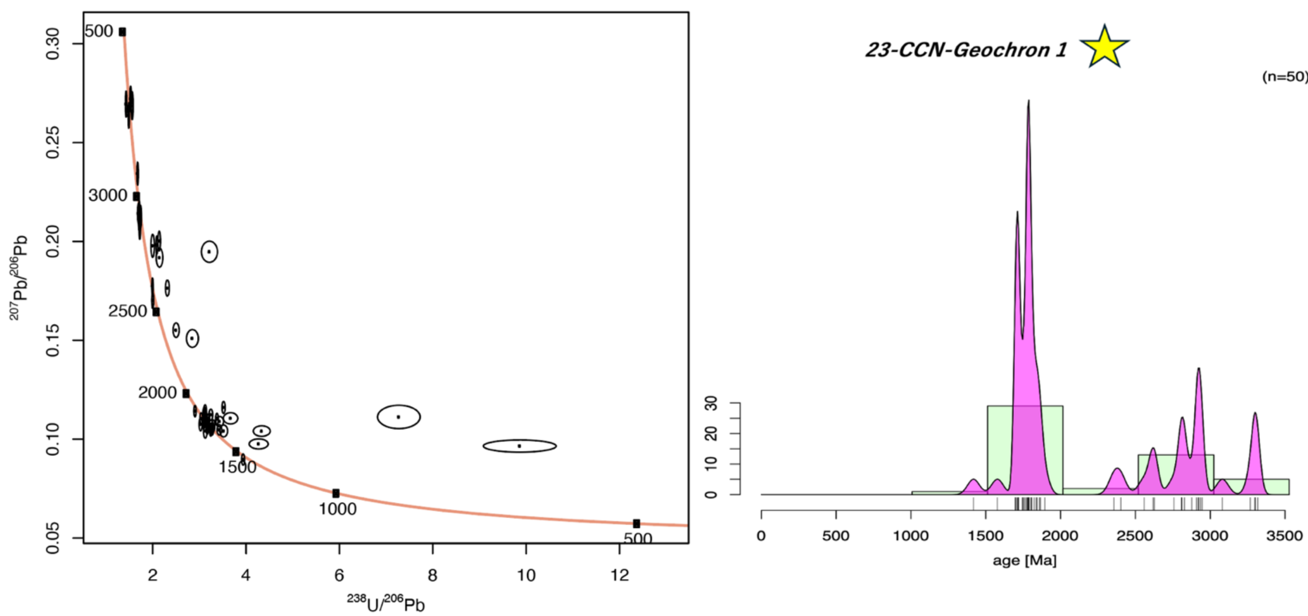

Fig. 2.26: *Tera-Wasserburg diagram (left side) and Kernel Density Estimation (KDE) plot (right side) for sample 23-CCN-Geochron 1, showing a bimodal detrital zircon age distribution. The spectrum is dominated by a Paleoproterozoic peak with subordinate Neoarchean and Mesoarchean age clusters.*

2.3.4 23-CCN-Geochron 3:

The detrital zircon age signature for this sample is characterized by a dominant Paleoproterozoic peak at ~ 1.7 Ga with subordinate age populations in the Mesoproterozoic and Archean (Fig. 2.27). Of the total grains analyzed, 68% (41 grains) yield Paleoproterozoic ages between 1.65 and 2.0 Ga and make up the principal age cluster. Ten grains record Mesoproterozoic ages scattered between 1.2 and 1.52 Ga, whereas the remaining grains are Archean and range from 2.65 to 3.3 Ga.

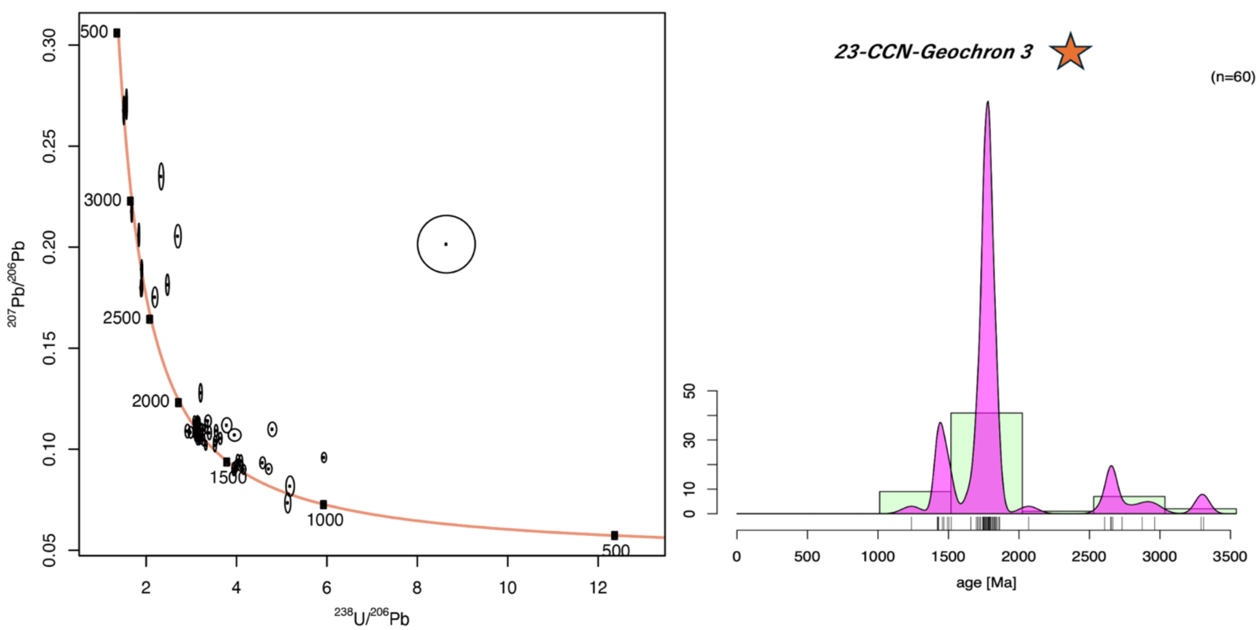

Fig. 2.27: *Tera-Wasserburg diagram (left side) and Kernel Density Estimation (KDE) plot (right side) for sample 23-CCN-Geochron 3, showing a bimodal age distribution. The spectrum is dominated by a Paleoproterozoic peak with subordinate Mesoproterozoic and Archean age clusters.*

2.3.5 Summarized Geochronology Results

The detrital zircon U–Pb age signature from the samples collected at the Castle Creek north outcrop are dominated consistently by a main Paleoproterozoic peak at ~ 1.8 Ga, with smaller but subordinate Archean and Mesoproterozoic populations, and rare Neoproterozoic grains. In all samples the most prominent grain cluster occurs between 1.65 and 2.1 Ga: 56% in 19-GC-4, 72% in 19-GC-5, 60% in 23-CCN-Geochron 1, and 68% in 23-CCN-Geochron 3. Archean aged grains, distributed between ~ 2.5 and 3.3 Ga, comprise 30% of the population in 19-GC-4, 23% in 19-GC-5, 30% in 23-CCN-Geochron 1, and 20% in 23-CCN-Geochron 3. Mesoproterozoic ages are consistently minor, ranging from 4–15% of the total across samples, with grains spanning 1.1–1.57 Ga. Distinctively, a Neoproterozoic signature (~620–750 Ma) occurs in 19-GC-4 and 19-GC-5, representing ~ 5% and ~ 1% of the respective grain populations. As noted above, this age cluster is unique to the Castle Creek succession between Isaac channel complexes 3 and 6, and also a single sample in the regional compilation of Hadlari et al. (2021). Being absent in Windermere strata elsewhere in the southern Canadian Cordillera suggests that the restricted stratigraphic occurrence of this age cluster may form a time horizon and therefore marker to aid in regional stratigraphic correlations.

Chapter 3: Characterization of Stratal Elements

3.1 Channel Units

3.1.1 Channel Units Summary

The channel units described in the study area range from approximately 7.5 m to 42 m thick, with an average of ~ 17 m, and are consistently bounded by erosional basal contacts. These contacts manifest as sharp, irregular surfaces displaying variable relief: common subtle scours ~ 10–20 cm deep (e.g., SR-4), and less common erosion surfaces up to 2 m deep, especially where channels incise underlying mud-rich/levee deposits (e.g., SR-6). The basal surfaces are typically marked by an abrupt increase in grain size to very coarse-grained sandstone or granule conglomerate. A ubiquitous characteristic across all channel units and their constituent fills is the pervasive presence of well-developed mudclast breccia. Channel units comprise between one to four channel fills. Individual channel fills are also bounded by erosional contacts, often expressed as sharp truncations of underlying strata with relief varying from a few centimeters to over a meter. These internal boundaries are typically overlain by mudclast breccia and marked by an abrupt increase in grain size. Channel fills are subdivided into two end-member types and are described next.

3.1.2 Type 1 Channels: Systematic upward-fining/-thinning with stratified tops and/or distinctive clasts

Type 1 channels (SR-3; SR-4; SR-5A and SR-5B; SR-6; SR-7) exhibit a systematic stratigraphic organization and a wide range of grain sizes and clast composition. Individual fills range from 2–17 m thick, with an average of ~ 8.5 m. Channel fills are typically bounded by erosional contacts characterized by scours up to ~ 2 m deep, though more commonly 30–60 cm and associated well-developed mudclast breccia. These fills typically display well-developed upward-fining and -thinning trends, transitioning from amalgamated, thick- to very thickly bedded, fine pebble or granule conglomerate (F1) with abundant mudclast breccia at their base to stratified fine- to medium-grained, thin- or medium-bedded T_{abde} or T_{abcde} turbidites at their tops. In the uppermost 1–2 m of Type 1 channel fills, sandstone beds become intercalated with fine-grained intervals with most fills capped by thin- to very thin-bedded upper division turbidites (F2.2 and F3). Distinctive clast suites are also a defining feature of this fill type, including quartz pebbles at the base of SR-4, SR-5A and SR-6, carbonate-cemented sandstone clasts in SR-5A and SR-6, and clasts of interstratified sand-mud.

3.1.3 Type 1 Channels Interpretation: Aggrading Channels

Type 1 channel fills are interpreted as the deposits of high-concentration, high-energy turbidity currents (Lowe, 1982) in channels that fill from the bottom upward (aggrading channel fill). Scoured basal contacts reflect incision and bypass followed by net deposition of amalgamated, thick- to very thick-bedded pebble or granule conglomerate and very coarse-grained sandstone (T_a) (F1), containing a variety of clast types including mud, quartz pebbles, carbonate-cemented sandstone and interstratified sand-mud, in the channel axis. As current energy waned with time, deposition shifted upward to finer-grained, thinner-bedded strata composed of more complete turbidites (T_{abcde}, T_{abde}) marking the upper part of the channel fill (Fig. 3.1). Laterally, these fills fine and thin exhibited by a change from amalgamated axial deposits, dominated by T_a beds (F1), to channel-margin successions composed primarily of medium- to fine-grained, upper-division turbidites (T_{cde}) (F2.2 and F3).

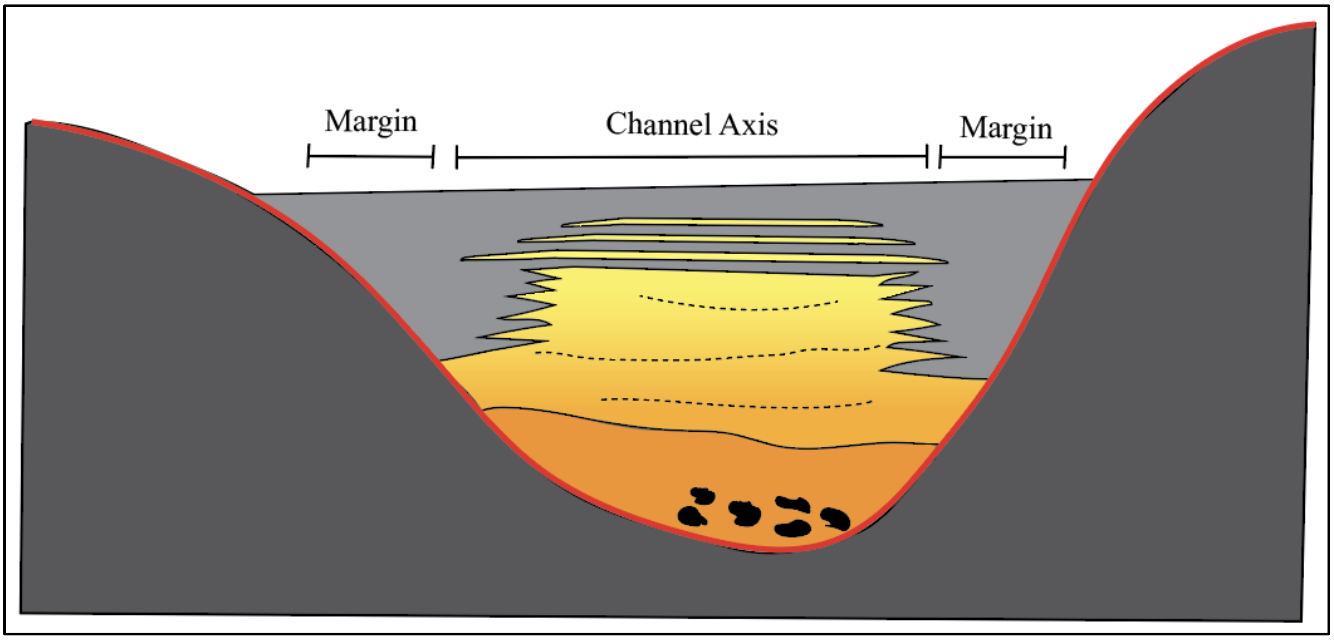

Fig. 3.1: *Schematic illustrating an individual aggrading channel fill with axial deposits consisting of amalgamated sandstone/conglomerate that become increasingly intercalated with fine-grained intervals vertically and laterally.*

The wide grain-size spectrum, ranging from mud to pebble in aggrading channel fills would have strongly influenced the vertical distribution of particles and therefore density, in the transporting flow, producing pronounced density stratification (Fig. 3.2). Differences in settling velocity between coarse- and fine-grained fractions likely concentrated the coarsest particles near the bed, overlain progressively by finer material, generating a vertically stratified flow. Such stratified turbidity currents are also subject to enhanced interfacial mixing with the ambient fluid and significant turbulence damping linked to high near-bed sediment concentration and stratification effects (Tilston et al., 2015).

These combined effects reduced transport capacity, promoting rapid deposition beneath collapsing turbulent suspensions (Arnott and Hand, 1989). The dense basal core of these currents was most likely confined to the deeper, axial part of the channel, but then became progressively more dilute laterally toward the channel margins (Dorrell et al., 2014). Consequently, axial settings were dominated by amalgamated coarse-grained sandstone and conglomerate, whereas thinner and finer strata accumulated toward the channel margins.

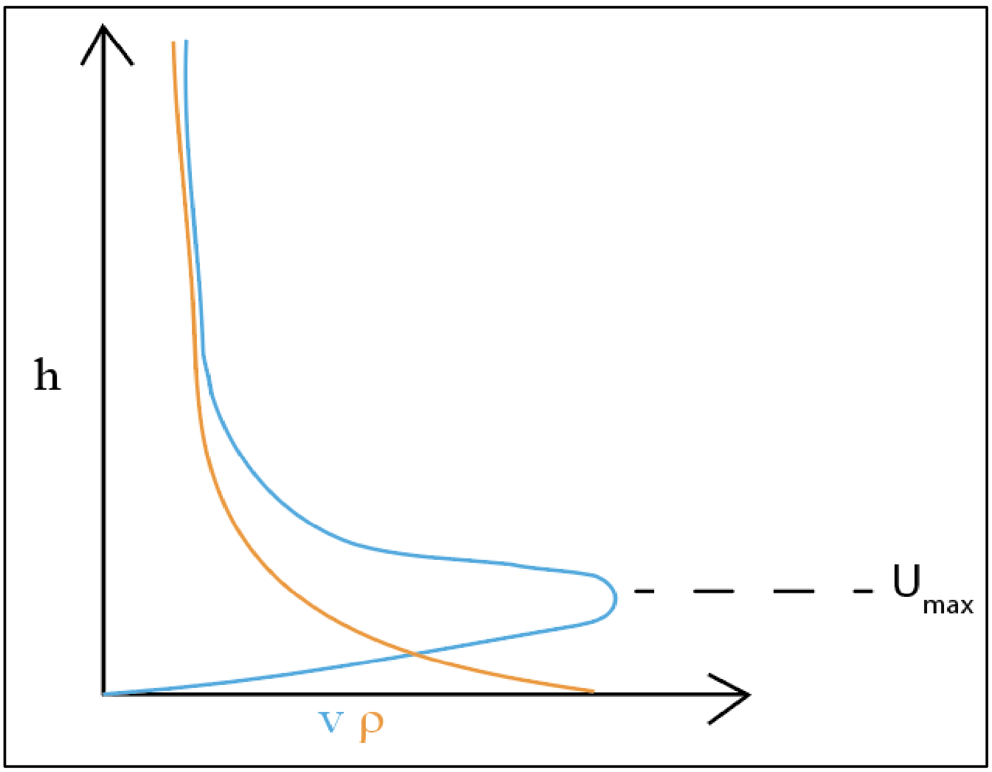

Fig. 3.2: *Schematic illustrating the density (orange) and velocity (blue) profiles in a highly stratified sediment gravity flow.*

3.1.4 Type 2 Channels: Coarse-grained dominated fills with little systematic upward change

Type 2 channels (SR-1, SR-2, SR-5C) are characterized by amalgamated, thick- to very thick-bedded (0.6–2.5 m) successions of upper very coarse-grained sandstone and fine granule conglomerate (F1). Fills range from 3.5–18 m thick and average ~ 10 m. Sandstone beds are commonly massive or grade upward to coarse-grain sandstone, with bed contacts marked by an abrupt grain size increase or subtle erosional relief. Well-developed mudclast breccia are present at the bases of fills, with clasts ranging from 2 to 50 cm in length and decreasing in abundance upward. Stratigraphically upward, channel fills show negligible upward-fining or -thinning, with an abrupt transition from very coarse-grained sandstone or conglomerate to fine-grained, upper-division turbidites (F2.2 and F3). In the case of SR-1, the uppermost fill shows evidence of traction transport with uncommon dune cross-stratification occurring near the top. Most notably, however, coarse-grained channel fill strata interfinger and pinch out abruptly into fine-grained, very thin- to thin-bedded, upper-division turbidites.

3.1.5 Type 2 Channels Interpretation: Laterally Accreting Channels

The dominance of very coarse-grained strata, the absence of upward-fining and -thinning (and lateral in the case of SR-1), together with their abrupt transition to fine-grained, upper-division turbidites at the top of Type 2 channel fills is interpreted to reflect lateral accretion deposition along the inner bends of sinuous, laterally migrating, deep-marine channels (Fig. 3.3) (Abreu et al., 2003; Arnott, 2007; Wynn et al., 2007). Consisting predominantly of very coarse-grained sandstone or gravel with comparatively little medium- or fine-grained sand, and no systematic upward change, these fills suggest a sediment supply comparatively better sorted and enriched in coarse-grained sediment than the sediment supply associated with aggrading channel fills of Type 1 (Fraino et al., 2022).

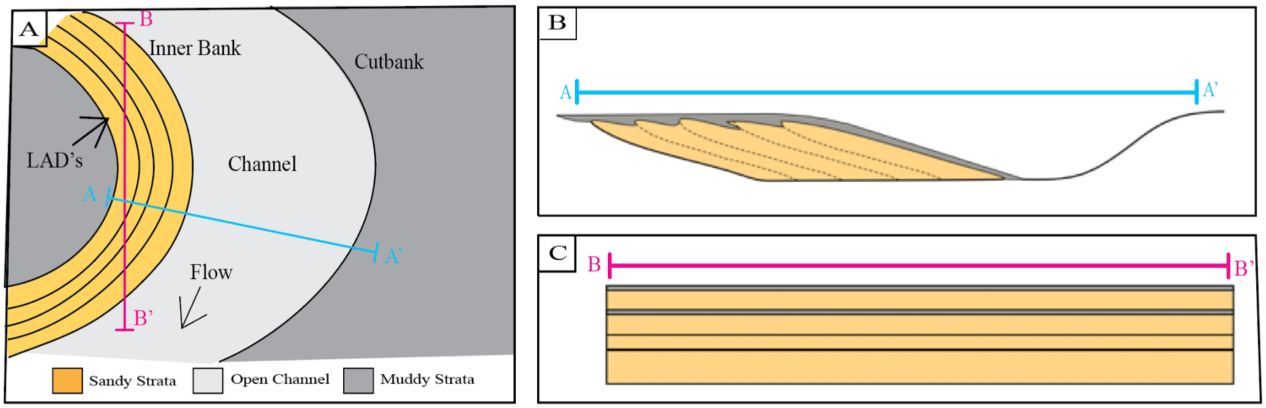

Fig. 3.3: *(A) Schematic illustrating the difference in the dip of laterally accreted strata as a function of the orientation of the outcrop surface versus the orientation of the inner bend of the channel. (B) Strata cut obliquely across the channel trend display distinct laterally accreting packages, whereas strata aligned parallel to the channel axis (C) appear predominantly horizontal (modified after Dumouchel, 2015).*

The improved sorting most likely produces flows that were poorly-density stratified (Fig. 3.4) with a more uniform coarse-grained, dense basal layer (plug-like) overlain sharply by a finer-grained, less dense upper layer. The steep density gradient between these layers would have suppressed turbulence production and reduced energy-consuming vertical mixing (Tilston et al., 2015). The plug-like density structure is broadly analogous to the density profile observed in open channel flows such as rivers. Consequently, deep-marine laterally accreting channels may be governed by similar fluid mechanical processes as it rounds a channel bed (Dumouchel, 2015). More specifically, as a turbidity current enters a channel bend centrifugal effects cause the high-concentration basal layer to be diverted towards the outer bank and enhancing erosion (Fraino et al., 2022). More importantly, the local increase in density along the outer bend causes the cross-channel density gradient to strengthen and steepen generating a density-driven secondary circulation that is directed toward and up the inner bend surface (Dumouchel, 2015; Arnott et al., 2021). In rivers a similar secondary circulation pattern is observed but rather than being density driven is hydraulically driven.

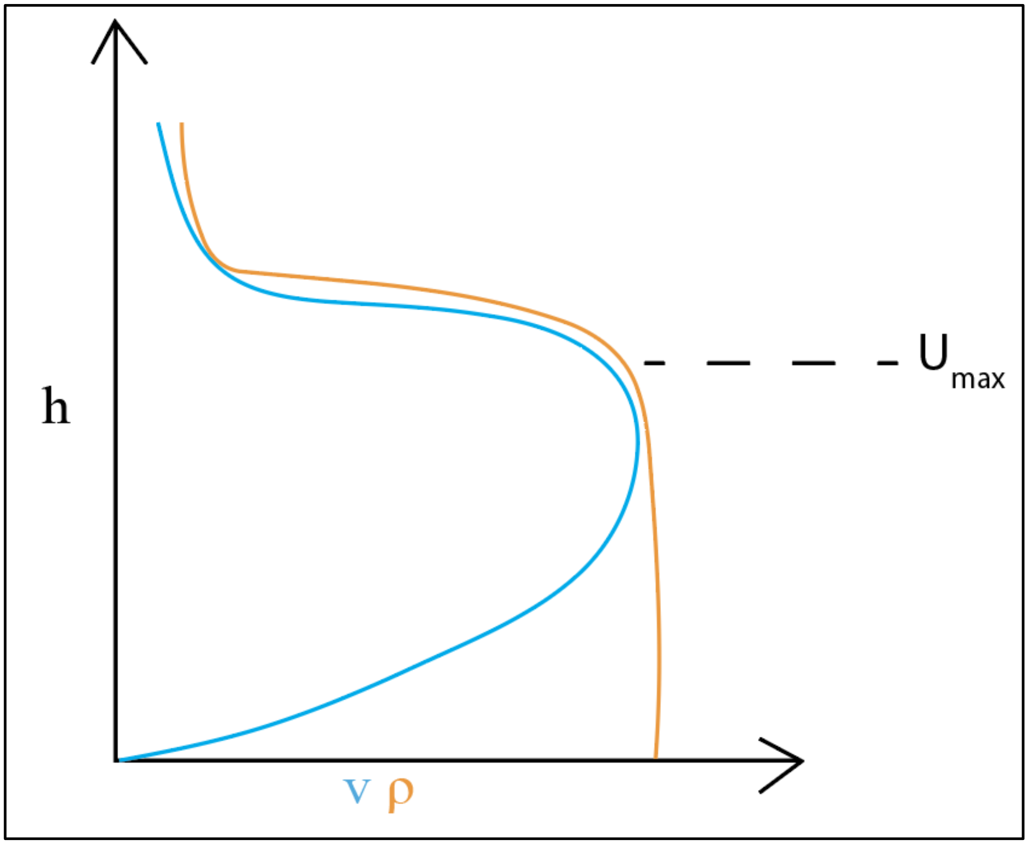

Fig. 3.4: *Schematic illustrating the density (orange) and velocity (blue) profiles through a poorly stratified sediment gravity flow. The steep density gradient between the basal, high-density plug-like layer and less dense upper part would hinder turbulence production and also reduce vertical mixing and energy expenditure.*

3.2 Mud-rich Units

3.2.1 Mud-rich Units Summary

Mud-rich intervals in the study area show variability in bed thickness, grain size and sand content, but recurring stratigraphic motifs allow them to be grouped into two kinds: (i) thick, coarse strata (Fig. 3.5), and (ii) thin, fine strata. Although one of the two kinds may occur locally in outcrop, where both are present they show a consistent stacking pattern with coarser, thicker strata overlain sharply or gradationally by finer, thinner-bedded strata. These mud-rich units comprise 364.6 m, or ~ 71% of the total study area interval measured in the Castle Creek north outcrop.

Thick, coarse mud-rich successions (except MR-8) are composed mostly of medium- to coarse-grained, medium- to thick-bedded (12–60 cm, locally up to 1.5 m), lower-division (T_{ab}; T_{bcde}; T_{abde}) turbidites (Fig. 3.6) intercalated with fine-grained beds. Bed contacts are commonly sharp and planar, although erosional surfaces and mud intraclasts occur locally at the base of some T_a beds (F1), which then stack to form stratal units ranging from 3.5 to 7 m thick and sand:mud ratios ranging from 60:40 to 90:10. MR-5 preserves the thickest example, an ~ 7 m interval of medium- to thick-bedded, coarse- to medium-grained T_{ade} and T_{abde} turbidites (F1 and F2.1) that then fines and thins upwards to fine-grained, thin-bedded, upper-division turbidites (F2.2 and F3). These sand-rich packages account for ~ 9.4% of the total measured section in the study area.

Fig. 3.5: *Outcrop example of mud-rich strata consisting mostly of stacked, sharp planar-based medium- to thick-bedded, coarse-grained lower-division turbidites (T_{abde}.). White arrow shows stratigraphic up. Field backpack for scale.*

Fig. 3.6: *Outcrop photograph of medium-bedded, medium-grained, lower-division turbidites (T_{bcde}). Pencil for scale.*

Thin, fine, mud-rich successions range from 2 – 60 m thick (average ~ 28 m) with sand:mud ratios ranging from ~ 20:80 to 40:60. Strata consist primarily of fine- to very fine-grained, very thin- to thin-bedded (1–8 cm, locally up to 25 cm), upper-division (T_{cde} or T_{de}) turbidites (F2.2 and F3) (Fig. 3.7). Ripple cross-stratified T_c divisions (F2.2) are ubiquitous and commonly occur as 1–15 cm-thick cosets composed of 2–5 sets. Bed contacts are typically sharp and planar (Fig. 3.8) – erosive bases and load structures are uncommon. Medium-bedded turbidites (10–25 cm) occur irregularly, particularly in MR-4, MR-6, and MR-7, and are composed primarily of very fine-grained, upper-division turbidites. MR-6 is distinctive in its coloration (deep red to orange hues) caused by oxidation of iron-rich calcite cement, while MR-8 is notable for intense weathering and organic enrichment (TOC ~ 0.2–0.3%). These thin, fine-grained mud-rich intervals account for 61.3% of the total measured section.

Fig. 3.7: *Outcrop photo of very fine- to fine-grained, very thin- to thin-bedded, upper-division turbidites (T_{cde} and T_{de}). Field backpack for scale.*

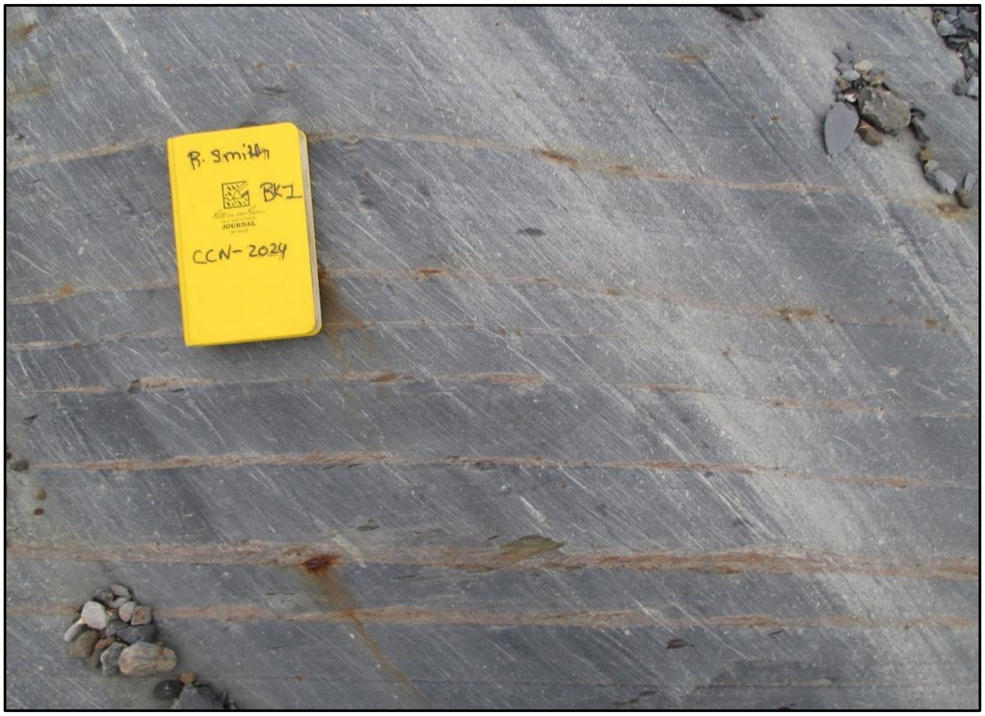

Fig. 3.8: *Outcrop photo of fine-grained, very thin- and thin-bedded, upper-division turbidites (T_{cde}). Field notebook for scale.*

Both levee types are also characterized by a notable vertical stacking pattern of T_{cde}, and less common T_{bcde} turbidites that display similar grain size, sedimentary structures, plus bed and internal division thickness — an attribute termed 'self-similar' by Cunningham and Arnott (2021). Collectively, a stack of self-similar beds make up a single *'bedset'* (Fig. 3.9), each sharply bounded by an abrupt shift in grain size, bed and division thickness, or kind of ripple cross-stratification, which commonly marks the base of a new bedset, and comprising 4–10 beds totalling 10–40 cm in thickness. Most beds in a bedset consist of medium- to very fine-grained, ripple cross-stratified (single-set to multiset) (Fig. 3.9) or planar laminated sandstone consistently capped by a thin siltstone or mudstone interval corresponding to the T_{de} divisions.

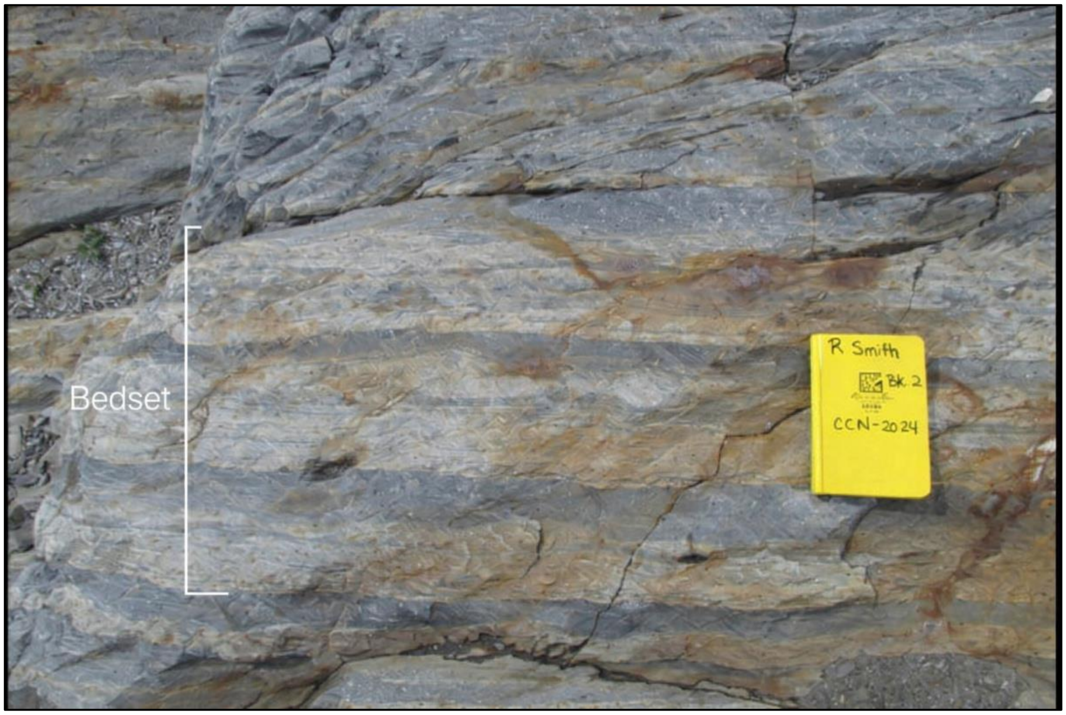

Fig. 3.9: *Example of a stack of self-similar T_{bcde} turbidites in which individual beds exhibit similar grain size and thickness, including the multiset ripple-cross-stratified part. Field notebook for scale.*

3.2.2 Mud-rich Units Interpretations

In this study, stratal units composed of mud-rich strata are interpreted to be extrachannel deposits, or more specifically, levee deposits, which typically are a poorly documented architectural element in most studies of ancient deep-marine channel–levee systems. At Castle Creek however, periglacial conditions, and therefore limited chemical weathering, has well preserved these mud-rich strata, and as result previous studies have focused on these strata (Khan and Arnott, 2010; Navarro, 2016; Bergen et al., 2022; Cunningham and Arnott, 2021), supported by insights from experimental and numerical modelling of turbidity current overspill (Straub and Mohrig, 2008; Kane et al., 2010; Halsey and Kumar, 2019), in addition to modern turbidite systems like the Amazon and Mississippi submarine fans (Garrison et al., 1983; Pirmez and Imran, 2003; Jegou et al., 2008).

In outcrop, the recognition of levee deposits is based on a combination of facies, grain size, stratigraphic organization, and where present, position adjacent to a genetically related channel fill. Levee deposits are typically laterally continuous (>1 km), very fine- to fine-grained, and dominated by traction-structured sandstone with systematic vertical and lateral fining and thinning.

Previous work by Khan and Arnott (2011) and Bergen et al. (2022) subdivided levee deposits into two end-member parts, namely proximal and distal levee deposits based on stratal characteristics and lateral distance from the channel margin (Fig. 3.9). Additionally, these authors showed that proximal levees comprise two parts: a basal part composed of intercalated coarse-grained, medium- to thick-bedded (T_a, T_{ab}, or T_{abc}), lower-division and fine-grained, thin-bedded, upper-division turbidites overlain sharply by an upper part consisting of very fine to fine-grained, thin-bedded, upper-division (T_{cde} or T_{de}) turbidites (Khan et al. 2011; Bergen et al., 2022).

In contrast, distal levees are characterized predominantly by mud-dominated, very thin- to thin-bedded, upper-division (T_{cde} or T_{de}) turbidites that have greater laterally continuity reflecting deposition by highly dilute overspill farther from the channel margin. Irregularly spaced coarse-grained, medium- to thick-bedded, lower-division (T_a, T_{ab}, or T_{abc}) turbidites have been interpreted to be formed by larger flows that bypassed the proximal levee and lost transport capacity and deposited over the distal levee. These interpretations are consistent with previous studies (e.g. Khan and Arnott, 2011; Khan et al., 2011; Bergen et al., 2021, Cunningham and Arnott, 2021) and provide a framework for identifying and interpreting the lateral and vertical organization of levee deposits, especially where only parts of the idealized succession is exposed.

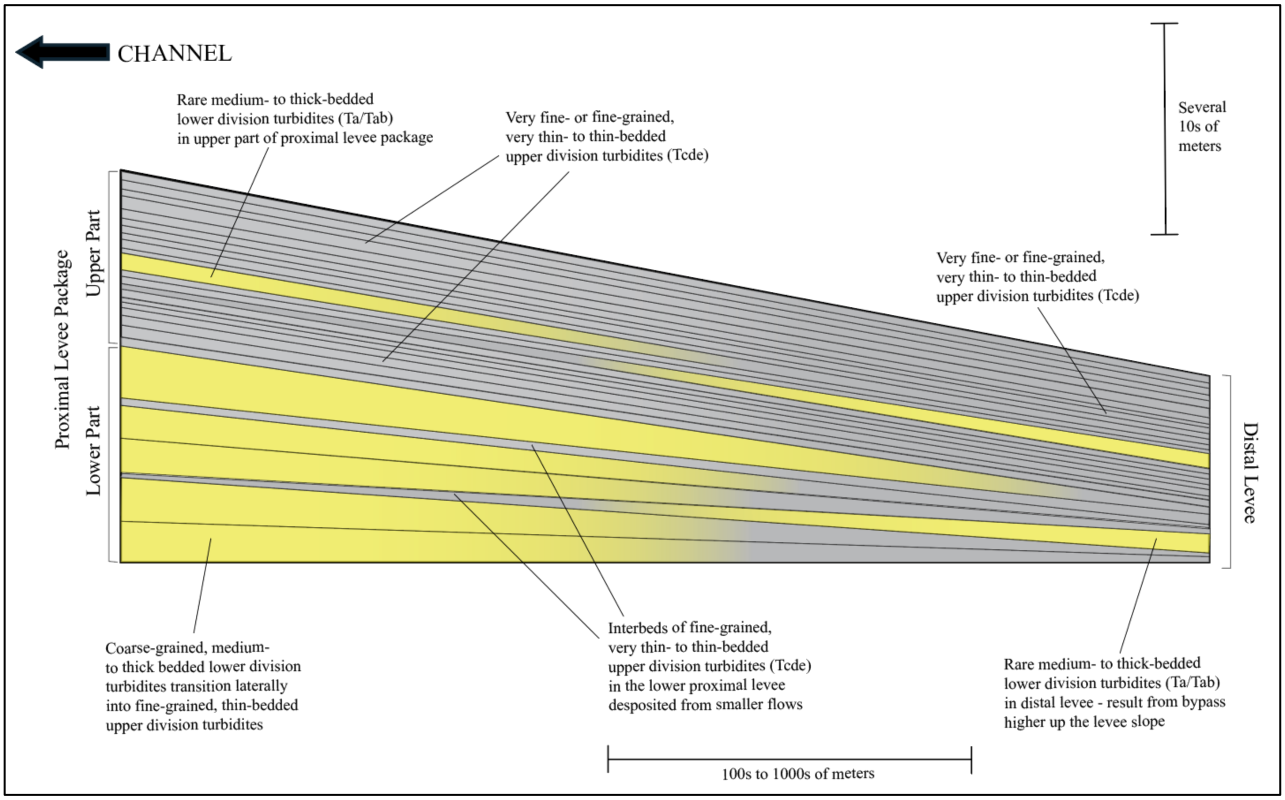

Fig. 3.10: *Schematic cross-section illustrating the stratigraphic organization of levee deposits adjacent to a submarine channel. The proximal levee package is subdivided into a lower part composed of coarse-grained, medium- to thick-bedded lower division turbidites (T_a/T_{ab}) interbedded with fine-grained, thin-bedded, upper division turbidites (T_{cde}), and an upper part dominated by very fine- to fine-grained, very thin- to thin-bedded, upper-division turbidites (T_{cde}) with rare medium- to thick-bedded, lower-division turbidites. Laterally, these deposits transition into the distal levee dominated by fine-grained, very thin- to thin-bedded, upper-division (T_{cde} and T_{de}) turbidites with rare medium- to thick-bedded, lower-division (T_a/T_{ab}) turbidites that indicate bypass over the proximal levee, associated with anomalously energetic flows, and deposition on the distal levee (modified from Cunningham and Arnott, 2021).*

The coarse-grained, medium- to thick-bedded lower-division (T_{ade} or T_{abde}) turbidites at the base of mud-rich intervals that sharply overlie channel units are interpreted as the lower part of proximal levee packages. During channel inception, low height levees formed along the margins of the early channelized flows (Fig. 3.11A). These initial flows are thought to have had a plug-like density structure with minimal vertical stratification and high transport efficiency (Tilston et al., 2015; Kneller et al., 2016; Bergen, 2017). Bergen (2017) suggested that the velocity maximum in these early flows was elevated above the height of the incipient levees, allowing the dense, lower portion of the flow to overspill more readily (Fig. 3.11B). This overspill deposited medium- to thick-bedded, coarse-grained, lower-division turbidites that constitute much of the lower part of proximal levee successions. Interbedded thin-bedded, finer-grained upper-division turbidites are attributed to deposition from lower-energy, lower-concentration flows during the same early phase of channel development.

The upper, very fine-grained, mud-rich interval may represent either the upper part of a proximal levee or distal levee deposits (Fig. 3.11C). However, because data collection was limited to a single vertical transect and did not capture lateral facies variations, it is not possible to confidently distinguish between the two. Nevertheless, in most cases thin-bedded, very fine-grained, mud-rich strata sharply overlie thick-bedded, coarse-grained strata (with the exception of MR-8), which then is more consistent with the upper and lower parts, respectively, of a proximal levee. With continued sediment transport, successive flows progressively built-up levee height, resulting in greater confinement of later flows. With ongoing deposition on the channel margins, levee height came to exceed the height of the velocity maximum. This allowed only the upper finer-grained part of the flow to overspill the channel margins and resulted in the deposition of mud-rich, very thin- to thin-bedded upper part of the proximal levee package. Coarser-grain, medium- to thick-bedded turbidites in this upper part of the levee package were deposited by anomalously large flows where the dense, lower part of the flow was able to overspill the channel margins.

Alternatively, if these fine-grained intervals represent distal levee deposits, they would have accumulated farther from the channel margins, beyond the primary locus of confined flow. Unlike proximal levees, which typically display coarse basal and fine upper parts, distal levees are commonly more monotonous, consisting of relatively uniform, thin-bedded, fine-grained, upper-division turbidites. These successions commonly contain rare medium-bedded turbidites and show limited evidence of systematic upward-fining or -thinning. Their stratigraphic and architectural character reflects deposition from flows that had lost much of their transport competence and capacity, leading to the preferential settling of very fine- to fine-grained sand and finer sediment at greater distances from the channel margin.

Additionally, the common occurrence of multi-set ripple cross-stratification and stacked self-similar T_{cde} turbidites forming sharply bounded bedsets are also indicative of levee deposition. Multi-set ripple cross-stratification is interpreted to reflect a stratified density structure that commonly develops as flows overtop the channel margins and collapse (Tilston et al., 2015). Self-similarity of component turbidites suggests recurring pulses from the same, long-lasting turbidity current events rather than multiple flows, and represents a condition that appears to be unique to levee deposition.

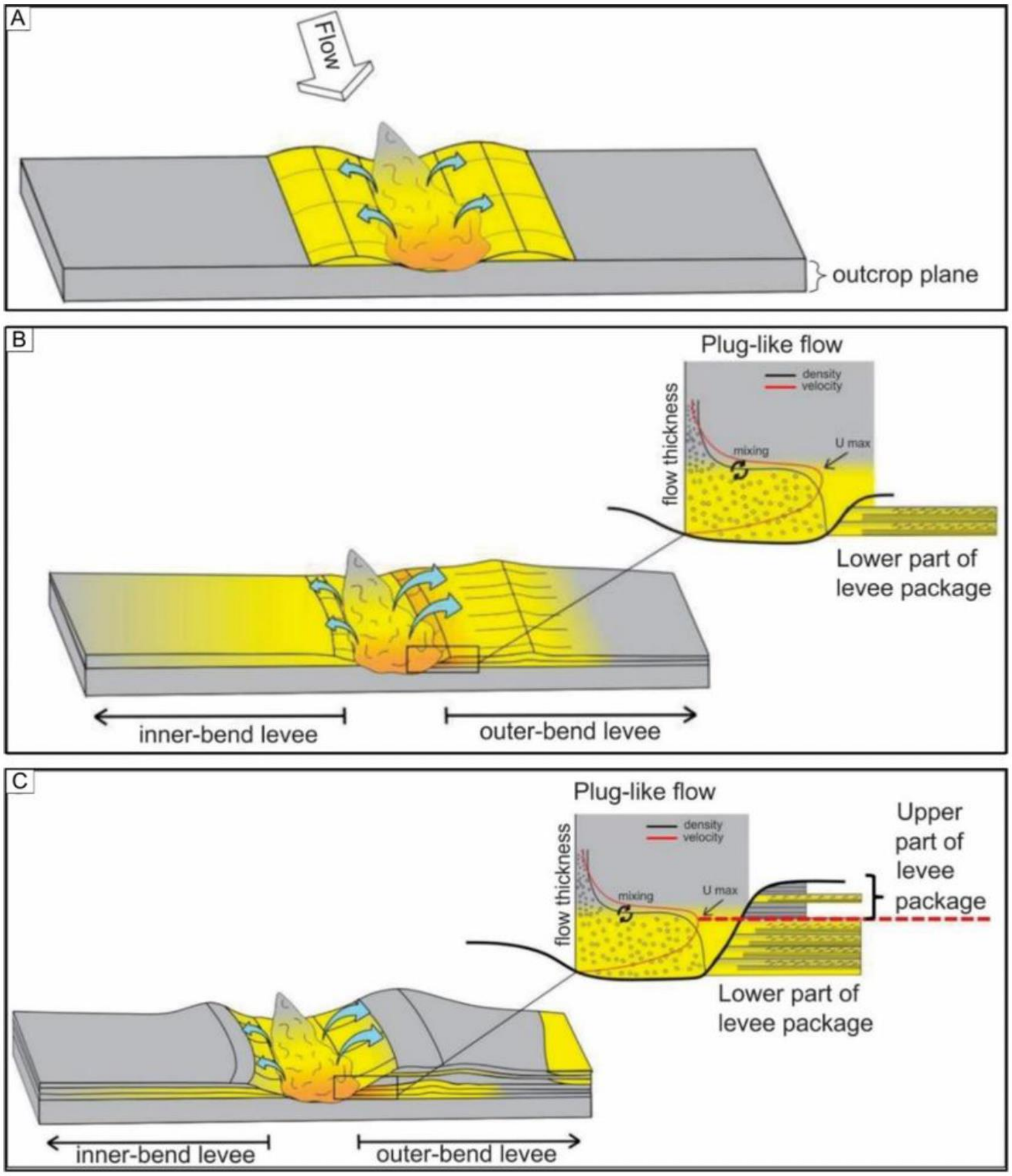

***Fig. 3.11**: Model by Bergen (2017) and Bergen et al. (2022) illustrating the development of a two-part (lower and upper) proximal levee package. A) Coarse-grained turbidites are interpreted to mark channel inception and the base of incipient levees that only poorly confined the axial part of channel-bounded flows. B) The plug-like density structure of the flow created efficient flows with negligible vertical stratification. The height of the velocity maximum exceeded the height of the incipient levees that allowed coarse-grained sediment to overspill depositing thick-bedded turbidites composing the lower proximal levee package. C) Continued deposition on the levee caused relief between the channel floor and levee crest to exceed the height of the velocity maximum of most flows. This, in turn, caused only the upper, fine-grained parts of turbidity currents to overspill and deposit the fine-grained, thin-bedded upper part of proximal levee packages.*

3.3 Debrite Element

3.3.1 Description

Debrite elements are uncommon in the Castle Creek north study area (~ 4% of the succession) and occur almost exclusively near the base of the measured section. Individual deposits range from 0.6–13 m in thickness and extend laterally for ~ 100–159 meters before being obscured by glacial cover or debris. These deposits consist of matrix-supported conglomerate (F4) composed of dispersed quartz granules and pebbles embedded in a silty mudstone matrix, along with cm- to m-scale lithic clasts. Lithic clasts range from 20–70 cm, with some exceeding 1 m, and are composed of mudstone, carbonate-cemented mudstone, and interstratified sandstone-mudstone fragments. Debrite intervals typically exhibit an erosional basal contact, incising up to 50 cm into underlying channel fills. In one instance, an ~ 60 cm-thick debrite unit is intercalated within fine-grained, upper-division turbidites, and can be traced along strike for ~ 70–80 m before pinching out. In outcrop, debrites are readily identified by quartz granules dispersed in a dark coloured mudstone matrix that imparts a distinctive ‘starry night’ appearance.

3.3.2 Interpretation

Debrites are interpreted as the product of submarine debris flows, which are cohesive sediment-gravity flows likely generated by the mechanical remobilization and reconstitution of a failed upslope seabed (Arnott, 2010). Within these flows, mudclasts and quartz gravel were supported by cohesive strength and buoyancy effects of the silty mudstone matrix that reduced particle settling and facilitated downslope transport (Mulder and Alexander, 2001). Slope failure may have been triggered by a combination of factors, including high sedimentation rates, seismic activity, elevated pore pressures, and/or relative sea-level fluctuations (Canals and Lastras, 2004). Deposition occurred through progressive frictional freezing and the progressive downward thickening of a rigid plug, which upon reaching the base of the flow, resulted in *en masse* deposition (Mulder and Alexander, 2001; Arnott, 2010). In the Castle Creek north study area, debrites are almost always overlain by channel fills and are commonly interpreted as resulting from slope instability caused by shelf-edge unloading and increased pore pressure during falling relative sea level or lowstand conditions (Arnott et al., 2011).

Chapter 4: Discussion

4.1 Relative Sea-Level Change and Deep-Marine Sedimentation

Sequence stratigraphy is the study of facies relationships within a chronostratigraphic framework, emphasizing genetically related sedimentary successions bounded by correlative disconformable or conformable surfaces. It is most readily applied to coastal and shallow-marine settings where stratigraphic architecture reflects changes in sediment supply, linked to continental weathering, and accommodation, controlled by the interplay between eustatic fluctuations and subsidence, collectively referred to as relative sea level (RSL) (Catuneanu et al., 2009). Fluctuations in RSL strongly influence the development of the continental shelf, which in turn has a profound influence on the transport of sediment into deep-marine settings. During lowstand fluvial systems may extend to the shelf edge resulting in increased delivery of coarse-grained sediment for remobilization into the deep sea. During highstand, on the other hand, flooding of the shelf causes the landward retreat of fluvial systems and a reduction in grain size and sediment flux available for basinward transport (Catuneanu, 2006; Posamentier and Walker, 2006; Catuneanu et al., 2009).

Deep-marine sedimentary systems that form basinward of wide continental shelves with a well-developed shelf–slope break, such as passive-margin basins, are often strongly influenced by variations in shelf accommodation (i.e. RSL change). This framework is commonly applied to the Neoproterozoic passive margin of northwestern Laurentia. However, not all turbidite systems are governed primarily by eustatic fluctuations. In many cases, tectonic activity and/or climatic factors exert greater control, with processes such as sedimentary and volcanic loading, crustal extension, and crustal thinning influencing basin subsidence and sediment delivery that are independent of sea-level change (Ingersoll, 2011). A variety of classification schemes exist to interpret such stratigraphic successions, but in this study the four-stage systems tract model of Hunt and Tucker

(1992) is applied to reconstruct the temporal and spatial evolution of the study interval. This model recognizes four genetic units: the falling-stage systems tract (FSST), lowstand systems tract (LST), transgressive systems tract (TST), and highstand systems tract (HST).

The falling-stage systems tract (FSST) (Fig. 4.1) is characterized by falling relative sea level (RSL), during which the shoreline shifts basinward and downward, progressively exposing the continental shelf (Posamentier et al., 1992; Plint and Nummedal, 2000; Catuneanu et al., 2009). Subaerial exposure of the shelf allows rivers to extend basinward, in some cases reaching the shelf–slope break. Where this occurs, rivers reintroduce fluvially transported sediment directly to the upper slope, which then is remobilized into deep-marine settings (Posamentier and Kolla, 2003). During this stage, sediment-gravity flows are often out of equilibrium with the existing slope gradient. As a result, flows commonly incise submarine canyons and channels along the upper- and mid-slope while bypassing large volumes of sediment to the base-of-slope and basin floor (Arnott, 2010; Dumouchel, 2015). Mass-wasting events including slides, slumps, and debris flows are also common during falling RSL, triggered by gravitational instabilities at the shelf edge and on the upper slope (Arnott, 2010; Fraino et al., 2022).

The transition to the lowstand systems tract (LST) occurs as relative sea level reaches its lowest position (Fig. 4.1). At this stage, sediment supply to the shelf–slope break is maximized, and downslope resedimentation increases. Shelf-delta progradation results in an increase in the sand:mud ratio of the transported sediment, culminating in a sediment supply dominated by sand-rich flows (Fraino et al., 2022). The basal surface of the LST represents the sequence boundary (SB) and the onset of a new depositional sequence. With increased sand content, the transport efficiency of turbidity currents decreases, steepening the equilibrium slope profile. In response, channels on the mid- to lower slope undergo systematic aggradation as deposition is required to re-establish equilibrium. During this adjustment, the basin floor may experience temporary sediment starvation and local retrogradation until slope equilibrium is restored, after which the active center of deposition shifts once more to the basin floor (Posamentier and Kolla, 2003).

As relative sea level begins to rise at the onset of the transgressive systems tract (TST), sediment derived from continental erosion becomes increasingly trapped on the aggrading coastal plain and deltas (Posamentier and Walker, 2006). This sequestration reduces the flux of siliciclastic sediment to the deep-marine environment, leaving it progressively sediment starved (Fig. 4.1). At the same time, gravitational instability along the shelf edge and upper slope intensifies as the slope equilibrium profile adjusts, leading to more frequent mass-wasting events and the deposition of associated mass-transport deposits (Posamentier and Kolla, 2003). Sediment gravity flows that do reach the slope during this stage typically have a low sand-to-mud ratio and are routed through highly confined, sinuous channel systems with well-developed levees. These channels tend to be strongly aggradational, recording limited lateral migration (Kneller, 2003; Neal and Abreu, 2009; Arnott, 2010; Fraino et al., 2022).

Transgression culminates once sea level approaches its next local maximum and sediment supply is once again exceeded, signaling the transition into the highstand systems tract (HST). During the HST, the continental shelf is often fully flooded and may support the development of a carbonate platform, depending on environmental conditions. If established, such platforms shed carbonate sediment downslope, where it mixes with reworked siliciclastic material (Fig. 4.1). With the shelf now at its widest extent, the delivery of coarse-grained sediment to the deep marine is significantly reduced. As a result, deposition in deep-marine settings during this stage is dominated by fine-grained sediment and may include the development of a condensed section (Allen and Posamentier, 1993; Plint and Nummedal, 2000).

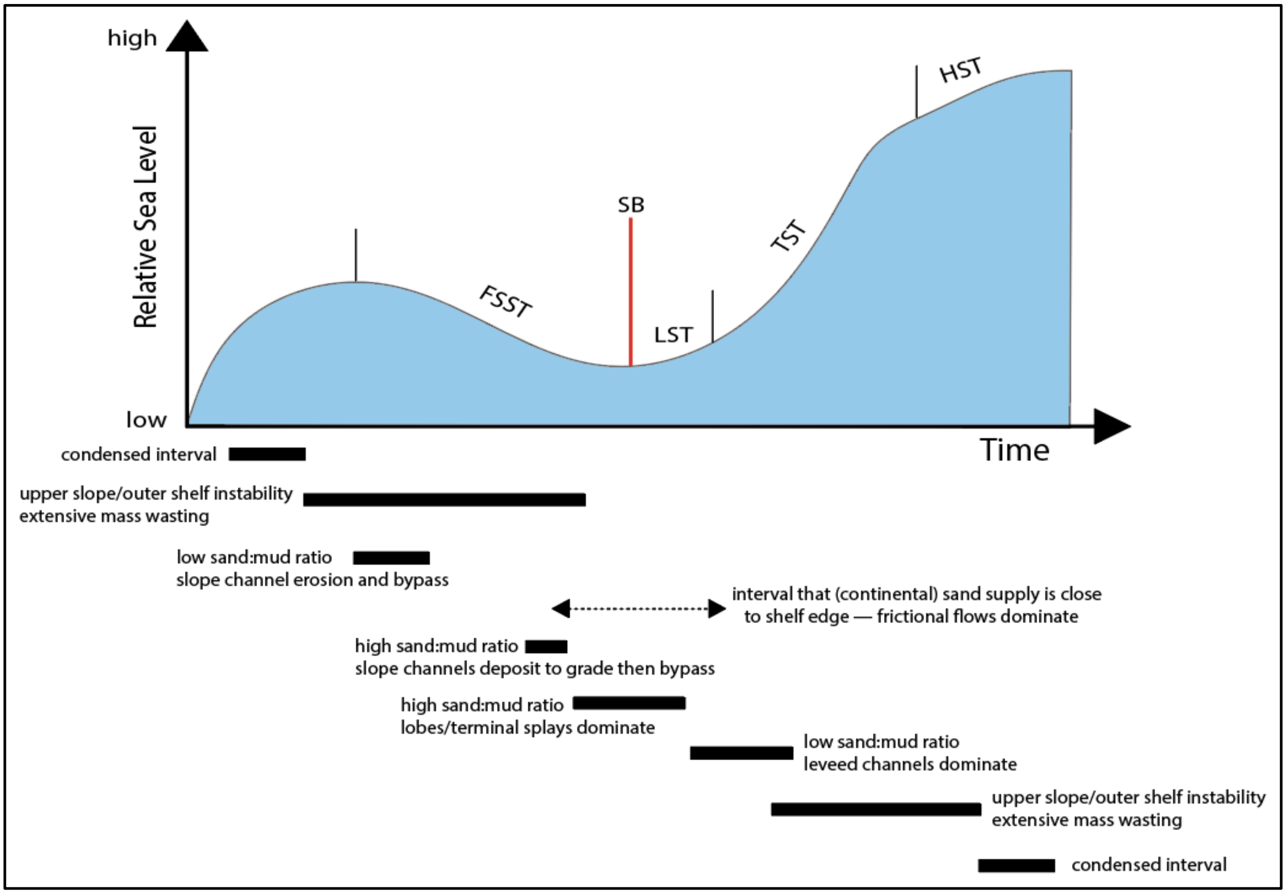

Fig. 4.1: *Conceptual model linking sediment transport and depositional patterns to fluctuations in relative sea level along a passive continental margin supplied by a single point source of sediment (modified from Arnott, 2010).*

4.2 Spatial and Temporal Evolution of Channel Complexes

Previous studies of deep-marine channel–levee complexes at the Castle Creek outcrop (Navarro et al., 2007; Schwarz and Arnott, 2007a,b; Dumouchel, 2015; Fraino et al., 2022) have applied stratigraphic analysis to evaluate the factors controlling the evolution and development of these systems. A recurring stratigraphic motif has been recognized within these channel complexes reflecting the combined influence of allogenic (external) and autogenic (internal) processes that govern their temporal and spatial evolution.

Allogenic controls, such as long-term eustatic fluctuation and climate change, strongly influence sediment supply to the shelf–slope break, particularly grain size and grain-size distribution, which in turn affect flow type and volume (Posamentier and Kolla, 2003; Catuneanu et al., 2009; Catuneanu, 2020), and profoundly, flow structure (Tilston et al., 2015). Autogenic mechanisms, including channel migration, stacking patterns and local confinement (McHargue et al., 2011), further modify the depositional style of slope channels and their composite channel complexes like those in the Isaac Formation. Lithological and compositional indicators such as the presence/absence of quartz pebbles, mud intraclasts, carbonate clasts, and mass-transport deposits provide stratigraphic proxies for interpreting long-term relative sea-level fluctuations. The combination of these allogenic and autogenic controls provides the framework for interpreting the stratal architecture and spatial–temporal evolution of the channel complexes identified in this study.

Five channel complexes (ICC5.1-3, ICC6.1-2) (Fig. 4.2) have been identified in the study interval based on stratigraphic data collected along a single vertical transect and mapping of architectural elements and major bounding surfaces from high-resolution drone photomosaics. Channel complexes range from ~ 60 –150 m thick and are separated by fine-grained, medium- to thin-bedded, complete and upper division turbidites and/or debrites. The base of most channel complexes is marked by debrites or other mass transport deposits (i.e. slide complex). These strata are then overlain by aggrading channel units in which the lowermost channel fills characteristically contain anomalously coarse-grained sediment (quartz pebbles) and uncommon carbonate clasts. More typically channel fills consist of thick-bedded, very coarse-grained sandstone or granule conglomerate grading upward to medium-bedded, medium- to fine-grained sandstone and exhibit a disorganized channel stacking pattern most probably related to avulsion and spatially random lateral displacement of younger channels due to limited lateral confinement. Stratigraphically upward, aggrading channel units transition to laterally accreting fills composed predominantly of very coarse- and coarse-grained sand with little vertical or lateral change in grain size or bed thickness. The top of these channel fills exhibit a distinctive interfingering of coarse-grained channel deposits pinching out abruptly into fine-grained, thin-bedded, upper-division turbidites, which are interpreted to be inner-bend levee deposits onto which the coarse-grained laterally accreting channel deposits onlap. Individual laterally accreting channel fills also show an organized offset stacking pattern that most likely reflects the effects of unfilled space in a confined channelized system. An idealized model relating the stratigraphic evolution of channel complexes to eustatic changes and its effect on sediment supply to the deep marine, which in turn reflect stacking patterns of stratal elements, is discussed next.

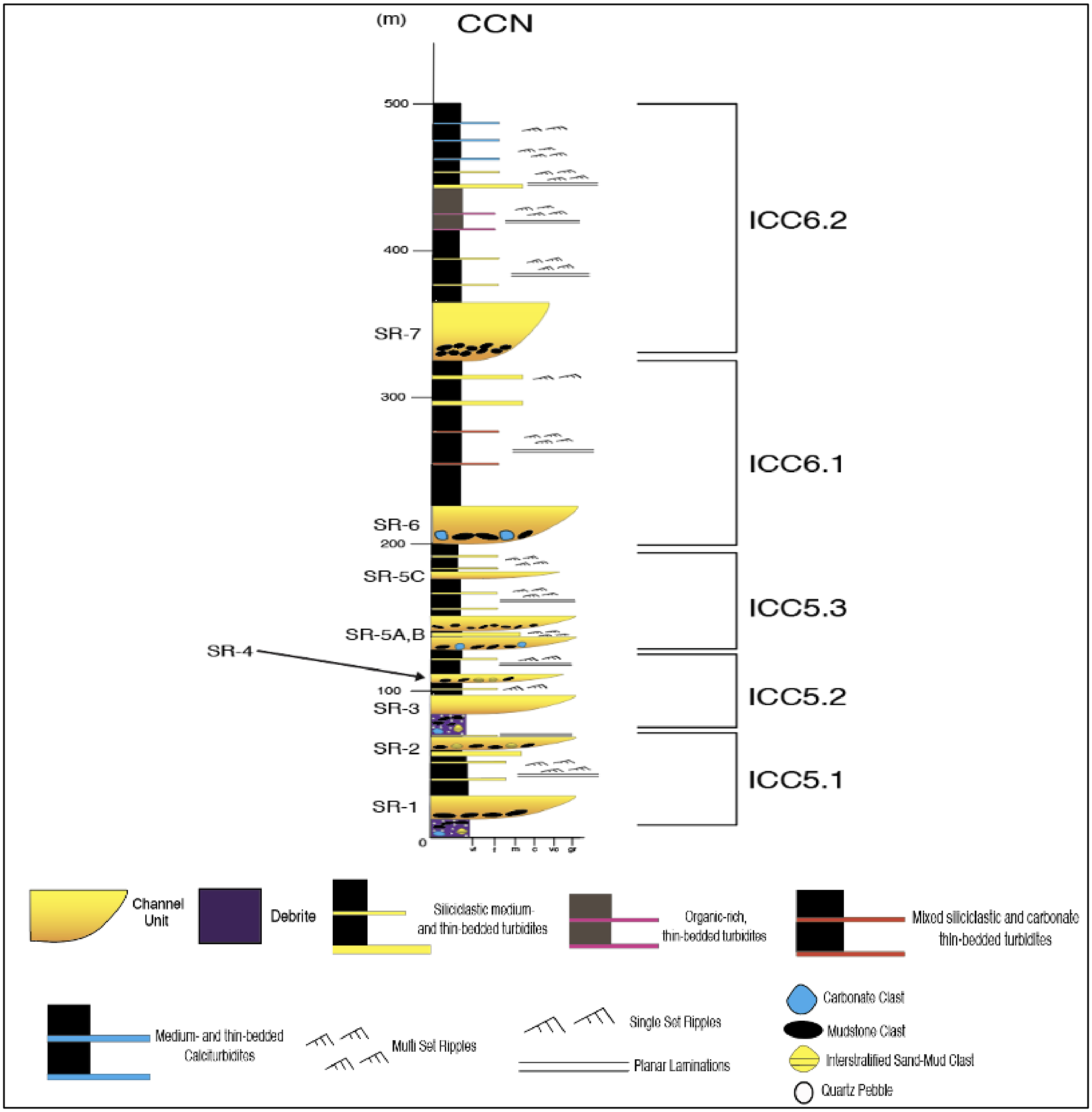

Fig. 4.2: *Measured stratigraphic section in the Castle Creek North study area along a vertical transect with channel complexes labelled.*

4.2.1 Stage 1: Deposition during late FSST to early LST

As sea-level approached its lowest position during the late falling stage tract, disequilibrium of the regional slope gradient would have been steepened by early carbonate cementation. The presence of carbonate clasts and carbonate cemented sandstone and mudstone clasts at the base of most channel complexes suggests at least some development of a carbonate platform that most likely would have a steeper continental slope compared to a siliciclastic system (Ross et al., 1994). With late falling stage and early lowstand conditions and the conversion from a mixed to purely siliciclastic system, gravitational instabilities, particularly along the upper part of the continental slope, would have triggered widespread mass wasting as the slope adjusted through erosion and sediment bypass. Within the study interval, the base of ICC5.1 and ICC5.2 are marked by debrites whereas in Castle Creek north ICC6.1 onlaps a thick slide complex (see Fig. 4.3 and Fig. 4.4), these basal strata are then overlain by channel units composed of aggrading channel fills (i.e. SR-3, SR-5A, SR-6, SR-7).

The initiation of these channel units was associated with highly erosive, incisional flows that were followed by a period of bypass, after which flows became net-depositional during the late falling-stage to early lowstand systems tracts. The dominant sediment supply during this stage consisted of remobilized, coarse-grained relict shelf sediment and material eroded from the older highstand shoreline. Evidence of this reworking occurs within the basal ~2–5 m of the lowermost channel fills, which distinctively contain anomalously coarse sediment, including quartz pebbles and carbonate-cemented sandstone and mud intraclasts. Stratigraphically upward, channel fills fine to coarse- and medium-grained sandstone with the disappearance of pebble grade sediment and carbonate and carbonate-cemented clasts suggesting a shift to a sediment supply sourced directly from the hinterland rather than from palimpsest and relict shelf deposits.

Channel-fill strata are polydispersed with grain size ranging from pebble to clay, which would result in highly density-stratified turbidity currents (Fraino et al., 2022). These flows most probably had a dense, high-concentration basal part that deposited amalgamated, very coarse-grained sandstone and fine-granule conglomerate in channel axes and finer-grained, thinner-bedded strata along the lower-energy flow and channel margins. Near-bed stratification effects and attendant intense interfacial mixing and turbulence damping (Kneller et al., 2016) would have caused these flows to be highly inefficient with high rates of in-channel sedimentation (Mohrig et al., 2000; Jerolmack and Paola, 2007). Channels likely overfilled causing younger channels to develop elsewhere and ultimately form a disorganized channel stacking pattern (McHargue et al., 2011).

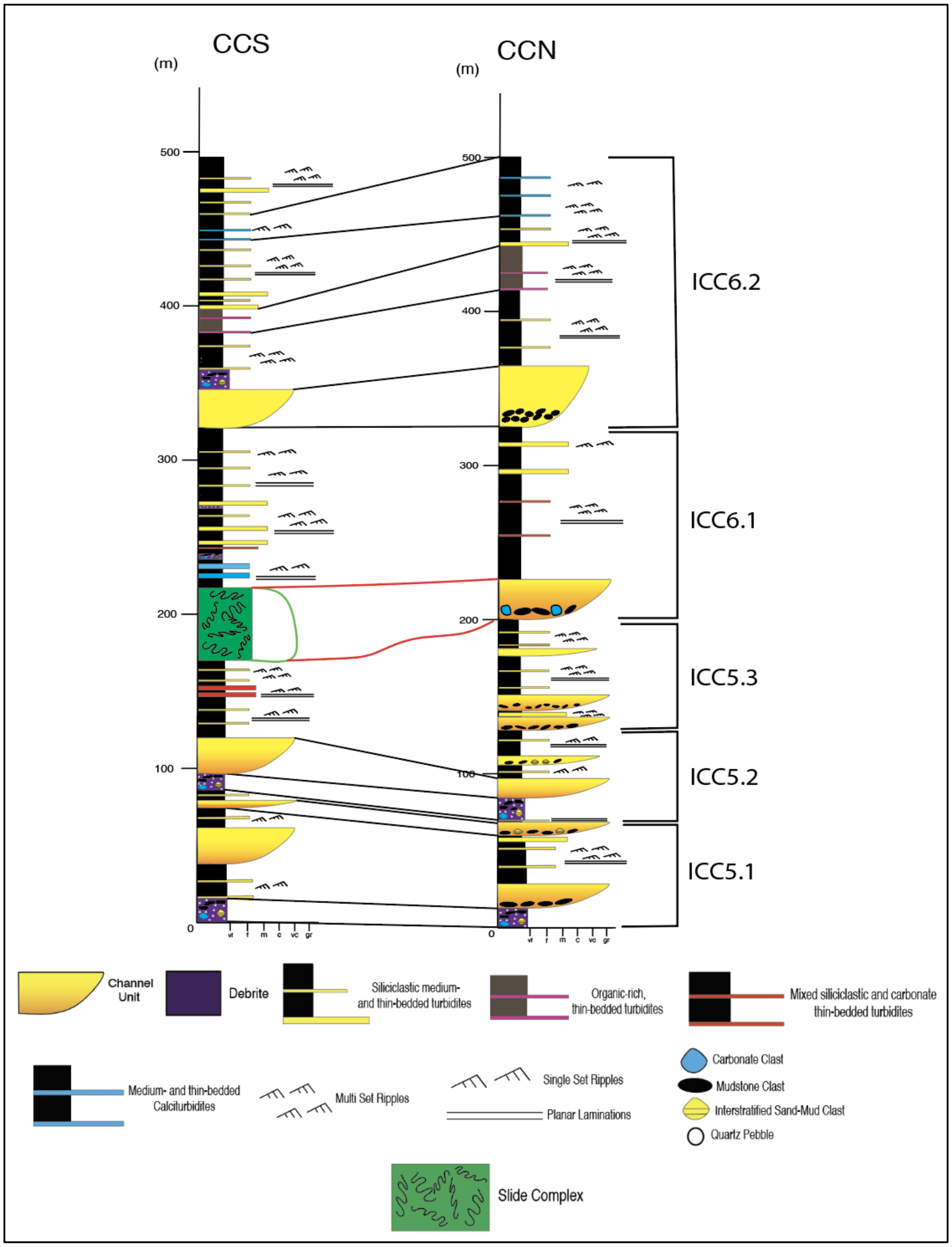

Fig. 4.3: *Measured stratigraphic sections in the Castle Creek north and south study areas transect with correlations of stratal elements across the glacial cover (~ 1 km).*

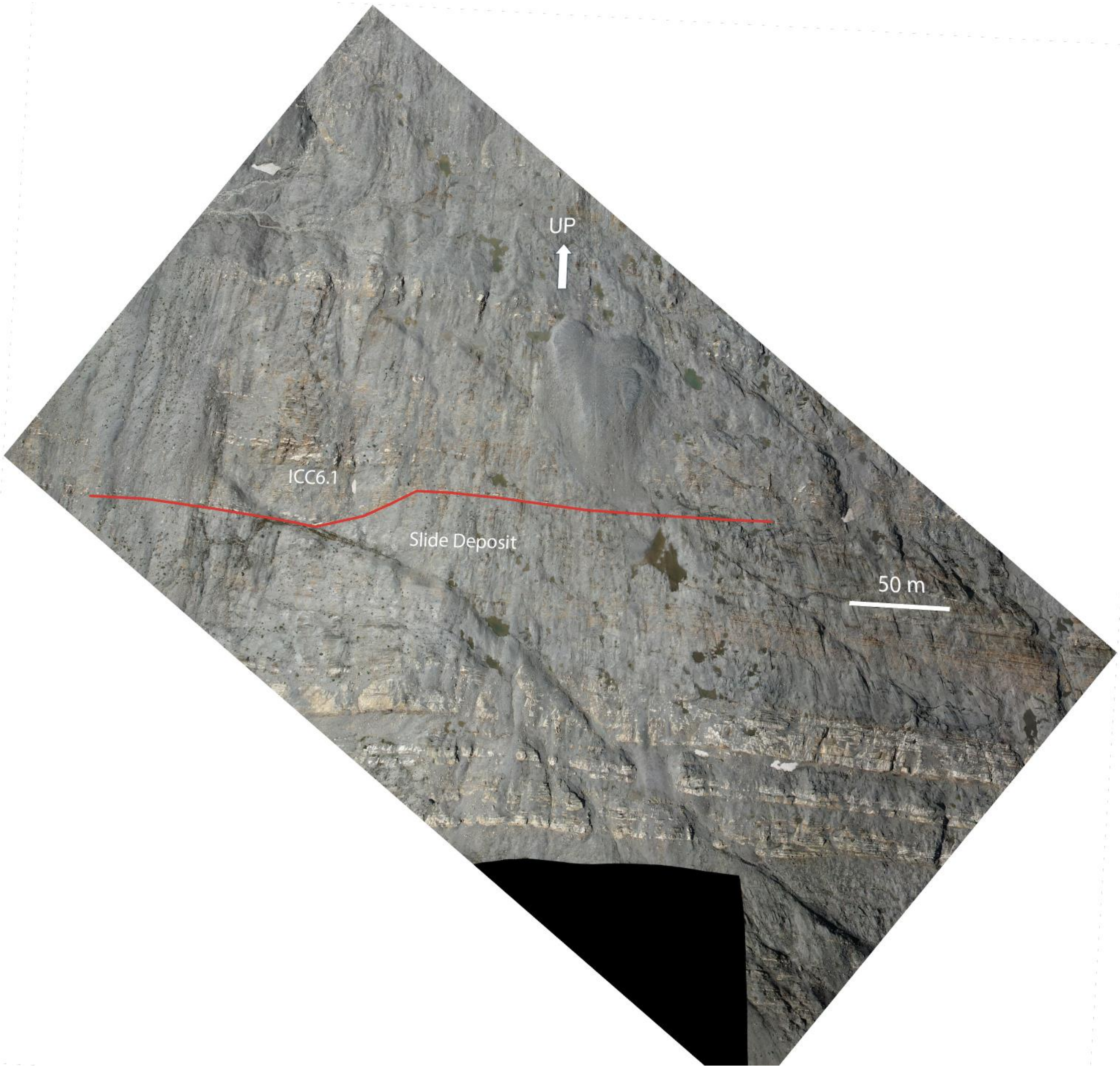

Fig. 4.4: *Drone photomosaic from Castle Creek south outcrop with the red line showing contact between ICC6.1 and slide deposit. Note the abrupt termination of sand-rich channel fill (ICC6.1) as it onlaps and then overlies the margin of the slide.*

4.2.2 Stage 2: Deposition during late LST to TST

With continued sea level rise during late lowstand tract into the transgressive systems tract channels remained aggradationally-filled with a spatially disorganized stacking pattern and a grain size spectrum from mud to granules exemplified by SR-4 and SR-5B. However, sediment flux from the hinterland was most probably considerably reduced as coarse sediment became sequestered on the proximal shelf and further landward as the shoreline retrograded during regional transgression. Channel fills during this time would show a similar architecture to the lowermost channel units (i.e. SR-5A and SR-6) but lack the anomalous pebble grade sediment along with carbonate and carbonate-cemented clasts.

4.2.3 Stage 3: Deposition during late TST to early FSST

The uppermost channel units of the channel complexes in the study area (SR-1, SR-2, and SR-5C) are characterized by the development of laterally accreting channel fills. These fills exhibit little upward or lateral fining or bed thinning and are composed of a distinctive grain-size assemblage dominated by comparatively well-sorted, very coarse- to coarse-grained sandstone and uncommon granule conglomerate. Due to the well-sorted nature of the sediment supply, flows were likely poorly density-stratified with a thick, dense basal layer of uniformly dispersed coarse sand overlain sharply by a lower-density, finer-grained upper layer. Such flows would have experienced minimal interfacial mixing and attendant energy loss (i.e. highly efficient flow) that allowed much of the sediment to bypass farther downslope and restricting sand deposition to the inner-bend margin of the channel.

Owing to the coarseness of the suspended sediment and its relatively uniform distribution in the basal part of the flow, secondary circulation in channel bends is interpreted to resemble that in fluvial systems (Arnott et al., 2021). More specifically, cross-channel density structure is interpreted to resemble the cross-channel hydraulic gradient observed in rivers, which in turn promotes similar styles of deposition, namely coarse sediment deposition on the inner bend point bar. The preferential deposition of coarse sediment along the inner bend rather than the channel axis, as in aggradational channel fills, caused the channel to remain an open and hydraulically efficient conduit. Following channel abandonment these underfilled channels became the preferred pathway during a later reactivation of the transport system, which resulted in the development of an organized stacking pattern of laterally offset channel elements.

A potential interpretation for the distinctively well-sorted grain-size composition of laterally accreting channel fills is that it reflects rising relative sea level (RSL) and associated transgression (Fraino et al., 2022). During this time, the hinterland-derived polydisperse sediment on the previously exposed shelf would have become isolated on the now-flooded shelf and subsequently reworked by marine processes. The more mobile sediment fractions, namely medium and finer sand, would have been redistributed landward and contributed to the development of barrier island complexes along the retrograding shoreline. Coarser palimpsest and relict sediment on the distal portion of the continental shelf became mixed with minor amounts of carbonate during continued transgression. This mixed siliciclastic–carbonate assemblage likely constituted the primary sediment supply for turbidity currents that were particularly active during short-term sea-level falls superimposed on the longer-term rise of relative sea level.

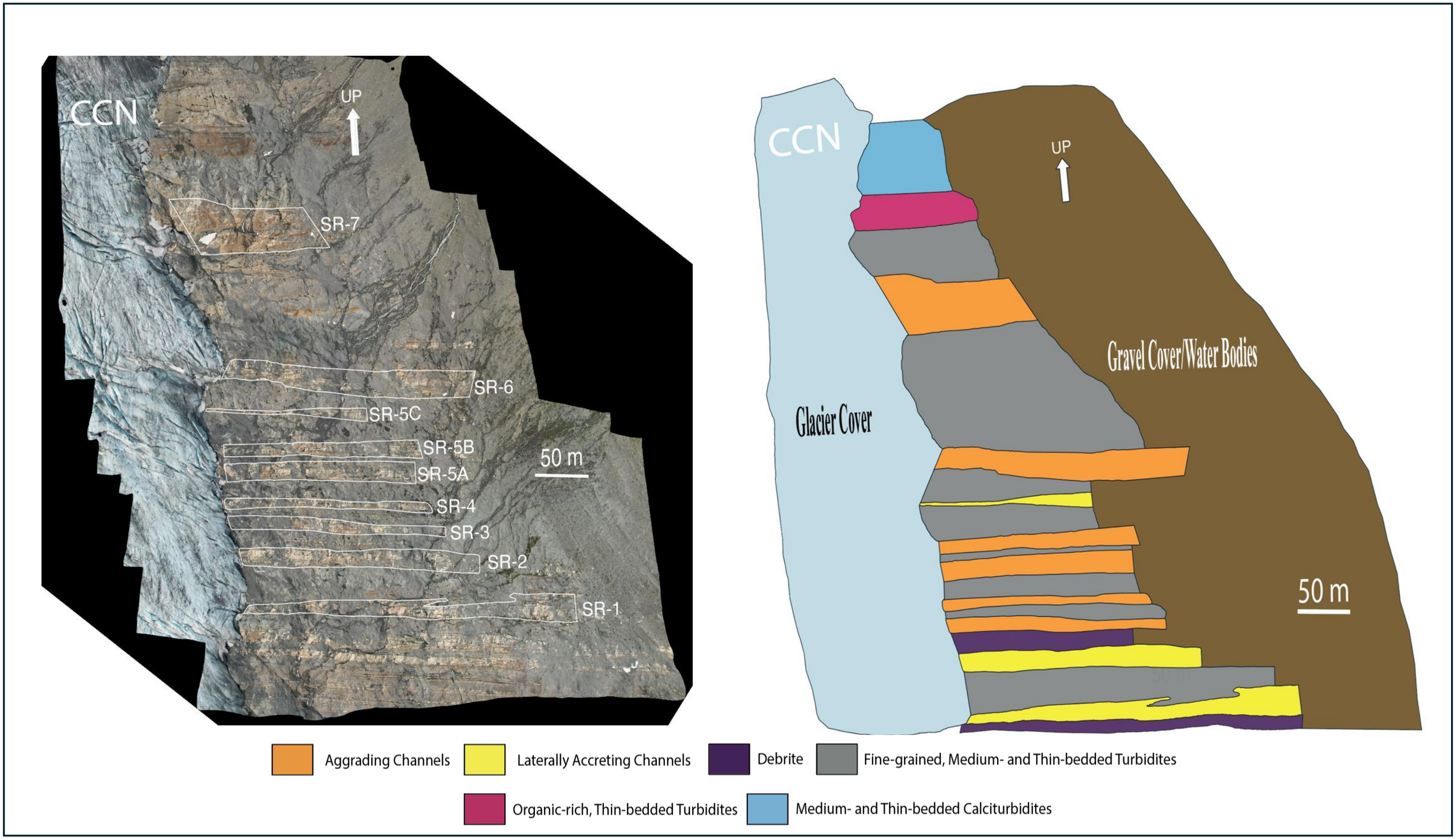

Fig. 4.5: *A.) Drone photomosaic from the Castle Creek North outcrop with channel units outlined. B.) Interpreted panel of the Castle Creek North outcrop showing the distribution of stratal elements.*

4.3 Comparison to Channel Complexes Within the Isaac Formation

4.3.1 Similarities

Slope leveed channel complexes of the Isaac Formation, informally termed ICC1 to ICC5, have been extensively studied in earlier studies, with variations in relative sea level (RSL) interpreted as a key control on their temporal and spatial stratal organization and composition. The channel complexes examined in this study interval display similar clast compositions, grain-size distributions, stacking architectures, and compositional trends to those previously documented but were deposited higher on the continental slope.

Channel complexes ICC1 to ICC5, and ICC5.2 to ICC6.2 (Fig. 4.6), display a systematic vertical stacking pattern. The lower portions of these complexes are characterized by aggrading channel fills with disorganized internal stacking that transition upward into laterally accreting channel fills exhibiting more organized stratigraphic architecture.

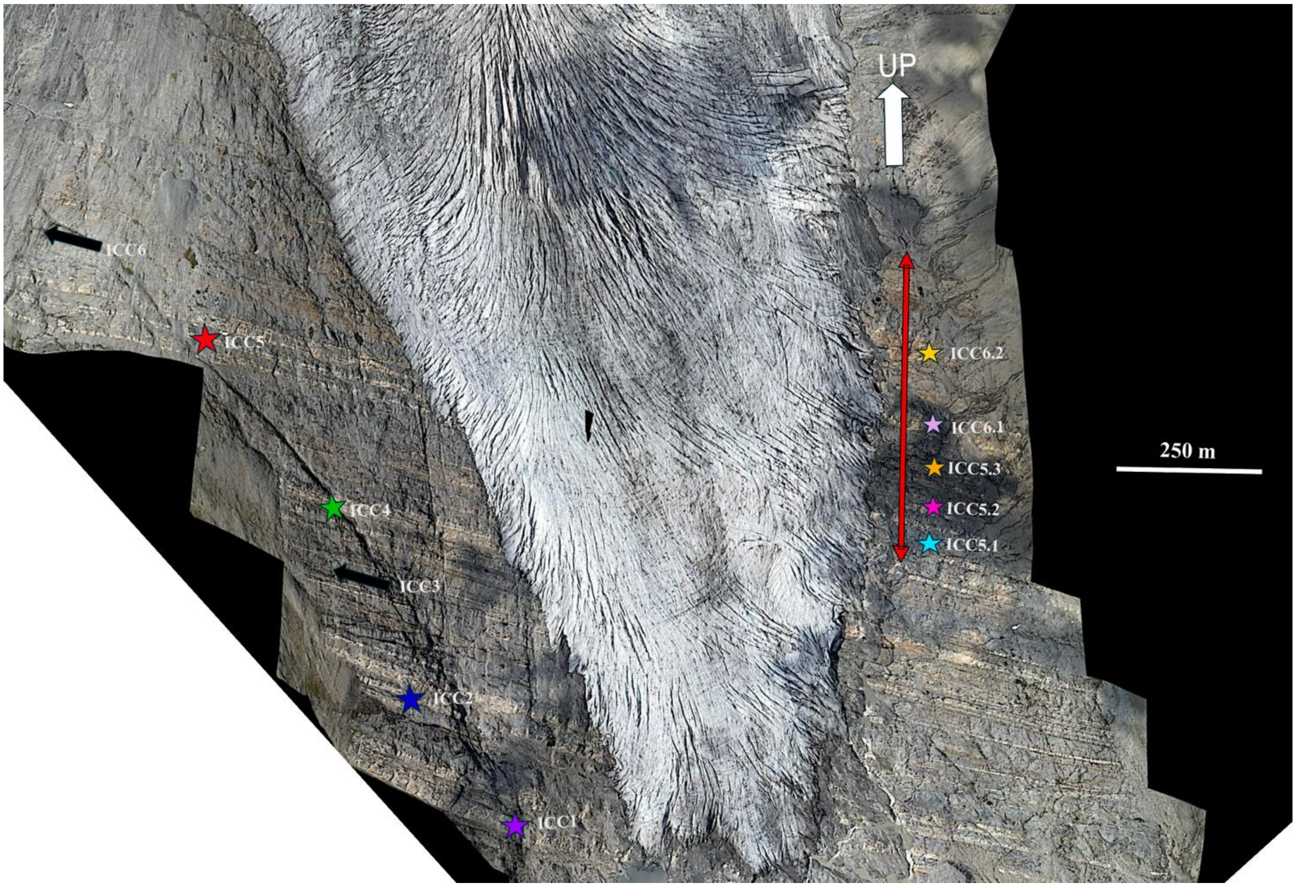

Fig. 4.6: *Annotated drone photomosaic showing the location of channel complexes ICC1–ICC6.2 within the Castle Creek study area. The main channel bodies of ICC3 and ICC6 are not captured in this field of view, only their associated levee deposits. Black arrows denote the off-image positions of these channel complexes. Red arrow shows the extent of the study interval.*

The bases of channel complexes in the Isaac Formation are typically defined by mass-transport deposits, like the up to 110 m-thick, regionally extensive, carbonate-clast, matrix-supported mass-transport complex underlying ICC3 (Arnott et al., 2011), or in some cases the basal units simply comprise anomalously coarse-grained (pebble conglomerate) channel fills with dispersed primary carbonate clasts and carbonate-cemented sandstone and mudstone fragments. The lowermost channel fills within ICC1, ICC3, and ICC5 consist predominantly of coarse-grained strata analogous to the basal fills of SR-3, SR-5A, and SR-6 in the present study area. These units exhibit upward-fining and -thinning trends and display lateral fining and thinning from channel axis to margin. Furthermore, the basal channel fills within the Isaac Formation show cut-and-fill geometries indicating multiple, erosively juxtaposed channel fills with a spatially disordered stacking pattern.

The upper channel fills of ICC1 to ICC5 record a transition in channel-element stacking from disorganized to organized arrangements. These upper fills, like those of SR-1, SR-2, and SR-5C in the study area, display a narrow grain-size distribution and lack observable vertical or lateral fining and thinning trends, features consistent with laterally accreting channel deposits. In particular, the upper channel unit of ICC1 (UC3; see Fraino et al., 2022) and channels 2.2 and 2.3 of ICC2 (Dumouchel, 2015) contain very coarse-grained sandstone or granule conglomerate with abundant mudclasts at the base of individual channel fills. The upper surfaces of these fills in UC3 (ICC1) and channel 2.2 and 2.3 (ICC2) exhibit a distinctive oblique interfingering with thin-bedded, fine-grained, upper-division turbidites, which are interpreted as contemporaneous inner levee deposits (Arnott, 2007). Similarly, the uppermost channel fill of ICC5 (C3.4; Schwarz and Arnott, 2007a,b) displays inclined (4–8°) strata that form flattened, lens-shaped geometries.

As discussed earlier the consistent upward change from mass-transport deposits and aggrading channel fills with disorganized stacking and limited lateral migration at the base of channel complexes to systematic, laterally-offset-stacked, laterally accreting channels is linked to long-term eustatic changes. This is similarly interpreted to reflect systematic changes in sediment supply, which in turn controls flow characteristics, and ultimately channel type and stacking pattern. This similarity develops irrespective of position on the continental slope, specifically base to mid-slope in previous studies, and upper slope in this study.

Levee deposits associated with these channel systems show architectural and compositional similarities to those documented stratigraphically lower in the Isaac Formation. Studies by Navarro et al. (2007), Khan and Arnott (2011), Khan et al. (2011), Bergen et al. (2022), and Cunningham and Arnott (2021) (Fig. 4.7) describe comparable proximal and distal facies that are interpreted to vary systematically with distance from the channel margin. Proximal levees are further subdivided into lower and upper parts, each generally 5–20 m thick. The lower proximal levee (3–10 m) consists of medium- to thick-bedded, medium- to coarse-grained, lower-division turbidites (T_{ab} or T_{bcde}), interbedded with very thin- to thin-bedded, fine-grained, upper-division turbidites. The upper proximal levee (3–16 m) is dominated by very thin- to thin-bedded, very fine-grained, upper-division turbidites intercalated with less common, thicker, medium-grained, lower-division beds. Laterally, the lower proximal package fines and thins away from the channel margin over several hundred meters, whereas the upper package shows little lateral change.

Distal levees, ranging from 2–30 m thick, are more challenging to identify in outcrop. However, Bergen (2022) and Cunningham and Arnott (2021) describe them as predominantly very fine-grained and very thin- to thin-bedded, with uncommon medium-bedded, medium-grained sandstone interbeds. The rare thick sandstone beds likely record overspilling turbidity currents that had sufficient inertia to bypass the proximal levee but then decelerate and deposit over the distal levee. Regardless of type, levee successions in the Isaac Formation consistently contain ubiquitous ripple cross-stratified sandstones (T_c divisions), consisting of single or multiset (3–5 sets) ripples. The abundance of ripple cross-stratification indicates that turbidity flows became rapidly depositional upon overspill, entering the ripple stability field as confinement was lost, flows collapsed and rapidly became density stratified over the levee.

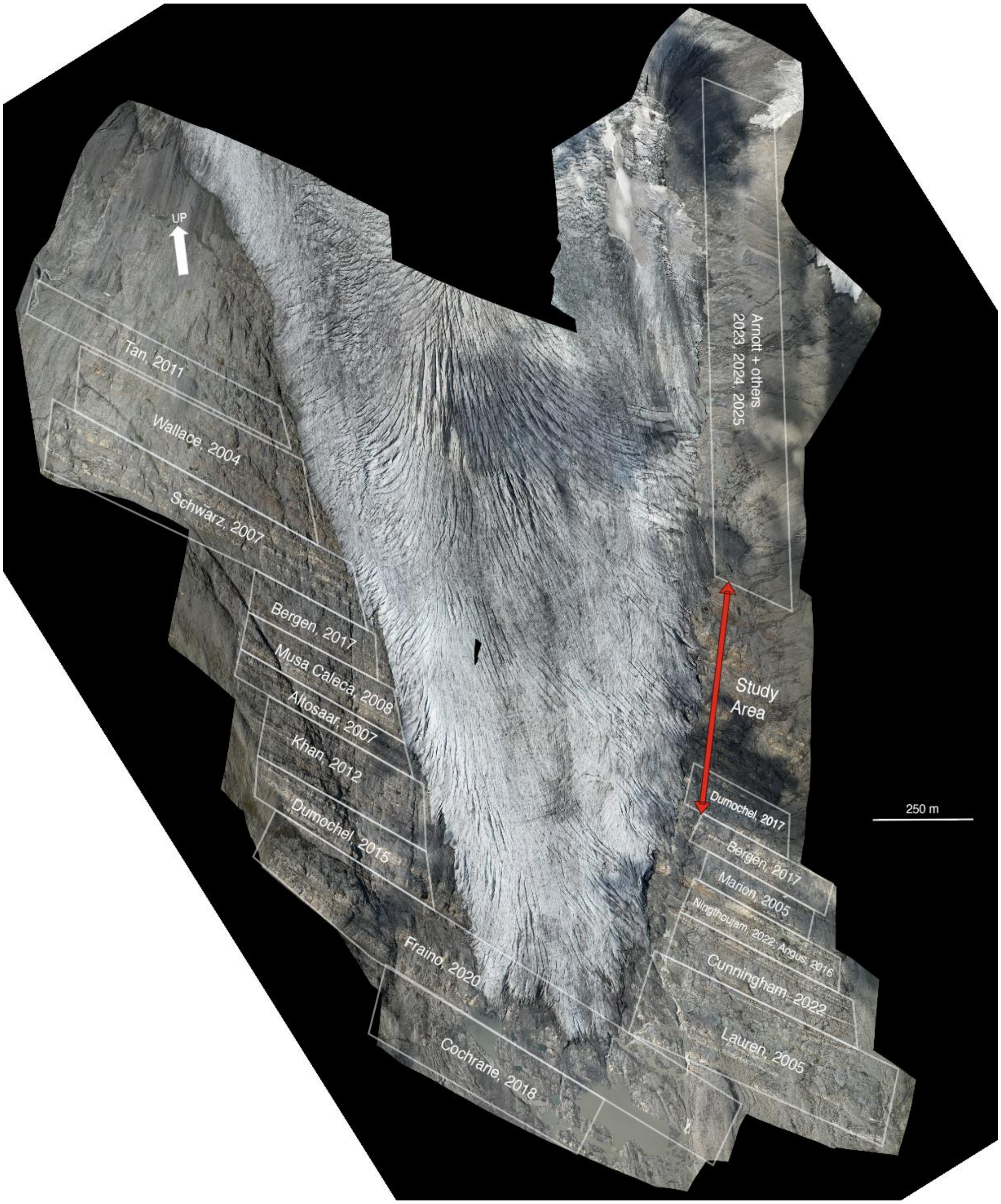

Fig. 4.7: *Annotated drone photomosaic showing the spatial extent of the current study area relative to previously investigated slope deposits in the Castle Creek study area. Location of studies are outlined for reference, providing spatial context for comparisons made in this section.*

In addition to these architectural and facies similarities, levee successions within the study interval also mirror the systematic organization of levee deposits documented previously by Cunningham and Arnott (2021). Like in their study, beds commonly stack to form sharply bounded, self-similar bedsets composed of T_{cde} divisions with consistent grain size, bed and division thickness, and style of ripple-cross-stratification. Such lithological and structural uniformity within sharply bounded bedsets, plus the characteristics mentioned above, point to similar flow processes and levee-building mechanisms operated throughout the Isaac Formation.

Lastly, detrital zircon age distributions from samples in the study area resemble those from stratigraphically lower strata, and therefore farther downslope, indicating no significant change in sediment provenance during the evolution of the system. Sediment supply to the Windermere turbidite system is well established as originating from an Archean and Paleoproterozoic cratonic (Fig. 4.8) hinterland of mainly granite–granodiorite composition (Ross and Arnott, 2007; Hadlari et al., 2021).

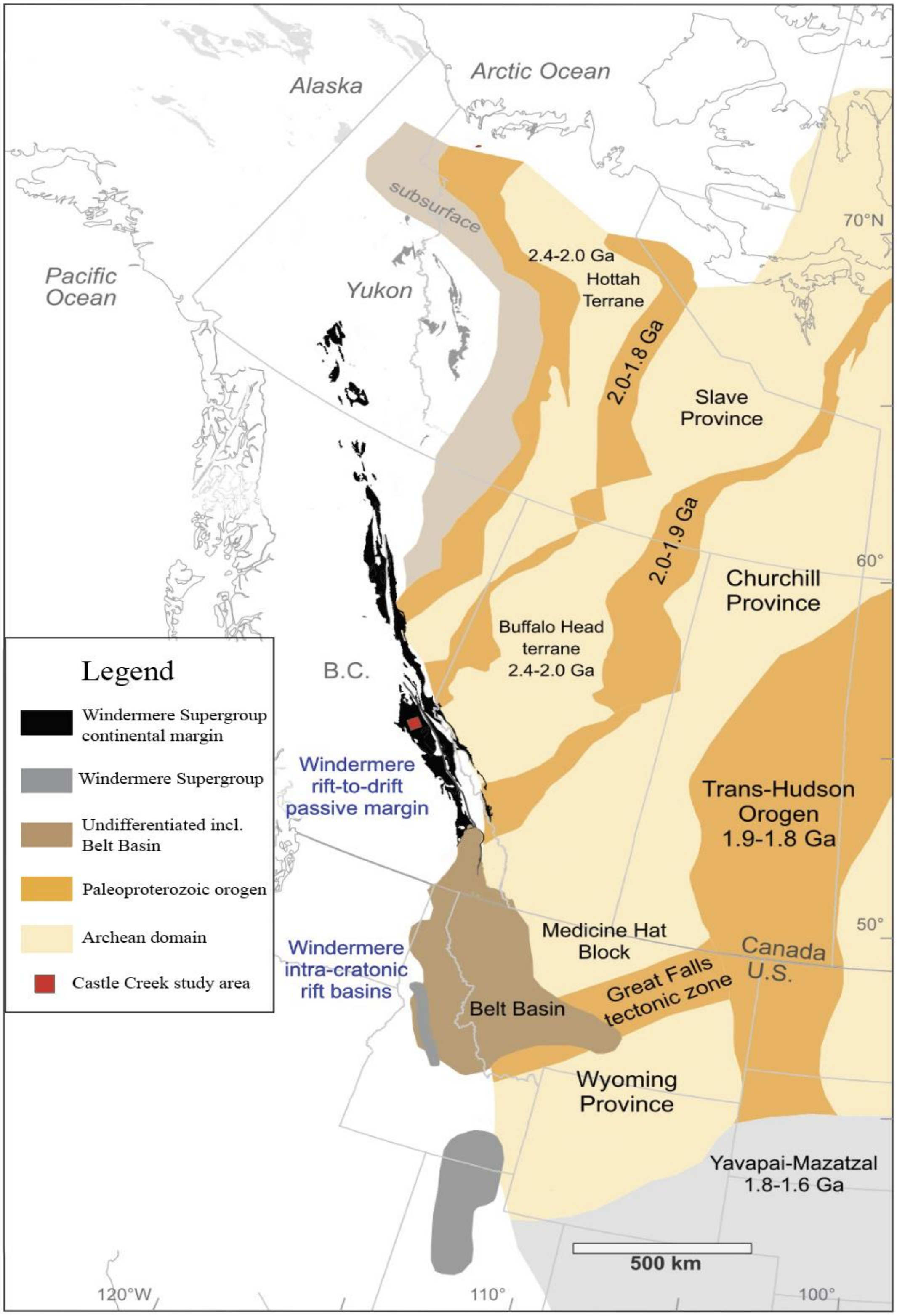

Fig. 4.8: *Map of western North America showing Laurentian basement domains, outcrop belts of the Windermere Supergroup and location of Caste Creek study area highlighted by red square (modified from Hadlari et al., 2024).*

Detrital zircon age spectra from the entire Isaac Formation (ICC1 to ICC6.2), and underlying Kaza Group, display a distinctive bimodal distribution dominated by Paleoproterozoic and Archean populations, with minor Mesoproterozoic input and a distinct ~ 650 Ma Neoproterozoic component in samples from the interval between, and including, ICC3 to ICC6 (Fig. 4.9). The dominant age assemblages indicate a northwestern Laurentian provenance derived from nearby Precambrian basement domains, principally to the southeast of the study area, that now are buried beneath western Canada (Hadlari et al., 2024). The Paleoproterozoic ages (1.65–2.0 Ga; peak at 1.8 Ga) correspond closely to the Rimbey Domain (1.85–1.79 Ga) and Trans-Hudson orogen (1.92-1.77 Ga), whereas the Archean ages (2.5–3.1 Ga; peaks at 2.55, 2.65, and 2.95 Ga) match several Archean terranes of western Laurentia (Pipe, 2023). These include the Medicine Hat Block (ca. 3.28–2.50 Ga), Wyoming Terrane (3.6–3.0 Ga) and subdivisions of the southern Hearne Province such as the Matzhiwin (ca. 2.59 Ga), Vulcan (ca. 2.75–2.63 Ga), Eyehill (ca. 2.84–2.56 Ga), and Loverna (ca. 3.04–2.71 Ga) domains (Pipe, 2023).

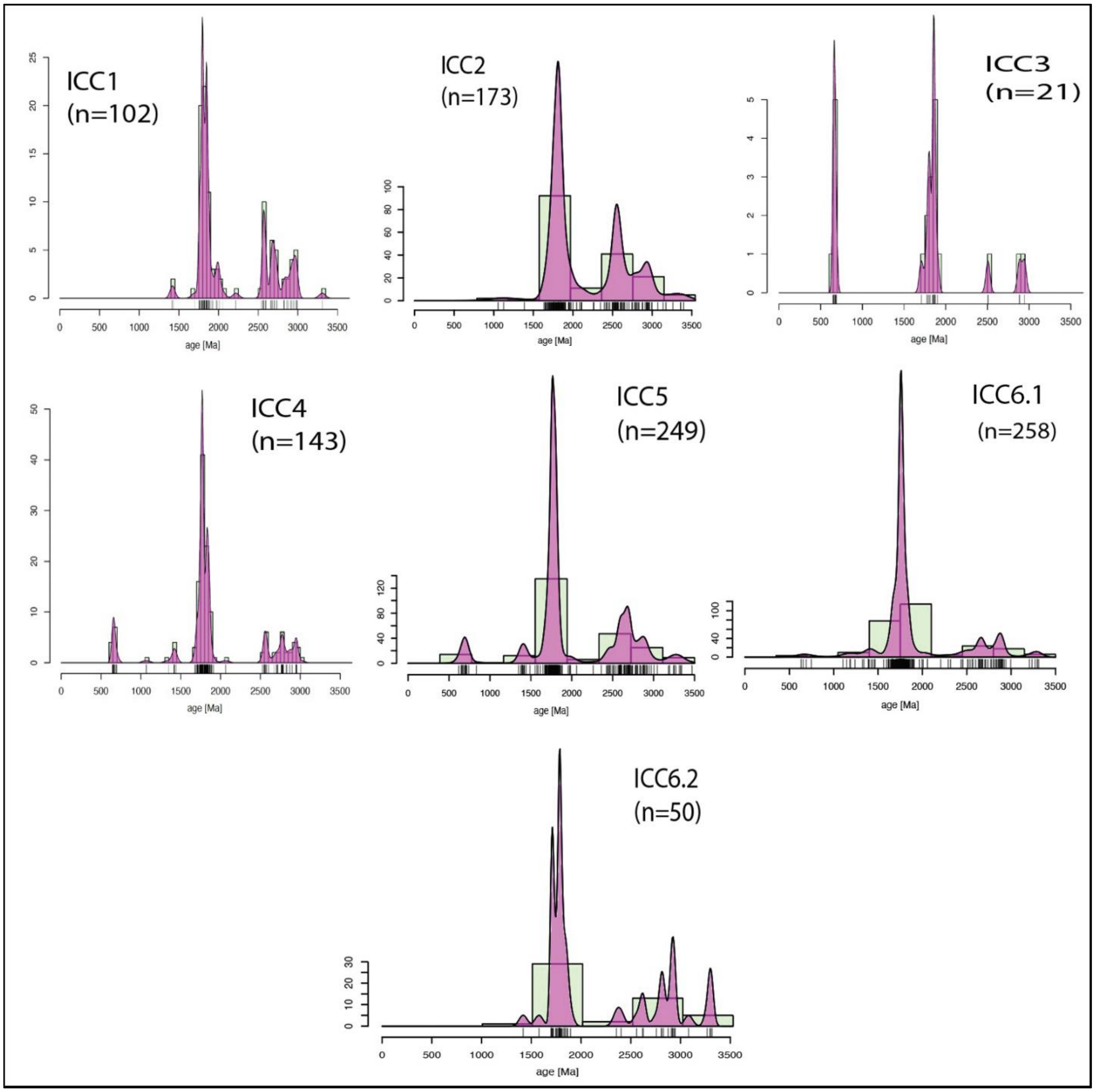

Fig. 4.9*: Kernel Density Estimation (KDE) plots for samples taken from each channel complex within the Isaac Formation (ICC1 to ICC6.2) showcasing a distinct bimodal distribution with Archean and Paleoproterozoic peaks and a distinct Neoproterozoic signature that is only present in samples between ICC3 and ICC6.1. Data for ICC1, ICC3, ICC4 and ICC5 taken from Pipe, 2023.*

The scarcity of Mesoproterozoic zircon ages suggests only minor sediment input from the Belt Supergroup to the south. Likewise, the absence or low abundance of zircons with Paleoproterozoic ages between 2.0 and 2.5 Ga implies that source terranes immediately to the east and northeast such as the Wabamun (ca. 2.32 Ga) and Thorsby (ca. 2.38–1.91 Ga) domains were likely not exposed at the time of deposition. The juvenile Neoproterozoic zircon population (660–650 Ma) is most plausibly linked to rift-related magmatism (665-650 Ma) in central Idaho (Fanning and Link, 2004 in Pipe, 2023), consistent with Hadlari et al. (2021) who proposed a short-lived magmatic episode in the Windermere Basin between 680 and 650 Ma.

4.3.2 Differences

Although the channel complexes deposited bathymetrically shallower on the slope (this study) share similarities with those developed farther downslope, notable differences occur in both channel units and levee strata. Most notably is the thickness of channel units and their associated fills, which in this study are considerably thinner. This thinning continues the upward trend observed in the Isaac Formation: channel units in ICC1 average approximately 40 m in thickness (range: 25–60 m). Channel units in ICC2 are typically 30 m thick (range: 20–40 m), those in ICC3 average 20 m (range: 15–22 m) and average 18 m (range: 17–20 m) in ICC4 and ICC5. Channel fills in ICC1 to ICC6 range from 4–15 m thick and average ~ 10 m thick but in this study area range from 2–8 m and average ~ 6 m thick. Notable also is the overall finer-grained make-up of the general slope succession, which is dominated by mud-rich levee strata comprising ~ 70% of the study area.

Despite the overall prevalence of finer-grained strata in the study area, individual channel fills are notably coarser grained compared to those lower in the Isaac Formation, consisting predominantly of very coarse-grained sandstone to granule conglomerate with limited upward fining. This contrasts with channel units lower on the slope, where coarse-grained deposits are typically confined to the base of fills, except in laterally accreting channels, and commonly fine upward into medium- to fine-grained sandstone beds interstratified with thin-bedded, upper-division turbidites. The comparatively coarser grained nature of the fills in the study area also coincides with more abundant and thicker (5–15 m) mudclast breccia zones. In channel fills deposited farther downslope mudclast breccia is mostly confined to the basalmost part of channel fills whereas in this study it tends to occur throughout channel fills (e.g., SR-6.2, SR-7.3).

Another key difference is the depth and length of scours. Erosional surfaces as much as 2–4 m deep and related to younger channels scouring older fills, underlying debrites or levee deposits are common. In most cases, only coarse-grained channel-axis deposits are preserved and individual channel fills are separated by scour surfaces mantled with mudclast breccia. This contrasts with channel fills farther downslope, where scours are largely confined to the basal parts of channel units, and, where present between discrete fills, are of the order of tens of centimeters rather than meter-scale observed in this study. Such extensive erosion and cannibalization produces a mostly lateral juxtaposition of variously-aged channel fills.

Differences in channel fill thickness, depth of channel base scour, grain size, mudclast abundance and preferential preservation of coarse channel axis deposits in this study compared to channel fills lower on the slope suggest differences in the character of turbidity currents that transited the system. Specifically, the flows that deposited strata in the study area were undercapacity (see next). The more deeply scoured, coarser-grained channel fills dominated by channel axis deposits with abundant mud intraclasts is indicative of energetic, most probably downslope accelerating turbidity current that passed over the steeper upper part of the continental slope (Fig. 4.10).

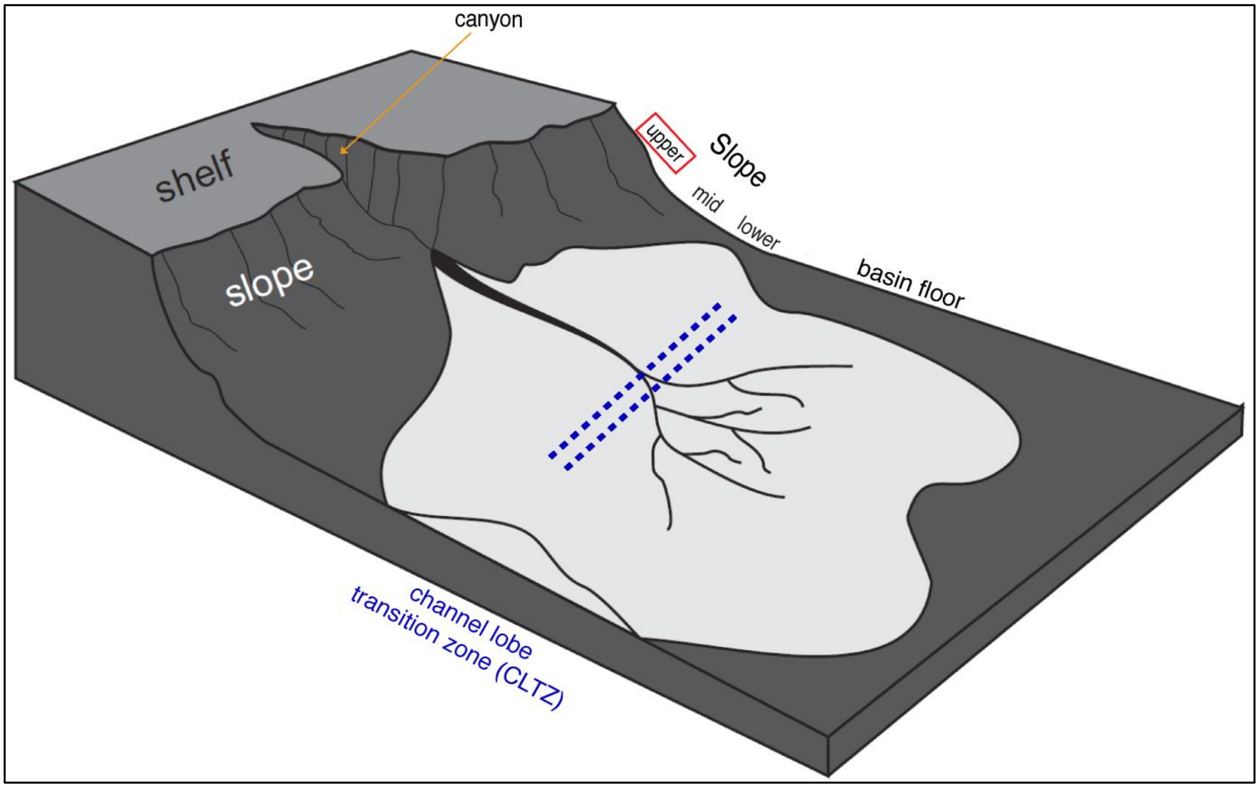

Fig. 4.10: *Schematic of a submarine slope partitioned into upper, mid to lower and base of slope parts. Blue dash line denotes the channel lobe transition zone (CLTZ) (modified from Khan, 2012).*

Turbidity currents in the deep marine can be modelled using a capacity-based framework, linking the available turbulent energy to the gravitational settling of suspended sediment. Eggenhuisen et al. (2017) formalized this relationship with the suspension-capacity parameter (Γ; their Eq. 13), expressed as the ratio of turbulent momentum flux near the bed to gravitational settling flux of suspended sediment:

$$\Gamma = \frac{u_*^3}{w_s g' h}$$

In this formulation, u_* represents the shear velocity, a measure of turbulent stress transmitted to the bed and governs the ability of the flow to entrain and maintain particles in suspension.

w_s denotes the particle settling velocity, the downward terminal velocity attained when the gravitational force acting on a grain is balanced by fluid drag. The term g' represents reduced gravity ($g' = g(\rho_{sediment} - \rho_{ambient}) / \rho_{ambient})$) quantifying the effective buoyancy force acting on the suspended particles, and h is flow thickness.

By comparing u_*^3 to $w_s g' h$, the suspension-capacity parameter (Γ) essentially contrasts the rate of turbulent kinetic energy production near the bed with the rate at which gravitational settling removes sediment from suspension. Eggenhuisen et al. (2017) propose that when $\Gamma > 1$ the turbulent energy flux in the boundary layer exceeds the downward flux of settling particles. Under these conditions the flow is dynamically 'undercapacity'— available turbulence exceeds that required to maintain the existing suspended sediment load. This surplus energy enables entrainment of additional sediment from the bed, often resulting in local erosion and an increase in both sediment concentration and bulk density as the current evolves downslope. Conversely, when $\Gamma < 1$ the rate of turbulent production falls below the gravitational dissipation rate associated with particle settling. The flow becomes dynamically 'overcapacity' with more sediment in suspension than turbulent energy can support. This imbalance leads to an increase in effective flow viscosity, and accordingly, energy dissipation, which then leads to reduced turbulent momentum transfer, reduced u_*, and triggering sediment fallout. The result is a shift from a high-energy erosive regime to a lower-energy depositional regime characterized by bed aggradation.

Although the suspension-capacity parameter (Γ) provides an instantaneous measure of a flow's ability to transport and entrain sediment, its value is inherently transient as the flow evolves downslope due to sediment entrainment, mixing with ambient water, and changes in seabed slope. Near the point of flow initiation, possibly related to a seabed failure, the sediment-fluid mixture is typically highly turbulent with elevated shear velocity (u_*) relative to flow thickness (h). Under these conditions, Γ commonly exceeds the proposed threshold (i.e. Γ = 1), indicating an undercapacity state. Accordingly, the flow erodes and entrains bed material causing sediment concentration and bulk density to increase and the flow to accelerate. As the current progresses downslope, several processes act to lower Γ. Firstly, turbulent entrainment of ambient seawater increases the flow volume and thickness (h) while simultaneously reducing bulk sediment concentration, ultimately reducing basal shear stress. Additionally, as slope and confinement decrease downslope, the gravitational driving component ($\rho g' \sin \theta$) weakens, further diminishing u_* and available turbulent kinetic energy. These factors lead to the transition from undercapacity (Γ > 1) to overcapacity (Γ < 1) conditions and a general shift from an erosional to a depositional regime.

This physical model is also consistent with field observations from the 1929 Grand Banks turbidity current (Clarke et al., 1990). Detailed bathymetric and submersible observations across the Eastern Valley on the modern Laurentian Fan (east coast Canada) show that the flow was erosive for more than 200 km downslope from the shelf break, incising valley-floor channels up to 60 m deep and entraining between 50 and 100 km^3 of sediment (Clarke et al., 1990) — features indicative of an undercapacity flow with high near bed shear stress (i.e. Γ > 1). Interestingly, these conditions occurred despite a reduction (~ 8° to 1°) rather than increase in valley-floor gradient. These authors suggest that the entrained sediment and commensurate increase in flow density overcompensated for the reduction in slope and classified the event as an 'ignitive turbidity current' sensu Parker et al. (1986).

While the flow-capacity framework describes the instantaneous hydraulic behaviour of individual turbidity currents, the concept of a channel equilibrium profile (Georgiopoulou and Carthwright, 2013) explains the long-term morphological and stratigraphic evolution of submarine channels in response to flows that transit the system. In an equilibrium state the channel's longitudinal gradient and geometry evolve such that the sediment transport capacity of average flows matches the supplied sediment load with no net aggradation or erosion (Pirmez and Beaubouef, 2000; Covault et al., 2016). This equilibrium reflects a self-regulating feedback between slope and flow intensity. Where equilibrium is disrupted channels respond dynamically: steeper, upper slope regions increase the downslope gravitational driving stress ($\tau_b = \rho g' h \sin\theta$) and hence the basal shear velocity ($u_* = \sqrt{\tau_b/\rho}$). Higher u_* promotes greater turbulence production and intensity and sediment transport capacity, promoting erosion and bypass.

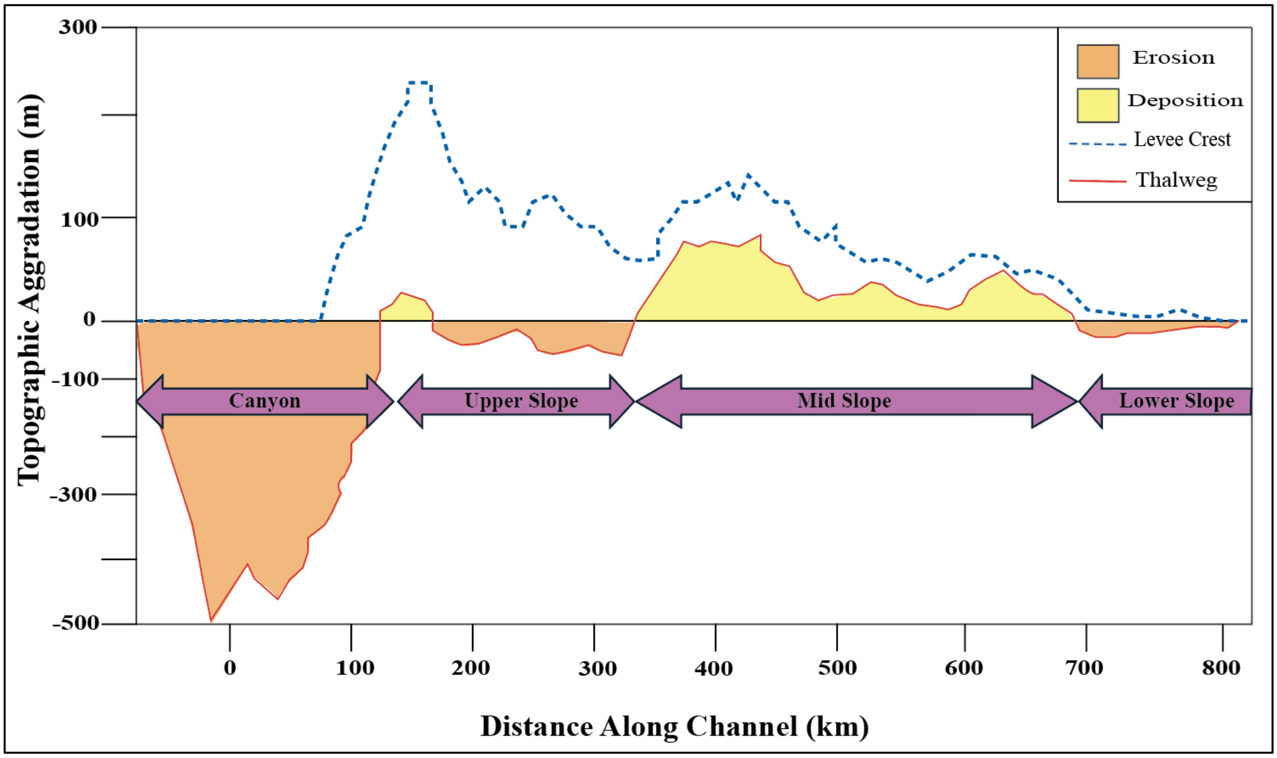

***Fig. 4.11**: Topographic aggradation pattern of the modern Amazon Channel showing the elevation difference between the thalweg and the levee crest (modified from Pirmez and Beaubouef, 2000). Note the change from erosion on the upper slope and canyon changing to deposition on the mid slope. Erosion on the lower slope is due to loss of channel confinement, flow expansion, and bedward shift of the flow's maximum velocity.*

The equilibrium concept is illustrated by the modern Amazon and Niger submarine channels, where Pirmez and Beaubouef (2000) (Fig. 4.11) documented systematic downstream flattening of channel gradients from > 0.5° on upper fan reaches to < 0.05° across the channel–lobe transition. Similarly, Stevenson et al. (2015) documented erosional upper-channel segments transitioning to depositional lower-channel reaches in the Marnoso–Arenacea Formation (Apennines) where flows incised into steep, confined areas (local slopes 0.8–1.2°) before depositing over lower-gradient surfaces (< 0.1°) farther basinward. These geometric adjustments reflect a long-term tendency toward a "graded" equilibrium profile, analogous to that long recognized in fluvial systems (e.g. Mackin, 1948).

The net-erosional, relatively thin turbidity currents that deposited the channel fills in this study also influenced the characteristics of the associated levee strata. Since these flows progressively incised deeper into the slope, the dense, sand-rich, lower part of flows was likely confined to the deep and progressively deepening axis of the channels by successive undercapacity turbidity currents, each also having experienced limited bulking (i.e. growth associated with sediment entrainment). This progressive incision would have eventually restricted the overspill of coarse-grained sediment to the very early stages of channel development followed by more protracted overspill of the finer-grained upper part of the flow – changes that should be manifest in levee strata.

Levee deposits in the study interval are notably dominated by very fine-grained and very thin- to thin-bedded, upper-division turbidites that resemble strata interpreted to form the upper parts of proximal levee packages or distal levee deposits by Khan et al. (2011) and Bergen et al. (2022). Compared to levee successions developed farther downslope, levee strata in this study exhibit similar thicknesses in the sand-rich lower part of levee packages (averaging 4–6 m), but the overlying finer-grained part of each package is notably thicker, averaging 20–25 m compared to 10–16 m in levee deposits lower on the slope. Additionally, compared to levee deposits lower on the slope, levee deposits in this study exhibit a much sharper transition from the sand-rich, medium- to thick-bedded, often complete turbidites that form the basal part of proximal levee packages to the upper part consisting of finer-grained, very thin- to thin-bedded, upper-division turbidites. Also, these fine-grained strata are not only finer and more thinly bedded, but also substantially more thickly developed compared to their stratigraphically lower counterparts.

Together, these features indicate an earlier and more pronounced restriction of coarse-grained overspill due to rapid channel deepening and sustained flow confinement, which limited lateral channel displacement following channel abandonment due to avulsion. This restricted areal displacement of successive channels resulted in local channel-base incision and cannibalization but continued deposition of fine-grained overspill and the upward building of the adjacent levees.

In this study the evolution of a typical channel unit started with high-energy, undercapacity turbidity currents that initially eroded previously deposited levee or mass-transport (MTD) strata. This was followed by a general condition of erosion and downslope sediment bypass, but due to limited lateral confinement were able to overspill the sand-rich basal part of the flows (Fig. 4.12).

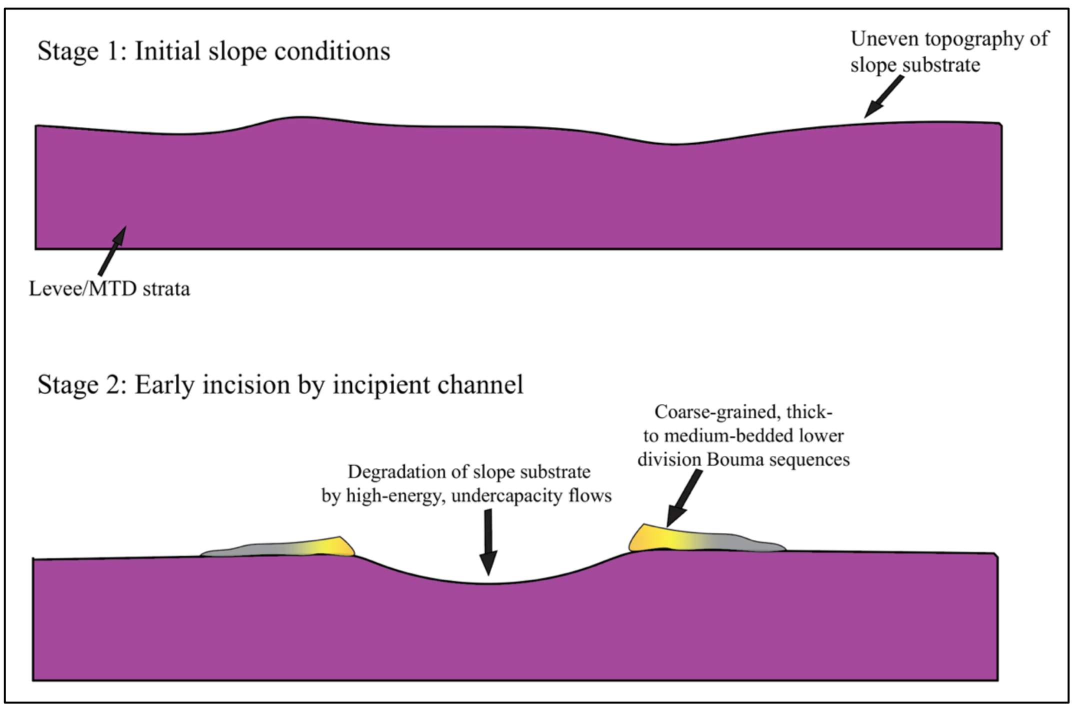

Fig. 4.12: *Schematic showing early channel evolution on the upper slope. Stage 1 shows the initial slope surface with uneven topography of underlying levee/MTD strata. Stage 2 depicts incision by high-energy, undercapacity turbidity currents forming an incipient channel. Overspill of the coarse-grained basal part of the minimally confined turbidity currents deposited medium- to thick-bedded, lower-division turbidites built-up along the channel margins.*

As successive turbidity currents continued to transit the area continued incision deepened the channel, increasing channel-levee relief and flow confinement. This confinement increasingly restricted the lateral movement of subsequent channel fills which then scoured and cannibalized older channel fills, ultimately forming a disorganized succession of laterally juxtaposed channels fills made up mostly of the preferentially preserved coarse axial part of individual channels (Fig. 4.13). Over the levee, however, continued sedimentation deposited a thick upward-fining and -thinning succession of fine-grained, upper-division turbidites.

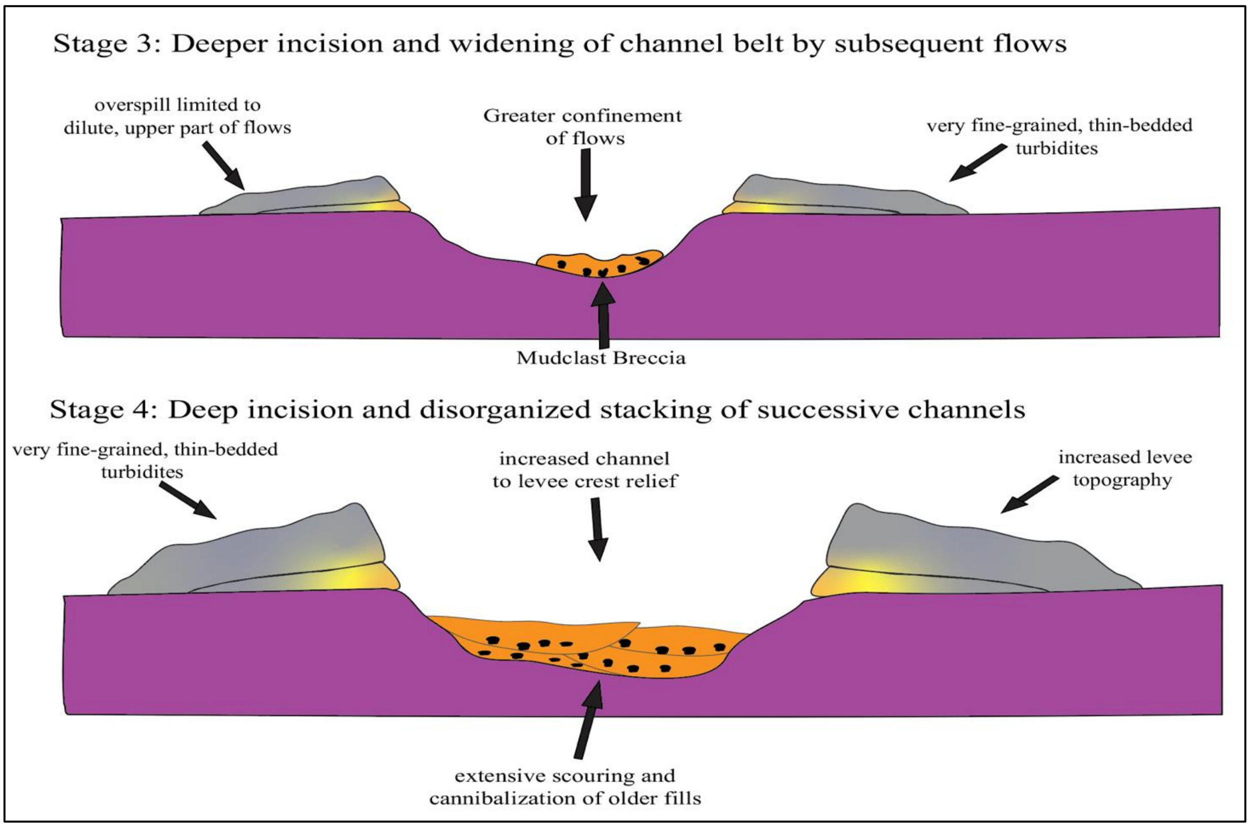

Fig. 4.13: *Conceptual model illustrating the transition from moderate to high relief in an evolving upper-slope channel–levee system. Stage 3 represents deeper incision and widening of the channel belt by subsequent turbidity currents, which become progressively more confined and restricts coarse-grained sediment to the channel axis. Only the dilute, very fine-grained upper part of the flows overspill onto the levees depositing very fine-grained, thin-bedded turbidites, whereas mudclast breccia accumulated in the channel axis. Stage 4 shows erosion and cannibalization of older channel fills as confinement increases, preventing channel avulsion and maintaining flow routing through the same entrenched pathway. Continued fine-grained overspill results in increased levee topography and thickening of thin-bedded turbidite packages.*

As flow energy and sediment-transport capacity declined, channel-fill strata of the youngest channel preserved the upward-fining and -thinning trend characteristic of submarine channels (Fig. 4.14) eventually marking the abandonment of the channel unit.

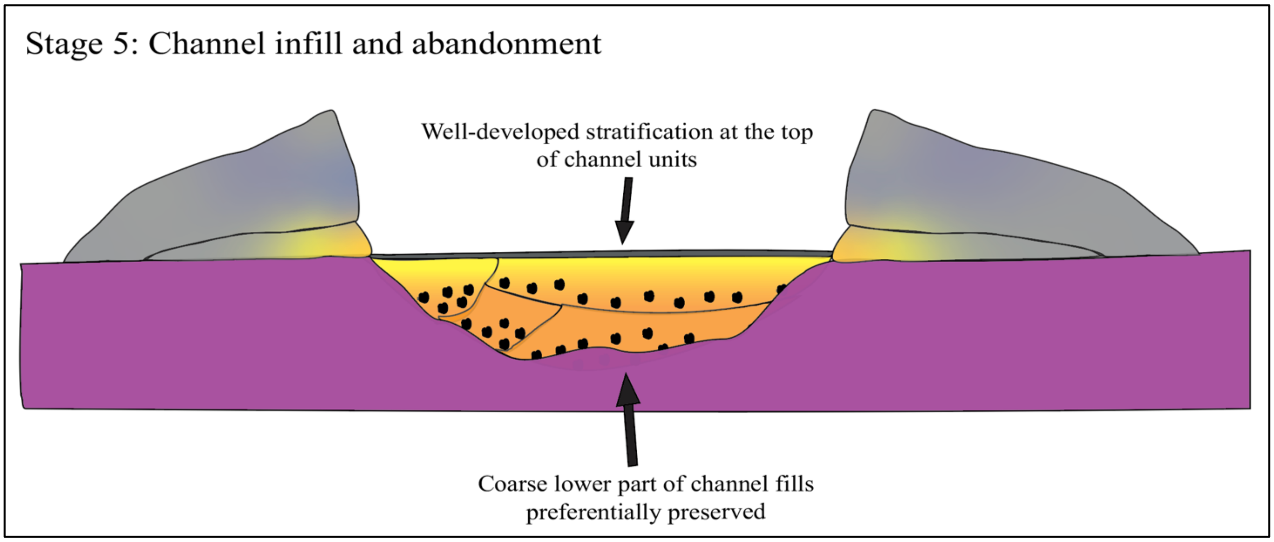

Fig. 4.14: *Schematic of late-stage channel evolution illustrating infill and abandonment. Following prolonged confinement and repeated cannibalization of earlier fills, the channel is infilled with laterally offset very coarse-grained deposits. Upward fining and well-developed stratification are only preserved at the top of the channel unit recording the abandonment of the channel unit.*

Chapter 5: Conclusion and Future Work

5.1 Conclusion

This study demonstrates that while upper-slope channel–levee deposits of the Isaac Formation share the same broad developmental motifs previously identified in ICC1–ICC5—most notably their characteristic upward transition from mass-transport deposits to aggrading followed by laterally accreting channel elements and associated levee deposits—their preserved stratal architecture deviates in fundamental ways compared to their mid- to lower-slope counterparts. These differences reveal that slope position governs the hydraulic behavior of turbidity currents transiting the system, and as a consequence the resulting channel and levee depositional stratigraphy.

On the upper slope (this study) channel units and their associated fills are significantly thinner, more deeply scoured, and dominated by mudclast-rich channel-axis deposits compared to those documented farther downslope. Whereas channel fills in ICC1–ICC5 commonly range from 4–15 m in thickness (average ~ 10 m) and fine upward to medium- and fine-grained, upper-division turbidites, in this study fills average only ~ 6 m and are dominated by very coarse sandstone to granule conglomerate with limited vertical fining. Individual fills also contain abundant mudclast breccia throughout, rather than only at their bases as is typical downslope. The prevalence of 2–4 m deep scours separating laterally and vertically juxtaposed fills and the preferential preservation of coarse-grained channel-axis deposits indicate repeated cannibalization of earlier channels by erosive bypass flows. These attributes reflect flows that had surplus turbulent energy relative to sediment load and thus operated in an undercapacity, erosion-dominated regime.

The capacity framework of Eggenhuisen et al. (2017) provides a physically based explanation for this contrast. On the steep upper part of the continental slope, high near-bed shear stress and limited early dilution promoted $\Gamma > 1$ conditions, enabling sustained erosion of underlying slope strata that increased flow density and caused the flow to accelerate – conditions termed flow ignition. As turbidity currents moved downslope entrainment of ambient fluid in addition to reduced slope angle caused the flow to thicken and reduce bulk density, which then trended Γ toward overcapacity conditions ($\Gamma < 1$), consistent with deposition of the thicker, aggradational channel fills documented previously on the mid to lower slope. However, the occurrence of laterally accreting above aggradationally filled channels everywhere along the slope suggests that the granulometric makeup of the sediment supply exceeds the influence of slope in determining the hydraulic regime and depositional characteristic of the flow.

In addition to the capacity framework, the channel equilibrium profile concept also helps to explain the difference in architecture and morphology of upper-slope channels compared to those farther downslope. Submarine channels tend to evolve toward a graded longitudinal profile in which slope and flow strength adjust so that the sediment-transport capacity of average turbidity currents matches the sediment load being transported through the system. Where this balance is disrupted, such as where slopes are oversteepened, channels respond by incising to reduce slope angle and re-establish the equilibrium profile. Channel deposits in this study relate well to this model, wherein the comparatively steeper angle on the upper part of the continental slope increased the downslope gravitational (driving) component, elevating basal shear velocity that favoured erosion rather than deposition.

Levee development on the upper slope similarly records the effects of early and then sustained confinement and net-erosion. Although the basal, sand-rich part of proximal levee packages resemble those described lower on the slope, the very fine-grained upper part is considerably thicker—averaging 20–25 m compared to 10–16 m in equivalent levee deposits downslope, and are dominated by very thin-bedded, finer-grained upper-division turbidites. This suggests a simple but substantial shift: rapid deepening of channels restricted coarse-grained overspill early in each channel's lifespan, while the dilute upper parts of flows continued to overspill accumulating thicker, very fine-grained levee deposits. Accordingly, upper-slope levees continued to aggrade vertically while channels experienced limited lateral migration following channel avulsion as they continuously scour and bypass this region of the slope.

Despite the pronounced architectural differences between the upper and lower slope, detrital zircon spectra across the Isaac Formation remain essentially uniform, indicating that sediment provenance did not change with time. The consistent bimodal Archean–Paleoproterozoic signature, with minor Mesoproterozoic and a stratigraphically restricted 650 Ma Neoproterozoic component, confirms a longstanding drainage system transporting sediment derived from the same northwestern Laurentian basement sources. Accordingly, the observed contrasts in channel and levee architecture cannot be attributed to changes in hinterland sediment supply or transport pathways but instead result from changes in sediment texture along the source to sink profile in addition to flow hydraulics controlled by position on the continental slope.

By integrating detailed sedimentology data with flow-capacity and channel-equilibrium concepts, this study contributes a mechanistic explanation for the systematic upward thinning of channel units and channel fills, and the coarsening of channel fills observed in the Isaac Formation. More broadly, it demonstrates that the upper slope occupies a critical but often underrepresented position in submarine channel systems; a zone where flows are undercapacity, leading to intense degradation of the channel floor and greater confinement of the transiting flows. This regime produced thin, very coarse-grained, deeply scoured, mudclast laden channel fills and unusually thick, very fine-grained levee successions.

5.2 Future Work

Although this study provides new insight into how upper-slope position influences the architecture of channel–levee complexes, its interpretations are based largely on a single vertical stratigraphic transect. Future work, therefore, should broaden observations along strike to capture additional 2D lateral variability in channel and levee deposits. Additional measuring of stratigraphic sections and high-resolution mapping would help establish the continuity of individual channel and levee elements, clarify the lateral extent of erosional surfaces, and better constrain how stacking patterns and facies change along-strike. Such lateral datasets are essential for building a more robust spatial and temporal model of upper-slope deposits and for systematically comparing their architectures with mid- and lower-slope counterparts. Furthermore, the self-similarity of beds documented here and in levee deposits of earlier studies should be tested in other thin-bedded turbidite successions from other parts of the Windermere turbidite system, for example in proximal and medial basin floor deposits of the upper and middle Kaza group and uppermost slope-canyon deposits near Lake Louise, Alberta.

In addition, a more comprehensive petrographic and granulometric analyses could be conducted to build a statistical dataset for comparison between channel complexes. Expanding compositional datasets through point counting and grain-size statistics would allow more rigorous comparison of aggradational versus laterally accreting channel fills in the study area. Such analyses would also help test the effects of relative sea-level change, as proposed in this thesis and in previous studies, in modulating sediment sorting and grain-size distributions across successive channel complexes. A more statistically robust petrographic dataset would further test the hypothesis that, despite their position higher on the slope, the upper-slope Isaac channels share the same fundamental developmental motifs documented in channel complexes farther downslope, differing mainly in the intensity of erosion and degree of confinement.

Lastly, differences in sandstone colour, namely brown, grey/white, and red/orange beds, likely reflect variations in carbonate content. However, the spatial distribution, depositional controls, and diagenetic evolution of these colour groups remain unresolved. Targeted petrographic, mineralogical, and geochemical characterization (e.g., cathodoluminescence, SEM–EDS) would help determine whether these colour differences primarily record variable carbonate input during deposition or early/late diagenesis.

References

Abreu, V., Sullivan M., Pirmez C., Mohrig D., and Mutti E. (2003). Lateral accretion packages (LAPs); an important reservoir element in deep water sinuous channels. Marine and Petroleum Geology, 20, p.631–648.

Aitken, J.D., (1969). Documentation of the sub-Cambrian unconformity, Rocky Mountain Main Ranges, Alberta. Canadian Journal of Earth Sciences, 6(2): 193-200.

Allen, G. P., and Posamentier, H. W. (1993). Sequence stratigraphy and facies model of an incised valley fill: The Gironde Estuary, France. Journal of Sedimentary Research, 63(3), 378–391.

Al-Mufti, O. N., and Arnott, R. W. C. (2024). The origin of planar lamination in fine-grained sediment deposited by subaqueous sediment gravity flows. The Depositional Record, 10(5), 496–514.

Amy, L. A., and Talling, P. J. (2006). Anatomy of turbidites and linked debrites based on long-distance (120 × 30 km) bed correlation, Marnoso Arenacea Formation, Northern Apennines, Italy. Sedimentology, 53(1), 161–212.

Arnott, R.W.C., (2007). Stratal architecture and origin of lateral accretion deposits (LADs) and conterminuous inner-bank levee deposits in a base-of-slope sinuous channel, lower Isaac Formation (Neoproterozoic), East-Central British Columbia, Canada. Marine and Petroleum Geology, 24(6-9): 515-528.

Arnott, R. W. C. (2010). Deep-marine sediments and sedimentary systems. In Facies models 4, p.295-322. Geological Association of Canada, St. John's, Newfoundland and Labrador.

Arnott, R.W.C. (2012) Turbidites, and the case of the missing dunes, Journal of Sedimentary Research, 82: 379-384.

Arnott, R. W. C., and Hand, B. M. (1989). Bedforms, primary structures and grain fabric in the presence of suspended sediment rain. Journal of Sedimentary Research, 59(6), 1062-1069.

Arnott, R. W. C., Wallace, K., and Laurin, J. (2011). Stratal architecture and temporal evolution of a passive margin mass-transport deposit, Neoproterozoic Isaac Formation, Cariboo Mountains, British Columbia, Canada. In Mass-Transport Deposits in Deepwater Settings (SEPM Special Publication No. 96, pp. 221–234). SEPM (Society for Sedimentary Geology).

Arnott, R. W. C. B., Tilston, M., Fraino, P., Navarro, L., Dumouchel, G., and Miklovich, N. (2021). Laterally accreting sinuous channels and their deposits; the Goldilocks of deep-water slope systems. Journal of Sedimentary Research, 91(5), 451–463.

Bagnold, R.A. (1962). Auto-suspension of transported sediments: turbidity currents. Proceedings of the Royal Society of London, A265, 315-319.

Bain, H. A., and Hubbard, S. M. (2016). Stratigraphic evolution of a long-lived submarine channel system in the Late Cretaceous Nanaimo Group, British Columbia, Canada. Sedimentary Geology, 337, 113-132.

Bergen, A. (2017). Vertical and lateral facies architectures of slope channels and genetically related levee deposits, Isaac Formation, Neoproterozoic Windermere Supergroup, Cariboo Mountains, B.C. M.Sc. thesis, University of Ottawa, Ottawa, ON.

Bergen, A.L., Cunningham, C.M., Terlaky, V., and Arnott, R.W.C., (2022), Influence of channelized-flow density structure on the stratal architecture of deep-marine levee deposits: Journal of Sedimentary Research, v. 92.4, p. 381-403.

Beaubouef, R. T. (2004). Deep-water leveed-channel complexes of the Cerro Toro Formation, Upper Cretaceous, southern Chile. AAPG Bulletin, 88(11), 1471–1500.

Billington, T. (2019). Sedimentologic and Petrographic Evidence of Flow Confinement in a Passive Continental Margin Slope Channel Complex, Isaac Formation, Windermere Supergroup, British Columbia, Canada. M.Sc. thesis, University of Ottawa, Ottawa, ON

Bond, G. C., and Kominz, M. A. (1984). Construction of tectonic subsidence curves for the early Paleozoic miogeocline, southern Canadian Rocky Mountains: Implications for subsidence mechanisms, age of breakup, and crustal thinning. Geological Society of America Bulletin, 95, 155-173.

Bouma, A.H., (1962). Sedimentology of some Flysh Deposits. A graphic approach to facies interpretation. Elsevier, Amsterdam, p.168.

Box, S. E., Pritchard, C. J., Stephens, T. S., and O'Sullivan, P. B. (2020). Between the supercontinents: Mesoproterozoic Deer Trail Group, an intermediate age unit between the Mesoproterozoic Belt–Purcell Supergroup and the Neoproterozoic Windermere Supergroup in northeastern Washington, USA. Canadian Journal of Earth Sciences, 57(12), 1411-1427.

Brady, J. F., and Bossis, G. (1985). The rheology of concentrated suspensions of spheres in simple shear flow by numerical simulation. Journal of Fluid Mechanics, 155, 105–129.

Campbell, D. C., and Geological Survey of Canada. (2005). Major Quaternary mass-transport deposits in southern Orphan Basin, offshore Newfoundland and Labrador. Natural Resources Canada, Geological Survey of Canada.

Canals, M., and Lastras, G. (2004). Slope failure dynamics and impacts from seafloor and shallow.

Catuneanu, O., (2006). Principles of Sequence Stratigraphy: Amsterdam, Elsevier 375

Catuneanu, O. (2020). Sequence stratigraphy of deep-water systems. Marine and Petroleum Geology, 114, Article 104238.

Catuneanu, O., Abreu, V., Bhattacharya, J. P., Blum, M. D., Dalrymple, R. W., Eriksson, P. G., and Giles, K. A. (2009). Towards the standardization of sequence stratigraphy. Earth-Science Reviews, 92(1-2), 1-33.

Clark, J. D., and Pickering, K. T. (1996). Architectural elements and growth patterns of submarine channels: application to hydrocarbon exploration. AAPG bulletin, 80(2), p.194-220.

Clarke, J. E. H., Shor, A. N., Piper, D. J. W., and Mayer, L. A. (1990). Large-scale current-induced erosion and deposition in the path of the 1929 Grand Banks turbidity current. Sedimentology, 37(4), 613–629.

Clemenceau, G. (1999). Abstract: Levee-overbank Turbidite Production from Ram/Powell Field, Deepwater Gulf of Mexico. AAPG Bulletin, 83.

Covault, J. A., Kostic, S., Paull, C. K., Ryan, H. F., and Fildani, A. (2014). Submarine channel initiation, filling and maintenance from sea-floor geomorphology and morphodynamic modelling of cyclic steps. Sedimentology, 61(4), p.1031-1054.

Covault, J. A., Sylvester, Z., Hubbard, S. M., Jobe, Z. R., and Sech, R. P. (2016). The Stratigraphic Record of Submarine-Channel Evolution. The Sedimentary Record, 14(3), 4–11.

Crowley, J. L. (1999). U-Pb geochronologic constraints on Paleoproterozoic tectonism in the Monashee complex, Canadian Cordillera: Elucidating an overprinted geologic history. Geological Society of America Bulletin, 111(4), 560-577.

Cunningham, C., and Arnott, R. W., University of Ottawa. Department of Earth and Environmental Sciences., & Ottawa-Carleton Geoscience Centre. (2021). Sedimentological and geochemical characterization of neoproterozoic deep-marine levees deposits [Université d'Ottawa / University of Ottawa].

Davies, R. (1968). The experimental study of the differential settling of particles in suspension at high concentrations. Powder Technology, 2(1), 43–51.

Deptuck, M. E., Steffens, G. S., Barton, M., and Pirmez, C. (2003). Architecture and evolution of upper fan channel-belts on the Niger Delta slope and in the Arabian Sea. Marine and Petroleum Geology, 20(6), 649–676.

Donald R. Lowe, (1979). "Sediment Gravity Flows: Their Classification and Some Problems of Application to Natural Flows and Deposits", Geology of Continental Slopes, Larry J. Doyle, Orrin H. Pilkey

Dorrell, R. M., Darby, S. E., Peakall, J., Sumner, E. J., Parsons, D. R., and Wynn, R. B. (2014). The critical role of stratification in submarine channels: implications for channelization and long runout of flows. Journal of Geophysical Research: Oceans, 119, 4, 2620-2641.

Dumouchel, I.G. (2015). Stratigraphic Architecture and Depositional History of Laterally-Accreted Channel Fills in the Lower Isaac Formation, Windermere Supergroup, British Columbia, Canada. M.Sc. thesis, University of Ottawa, Ottawa, ON

Eggenhuisen, J. T., Cartigny, M. J. B., and de Leeuw, J. (2017). Physical theory for near-bed turbulent particle suspension capacity. Earth Surface Dynamics, 5(2), 269–281.

Fanning, C. M., and Link, P. K. (2004). U-Pb SHRIMP ages of Neoproterozoic (Sturtian) glaciogenic Pocatello Formation, southeastern Idaho. Geology, 32(10).

Fraino, P. E., Arnott, R. W. C., and Navarro, L. (2022). The influence of sediment supply on the stratigraphic evolution of an ancient passive margin deep-marine slope channel system, Windermere Supergroup, British Columbia, Canada. Journal of Sedimentary Research, 92(3), 232-256.

Fisher, R.V. (1983). Flow transformation in sediment gravity flows, Geology. 11, 273-274.

Gardner, M. H., J. M. B. (2000). Abstract: Submarine channel architecture along a slope to basin profile, Brushy Canyon Formation, West Texas. AAPG Bulletin, 84 (2000).

Gardner, J. V., and Kidd, R. B. (1983). Sedimentary processes on the Iberian continental margin viewed by long-range side-can sonar. I: Gulf of Cadiz. Oceanologica Acta, 6(3), 245–254.

Garrison, L. E., Kenyon, N. H., and Bouma, A. H. (1982). Channel systems and lobe construction in the Mississippi Fan. Geo-Marine Letters, 2(1–2), 31–39.

Gehrels, G. (2011). Detrital zircon U-Pb geochronology: current methods and new opportunities. University of Arizona, Tucson, AZ: Blackwell Publishing Ltd.

Georgiopoulou, A., and Cartwright, J. A. (2013). A critical test of the concept of submarine equilibrium profile. Marine and Petroleum Geology, 41, 35–47.

Gordey, S.P., and Anderson, R.G., 1993, Evolution of the northern Cordilleran miogeocline, Nahanni map area (105I), Yukon and Northwest Territories: Geological Survey of Canada Memoir 428, 214 p.

Hadlari, T., Arnott, R. W. C., Matthews, W. A., Poulton, T. P., Root, K., and Madronich, L. I. (2021). Provenance of the incipient passive margin of NW Laurentia (Neoproterozoic); detrital zircon from continental slope and basin floor deposits of the Windermere Supergroup, southern Canadian Cordillera. Lithosphere, 2021(1).

Hadlari, T., Rayner, N. M., Poulton, T. P., and Arnott, R. W. C. (2024). Syn-rift volcanism (ca. 670 Ma) in the lower Windermere Supergroup, southern Canadian Cordillera: New constraints on the syn- to post-rift transition for northwestern Laurentia. Precambrian Research, 414, Article 107604.

Hampton, M.A (1975) Competence of fine-grained debris flows. J. Sed. Petrol., 45, 834-844.

Halsey, T. C., and Kumar, A. (2019). Levees Formed by Turbidity Currents: A Depth-Averaged Modeling Treatment. Journal of Geophysical Research. Oceans, 124(7), 4389–4415.

Hay, A. E., Murray, J. W., and Burling, R. W. (1983). Submarine channels in rupert inlet, British Columbia: II. Sediments and sedimentary structures. Sedimentary Geology, 36(2), 317–339.

Hiscott, R. N., Pickering, K. T., Bouma, A., Hand, B. M., Kneller, B. C., Postma, G., and Soh, W. (1997). Basin-Floor Fans in the North Sea: Sequence Stratigraphic Models vs. Sedimentary Facies: Discussion. AAPG Bulletin, 81 (1997)(4), 662–665.

Hoffman, P. F. (1988). United plates of America, the birth of a craton: Early Proterozoic assembly and growth of Laurentia. Ann. Rev. Earth Planet. Sci, 16, 543-603.

Hoffman, P. F. (1991). Did the breakout of Laurentia turn Godwanaland inside-out? Science, 525, 1409-1412.

Hubbard, S. M., Covault, J. A., Fildani, A., and Romans, B. W. (2014). Sediment transfer and deposition in slope channels: Deciphering the record of enigmatic deep-sea processes from outcrop. Bulletin, 126(5-6), 857-871.

Hunt, D. and Tucker, M.E. (1992). Stranded parasequences and the forced regressive wedge systems tract: deposition during base-level fall. Sedimentary Geology, 81, 1-9.

Ingersoll, R. V. (2011). Tectonics of Sedimentary Basins, with Revised Nomenclature. In A. Azor and C. Busby (Eds.), Tectonics of Sedimentary Basins: Recent Advances (pp. 1–43). John Wiley & Sons, Ltd.

Iverson, R. M., Reid, M. E., and LaHusen, R. G. (1997). Debris-flow mobilization from landslides. Annual Review of Earth and Planetary Sciences, 25(1), 85-138.

J Hoover Mackin; Concept of the Graded River. GSA Bulletin 1948; 59 (5): 463–512.

Jegou, I., Savoye, B., Pirmez, C., and Droz, L. (2008). Channel-mouth lobe complex of the recent Amazon Fan: The missing piece. Marine Geology, 252(1), 62–77.

Jerolmack, D. J., and Paola, C. (2007). Complexity in a cellular model of river avulsion. Geomorphology, 91(3-4), 259-270.

Jobe, Z. R., Lowe, D. R., and Uchytil, S. J. (2011). Two fundamentally different types of submarine canyons along the continental margin of Equatorial Guinea. Marine and Petroleum Geology, 28(3), 843–860.

Jobe, Z.R., Hower, N.C., and Auchter, N.C. (2016). Comparing submarine and fluvial channel kinematics: Implications for stratigraphic architecture. The Geological Society of America, 44(11), p.931-934.

Kane, I. A., Kneller, B. C., Dykstra, M., Kassem, A., and McCaffrey, W. D. (2007) Anatomy of a submarine channel-levee: An example from Upper Cretaceous slope sediments, Rosario Formation, Baja California, Mexico. Marine and Petroleum Geology, 24, 540-563.

Kane, I. A., McCaffrey, W. D., Peakall, J. and Kneller, B. C. (2010) Submarine channel levee shape and sediment waves from physical experiments. Sedimentary Geology, 223, 75–85.

Khan, Z. (2012). Origin and architecture of deep-water level deposits: Insight from the ancient rock record and experiments, Ph.D. thesis, University of Ottawa, Ottawa, ON.

Khan, Z.A., and Arnott, R.W.C. (2011). Stratal attributes and evolution of asymmetric inner- and outer-bend levee deposits associated with an ancient deep-water channel-levee complex within the Isaac Formation, southern Canada, Marine and Petroleum Geology, 28: 824-842.

Khan, Z. A., Arnott, B., and Pugin, A. (2011). An alternative model of producing topography in the crest region of deep-water levees. AAPG Bulletin, 95(12), 2085–2106.

Kneller, B. C., and Branney, M. J. (1995). Sustained high-density turbidity currents and the deposition of thick massive sands. Sedimentology, 42(4), 607–616.

Kneller, B.C., and Buckee, C. (2000). The structure and fluid mechanics of turbidity currents: a review of some recent studies and their geologic implications. Sedimentology, 47 (Suppl. 1), 62-94.

Kneller, B. C. (2003) The influence of flow parameters on turbidite channel slope Architecture. Marine and Petroleum Geology, 20, p.901–910.

Kneller, B., Dykstra, M., Fairweather, L., and Milana, J. P. (2016). Mass-transport and slope accommodation; implications for turbidite sandstone reservoirs. AAPG Bulletin, 100(2), 213–235.

Konsoer, K., Zinger, J., and Parker, G. (2013). Bankfull hydraulic geometry of submarine channels created by turbidity currents: Relations between bankfull channel characteristics and formative flow discharge. Journal of Geophysical Research: Earth Surface, 118(1), 216-228.

Li, Z. X., Bogdanova, S. V., Collins, A. S., Davidson, A., De Waele, B., Ernst, R. E., Fitzsimons, I. C. W., Fuck, R. A., Gladkochub, D. P., Jacobs, J., Karlstrom, K. E., Lu, S., Natapov, L. M., Pease, V., Pisarevsky, S. A., Thrane, K., and Vernikovsky, V. (2008). Assembly, configuration, and break-up history of Rodinia: A synthesis. Precambrian Research, 160(1), 179–210.

Li, Z. X., Evans, D. A. D., and Halverson, G. P. (2013). Neoproterozoic glaciations in a revised global palaeogeography from the breakup of Rodinia to the assembly of Gondwanaland. Sedimentary Geology, 294, 219-232.

Link, P. K., Christie-Blick, N., Devlin, W. J., Elston, D. P., Horodyski, R. J., Levy, M., ... Wrucke, C. T. (2003). Middle and late Proterozoic stratified rocks in the western U.S. Cordillera, Colorado Plateau, and Basin and Range Province. In J. C. Reed Jr., M. E. Bickford, R. S. Houston, P. K. Link, D. W. Rankin, P. K. Sims, and W. R. Van Schmus (Eds.), Precambrian: Conterminous U.S., The Geology of North America: Geological Society of America Decade of North American Geology Series, v. c-3 (pp. 474-690).

Lowe, D.R. (1982). Sediment gravity flows: II. Depositional models with special reference to the deposits of high-density turbidity currents, Journal of Sedimentary Petrology, 52: 279-297.

Matthews, W., Guest, B., and Madronich, L., (2017). Latest Neoproterozoic to Cambrian detrital zircon facies of western Laurentia. Geosphere, 14(1): 243-264.

Meyer, L. (2004). Internal architecture of an ancient deep-water, passive margin, basin-floor fan system, Upper Kaza Group, Windermere Supergroup, Castle Creek, British Columbia, M.Sc. thesis, University of Calgary, Calgary, AB.

Middleton, G.V. and Hampton, M.A., (1973). Sediment Gravity Flows: mechanics of flow and deposition, in Middletong, G.V and A.H Bouma, eds., Turbidites and Deep Water Sedimentation. Short Course Notes, No 1, SEPM (Pacific Section), Los Angeles, p. 1-38.

McHargue, T., Pyrcz, M. J., Sullivan, M. D., Clark, J. D., Fildani, A., Romans, B. W., Covault, J. A., Levy, M., Posamentier, H. W., and Drinkwater, N. J. (2011). Architecture of turbidite channel systems on the continental slope: Patterns and predictions. Marine and Petroleum Geology, 28(3), 728–743.

McMechan, M. E. (2015). The Neoproterozoic succession of the central Rocky Mountains, Canada. Bulletin of Canadian Petroleum Geology, 63(3), 243-273.

Mohrig, D., and Marr, J. G. (2003). Constraining the efficiency of turbidity current generation from submarine debris flows and slides using laboratory experiments. *Marine and Petroleum Geology*, *20*(6), 883–899.

Moynihan, D. P., Strauss, J. V., Nelson, L. L., and Padget, C. D. (2019). Upper Windermere Supergroup and the transition from rifting to continent-margin sedimentation, Nadaleen River area, northern Canadian Cordillera. Geological Society of America Bulletin, 131(9–10), 1673–1701.

Murphy, D.C., and Rees, C.J. (1983). Structural transition and stratigraphy in the Cariboo Mountains, British Columbia. In Current Research Part A, Geological Survey of Canada Paper 83-1A, 245-252.

Murphy, D.C. (1987a). Kaza Group, eastern wells gray park, British Columbia, Geological Survey of Canada Paper 87-1A, pp. 735-742.

Murphy, D.C., (1987b). Suprastructure/infrastructure transition, east-central Cariboo Mountains, British Columbia; geometry, kinematics and tectonic implications, Journal of Structural Geology, 9: 13-29.

Mulder, T., and Alexander, J., (2001). The physical character of subaqueous sedimentary density flows and their deposits. Sedimentology, 48, p. 269-299.

Mutti, E., and Normark, W. R. (1987). Comparing examples of modern and ancient turbidite systems: problems and concepts, in J. R. Leggett, and G. G. Zuffa, eds., Marine Clastic Sedimentology: Concepts and Case Studies: London, Graham and Trotman, p.1–37.

Navarro, L. (2005). Depositional architecture and evolution of deep-water base-of-slope and slope channel complexes in a passive margin setting: Isaac Formation, Windermere Supergroup (Neoproterozoic) southern Canadian Cordillera. M.Sc. thesis, Université d'Ottawa/University of Ottawa, 272 p.

Navarro, L., Z. Khan, and R. W. C. Arnott, (2007). Depositional architecture and evolution of a deep-marine channel-levee complex: Isaac Formation (Windermere Supergroup), Southern

Canadian Cordillera., in T. H. Nilsen, R.D. Shew, G. S. Steffens, and J. R. J. Studlik, eds., Atlas of Deep-water Outcrops., v. CD-ROM: Tulsa, AAPG Studies in Geology 56, CD-ROM, p.22.

Navarro, L. (2016). Stratigraphic architecture depositional processes and reservoir implications of the basin floor to slope transition, Neoproterozoic Windermere turbidite system, Canada: Ph.D. thesis, University of Ottawa, Ottawa, ON.

Neal, J., and Abreu, V. (2009). Sequence stratigraphy hierarchy and the accommodation succession method. Geology (Boulder), 37(9), 779–782.

Normandeau, A., Bourgault, D., Neumeier, U., Lajeunesse, P., St-Onge, G., Gostiaux, L., Chavanne, C., and Felletti, F. (2020). Storm-induced turbidity currents on a sediment-starved shelf: Insight from direct monitoring and repeat seabed mapping of upslope migrating bedforms. Sedimentology, 67(2), 1045–1068.

Parker, G., Fukushima, Y., and Pantin, H. M. (1986). Self-accelerating turbidity currents. Journal of Fluid Mechanics, 171, 145–181.

Peakall, J., McCaffrey, W. D. and Kneller, B. C. (2000). A process model for the evolution, morphology, and architecture of sinuous submarine channels. Journal of Sedimentary Research, 70, p.434–448.

Plint, A. G., and Nummedal, D. (2000). The falling stage systems tract: recognition and importance in sequence stratigraphic analysis. Geological Society, London, Special Publications, 172(1), 1-17.

Pickering, K., Stow, D., Watson, M., and Hiscott, R. (1986). Deep-water facies, processes and models: a review and classification scheme for modern and ancient sediments. Earth-Science Reviews, 23(2), 75–174.

Pickering, K. T., Clark, J. D., Smith, R. D. A., Hiscott, R. N., Lucchi, F. R. and Kenyon, N. H. (1995). Architectural element analysis of turbidite systems, and selected topical problems for sand-prone deep-water systems, Atlas of deep water environments, Springer, p. 1-10.

Pipe, A., Arnott, R. W., and University of Ottawa. Department of Earth and Environmental Sciences. (2023). Sediment provenance using detrital-Zircons, Nd-Sr isotopes, and bulk rock geochemistry : implications for sediment routing in the Neoproterozoic Windermere Supergroup, southern Canadian Cordillera [Université d'Ottawa / University of Ottawa].

Piper, D. J. W., and Normark, W. R. (1983). Turbidite depositional patterns and flow characteristics, Navy Submarine Fan, California Borderland. Sedimentology, 30(5), 681–694.

Piper, D. J. W., and Normark, W. R. (2001). Sandy fans – from Amazon to Hueneme and beyond. AAPG Bulletin, 85, 1407–1438.

Pirmez, C., Beaubouef, R., Friedmann, S. and Mohrig, D. (2000). Equilibrium Profile and Baselevel in Submarine Channels: Examples from Late Pleistocene Systems and Implications for the Architecture of Deepwater Reservoirs.

Pirmez, C., and Imran, J. (2003). Reconstruction of turbidity currents in Amazon Channel. Marine and Petroleum Geology, 20(6), 823–849.

Posamentier, H. W., Allen, G. P., James, D. P., and Tesson, M. (1992). Forced regressions in a sequence stratigraphic framework: concepts, examples, and exploration significance. AAPG bulletin, 76(11), 1687-1709.

Posamentier, H. W., and Kolla, V. (2003). Seismic geomorphology and stratigraphy of depositional elements in deep-water settings. Journal of sedimentary research, 73(3), 367-388.

Posamentier, H. W., and R. G. Walker, (2006). Deep-water turbidites and submarine fans: SEPM Special Publication, v. 84, p. 397–520.

Prélat, A., Hodgson, D. M., and Flint, S. S. (2009). Evolution, architecture and hierarchy of distributary deep-water deposits: a high-resolution outcrop investigation from the Permian Karoo Basin, South Africa. Sedimentology, 56(7), 2132–2154.

Rainbird, R. H., McNicoll, V. J., Thériault, R. J., Heaman, L. M., Abbott, J. G., Long, D. G. F., and Thorkelson, D. J. (1997). Pan-Continental River System Draining Grenville Orogen Recorded by U-Pb and Sm-Nd Geochronology of Neoproterozoic Quartzarenites and Mudrocks, Northwestern Canada. The Journal of Geology, 105(1), 1–17.

Reid, L.F., Simony, P.S., and Ross, G.M., (2002). Dextral strike-slip faulting in the Cariboo Mountains, British Columbia: a natural example of wrench tectonics in relation to Cordilleran tectonics. Canadian Journal of Earth Sciences, 39(6): 953-970.

Rodine, J. D., and Johnson, A. M. (1976). The ability of debris, heavily freighted with coarse clastic materials, to flow on gentle slopes. Sedimentology, 23(2), 213–234.

Ross, G. M. (1991). Tectonic setting of the Windermere Supergroup revisited. Geology, 19, 1125-1128.

Ross, G.M., and Arnott, R.W.C., (2007). Regional Geology of the Windermere Supergroup, Southern Canadian Cordillera and Stratigraphic Setting of the Castle Creek Study Area, Canada. Atlas of deep-water outcrops: AAPG Studies in Geology.

Ross, G. M., Bloch, J. D., and Krouse, H. R. (1995). Neoproterozoic strata of the southern Canadian Cordillera and the isotopic evolution of seawater sulfate. Precambrian Research, 73, 71-99.

Ross, G. M., and Murphy, D. C. (1988). Transgressive stratigraphy, anoxia, and regional correlations within the late Precambrian Windermere grit of the southern Canadian Cordillera. Geology, 16, 139-143.

Ross, G.M., and Parrish, R.R., (1991). Detrital zircon geochronology of metasedimentary rocks in the southern Omineca Belt, Canadian Cordillera. Canadian Journal of Earth Sciences, 28: 1254-1270.

Ross, W. C., Halliwell, B. A., May, J. A., Watts, D. E., and Syvitski, J. P. M. (1994). Slope readjustment: a new model for the development of submarine fans and aprons. Geology, 22(6), 511-514.

Rowe, C. E. (2003). The Cunningham formation: a ramp to platform carbonate in the terminal Proterozoic of the Cariboo Mountains, British Columbia, M.Sc. thesis, University of Calgary, Calgary, AB.

Samuel, A., Kneller, B., Raslan, S., Sharp, A., and Parsons, C. (2003). Prolific deep-marine slope channels of the Nile Delta, Egypt. AAPG bulletin, 87(4), 541-560.

Schwarz, E., and Arnott, R.W.C. (2007a). Anatomy and evolution of a slope channel-complex set (Neoproterozoic Isaac Formation, Windermere Supergroup, southern Canadian Cordillera): implications for reservoir characterization, Journal of Sedimentary Research, 77: 89-109.

Schwarz, E., and Arnott, R.W.C. (2007b). Outcrop characterization of a passive- margin channel-complex set: Isaac Channel 5, Neoproterozoic Isaac Formation, British Columbia, Canada. . In Atlas of deep-water outcrops: AAPG Studies in Geology 56. Edited by T. H. Nilsen, R. D. Shew, G. S. Steffens, and J. R. J. Studlick, CD-ROM, 15 p.

Smith, M. D., Arnott, R. W. C., and Ross, G. M. (2014). The Old Fort Point Formation: Redefinition and formal subdivision of a distinctive stratigraphic marker in the Neoproterozoic Windermere Supergroup, southern Canadian Cordillera. Bulletin of Canadian Petroleum Geology, 62(1), 1-13.

Shanmugam, G., Lehtonen, L. R., Straume, T., Syvertsen, S. E., Hodgkinson, R. J., and Skibeli, M. (1994). Slump and debris-flow dominated upper slope facies in the Cretaceous of the Norwegian and northern North seas (61-67°N); implications for sand distribution. AAPG Bulletin, 78(6), 910–937.

Shanmugam, G., and Moiola, R. J. (1997). Reinterpretation of Depositional Processes in a Classic Flysch Sequence (Pennsylvanian Jackfork Group), Ouachita Mountains, Arkansas and Oklahoma: Reply. AAPG Bulletin, 81 (1997)(3), 476–491.

Shanmugam, G. (2006). Deep-water processes and facies models: Implications for sandstone petroleum reservoirs. Elsevier, New York, U.SA.

Shanmugam, G. (2021). Gravity flows: debris flows, grain flows, liquefied/fluidized flows, turbidity currents, hyperpycnal flows, and contour c. In Mass Transport, Gravity Flows, and Bottom Currents. Elsevier.

Sprague, A. R., M. D. Sullivan, K. M. Campion, G. N. Jensen, D. K. Goulding, D. K.Sickafoose, and D. C. Jennette, (2002). The physical stratigraphy of deep-water strata: a hierarchical approach to the analysis of genetically related elements for improved reservoir prediction, AAPG Annual Convention and Exhibition. Abstracts. : Houston, Texas, p. 10-13.

Straub, K. M., Mohrig, D., McElroy, B., Buttles, J., and Pirmez, C. (2008). Interactions between turbidity currents and topography in aggrading sinuous submarine channels: A laboratory study. Geological Society of America Bulletin, 120(3-4), 368-385.

Stewart, J. H. (1972). Initial deposits in the Cordilleran geosyncline; evidence of a late Precambrian (<850 m.y.) continental separation. Geological Society of America Bulletin, 83, 1345-1360.

Stevenson, C. J., Jackson, C. A. L., Hodgson, D. M., Hubbard, S. M., and Eggenhuisen, J. T. (2015). Deep-water sediment bypass. Journal of Sedimentary Research, 85(9), 1058–1081.

Stow, D. A. V. (1985). Fine-grained sediments in deep water: An overview of processes and facies models. Geo-Marine Letters, 5(1), 17–23.

Stow, D. A. V., and Bowen, A. J. (1980). A physical model for the transport and sorting of fine-grained sediment by turbidity currents. Sedimentology, 27(1), 31–46.

Sylvester, Z., Pirmez, C., and Cantelli, A. (2011). A model of submarine channel-levee evolution based on channel trajectories: Implications for stratigraphic architecture. Marine and Petroleum Geology, 28(3), 716-727.

Talling, P. J. (2014). On the triggers, resulting flow types and frequencies of subaqueous sediment density flows in different settings. Marine Geology, 352, 155–182.

Talling, P. J., D. G. Masson, E. J. Sumnet, and G. Malgesini, (2012). Subaqueous sediment density flows: Depositional processes and deposit types: Sedimentology, v. 59, p. 1937-2003.

Talling, P. J., C. K. Paull, and D. J. W. Piper, (2013). How are subaqueous sediment density flows triggered, what is their internal structure and how does it evolve? Direct observations from monitoring of active flows: Earth-Science Reviews, v. 125, p. 244-287.

Terlaky, V., Rocheleau, J., Arnott, R.W.C., and Talling, P., (2015). Stratal composition and stratigraphic organization of stratal elements in an ancient deep-marine basin-floor succession, Neoproterozoic Windermere Supergroup, British Columbia, Canada. Sedimentology, 63(1): 136-175.

Tilston, M., Arnott, R.W.C., Rennie, C.D., and Long, B. (2015). The influence of grain size on the velocity and sediment concentration profiles and depositional record of turbidity currents, Geology, 43: 839-842.

Udden, J. A. (1914). Mechanical composition of clastic sediments. Bulletin of the Geological Society of America, 25(1), 655-744.

Venditti, J.G., Church, M., and Bennett, S.J. (2005). Bed form initiation from a flat sand bed, Journal of Geophysical Research, 110: F01009, 1-19.

Venditti, J.G., Church, M., and Bennett, S.J. (2006). On interfacial instability as a cause of transverse subcritical bed forms, Water Resources Research, 42: W07423.

Whitmeyer, S. J., and Karlstrom, K. E. (2007). Tectonic model for the Proterozoic growth of North America. *Geosphere, 3(4), 220–259.

Young, F. G., Campbell, R. B., and Poulton, T. P. (1973). The Windermere Supergroup of the southeastern Canadian Cordillera. Belt Symposium, Moscow, Idaho, USA.

Young, G. M. (1984). Proterozoic plate tectonics in Canada, with emphasis on evidence for a late Proterozoic rifting event. Precambrian Research, 25, 233–256.

Young, G. M., Jefferson, C. W., Delaney, G. D., and Yeo, G. M. (1979). Middle and late Proterozoic evolution of the northern Canadian Cordillera and Shield. Geology (Boulder), 7(3), 125–128.

Wentworth, C. K. (1922). A scale of grade and class terms for clastic sediments. Journal of Geology, 30(5), 377-392.

Wiedenbeck, M., Allé, P., Corfu, F., Griffin, W. L., Meier, M., Oberli, F., Quadt, A. V., Roddick, J. C., and Spiegel, W. (1995). Three natural zircon standards for U-Th-Pb, Lu-Hf, trace element and REE analyses. Geostandards Newsletter, 19(1), 1–23.

Wynn, R.B., Cronin, B.T., and Peakall, J. (2007). Sinuous deep-water channels: Genesis, geometry, architecture, Marine and Petroleum Geology, 24, p.341-387.

Appendix

Supplementary Zircon Images and Geochronology Data

This appendix presents supporting analytical data for zircon U–Pb geochronology, including cathodoluminescence (CL) images of analyzed grains, locations of analytical spots, and full isotopic datasets. Tables include measured isotopic ratios, propagated uncertainties, and calculated ages used in Kernel Density Estimation and Tera–Wasserburg plots. These data support the provenance interpretations and age constraints discussed in Chapters 2 and 4.

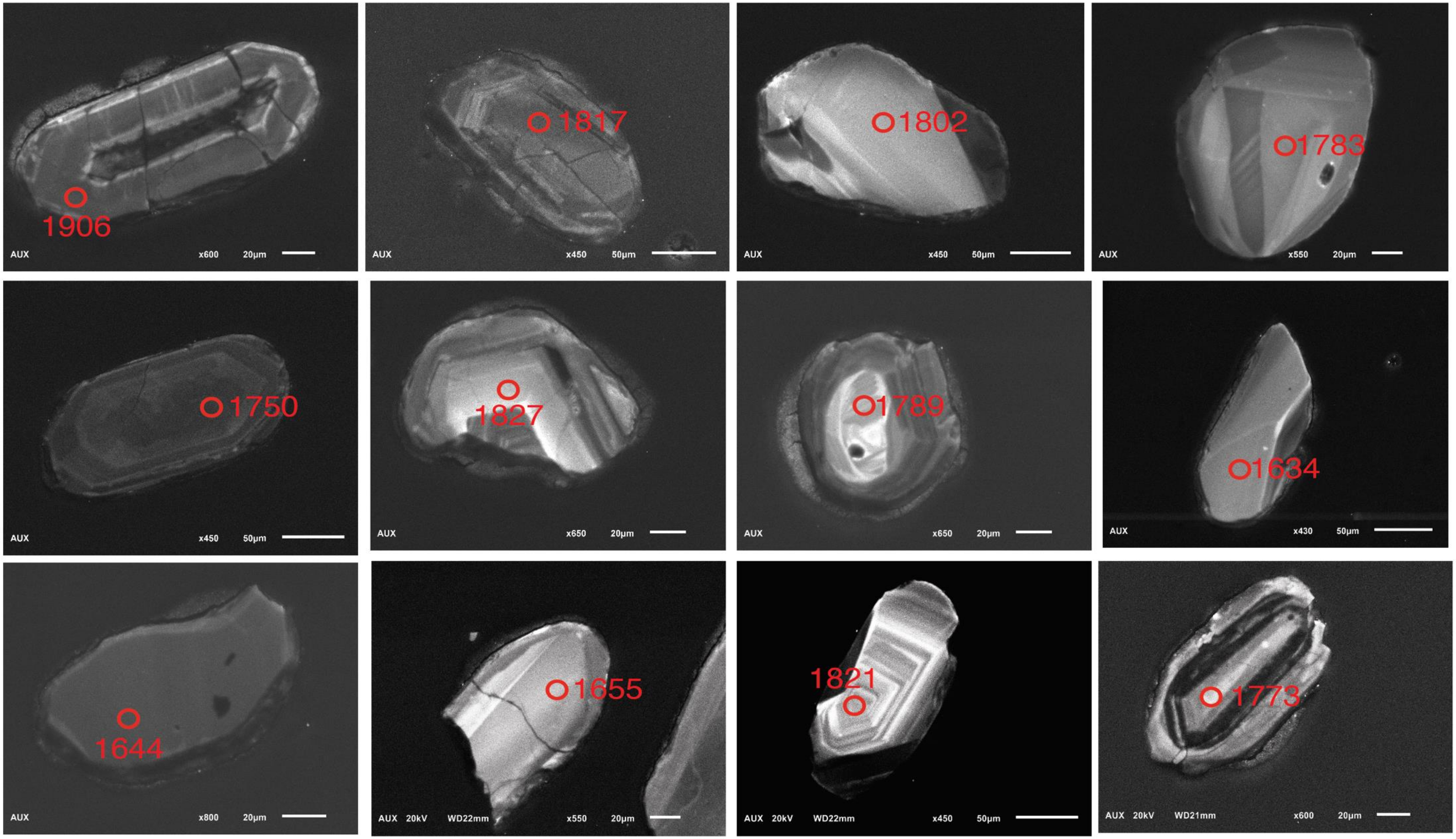

Figure A 1: *SEM cathodoluminescence (CL) images of representative zircon grains yielding Paleoproterozoic ages illustrating internal zoning and growth domains. Laser ablation analysis spots are indicated by red circles, and the corresponding 207Pb/206Pb ages (Ma) are shown. CL imaging was used to target specific growth zones and avoid inclusions or fractures during U–Pb analysis.*

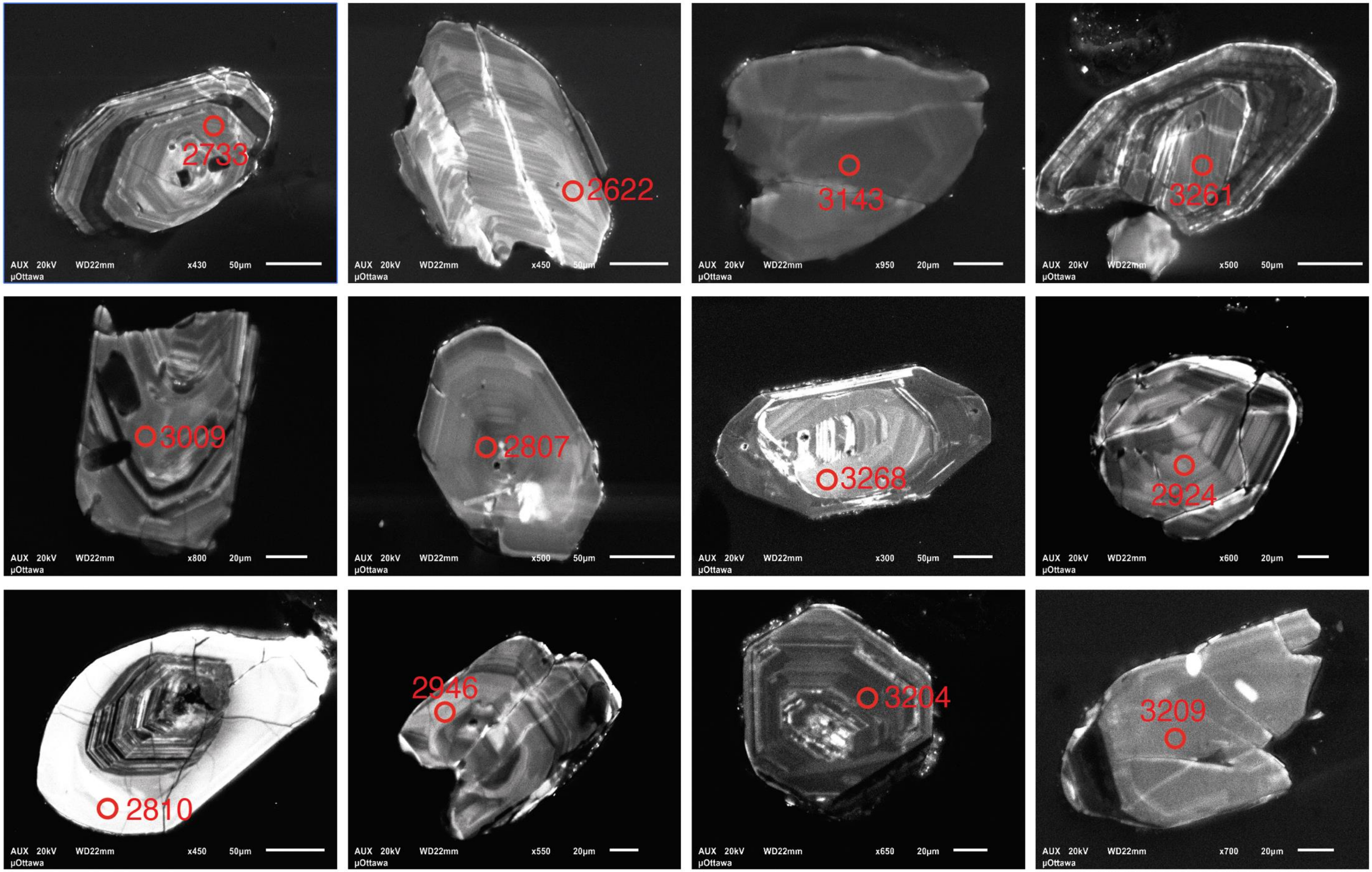

Figure A 2: *SEM images of representative detrital zircon grains with Archean ages. Internal zoning and core–rim relationships are visible in CL imagery. Laser ablation analysis spots are marked by red circles, and the corresponding 207Pb/207Pb ages (Ma) are labeled for each grain.*

	Dates							
Sample	$^{207}Pb/^{206}Pb$	$2s_x$ (ABS)	$^{206}Pb/^{238}U$	$2s_x$ (ABS)	$^{207}Pb/^{235}Pb$	$2s_x$ (ABS)	Concordant filter	20% discordant filter, 5% reverse discordant filter
19-GC-4	840.9	240.5	606.2	32.4	658.2	60.3	72.09	discorndant
19-GC-4	653.3	69.8	634.3	14.2	638.5	18.9	97.09	Concordant
19-GC-4	570.8	204.6	636.6	30.1	622.4	48.2	111.53	>5% revdisc
19-GC-4	617.9	91.6	642.5	18.0	637.1	24.3	103.98	Concordant
19-GC-4	704.9	120.9	644.2	22.0	657.9	32.2	91.39	Concordant
19-GC-4	711.6	98.7	650.1	19.2	664.0	27.0	91.36	Concordant
19-GC-4	670.7	123.1	651.8	22.1	656.0	32.3	97.18	Concordant
19-GC-4	660.3	144.4	654.1	23.9	655.5	36.9	99.06	Concordant
19-GC-4	741.6	156.5	657.6	27.2	676.9	41.7	88.67	Concordant
19-GC-4	646.3	113.5	658.8	20.7	656.0	29.8	101.93	Concordant
19-GC-4	581.8	170.5	660.0	26.6	642.5	41.6	113.44	>5% revdisc
19-GC-4	704.9	47.9	660.5	12.6	670.7	14.8	93.70	Concordant
19-GC-4	674.1	111.2	661.1	21.1	664.1	29.9	98.07	Concordant
19-GC-4	578.1	157.4	663.4	24.4	644.4	38.4	114.76	>5% revdisc
19-GC-4	718.3	81.4	665.2	17.7	677.4	23.3	92.61	Concordant
19-GC-4	708.2	76.0	671.0	17.3	679.6	22.1	94.75	Concordant
19-GC-4	574.5	175.2	671.0	26.5	649.3	42.5	116.80	>5% revdisc
19-GC-4	691.3	215.5	671.0	32.1	675.7	54.2	97.06	Concordant
19-GC-4	639.2	118.3	680.3	22.0	670.8	31.4	106.43	>5% revdisc
19-GC-4	834.7	288.6	696.5	43.2	730.1	77.0	83.44	Concordant
19-GC-4	1404.2	84.0	1347.1	41.1	1369.3	41.7	95.93	Concordant
19-GC-4	1417.0	72.1	1349.7	35.9	1376.0	36.1	95.25	Concordant
19-GC-4	1375.9	74.2	1364.3	37.8	1368.8	37.2	99.16	Concordant
19-GC-4	1421.3	61.9	1365.9	34.5	1387.6	32.5	96.10	Concordant
19-GC-4	1349.4	59.8	1376.3	33.5	1365.8	31.0	101.99	Concordant
19-GC-4	1419.2	197.1	1391.9	73.3	1402.7	89.7	98.08	Concordant
19-GC-4	1393.4	54.9	1410.0	32.5	1403.4	29.4	101.19	Concordant

19-GC-4	1389.0	64.3	1412.1	36.0	1402.9	33.5	101.66	Concordant
19-GC-4	1404.2	64.2	1430.2	36.1	1419.8	33.6	101.85	Concordant
19-GC-4	1397.7	81.8	1485.7	45.0	1449.9	42.2	106.30	>5% revdisc
19-GC-4	1574.9	66.5	1617.5	42.6	1599.1	37.5	102.70	Concordant
19-GC-4	1590.2	57.1	1525.0	37.5	1552.6	32.9	95.90	Concordant
19-GC-4	1616.6	65.8	1637.0	40.9	1628.1	36.8	101.26	Concordant
19-GC-4	1668.1	95.5	1736.8	61.8	1705.8	54.5	104.12	Concordant
19-GC-4	1673.5	58.8	1626.5	40.8	1647.1	34.9	97.19	Concordant
19-GC-4	1675.3	49.2	1663.5	37.6	1668.7	30.4	99.30	Concordant
19-GC-4	1678.9	69.8	1713.6	48.5	1698.0	41.2	102.07	Concordant
19-GC-4	1684.2	70.0	1632.5	44.5	1655.3	40.1	96.93	Concordant
19-GC-4	1687.8	72.7	1691.8	50.2	1690.0	42.9	100.24	Concordant
19-GC-4	1691.4	50.2	1713.1	38.8	1703.3	31.1	101.28	Concordant
19-GC-4	1694.9	54.3	1666.0	40.0	1678.8	33.1	98.29	Concordant
19-GC-4	1709.1	48.0	1666.5	37.5	1685.4	30.2	97.51	Concordant
19-GC-4	1709.1	48.1	1678.9	39.2	1692.3	30.9	98.23	Concordant
19-GC-4	1712.6	38.3	1682.4	30.9	1695.9	24.4	98.24	Concordant
19-GC-4	1719.6	54.9	1724.4	42.2	1722.2	34.0	100.28	Concordant
19-GC-4	1719.6	61.5	1721.5	45.1	1720.6	37.4	100.11	Concordant
19-GC-4	1721.3	52.3	1675.9	40.7	1696.2	32.9	97.36	Concordant
19-GC-4	1723.0	48.0	1693.8	39.1	1706.9	30.8	98.31	Concordant
19-GC-4	1726.5	45.7	1711.1	37.2	1718.1	29.2	99.11	Concordant
19-GC-4	1728.3	40.1	1755.5	32.4	1743.1	25.4	101.57	Concordant
19-GC-4	1733.5	37.7	1735.8	43.1	1734.7	29.3	100.13	Concordant
19-GC-4	1740.4	34.7	1741.2	31.6	1740.8	23.5	100.05	Concordant
19-GC-4	1742.1	49.8	1767.7	41.9	1756.0	32.3	101.47	Concordant
19-GC-4	1747.2	47.5	1690.8	37.4	1716.2	30.1	96.77	Concordant
19-GC-4	1747.2	78.2	1734.8	51.4	1740.4	45.6	99.29	Concordant
19-GC-4	1748.9	32.5	1725.9	29.6	1736.4	22.1	98.68	Concordant
19-GC-4	1748.9	55.0	1757.4	42.0	1753.5	34.1	100.49	Concordant
19-GC-4	1752.4	53.0	1754.0	41.1	1753.2	33.1	100.09	Concordant
19-GC-4	1752.4	28.3	1724.4	24.0	1737.1	18.5	98.40	Concordant

19-GC-4	1754.1	58.9	1747.1	45.7	1750.3	36.9	99.60	Concordant
19-GC-4	1755.8	34.9	1795.1	32.6	1777.0	23.8	102.24	Concordant
19-GC-4	1755.8	67.8	1778.0	49.3	1767.8	41.1	101.26	Concordant
19-GC-4	1759.2	34.0	1718.5	31.2	1736.9	23.2	97.69	Concordant
19-GC-4	1760.9	47.8	1742.7	40.1	1751.0	31.1	98.97	Concordant
19-GC-4	1760.9	56.0	1770.2	56.2	1765.9	40.1	100.53	Concordant
19-GC-4	1760.9	58.2	1777.5	43.9	1769.9	35.9	100.94	Concordant
19-GC-4	1762.6	31.1	1746.6	28.7	1753.9	21.2	99.09	Concordant
19-GC-4	1762.6	98.8	1760.4	65.5	1761.4	57.9	99.88	Concordant
19-GC-4	1764.3	32.6	1763.8	31.3	1764.0	22.7	99.97	Concordant
19-GC-4	1764.3	54.4	1727.9	42.5	1744.4	34.3	97.94	Concordant
19-GC-4	1765.9	48.4	1708.1	37.8	1734.3	30.6	96.73	Concordant
19-GC-4	1767.6	108.4	1833.5	71.7	1802.9	63.2	103.73	Concordant
19-GC-4	1767.6	66.1	1724.0	48.2	1743.8	40.4	97.53	Concordant
19-GC-4	1767.6	47.0	1753.0	38.0	1759.7	30.0	99.17	Concordant
19-GC-4	1769.3	47.7	1757.4	40.1	1762.9	31.0	99.33	Concordant
19-GC-4	1776.1	51.4	1736.3	40.6	1754.4	32.6	97.76	Concordant
19-GC-4	1777.7	64.5	1735.3	47.2	1754.6	39.5	97.61	Concordant
19-GC-4	1777.7	39.3	1753.5	32.9	1764.6	25.5	98.64	Concordant
19-GC-4	1777.7	55.7	1754.5	44.7	1765.1	35.5	98.69	Concordant
19-GC-4	1779.4	68.9	1745.1	51.5	1760.8	42.6	98.07	Concordant
19-GC-4	1782.8	83.1	1699.7	55.6	1737.3	49.2	95.34	Concordant
19-GC-4	1786.1	32.9	1748.6	30.7	1765.7	22.7	97.90	Concordant
19-GC-4	1786.1	30.5	1793.6	29.1	1790.2	21.2	100.42	Concordant
19-GC-4	1786.1	47.5	1787.3	41.5	1786.7	31.5	100.07	Concordant
19-GC-4	1786.1	45.1	1747.6	39.0	1765.2	29.9	97.84	Concordant
19-GC-4	1786.1	48.5	1741.7	39.2	1762.0	31.1	97.51	Concordant
19-GC-4	1787.8	80.9	1743.2	57.7	1763.5	49.1	97.51	Concordant
19-GC-4	1789.4	63.1	1776.5	47.4	1782.5	39.0	99.28	Concordant
19-GC-4	1794.4	68.7	1780.4	51.2	1786.9	42.4	99.22	Concordant
19-GC-4	1796.1	31.8	1794.1	33.2	1795.0	23.3	99.89	Concordant
19-GC-4	1796.1	112.4	1748.1	68.6	1770.1	64.2	97.33	Concordant

19-GC-4	1797.7	37.0	1783.9	34.3	1790.3	25.3	99.23	Concordant
19-GC-4	1797.7	53.1	1817.5	42.9	1808.3	33.8	101.10	Concordant
19-GC-4	1799.4	95.0	1804.9	65.4	1802.3	56.6	100.31	Concordant
19-GC-4	1801.1	38.1	1757.9	35.2	1777.7	26.2	97.60	Concordant
19-GC-4	1802.7	46.3	1761.3	37.1	1780.4	29.6	97.70	Concordant
19-GC-4	1804.4	48.7	1836.9	43.8	1821.7	32.7	101.80	Concordant
19-GC-4	1807.7	46.9	1770.2	40.3	1787.4	31.0	97.93	Concordant
19-GC-4	1810.9	48.3	1845.6	42.1	1829.4	31.8	101.92	Concordant
19-GC-4	1815.9	42.3	1844.7	38.5	1831.2	28.5	101.59	Concordant
19-GC-4	1819.1	32.9	1792.7	30.3	1804.9	22.5	98.55	Concordant
19-GC-4	1824.0	44.1	1820.4	40.9	1822.1	30.2	99.80	Concordant
19-GC-4	1825.6	38.5	1784.4	36.1	1803.5	26.6	97.74	Concordant
19-GC-4	1825.6	49.4	1764.3	41.0	1792.6	32.2	96.64	Concordant
19-GC-4	1827.3	50.1	1850.0	42.5	1839.3	32.7	101.24	Concordant
19-GC-4	1830.5	91.1	1833.5	63.8	1832.1	54.8	100.16	Concordant
19-GC-4	1838.6	95.1	1799.5	65.6	1817.7	57.2	97.87	Concordant
19-GC-4	1841.8	46.8	1796.6	41.4	1817.6	31.5	97.55	Concordant
19-GC-4	1845.0	31.0	1812.2	30.1	1827.5	21.8	98.22	Concordant
19-GC-4	1956.2	45.0	1920.7	45.5	1937.9	32.4	98.19	Concordant
19-GC-4	1979.8	57.2	1925.0	53.1	1951.6	39.5	97.23	Concordant
19-GC-4	2361.8	71.3	2341.7	79.3	2352.4	53.8	99.15	Concordant
19-GC-4	2423.6	37.1	2375.2	52.1	2401.4	31.7	98.00	Concordant
19-GC-4	2438.7	16.4	2456.8	30.8	2446.9	16.6	100.74	Concordant
19-GC-4	2445.1	45.2	2377.4	58.9	2414.0	37.1	97.23	Concordant
19-GC-4	2455.7	44.4	2404.1	59.4	2432.1	36.8	97.90	Concordant
19-GC-4	2510.6	22.3	2528.6	38.7	2518.6	21.3	100.72	Concordant
19-GC-4	2539.8	22.7	2507.2	41.9	2525.3	22.8	98.72	Concordant
19-GC-4	2577.2	30.0	2549.0	49.0	2564.7	27.6	98.91	Concordant
19-GC-4	2579.1	45.9	2588.0	66.9	2583.0	39.4	100.35	Concordant
19-GC-4	2579.1	42.9	2553.3	71.9	2567.8	40.3	99.00	Concordant
19-GC-4	2586.9	27.2	2553.3	47.1	2572.1	26.0	98.70	Concordant
19-GC-4	2590.7	86.3	2483.6	99.0	2543.0	66.7	95.87	Concordant

19-GC-4	2595.5	32.9	2531.6	63.1	2567.3	34.0	97.54	Concordant
19-GC-4	2598.4	47.8	2639.5	72.4	2616.3	41.8	101.58	Concordant
19-GC-4	2637.1	42.6	2711.9	68.0	2669.3	38.1	102.84	Concordant
19-GC-4	2639.0	42.0	2609.5	64.2	2626.1	37.1	98.88	Concordant
19-GC-4	2642.7	33.5	2677.9	53.9	2657.9	30.2	101.33	Concordant
19-GC-4	2642.7	45.8	2566.3	65.6	2609.2	39.3	97.11	Concordant
19-GC-4	2642.7	25.0	2602.6	44.3	2625.2	24.2	98.48	Concordant
19-GC-4	2663.0	41.8	2631.0	63.5	2649.1	36.8	98.80	Concordant
19-GC-4	2679.3	45.9	2665.2	68.7	2673.2	39.9	99.47	Concordant
19-GC-4	2681.2	43.3	2703.4	66.6	2690.7	38.0	100.83	Concordant
19-GC-4	2687.5	26.4	2692.4	48.2	2689.6	25.8	100.18	Concordant
19-GC-4	2692.8	39.3	2690.7	68.7	2691.9	37.4	99.92	Concordant
19-GC-4	2698.2	40.1	2673.7	61.1	2687.7	35.2	99.09	Concordant
19-GC-4	2704.4	75.5	2770.9	99.7	2732.6	61.0	102.46	Concordant
19-GC-4	2709.8	19.2	2699.2	39.6	2705.2	20.3	99.61	Concordant
19-GC-4	2716.8	41.8	2669.4	67.1	2696.5	38.0	98.26	Concordant
19-GC-4	2732.6	42.7	2783.4	70.4	2754.1	38.8	101.86	Concordant
19-GC-4	2740.4	38.7	2682.2	60.0	2715.5	34.4	97.88	Concordant
19-GC-4	2744.8	41.8	2800.2	72.1	2768.1	39.0	102.02	Concordant
19-GC-4	2776.4	31.7	2787.6	59.2	2781.1	31.1	100.40	Concordant
19-GC-4	2804.0	31.5	2754.9	55.5	2783.3	30.0	98.25	Concordant
19-GC-4	2831.9	38.3	2804.3	67.9	2820.4	36.5	99.03	Concordant
19-GC-4	2868.8	39.4	2800.2	75.1	2840.2	39.5	97.61	Concordant
19-GC-4	2920.9	27.9	2879.0	54.7	2903.7	28.2	98.57	Concordant
19-GC-4	2946.6	28.2	2911.9	60.9	2932.5	30.3	98.82	Concordant
19-GC-4	3045.1	24.6	3062.0	58.2	3051.8	27.6	100.55	Concordant
19-GC-4	3183.5	43.8	3105.9	84.7	3153.2	43.3	97.56	Concordant
19-GC-4	3197.4	24.4	3153.5	63.7	3180.4	29.2	98.63	Concordant
19-GC-4	3244.9	25.5	3216.5	65.6	3234.0	30.0	99.12	Concordant
19-GC-4	3272.5	20.8	3216.5	55.3	3251.1	25.1	98.29	Concordant
19-GC-4	3315.3	16.1	3317.4	47.4	3316.1	20.6	100.06	Concordant
19-GC-4	3330.8	18.5	3321.3	48.7	3327.2	21.8	99.71	Concordant

19-GC-4	3343.8	16.0	3298.5	47.0	3326.8	20.5	98.65	Concordant
19-GC-4	701.5	58.2	638.4	13.7	652.5	17.0	91.00	Concordant
19-GC-4	837.8	123.4	654.7	22.0	697.5	34.4	78.15	discorndant
19-GC-4	1442.4	56.8	1360.1	32.5	1392.5	30.3	94.29	Concordant
19-GC-4	1487.9	74.2	1381.0	40.1	1423.6	39.0	92.82	Concordant
19-GC-4	1347.1	64.4	1423.5	36.1	1393.2	33.2	105.67	>5% revdisc
19-GC-4	1547.8	74.7	1638.0	47.6	1598.9	41.7	105.83	>5% revdisc
19-GC-4	1684.2	57.2	1781.9	45.5	1737.4	35.6	105.80	>5% revdisc
19-GC-4	1694.9	39.3	1594.4	30.5	1638.2	24.8	94.07	Concordant
19-GC-4	1694.9	78.2	1819.0	53.8	1761.9	45.7	107.32	>5% revdisc
19-GC-4	1716.1	56.1	1623.5	39.1	1664.3	33.6	94.60	Concordant
19-GC-4	1721.3	100.2	1857.7	66.7	1794.3	57.9	107.92	>5% revdisc
19-GC-4	1721.3	56.8	1646.0	43.1	1679.4	35.4	95.63	Concordant
19-GC-4	1723.0	35.5	1652.5	30.5	1683.8	23.5	95.91	Concordant
19-GC-4	1740.4	37.8	1673.4	32.2	1703.4	25.0	96.15	Concordant
19-GC-4	1742.1	27.1	1689.8	26.0	1713.3	19.0	97.00	Concordant
19-GC-4	1750.6	42.0	1690.8	34.5	1717.7	27.2	96.58	Concordant
19-GC-4	1759.2	25.9	1723.0	25.8	1739.4	18.5	97.94	Concordant
19-GC-4	1760.9	45.2	1682.4	37.2	1717.6	29.3	95.54	Concordant
19-GC-4	1762.6	42.1	1819.5	36.6	1793.1	27.6	103.23	Concordant
19-GC-4	1764.3	40.4	1701.2	34.1	1729.7	26.5	96.42	Concordant
19-GC-4	1765.9	36.6	1704.2	31.6	1732.1	24.3	96.51	Concordant
19-GC-4	1767.6	37.5	1674.4	32.5	1716.2	25.1	94.73	Concordant
19-GC-4	1779.4	27.0	1721.5	26.8	1747.8	19.3	96.75	Concordant
19-GC-4	1782.8	38.3	1724.0	33.1	1750.7	25.4	96.70	Concordant
19-GC-4	1789.4	42.5	1661.5	35.3	1718.8	27.9	92.85	Concordant
19-GC-4	1791.1	51.5	1725.9	43.3	1755.6	33.8	96.36	Concordant
19-GC-4	1797.7	30.6	1739.7	29.1	1766.2	21.4	96.77	Concordant
19-GC-4	1799.4	29.1	1734.8	27.6	1764.3	20.3	96.41	Concordant
19-GC-4	1802.7	34.5	1734.8	31.7	1765.8	23.7	96.23	Concordant
19-GC-4	1804.4	25.2	1750.0	23.4	1774.9	17.4	96.99	Concordant
19-GC-4	1804.4	46.1	1700.7	37.4	1747.7	29.9	94.25	Concordant

19-GC-4	1809.3	29.4	1734.3	27.0	1768.6	20.2	95.85	Concordant
19-GC-4	1815.9	38.5	1728.4	35.6	1768.3	26.6	95.18	Concordant
19-GC-4	1819.1	60.9	1712.6	45.4	1761.1	37.9	94.15	Concordant
19-GC-4	1820.8	48.9	1921.7	46.3	1873.6	33.3	105.54	>5% revdisc
19-GC-4	1825.6	39.0	1750.5	36.7	1785.1	27.2	95.89	Concordant
19-GC-4	1825.6	38.0	1718.0	34.1	1767.1	26.0	94.11	Concordant
19-GC-4	1828.9	37.8	1768.7	35.2	1796.5	26.2	96.71	Concordant
19-GC-4	1840.2	35.7	1732.3	33.2	1781.8	24.9	94.14	Concordant
19-GC-4	1846.6	31.7	1798.0	31.1	1820.6	22.5	97.37	Concordant
19-GC-4	1846.6	33.6	1751.0	32.8	1795.1	24.0	94.82	Concordant
19-GC-4	1873.6	78.5	1735.8	55.8	1799.2	48.3	92.65	Concordant
19-GC-4	2493.2	30.6	2435.1	47.2	2466.9	27.5	97.67	Concordant
19-GC-4	2517.7	20.9	2472.6	36.3	2497.4	20.2	98.21	Concordant
19-GC-4	2562.6	21.6	2479.2	38.9	2525.3	21.4	96.75	Concordant
19-GC-4	2577.2	22.2	2529.4	40.2	2556.0	21.9	98.15	Concordant
19-GC-4	2588.8	22.9	2521.6	39.9	2559.0	22.1	97.40	Concordant
19-GC-4	2597.5	37.2	2531.6	55.0	2568.3	32.5	97.46	Concordant
19-GC-4	2639.9	19.3	2583.2	37.8	2615.1	20.1	97.85	Concordant
19-GC-4	2692.0	41.8	2570.7	62.9	2639.1	37.0	95.49	Concordant
19-GC-4	2716.8	41.7	2626.7	68.1	2677.9	38.5	96.68	Concordant
19-GC-4	2805.6	24.1	2740.2	47.2	2778.0	24.6	97.67	Concordant
19-GC-4	2919.4	23.5	2981.3	52.9	2944.5	25.6	102.12	Concordant
19-GC-4	3004.6	29.2	2895.5	69.6	2960.3	33.9	96.37	Concordant
19-GC-4	3252.1	18.9	3198.1	47.9	3231.4	22.0	98.34	Concordant
19-GC-4	1703.8	35.7	1083.3	37.4	1310.2	31.4	63.58	discorndant
19-GC-4	2789.0	20.4	2469.5	40.1	2648.9	22.0	88.54	Concordant
19-GC-4	1735.2	25.4	1642.5	24.6	1683.6	18.1	94.66	Concordant
19-GC-4	1736.9	37.1	1581.8	30.8	1649.5	24.4	91.07	Concordant
19-GC-4	1675.3	33.3	816.3	35.6	1085.8	33.7	48.73	discorndant
19-GC-4	2610.8	20.4	2505.5	38.2	2564.1	20.8	95.97	Concordant
19-GC-4	1887.7	24.9	950.7	18.7	1280.8	18.5	50.36	discorndant
19-GC-4	2676.6	29.2	2552.9	51.3	2622.5	28.4	95.38	Concordant

19-GC-4	2256.6	28.4	888.6	19.9	1382.4	22.1	39.38	discorndant
19-GC-4	2586.9	23.3	1911.6	36.1	2257.1	23.6	73.90	discorndant
19-GC-4	2784.0	22.5	2888.9	49.0	2827.5	24.1	103.77	Concordant
19-GC-4	1752.4	21.8	1411.6	23.0	1553.6	17.4	80.55	Concordant
19-GC-4	2512.6	21.0	1484.7	51.6	1962.7	36.0	59.09	discorndant
19-GC-4	1762.6	33.2	1649.0	29.8	1699.6	22.7	93.55	Concordant
19-GC-4	2151.0	83.8	1266.0	35.6	1636.1	46.5	58.86	discorndant
19-GC-4	2882.2	72.9	2648.1	98.4	2782.9	61.4	91.88	Concordant
19-GC-4	2800.7	20.3	2699.2	42.6	2757.6	21.9	96.38	Concordant
19-GC-4	1862.5	34.4	1631.5	31.6	1735.2	24.3	87.60	Concordant
19-GC-4	1807.7	78.1	1593.4	53.8	1688.0	47.6	88.15	Concordant
19-GC-4	1736.9	24.9	1288.2	20.4	1467.3	17.2	74.17	discorndant
19-GC-4	2637.1	22.9	1823.8	39.2	2235.4	25.8	69.16	discorndant
19-GC-4	895.7	57.7	555.5	13.4	627.4	17.6	62.02	discorndant
19-GC-4	3172.0	34.1	1686.3	73.3	2455.3	50.7	53.16	discorndant
19-GC-4	2049.9	31.0	1057.7	20.7	1435.1	21.3	51.60	discorndant
19-GC-4	1721.3	43.3	1329.3	36.6	1487.6	30.3	77.23	discorndant
19-GC-4	1344.9	43.2	750.1	16.2	917.4	19.4	55.77	discorndant
19-GC-4	1787.8	47.5	1361.2	33.0	1536.9	29.8	76.14	discorndant
19-GC-4	1693.2	37.6	1563.6	31.4	1619.6	24.8	92.35	Concordant
19-GC-4	2708.9	20.3	2382.8	38.2	2563.0	21.4	87.96	Concordant
19-GC-4	2635.3	28.5	1818.0	40.5	2231.1	28.0	68.99	discorndant
19-GC-4	2660.2	34.9	2502.8	54.4	2590.7	31.7	94.08	Concordant
19-GC-4	1696.7	37.5	1267.1	25.4	1436.3	23.2	74.68	discorndant
19-GC-4	2575.3	19.7	1934.6	37.2	2263.3	23.0	75.12	discorndant
19-GC-4	2687.5	26.7	2570.2	46.4	2636.3	25.8	95.64	Concordant
19-GC-4	1755.8	41.4	1524.5	31.6	1624.2	26.5	86.83	Concordant
19-GC-4	1791.1	30.3	1358.6	25.2	1536.6	21.1	75.85	discorndant
19-GC-4	2716.0	51.9	1770.2	91.8	2247.5	62.0	65.18	discorndant
19-GC-4	1787.8	24.2	1607.5	26.1	1687.2	18.7	89.91	Concordant
19-GC-4	1786.1	32.6	1644.5	29.2	1707.7	22.4	92.07	Concordant
19-GC-4	1648.1	29.0	1341.3	23.0	1464.5	19.2	81.38	Concordant

19-GC-4	2503.5	27.2	1881.9	106.2	2195.9	61.6	75.17	discorndant
19-GC-4	1738.6	32.3	1433.3	38.2	1561.2	27.8	82.44	Concordant
19-GC-4	2606.0	20.6	2079.1	31.5	2356.5	19.9	79.78	discorndant
19-GC-4	2875.1	21.3	2466.0	77.3	2697.1	38.2	85.77	Concordant
19-GC-4	1742.1	31.5	1522.0	30.8	1616.6	23.2	87.37	Concordant
19-GC-4	1875.2	35.2	743.2	18.1	1092.4	21.8	39.63	discorndant
19-GC-4	2607.0	41.0	2101.9	52.2	2368.7	35.3	80.63	Concordant
~~19-GC-4~~	~~1985.7~~	~~105.7~~	~~1755.5~~	~~66.1~~	~~1863.2~~	~~63.0~~	88.41	Concordant
19-GC-4	1856.2	27.3	1458.6	27.5	1628.8	21.1	78.58	discorndant
19-GC-4	2603.2	40.6	810.6	22.5	1463.8	29.9	31.14	discorndant
19-GC-4	1616.6	32.9	607.4	10.9	870.5	15.1	37.57	discorndant
19-GC-4	2565.5	23.1	1846.6	33.7	2209.5	22.8	71.98	discorndant
19-GC-4	2879.1	31.4	2413.0	56.9	2674.8	32.6	83.81	Concordant
19-GC-4	2698.2	181.6	1886.7	111.7	2304.2	119.2	69.92	discorndant
19-GC-4	1543.9	39.6	653.6	25.1	892.9	27.3	42.33	discorndant
19-GC-4	1972.5	24.2	1812.6	28.5	1888.3	19.4	91.89	Concordant
19-GC-4	2059.6	32.6	1933.6	35.4	1995.2	24.7	93.88	Concordant
19-GC-4	1764.3	27.0	1433.3	34.6	1572.3	24.8	81.24	Concordant
19-GC-4	1807.7	40.3	1686.3	34.9	1741.2	27.1	93.28	Concordant
19-GC-4	1787.8	31.0	1218.2	50.9	1441.2	38.2	68.14	discorndant
19-GC-4	1807.7	25.5	1475.0	24.7	1617.2	19.0	81.60	Concordant
19-GC-4	2971.9	29.9	2812.7	57.5	2906.3	30.2	94.64	Concordant
19-GC-4	2395.2	38.6	1468.3	40.0	1892.1	32.9	61.30	discorndant
19-GC-4	2676.6	22.5	1872.2	63.5	2284.3	38.1	69.95	discorndant
19-GC-4	2472.5	16.4	2052.9	37.7	2270.4	21.5	83.03	Concordant
19-GC-4	2849.7	30.4	2430.7	52.1	2666.0	30.2	85.30	Concordant
19-GC-4	2837.6	19.3	2364.1	60.8	2627.7	31.2	83.31	Concordant
19-GC-4	1802.7	25.7	1583.8	24.6	1680.2	18.6	87.86	Concordant
19-GC-4	1764.3	29.6	1637.5	27.3	1693.8	20.6	92.81	Concordant
19-GC-4	1553.6	66.4	1289.3	34.5	1392.2	35.0	82.99	Concordant
19-GC-4	1854.6	64.7	1515.4	43.1	1662.9	39.5	81.71	Concordant
19-GC-4	2208.5	39.0	1735.8	35.9	1961.3	28.5	78.60	discorndant

19-GC-4	1764.3	33.0	1671.9	29.0	1713.3	22.2	94.76	Concordant
19-GC-4	2682.1	20.4	2430.3	39.5	2570.0	21.7	90.61	Concordant
19-GC-4	2634.3	32.0	2001.1	61.3	2331.2	37.4	75.96	discorndant
19-GC-4	2642.7	41.9	2373.0	59.4	2521.2	36.7	89.79	Concordant
19-GC-4	2914.8	15.2	2690.7	41.3	2820.6	20.1	92.31	Concordant
19-GC-4	1828.9	24.6	1601.4	24.3	1702.3	18.1	87.56	Concordant
19-GC-4	1728.3	28.9	1558.5	33.0	1632.1	23.3	90.18	Concordant
19-GC-4	2889.2	22.6	2780.5	48.0	2844.0	24.4	96.24	Concordant
19-GC-4	2493.2	29.4	1596.4	45.4	2023.8	32.4	64.03	discorndant
19-GC-4	2466.2	22.4	2255.5	37.6	2367.9	22.0	91.46	Concordant
19-GC-4	1673.5	51.3	1514.4	38.6	1582.0	32.1	90.49	Concordant
19-GC-4	2261.4	60.1	1826.7	49.8	2039.1	41.5	80.78	Concordant
19-GC-4	3470.2	17.8	3198.8	48.5	3368.0	22.1	92.18	Concordant
19-GC-4	2897.8	19.4	2613.8	42.7	2777.0	22.2	90.20	Concordant
19-GC-4	2662.1	50.2	2127.5	63.2	2412.2	43.0	79.92	discorndant
19-GC-4	1883.0	44.1	1739.2	38.8	1805.6	30.0	92.36	Concordant
19-GC-4	1551.7	108.5	868.4	35.4	1085.5	48.3	55.96	discorndant

Table A. 1: *Complete U-Pb isotopic dataset for detrital zircon grains from sample 19-GC-4. Reported parameters include measured isotopic ratios, calculated 206Pb/238U, 207Pb/235U, and 207Pb/206Pb ages (Ma), analytical uncertainties (2σ), and concordance values.*

	Dates							
Sample	$^{207}Pb/^{206}Pb$	$2s_x$ (ABS)	$^{206}Pb/^{238}U$	$2s_x$ (ABS)	$^{207}Pb/^{235}Pb$	$2s_x$ (ABS)	Concordant filter	20% discordant filter, 5% reverse discordant filter
19-GC-5	632.2	152.4	640.1	24.1	638.4	37.7	101.2	Concordant
19-GC-5	691.3	114.6	667.5	21.1	673.0	30.7	96.6	Concordant
19-GC-5	656.8	160.1	669.8	26.7	666.9	41.1	102.0	Concordant
19-GC-5	748.2	184.5	673.9	28.4	691.3	48.0	90.1	Concordant
19-GC-5	1146.9	45.2	1111.1	21.7	1123.2	21.2	96.9	Concordant
19-GC-5	1189.6	129.3	1144.1	43.5	1159.9	53.4	96.2	Concordant
19-GC-5	1182.1	84.0	1164.6	33.1	1170.7	36.6	98.5	Concordant
19-GC-5	1240.7	103.5	1216.0	40.6	1225.0	45.7	98.0	Concordant
19-GC-5	1324.6	81.0	1310.9	38.6	1316.1	39.2	99.0	Concordant
19-GC-5	1340.4	51.1	1326.1	29.8	1331.6	27.0	98.9	Concordant
19-GC-5	1399.8	87.9	1333.5	39.7	1359.2	42.3	95.3	Concordant
19-GC-5	1280.9	130.3	1345.0	52.1	1320.5	58.6	105.0	>5% revdisc
19-GC-5	1280.9	141.7	1376.3	59.1	1339.4	64.6	107.4	>5% revdisc
19-GC-5	1442.4	83.9	1383.6	41.3	1406.9	42.1	95.9	Concordant
19-GC-5	1467.4	75.5	1406.4	38.7	1430.9	38.6	95.8	Concordant
19-GC-5	1425.5	59.5	1432.8	34.2	1429.9	31.5	100.5	Concordant
19-GC-5	1389.0	88.1	1455.0	44.1	1428.4	43.8	104.8	Concordant
19-GC-5	1461.2	65.9	1472.9	37.0	1468.1	34.7	100.8	Concordant
19-GC-5	1595.9	56.7	1575.2	37.8	1584.1	32.8	98.7	Concordant
19-GC-5	1614.8	63.1	1572.7	41.6	1590.8	36.4	97.4	Concordant
19-GC-5	1620.4	61.0	1675.9	42.5	1651.4	35.8	103.4	Concordant
19-GC-5	1637.0	62.5	1705.2	44.4	1674.8	37.0	104.2	Concordant
19-GC-5	1655.4	43.3	1703.7	34.4	1682.1	27.1	102.9	Concordant
19-GC-5	1659.0	42.1	1652.5	33.5	1655.4	26.5	99.6	Concordant
19-GC-5	1660.8	36.3	1682.4	30.6	1672.8	23.5	101.3	Concordant
19-GC-5	1660.8	44.2	1698.7	35.8	1681.8	27.9	102.3	Concordant

19-GC-5	1664.5	80.9	1670.4	52.4	1667.8	46.4	100.4	Concordant
19-GC-5	1666.3	35.0	1696.8	30.2	1683.2	22.9	101.8	Concordant
19-GC-5	1669.9	70.5	1708.1	48.6	1691.0	41.4	102.3	Concordant
19-GC-5	1669.9	50.6	1716.1	39.2	1695.4	31.3	102.8	Concordant
19-GC-5	1677.1	49.7	1663.5	35.7	1669.5	29.9	99.2	Concordant
19-GC-5	1678.9	35.8	1657.0	30.3	1666.7	23.3	98.7	Concordant
19-GC-5	1678.9	104.7	1750.5	63.0	1718.1	58.3	104.3	Concordant
19-GC-5	1682.5	49.2	1684.9	37.5	1683.8	30.3	100.1	Concordant
19-GC-5	1689.6	31.2	1666.5	26.7	1676.7	20.5	98.6	Concordant
19-GC-5	1689.6	41.5	1678.9	33.9	1683.7	26.5	99.4	Concordant
19-GC-5	1694.9	61.7	1688.8	44.5	1691.6	37.2	99.6	Concordant
19-GC-5	1703.8	49.8	1651.0	36.9	1674.4	30.5	96.9	Concordant
19-GC-5	1703.8	75.3	1724.9	52.3	1715.4	44.6	101.2	Concordant
19-GC-5	1707.3	58.8	1666.5	43.1	1684.6	35.9	97.6	Concordant
19-GC-5	1710.8	45.2	1686.3	38.8	1697.3	29.8	98.6	Concordant
19-GC-5	1714.3	63.9	1729.9	46.0	1722.8	38.4	100.9	Concordant
19-GC-5	1717.8	53.5	1736.8	40.9	1728.2	33.1	101.1	Concordant
19-GC-5	1723.0	63.9	1682.4	45.3	1700.6	38.4	97.6	Concordant
19-GC-5	1726.5	22.7	1704.2	23.2	1714.2	16.5	98.7	Concordant
19-GC-5	1728.3	42.6	1686.3	35.8	1705.1	27.8	97.6	Concordant
19-GC-5	1730.0	59.0	1719.0	43.7	1724.0	36.1	99.4	Concordant
19-GC-5	1731.7	33.3	1732.8	31.2	1732.3	22.9	100.1	Concordant
19-GC-5	1731.7	49.5	1753.0	40.4	1743.3	31.6	101.2	Concordant
19-GC-5	1731.7	53.7	1792.7	42.5	1764.7	33.6	103.5	Concordant
19-GC-5	1733.5	51.8	1719.0	40.9	1725.5	32.7	99.2	Concordant
19-GC-5	1733.5	50.8	1796.6	43.6	1767.6	33.1	103.6	Concordant
19-GC-5	1738.6	37.9	1739.2	33.6	1739.0	25.3	100.0	Concordant
19-GC-5	1738.6	49.6	1737.8	39.7	1738.2	31.4	100.0	Concordant
19-GC-5	1740.4	28.5	1752.5	26.6	1747.0	19.5	100.7	Concordant
19-GC-5	1740.4	36.1	1708.6	30.5	1722.9	23.6	98.2	Concordant

19-GC-5	1742.1	27.4	1774.6	27.3	1759.7	19.4	101.9	Concordant
19-GC-5	1743.8	30.8	1766.2	30.0	1756.0	21.5	101.3	Concordant
19-GC-5	1743.8	69.3	1712.1	46.4	1726.4	40.7	98.2	Concordant
19-GC-5	1743.8	34.2	1749.1	31.5	1746.7	23.3	100.3	Concordant
19-GC-5	1743.8	33.9	1772.1	30.8	1759.2	22.8	101.6	Concordant
19-GC-5	1743.8	23.4	1774.1	25.2	1760.2	17.4	101.7	Concordant
19-GC-5	1743.8	59.4	1782.9	44.3	1765.0	36.3	102.2	Concordant
19-GC-5	1743.8	40.7	1750.0	35.2	1747.2	26.8	100.4	Concordant
19-GC-5	1743.8	38.4	1703.2	34.0	1721.5	25.7	97.7	Concordant
19-GC-5	1745.5	25.9	1733.3	25.7	1738.9	18.4	99.3	Concordant
19-GC-5	1748.9	29.9	1730.4	28.5	1738.8	20.8	98.9	Concordant
19-GC-5	1750.6	54.2	1740.7	41.6	1745.2	33.7	99.4	Concordant
19-GC-5	1750.6	80.8	1750.5	54.2	1750.6	47.5	100.0	Concordant
19-GC-5	1752.4	30.6	1723.0	29.0	1736.3	21.2	98.3	Concordant
19-GC-5	1752.4	42.8	1764.8	37.2	1759.1	28.2	100.7	Concordant
19-GC-5	1752.4	35.3	1763.8	32.1	1758.6	23.9	100.7	Concordant
19-GC-5	1752.4	43.8	1747.1	39.0	1749.5	29.3	99.7	Concordant
19-GC-5	1754.1	35.0	1733.3	32.6	1742.7	24.1	98.8	Concordant
19-GC-5	1755.8	47.4	1714.6	38.2	1733.2	30.3	97.7	Concordant
19-GC-5	1755.8	36.0	1771.6	31.8	1764.4	23.9	100.9	Concordant
19-GC-5	1755.8	48.0	1768.2	38.8	1762.5	30.5	100.7	Concordant
19-GC-5	1757.5	41.7	1764.8	35.8	1761.4	27.3	100.4	Concordant
19-GC-5	1757.5	55.0	1791.7	43.5	1775.9	34.5	101.9	Concordant
19-GC-5	1759.2	26.7	1746.6	29.2	1752.3	20.1	99.3	Concordant
19-GC-5	1759.2	42.3	1755.5	36.7	1757.1	27.9	99.8	Concordant
19-GC-5	1759.2	64.1	1792.2	49.1	1777.0	39.7	101.9	Concordant
19-GC-5	1760.9	26.8	1729.9	26.6	1743.9	19.1	98.2	Concordant
19-GC-5	1760.9	33.9	1750.0	31.3	1755.0	23.2	99.4	Concordant
19-GC-5	1762.6	31.6	1739.7	31.0	1750.1	22.4	98.7	Concordant
19-GC-5	1764.3	41.2	1724.0	35.0	1742.2	27.1	97.7	Concordant

19-GC-5	1764.3	36.7	1767.7	33.2	1766.1	24.7	100.2	Concordant
19-GC-5	1764.3	21.7	1755.9	22.7	1759.7	15.9	99.5	Concordant
19-GC-5	1765.9	39.1	1787.8	36.7	1777.7	26.8	101.2	Concordant
19-GC-5	1765.9	44.8	1768.7	37.9	1767.4	29.2	100.2	Concordant
19-GC-5	1767.6	30.1	1747.1	29.1	1756.5	21.1	98.8	Concordant
19-GC-5	1767.6	53.6	1806.3	43.6	1788.4	34.1	102.2	Concordant
19-GC-5	1769.3	31.3	1764.3	29.8	1766.6	21.7	99.7	Concordant
19-GC-5	1769.3	83.6	1778.5	58.0	1774.3	49.8	100.5	Concordant
19-GC-5	1771.0	31.6	1768.2	28.2	1769.5	21.1	99.8	Concordant
19-GC-5	1771.0	32.5	1800.0	30.5	1786.6	22.2	101.6	Concordant
19-GC-5	1771.0	57.1	1762.3	44.7	1766.3	35.9	99.5	Concordant
19-GC-5	1776.1	33.9	1734.8	31.0	1753.6	23.2	97.7	Concordant
19-GC-5	1777.7	63.1	1781.9	47.3	1780.0	38.9	100.2	Concordant
19-GC-5	1777.7	36.0	1744.6	33.1	1759.8	24.6	98.1	Concordant
19-GC-5	1781.1	37.0	1828.7	34.8	1806.5	25.3	102.7	Concordant
19-GC-5	1781.1	31.9	1774.1	33.2	1777.3	23.3	99.6	Concordant
19-GC-5	1781.1	35.3	1801.0	33.4	1791.8	24.3	101.1	Concordant
19-GC-5	1782.8	91.3	1823.3	62.3	1804.5	54.0	102.3	Concordant
19-GC-5	1784.4	46.9	1745.6	42.8	1763.4	32.0	97.8	Concordant
19-GC-5	1784.4	33.2	1772.1	31.7	1777.8	23.1	99.3	Concordant
19-GC-5	1784.4	34.9	1755.5	31.7	1768.7	23.7	98.4	Concordant
19-GC-5	1786.1	44.4	1774.6	36.2	1779.9	28.5	99.4	Concordant
19-GC-5	1787.8	39.1	1818.5	34.3	1804.2	25.8	101.7	Concordant
19-GC-5	1787.8	62.5	1816.0	49.7	1802.9	39.5	101.6	Concordant
19-GC-5	1789.4	25.0	1773.6	27.1	1780.9	18.8	99.1	Concordant
19-GC-5	1789.4	52.0	1780.4	40.9	1784.6	32.8	99.5	Concordant
19-GC-5	1792.8	40.3	1761.3	34.5	1775.8	26.5	98.2	Concordant
19-GC-5	1794.4	34.7	1752.5	32.0	1771.7	23.8	97.7	Concordant
19-GC-5	1794.4	41.7	1828.7	37.2	1812.7	27.8	101.9	Concordant
19-GC-5	1794.4	53.6	1774.1	43.8	1783.5	34.5	98.9	Concordant

19-GC-5	1796.1	40.5	1776.5	36.0	1785.5	27.2	98.9	Concordant
19-GC-5	1797.7	126.9	1784.8	76.7	1790.8	72.2	99.3	Concordant
19-GC-5	1799.4	34.4	1803.9	32.7	1801.8	23.8	100.3	Concordant
19-GC-5	1806.0	59.3	1745.6	45.5	1773.3	37.2	96.7	Concordant
19-GC-5	1807.7	78.6	1733.8	54.3	1767.6	47.3	95.9	Concordant
19-GC-5	1812.6	46.5	1817.0	40.4	1815.0	30.7	100.2	Concordant
19-GC-5	1814.2	82.8	1782.9	57.9	1797.4	49.9	98.3	Concordant
19-GC-5	1817.5	38.4	1779.0	35.6	1796.8	26.4	97.9	Concordant
19-GC-5	1819.1	95.7	1760.4	65.3	1787.4	57.3	96.8	Concordant
19-GC-5	1824.0	52.8	1831.1	45.0	1827.8	34.6	100.4	Concordant
19-GC-5	1828.9	44.7	1870.3	38.3	1850.8	29.2	102.3	Concordant
19-GC-5	1835.4	68.1	1814.1	52.4	1824.0	42.7	98.8	Concordant
19-GC-5	1840.2	58.6	1786.3	43.9	1811.3	36.4	97.1	Concordant
19-GC-5	1845.0	50.1	1882.8	44.1	1864.9	33.2	102.0	Concordant
19-GC-5	1845.0	33.9	1801.9	33.4	1822.0	24.1	97.7	Concordant
19-GC-5	1846.6	51.5	1818.0	42.7	1831.4	33.4	98.5	Concordant
19-GC-5	1849.8	54.3	1823.8	43.1	1836.0	34.6	98.6	Concordant
19-GC-5	1893.9	103.9	1813.1	70.0	1851.0	62.4	95.7	Concordant
19-GC-5	1906.3	105.4	1814.1	73.9	1857.4	64.4	95.2	Concordant
19-GC-5	1995.9	26.5	1970.8	30.7	1983.0	20.5	98.7	Concordant
19-GC-5	2055.5	42.7	2001.1	43.4	2028.0	30.9	97.4	Concordant
19-GC-5	2055.5	92.3	2020.0	74.6	2037.6	60.0	98.3	Concordant
19-GC-5	2435.4	26.7	2431.6	40.0	2433.7	23.5	99.8	Concordant
19-GC-5	2454.6	33.4	2509.8	53.4	2479.4	30.3	102.2	Concordant
19-GC-5	2508.6	51.6	2509.8	68.6	2509.1	42.3	100.0	Concordant
19-GC-5	2512.6	17.5	2501.1	51.2	2507.5	25.1	99.5	Concordant
19-GC-5	2572.3	16.4	2562.0	33.6	2567.8	17.5	99.6	Concordant
19-GC-5	2601.3	28.7	2631.0	56.5	2614.2	29.6	101.1	Concordant
19-GC-5	2633.4	21.5	2659.2	40.8	2644.6	21.5	101.0	Concordant
19-GC-5	2641.8	32.7	2644.7	54.6	2643.0	30.3	100.1	Concordant

19-GC-5	2651.0	19.9	2633.5	40.0	2643.4	20.9	99.3	Concordant
19-GC-5	2651.9	22.1	2660.9	42.3	2655.8	22.3	100.3	Concordant
19-GC-5	2663.9	36.2	2639.5	60.0	2653.3	33.5	99.1	Concordant
19-GC-5	2679.3	28.3	2652.4	48.6	2667.7	26.7	99.0	Concordant
~~19-GC-5~~	~~2702.7~~	~~17.5~~	~~2672.0~~	~~38.3~~	~~2689.5~~	~~19.5~~	98.9	Concordant
19-GC-5	2714.2	44.0	2673.7	66.2	2696.8	38.4	98.5	Concordant
19-GC-5	2768.7	26.8	2804.3	52.9	2783.7	27.2	101.3	Concordant
19-GC-5	2804.0	24.5	2762.5	50.1	2786.5	25.7	98.5	Concordant
19-GC-5	2821.3	41.3	2762.5	67.3	2796.6	37.6	97.9	Concordant
19-GC-5	2832.7	27.0	2829.3	48.2	2831.3	25.7	99.9	Concordant
19-GC-5	2840.8	27.4	2862.5	60.1	2849.8	29.8	100.8	Concordant
19-GC-5	2877.5	22.2	2870.8	46.9	2874.7	23.5	99.8	Concordant
19-GC-5	2884.6	23.6	2934.0	46.1	2904.8	23.5	101.7	Concordant
19-GC-5	2902.5	43.1	2866.6	75.8	2887.7	40.8	98.8	Concordant
19-GC-5	2905.5	20.9	2907.8	48.6	2906.5	23.5	100.1	Concordant
19-GC-5	2921.7	44.5	2940.6	81.3	2929.4	42.7	100.6	Concordant
19-GC-5	2996.0	21.6	3021.8	46.6	3006.3	22.8	100.9	Concordant
19-GC-5	3293.2	31.9	3232.1	78.1	3269.9	36.3	98.1	Concordant
19-GC-5	3294.9	32.8	3302.0	80.1	3297.6	36.9	100.2	Concordant
19-GC-5	3309.5	31.5	3278.8	76.4	3297.9	35.4	99.1	Concordant
19-GC-5	3508.4	26.6	3526.0	74.1	3514.8	32.0	100.5	Concordant
19-GC-5	491.5	193.6	677.4	29.7	636.0	45.8	137.8	>5% revdisc
~~19-GC-5~~	~~1391.2~~	~~106.4~~	~~1224.6~~	~~46.4~~	~~1286.4~~	~~50.6~~	88.0	Concordant
~~19-GC-5~~	~~1563.3~~	~~46.3~~	~~1495.0~~	~~40.3~~	~~1523.5~~	~~31.0~~	95.6	Concordant
19-GC-5	1648.1	55.1	1529.6	37.8	1580.1	32.7	92.8	Concordant
19-GC-5	1659.0	91.2	1765.3	61.3	1717.2	52.7	106.4	>5% revdisc
19-GC-5	1669.9	39.0	1725.4	34.2	1700.5	25.6	103.3	Concordant
19-GC-5	1671.7	35.9	1594.4	31.6	1628.0	24.1	95.4	Concordant
19-GC-5	1677.1	33.3	1765.3	30.7	1725.3	22.4	105.3	>5% revdisc
19-GC-5	1677.1	35.9	1612.0	30.1	1640.4	23.5	96.1	Concordant

19-GC-5	1702.0	40.9	1647.0	32.9	1671.3	26.1	96.8	Concordant
19-GC-5	1716.1	42.9	1643.0	36.1	1675.3	28.2	95.7	Concordant
19-GC-5	1716.1	33.1	1760.4	30.2	1740.2	22.3	102.6	Concordant
19-GC-5	1733.5	39.7	1653.0	31.6	1688.8	25.3	95.4	Concordant
19-GC-5	1748.9	36.5	1700.7	31.5	1722.4	24.2	97.2	Concordant
19-GC-5	1752.4	47.5	1666.5	36.7	1704.9	29.9	95.1	Concordant
19-GC-5	1754.1	53.5	1676.9	40.7	1711.5	33.4	95.6	Concordant
19-GC-5	1755.8	46.0	1661.5	36.3	1703.6	29.3	94.6	Concordant
19-GC-5	1759.2	28.4	1698.2	27.4	1725.7	20.0	96.5	Concordant
19-GC-5	1759.2	50.0	1653.0	35.9	1700.3	30.5	94.0	Concordant
19-GC-5	1762.6	43.3	1825.8	38.4	1796.4	28.7	103.6	Concordant
19-GC-5	1764.3	64.5	1622.5	44.6	1685.3	38.9	92.0	Concordant
19-GC-5	1769.3	40.0	1849.0	37.8	1811.8	27.3	104.5	Concordant
19-GC-5	1771.0	35.5	1841.8	34.5	1808.8	24.6	104.0	Concordant
19-GC-5	1772.7	24.2	1717.5	26.3	1742.6	18.3	96.9	Concordant
19-GC-5	1777.7	47.2	1710.1	38.4	1740.8	30.4	96.2	Concordant
19-GC-5	1786.1	34.4	1838.4	32.5	1814.0	23.6	102.9	Concordant
19-GC-5	1787.8	25.5	1724.9	26.6	1753.5	18.8	96.5	Concordant
19-GC-5	1797.7	24.4	1747.1	25.5	1770.3	18.0	97.2	Concordant
19-GC-5	1809.3	48.2	1749.1	39.5	1776.7	31.2	96.7	Concordant
19-GC-5	1815.9	32.5	1766.7	30.6	1789.4	22.6	97.3	Concordant
19-GC-5	1820.8	28.1	1765.8	29.0	1791.1	20.6	97.0	Concordant
19-GC-5	1822.4	24.9	1753.5	26.2	1785.2	18.5	96.2	Concordant
19-GC-5	1825.6	43.1	1896.8	39.1	1863.0	28.9	103.9	Concordant
19-GC-5	1833.7	64.1	1730.4	50.8	1777.7	41.2	94.4	Concordant
19-GC-5	1843.4	56.9	1719.5	45.0	1776.2	36.6	93.3	Concordant
19-GC-5	1857.8	39.3	1800.5	35.3	1827.2	26.6	96.9	Concordant
19-GC-5	1864.1	63.5	1715.6	47.6	1783.6	40.0	92.0	Concordant
19-GC-5	1876.7	37.0	1823.8	36.7	1848.7	26.5	97.2	Concordant
19-GC-5	1881.5	34.5	1825.3	35.2	1851.7	25.1	97.0	Concordant

19-GC-5	1887.7	41.1	1824.3	38.1	1854.1	28.4	96.6	Concordant
19-GC-5	1904.7	48.3	1988.8	46.3	1947.9	33.3	104.4	Concordant
19-GC-5	2559.6	17.9	2474.3	32.1	2521.5	17.7	96.7	Concordant
19-GC-5	2633.4	35.8	2522.5	53.9	2584.4	31.7	95.8	Concordant
19-GC-5	2677.5	26.7	2590.1	47.9	2639.5	26.2	96.7	Concordant
19-GC-5	2874.3	19.8	2825.2	43.2	2854.0	21.6	98.3	Concordant
19-GC-5	2896.3	37.5	2808.5	71.8	2859.9	37.7	97.0	Concordant
19-GC-5	2897.0	39.5	2804.3	73.4	2858.6	39.0	96.8	Concordant
19-GC-5	2941.4	17.1	2886.4	43.3	2918.9	20.6	98.1	Concordant
19-GC-5	3204.9	17.5	3121.8	47.4	3172.6	21.6	97.4	Concordant
19-GC-5	3234.5	18.5	3165.4	51.0	3207.9	23.0	97.9	Concordant
19-GC-5	3268.4	26.8	3185.1	59.9	3236.4	28.7	97.5	Concordant
19-GC-5	1277.0	15.6	601.5	7.0	764.7	7.9	47.1	discorndant
19-GC-5	1700.2	40.3	1554.0	34.1	1617.1	26.9	91.4	Concordant
19-GC-5	2441.9	21.6	1143.0	63.1	1682.8	51.7	46.8	discorndant
19-GC-5	1624.1	82.2	1318.8	46.6	1440.1	45.6	81.2	Concordant
19-GC-5	1538.0	40.1	884.1	59.3	1093.5	51.2	57.5	discorndant
19-GC-5	1724.8	24.7	1445.2	22.4	1562.5	17.6	83.8	Concordant
19-GC-5	2571.4	38.0	1750.5	66.4	2157.7	44.4	68.1	discorndant
19-GC-5	1629.7	31.9	1059.3	26.1	1263.3	23.1	65.0	discorndant
19-GC-5	1797.7	41.1	1663.5	35.7	1723.8	27.7	92.5	Concordant
19-GC-5	1987.1	28.9	1182.8	25.2	1502.2	22.4	59.5	discorndant
19-GC-5	1689.6	45.8	1328.2	29.2	1473.5	27.2	78.6	discorndant
19-GC-5	1735.2	26.6	1607.0	24.3	1663.3	18.4	92.6	Concordant
19-GC-5	1463.3	31.8	713.3	35.4	922.6	33.8	48.7	discorndant
19-GC-5	2799.0	21.3	2509.4	40.8	2672.9	22.3	89.7	Concordant
19-GC-5	1524.1	26.1	1094.2	32.8	1248.0	25.6	71.8	discorndant
19-GC-5	1728.3	27.4	1644.0	27.1	1681.4	19.7	95.1	Concordant
19-GC-5	2862.5	16.9	2731.8	39.1	2807.5	19.5	95.4	Concordant
19-GC-5	1620.4	35.0	1313.0	24.8	1434.8	21.7	81.0	Concordant

19-GC-5	1742.1	27.1	1169.9	40.1	1388.4	30.9	67.2	discorndant
19-GC-5	1629.7	36.3	1195.7	24.6	1360.4	22.5	73.4	discorndant
19-GC-5	2671.2	17.0	2557.7	34.7	2621.5	18.3	95.8	Concordant
19-GC-5	1710.8	43.8	1533.2	31.8	1609.5	27.0	89.6	Concordant
19-GC-5	1745.5	26.6	1557.0	24.5	1638.9	18.7	89.2	Concordant
19-GC-5	1616.6	59.0	1358.6	36.7	1462.4	34.0	84.0	Concordant
19-GC-5	1859.4	44.8	1413.7	31.1	1602.0	28.2	76.0	discorndant
19-GC-5	1740.4	34.7	1469.3	28.8	1584.1	23.3	84.4	Concordant
19-GC-5	1671.7	33.1	1813.6	34.1	1748.6	23.5	108.5	>5% revdisc
19-GC-5	2860.9	18.6	2367.6	37.9	2642.8	21.1	82.8	Concordant
19-GC-5	1838.6	35.5	1594.4	30.4	1702.6	24.1	86.7	Concordant
19-GC-5	2855.3	13.9	2701.3	33.9	2790.3	16.8	94.6	Concordant
19-GC-5	1754.1	24.8	1454.4	27.4	1580.9	20.2	82.9	Concordant
19-GC-5	1767.6	32.6	1552.5	29.3	1646.0	22.7	87.8	Concordant
19-GC-5	1781.1	36.8	596.8	30.8	912.5	35.2	33.5	discorndant
19-GC-5	1707.3	26.6	1448.8	30.0	1557.1	21.9	84.9	Concordant
19-GC-5	2535.8	18.9	2424.1	35.8	2485.4	19.6	95.6	Concordant
19-GC-5	1614.8	58.6	1761.3	46.0	1695.4	36.0	109.1	>5% revdisc
19-GC-5	1668.1	34.0	1048.9	28.3	1270.5	25.2	62.9	discorndant
19-GC-5	2851.3	15.9	2235.9	33.9	2573.5	19.2	78.4	discorndant
19-GC-5	2774.7	19.6	1896.3	39.4	2352.0	24.7	68.3	discorndant
19-GC-5	1835.4	32.2	1711.6	31.9	1768.0	23.3	93.3	Concordant
19-GC-5	2707.1	18.6	1736.8	30.5	2223.1	20.9	64.2	discorndant
19-GC-5	2881.4	15.2	2345.3	33.6	2644.1	18.4	81.4	Concordant
19-GC-5	1644.4	26.7	1308.2	25.5	1441.7	20.1	79.6	discorndant
19-GC-5	1105.6	46.5	977.3	20.8	1017.7	21.0	88.4	Concordant
19-GC-5	1764.3	18.6	1637.0	20.9	1693.6	14.6	92.8	Concordant
19-GC-5	1817.5	28.1	1412.6	39.5	1582.8	28.1	77.7	discorndant
19-GC-5	1728.3	32.7	1460.1	31.0	1573.1	23.9	84.5	Concordant
19-GC-5	2758.5	21.9	1794.6	48.7	2285.2	31.0	65.1	discorndant

19-GC-5	1723.0	46.4	1858.7	41.5	1795.6	30.5	107.9	>5% revdisc
19-GC-5	2007.4	21.0	1797.5	27.6	1896.9	18.3	89.5	Concordant
19-GC-5	1605.4	23.8	1145.7	20.4	1316.0	17.2	71.4	discorndant
19-GC-5	1494.0	60.9	508.0	17.0	731.3	24.8	34.0	discorndant
19-GC-5	2455.7	21.2	2153.8	37.4	2312.5	22.0	87.7	Concordant
19-GC-5	1696.7	51.1	1548.4	36.3	1612.3	31.1	91.3	Concordant
19-GC-5	1646.2	33.6	1441.1	33.2	1526.2	25.0	87.5	Concordant
19-GC-5	1526.1	36.4	966.8	20.1	1154.4	20.5	63.4	discorndant
19-GC-5	1682.5	24.0	1342.9	22.5	1480.0	17.7	79.8	discorndant
19-GC-5	2845.6	23.2	2251.4	49.7	2577.9	28.1	79.1	discorndant
19-GC-5	1772.7	44.9	1511.8	33.0	1624.0	28.3	85.3	Concordant
19-GC-5	2773.8	20.8	1652.5	31.9	2208.7	22.9	59.6	discorndant
19-GC-5	1159.6	77.5	678.6	40.5	801.2	41.5	58.5	discorndant
19-GC-5	2533.8	27.2	1591.4	42.1	2041.9	30.2	62.8	discorndant
19-GC-5	2667.5	28.5	2491.4	48.4	2589.7	27.4	93.4	Concordant
19-GC-5	1784.4	32.5	1573.2	30.7	1665.7	23.3	88.2	Concordant
19-GC-5	1752.4	22.2	1476.5	29.3	1593.7	20.5	84.3	Concordant
19-GC-5	1786.1	39.3	1509.3	32.0	1628.5	26.2	84.5	Concordant
19-GC-5	2737.8	27.6	2501.5	48.9	2634.2	27.4	91.4	Concordant
19-GC-5	1609.1	25.8	936.7	18.6	1161.6	17.7	58.2	discorndant
19-GC-5	1849.8	23.4	1609.5	24.7	1716.6	18.0	87.0	Concordant
19-GC-5	1815.9	44.0	1634.5	35.8	1715.5	28.9	90.0	Concordant
19-GC-5	1966.6	41.2	1651.5	43.4	1795.3	32.0	84.0	Concordant
19-GC-5	2317.1	26.3	2048.2	48.1	2185.6	28.5	88.4	Concordant
19-GC-5	2524.8	28.9	1884.3	32.9	2208.6	24.0	74.6	discorndant
19-GC-5	2778.9	19.5	2673.7	38.9	2734.0	20.4	96.2	Concordant
19-GC-5	1794.4	55.8	1672.9	41.9	1727.6	34.9	93.2	Concordant
19-GC-5	1664.5	58.7	1821.9	46.2	1749.7	36.1	109.5	>5% revdisc
19-GC-5	1743.8	20.1	1652.5	24.5	1693.1	16.6	94.8	Concordant
19-GC-5	1638.9	36.1	1153.8	48.5	1335.0	37.6	70.4	discorndant

~~19-GC-5~~	~~2291.3~~	~~52.1~~	~~2150.6~~	~~60.4~~	~~2223.5~~	~~40.8~~	93.9	Concordant
19-GC-5	2322.9	22.3	1632.5	29.7	1958.4	21.3	70.3	discorndant
19-GC-5	2207.3	45.4	1982.2	60.4	2094.8	39.5	89.8	Concordant
19-GC-5	1764.3	31.4	1428.2	41.5	1569.1	29.6	80.9	Concordant

Table A. 2: *Complete U-Pb isotopic dataset for detrital zircon grains from sample 19-GC-5. Reported parameters include measured isotopic ratios, calculated 206Pb/238U, 207Pb/235U, and 207Pb/206Pb ages (Ma), analytical uncertainties (2σ), and concordance values.*

	Dates							
Sample	**$^{207}Pb/^{206}Pb$**	**$2s_x$ (ABS)**	**$^{206}Pb/^{238}U$**	**$2s_x$ (ABS)**	**$^{207}Pb/^{235}Pb$**	**$2s_x$ (ABS)**	**Concordant filter**	**20% discordant filter, 5% reverse discordant filter**
23-CCN-Geochron 1	1744.02	39.46	1705.00	14.01	1723.51735	38.3063307	97.76	Concordant
23-CCN-Geochron 1	3302.51	64.84	3412.30	28.50	< DL	15993.9499	103.32	Concordant
23-CCN-Geochron 1	1801.60	37.70	1671.40	12.10	2733.00328	75.0763643	92.77	Concordant
23-CCN-Geochron 1	1786.24	40.17	1773.90	12.26	1819.57625	46.1645314	99.31	Concordant
23-CCN-Geochron 1	2355.86	56.28	1996.90	64.83	2622.94264	51.6667618	84.76	Concordant
23-CCN-Geochron 1	1788.96	36.28	1798.60	11.78	3288.89113	63.5552171	100.54	Concordant
23-CCN-Geochron 1	1790.03	41.17	1759.00	13.96	2673.40328	58.9225937	98.27	Concordant
23-CCN-Geochron 1	1842.84	44.97	1799.60	14.97	1769.2963	39.4191928	97.65	Concordant
23-CCN-Geochron 1	1708.37	34.15	1649.80	19.16	2583.84491	50.7730793	96.57	Concordant
23-CCN-Geochron 1	1807.44	37.38	1585.40	45.96	3343.50747	66.7060774	87.72	Concordant
23-CCN-Geochron 1	2756.92	55.25	2492.50	64.68	1731.23645	37.0609619	90.41	Concordant
23-CCN-Geochron 1	1697.56	35.05	1362.80	38.28	1779.99066	40.8672409	80.28	Concordant
23-CCN-Geochron 1	3297.35	69.57	3197.20	33.02	2191.50796	101.726142	96.96	Concordant
23-CCN-Geochron 1	1698.88	39.42	1620.40	28.91	1794.99204	36.609907	95.38	Concordant
23-CCN-Geochron 1	1699.93	48.59	1791.40	20.44	1773.81486	40.6764815	105.38	>5% revdisc
23-CCN-Geochron 1	1786.20	35.97	1804.30	13.15	1821.06321	47.6084026	101.01	Concordant
23-CCN-Geochron 1	1806.06	37.97	1833.50	13.75	1675.91311	38.4535162	101.52	Concordant

23-CCN-Geochron 1	1819.11	77.76	889.00	51.72	1679.12879	64.4429013	48.87	discorndant
23-CCN-Geochron 1	1775.87	37.91	1798.40	13.11	2641.8436	96.2495392	101.27	Concordant
23-CCN-Geochron 1	1417.98	35.94	1457.60	10.88	1501.63781	59.3269863	102.79	Concordant
23-CCN-Geochron 1	2807.32	66.02	2623.20	38.83	3261.30204	77.2400674	93.44	Concordant
23-CCN-Geochron 1	1699.48	35.91	1730.50	13.32	1655.90986	49.3641866	101.83	Concordant
23-CCN-Geochron 1	1577.63	33.05	1400.00	56.14	1750.18301	51.0531919	88.74	Concordant
23-CCN-Geochron 1	3268.15	64.84	3310.60	24.14	1796.36105	36.642093	101.30	Concordant
23-CCN-Geochron 1	3081.09	61.72	3009.60	21.94	1821.74529	38.9749032	97.68	Concordant
23-CCN-Geochron 1	1719.81	40.76	1714.60	13.85	1187.08942	70.2304393	99.70	Concordant
23-CCN-Geochron 1	1749.08	36.86	1755.60	14.11	944.182636	70.8397149	100.37	Concordant
23-CCN-Geochron 1	1756.30	43.32	1839.60	17.08	1788.66072	37.8161913	104.74	Concordant
23-CCN-Geochron 1	2924.28	62.92	2923.60	27.99	1441.62636	35.630786	99.98	Concordant
23-CCN-Geochron 1	2917.44	62.31	2963.40	30.54	1717.45537	35.3090918	101.58	Concordant
23-CCN-Geochron 1	1859.26	47.92	1786.60	17.92	1472.23361	69.6835345	96.09	Concordant
23-CCN-Geochron 1	1715.97	40.77	1720.10	14.04	3286.33384	66.4665304	100.24	Concordant
23-CCN-Geochron 1	1895.09	40.07	1611.10	14.43	3054.23933	61.9380605	85.01	Concordant
23-CCN-Geochron 1	1713.89	32.55	1767.00	12.59	1718.00339	40.546763	103.10	Concordant
23-CCN-Geochron 1	2810.60	51.69	2519.40	19.26	1753.98521	36.3407802	89.64	Concordant
23-CCN-Geochron 1	1836.35	37.44	1733.70	18.89	1801.5479	45.6639778	94.41	Concordant
23-CCN-Geochron 1	2618.58	48.42	2326.10	32.58	2924.7322	61.0653272	88.83	Concordant
23-CCN-Geochron 1	1780.25	43.44	1802.60	15.64	2938.31524	63.0382949	101.26	Concordant
23-CCN-Geochron 1	1823.41	48.58	1789.30	17.45	1720.36259	4981.0074	98.13	Concordant
23-CCN-Geochron 1	2908.19	56.15	2942.40	20.61	1739.65998	41.015628	101.18	Concordant
23-CCN-Geochron 1	2876.63	59.60	2947.00	22.39	1744.68683	37.5766521	102.45	Concordant
23-CCN-Geochron 1	2626.01	51.69	2616.30	17.14	2685.33504	33.4894628	99.63	Concordant
23-CCN-Geochron 1	2782.28	61.44	1758.80	74.24	1786.26368	49.7192118	63.21	discorndant
23-CCN-Geochron 1	1718.98	33.41	1733.20	13.10	2489.53488	35.9283704	100.83	Concordant
23-CCN-Geochron 1	2936.94	55.71	2989.60	30.91	1793.53061	57.1907562	101.79	Concordant
23-CCN-Geochron 1	2946.44	54.02	2963.60	21.28	1806.36048	42.5654549	100.58	Concordant
23-CCN-Geochron 1	1866.51	37.72	1907.20	14.33	2923.43309	49.9484212	102.18	Concordant

23-CCN-Geochron 1	1780.43	34.24	1662.10	30.74	2905.80279	55.2976921	93.35	Concordant
23-CCN-Geochron 1	2402.44	45.70	2195.90	44.72	2274.16731	59.1720859	91.40	Concordant
23-CCN-Geochron 1	3317.55	62.80	3241.80	28.18	1727.54972	110.765938	97.72	Concordant
23-CCN-Geochron 1	2827.42	56.77	2471.00	26.16	2958.82925	33.865933	87.39	Concordant
23-CCN-Geochron 1	1769.05	39.50	1768.20	14.92	2956.2388	58.3462473	99.95	Concordant
23-CCN-Geochron 1	2559.17	49.48	2612.70	20.59	1889.45625	53.4909738	102.09	Concordant

Table A. 3: *Complete U-Pb isotopic dataset for detrital zircon grains from sample 23-CCN-Geochron 1. Reported parameters include measured isotopic ratios, calculated 206Pb/238U, 207Pb/235U, and 207Pb/206Pb ages (Ma), analytical uncertainties (2σ), and concordance values.*

	Dates							
Sample	**^{207}Pb/^{206}Pb**	**2s$_x$ (ABS)**	**^{206}Pb/^{238}U**	**2s$_x$ (ABS)**	**^{207}Pb/^{235}Pb**	**2s$_x$ (ABS)**	**Concordant filter**	**20% discordant filter, 5% reverse discordant filter**
23-CCN-Geochron 3	2068.45	59.22	1748.80	14.33	1906.33	58.46	84.55	Concordant
23-CCN-Geochron 3	1819.08	44.66	1689.70	14.40	1817.54	43.42	92.89	Concordant
23-CCN-Geochron 3	1492.78	37.22	1277.90	14.71	1192.15	24.36	85.61	Concordant
23-CCN-Geochron 3	1728.51	43.09	1740.90	15.19	1452.36	40.63	100.72	Concordant
23-CCN-Geochron 3	1779.60	42.86	1817.10	13.48	1792.20	40.53	102.11	Concordant
23-CCN-Geochron 3	2664.56	61.94	2187.80	24.71	2484.11	77.69	82.11	Concordant
23-CCN-Geochron 3	1761.88	40.83	1798.00	15.17	2844.57	59.62	102.05	Concordant
23-CCN-Geochron 3	3085.44	69.67	2316.20	43.90	2542.07	78.64	75.07	discorndant
23-CCN-Geochron 3	1796.79	42.01	1811.80	14.69	1712.38	42.40	100.84	Concordant
23-CCN-Geochron 3	3309.40	73.80	3176.20	27.09	1750.32	41.20	95.98	Concordant
23-CCN-Geochron 3	1845.21	49.40	1781.30	15.72	1363.13	31.63	96.54	Concordant
23-CCN-Geochron 3	1831.53	46.08	1802.10	15.55	1736.55	40.58	98.39	Concordant
23-CCN-Geochron 3	1658.59	41.59	1609.80	12.69	1802.43	40.62	97.06	Concordant
23-CCN-Geochron 3	1468.17	34.82	1411.60	17.50	2446.88	62.23	96.15	Concordant
23-CCN-Geochron 3	1800.38	37.39	1784.20	14.58	1783.96	40.28	99.10	Concordant

23-CCN-Geochron 3	1862.93	38.09	1677.40	27.98	2756.03	79.18	90.04	Concordant
23-CCN-Geochron 3	1799.99	36.78	1765.80	13.55	1807.38	39.81	98.10	Concordant
23-CCN-Geochron 3	2962.77	58.44	3000.70	26.58	3260.67	70.73	101.28	Concordant
23-CCN-Geochron 3	1789.24	36.82	1713.40	15.38	1813.87	47.42	95.76	Concordant
23-CCN-Geochron 3	1762.68	36.20	1797.70	13.80	1634.12	39.41	101.99	Concordant
23-CCN-Geochron 3	1770.81	37.43	1869.40	28.69	1435.91	35.78	105.57	>5% revdisc
23-CCN-Geochron 3	1544.86	31.53	1004.20	8.07	1794.22	36.11	65.00	discorndant
23-CCN-Geochron 3	1771.91	37.38	1800.50	13.82	1761.97	42.34	101.61	Concordant
23-CCN-Geochron 3	1809.18	40.03	1775.00	15.04	1783.44	34.33	98.11	Concordant
23-CCN-Geochron 3	1826.57	40.83	1802.40	15.71	2980.09758	55.9429309	98.68	Concordant
23-CCN-Geochron 3	1742.32	36.72	1798.90	15.70	1749.13847	35.9099592	103.25	Concordant
23-CCN-Geochron 3	1773.32	40.54	1795.40	14.66	< DL	4559.31185	101.25	Concordant
23-CCN-Geochron 3	1828.81	48.38	1522.30	38.69	1784.01074	35.4095837	83.24	Concordant
23-CCN-Geochron 3	1781.72	43.94	1897.30	26.80	1827.44235	46.1141983	106.49	>5% revdisc
23-CCN-Geochron 3	1424.64	30.50	1387.60	12.45	1789.07668	35.4711682	97.40	Concordant
23-CCN-Geochron 3	1237.36	61.14	1134.50	13.90	1791.67417	36.1256178	91.69	Concordant
23-CCN-Geochron 3	1025.46	55.70	1146.40	13.34	1815.02621	39.1120372	111.79	>5% revdisc
23-CCN-Geochron 3	1796.04	46.49	1227.00	19.33	1775.49671	37.0359367	68.32	discorndant
23-CCN-Geochron 3	2650.60	51.54	2734.70	18.84	1785.86446	38.8804758	103.17	Concordant
23-CCN-Geochron 3	1428.69	41.80	1457.50	14.06	1660.33502	42.5832879	102.02	Concordant
23-CCN-Geochron 3	1421.59	30.45	1446.40	10.65	1845.59538	50.8474286	101.74	Concordant
23-CCN-Geochron 3	2654.60	54.63	2715.50	20.33	1402.88899	28.82496	102.29	Concordant
23-CCN-Geochron 3	1707.20	32.91	1762.10	12.56	1172.31	63.0362043	103.22	Concordant
23-CCN-Geochron 3	1857.54	37.70	1816.70	15.85	1106.07715	59.2416222	97.80	Concordant
23-CCN-Geochron 3	1719.42	39.14	1561.40	13.38	2687.88899	51.7184418	90.81	Concordant
23-CCN-Geochron 3	1658.96	31.75	1695.60	11.68	1446.75647	41.8345138	102.21	Concordant
23-CCN-Geochron 3	2731.30	56.10	2717.80	21.96	1436.9302	30.0897458	99.51	Concordant
23-CCN-Geochron 3	1753.96	34.31	1782.70	13.35	2681.33228	54.6879764	101.64	Concordant
23-CCN-Geochron 3	1796.99	42.46	1784.00	14.13	1738.07258	33.8029287	99.28	Concordant
23-CCN-Geochron 3	1742.10	36.64	1792.20	21.27	1837.24124	38.0175291	102.88	Concordant

23-CCN-Geochron 3	1520.09	35.55	1426.30	11.30	1630.0609	37.9120119	93.83	Concordant
23-CCN-Geochron 3	1696.79	34.54	1604.20	14.44	1680.4472	31.9433044	94.54	Concordant
23-CCN-Geochron 3	1503.04	44.21	1406.60	13.08	2726.05963	55.6919553	93.58	Concordant
23-CCN-Geochron 3	1754.80	35.18	1761.30	13.12	1769.90918	34.4323102	100.37	Concordant
23-CCN-Geochron 3	3291.53	69.38	3277.40	31.32	1771.07898	42.3702544	99.57	Concordant
23-CCN-Geochron 3	1719.36	41.77	1783.20	16.44	1463.90358	33.6515104	103.71	Concordant
23-CCN-Geochron 3	1749.79	39.07	1766.10	12.84	1644.95244	35.7852656	100.93	Concordant
23-CCN-Geochron 3	1429.65	33.19	1239.90	15.92	1446.77623	44.7074445	86.73	Concordant
23-CCN-Geochron 3	2868.87	64.56	2039.10	43.51	1758.5046	35.2453065	71.08	discorndant
23-CCN-Geochron 3	1749.83	39.50	1740.40	12.65	< DL		99.46	Concordant
23-CCN-Geochron 3	1748.56	39.47	1468.90	41.07	3286.18897	68.9122929	84.01	Concordant
23-CCN-Geochron 3	1781.51	40.89	1782.30	15.32	1754.82769	44.075773	100.04	Concordant
23-CCN-Geochron 3	1706.23	37.91	1717.60	14.93	1758.90999	39.1228033	100.67	Concordant
23-CCN-Geochron 3	1783.92	41.56	1775.10	13.18	1310.46858	34.258595	99.51	Concordant
23-CCN-Geochron 3	1784.54	40.17	1599.60	14.49	1744.85728	40.3923662	89.64	Concordant
23-CCN-Geochron 3	1838.65	47.36	1766.00	14.84	1455.2756	39.6493965	96.05	Concordant
23-CCN-Geochron 3	1790.67	43.05	1735.50	13.43	1584.46479	57.7996298	96.92	Concordant
23-CCN-Geochron 3	2874.07	64.19	2796.20	20.37	1784.51468	41.8758376	97.29	Concordant
23-CCN-Geochron 3	1815.24	41.99	1800.60	14.00	1712.00418	38.5378124	99.19	Concordant
23-CCN-Geochron 3	1456.73	35.97	1437.80	13.56	1778.93405	41.9140817	98.70	Concordant
23-CCN-Geochron 3	2607.24	60.01	2447.50	51.99	1793.69565	44.4213743	93.87	Concordant
23-CCN-Geochron 3	1766.22	43.85	1665.40	16.49	1681.14595	39.3714281	94.29	Concordant

Table A. 4: *Complete U-Pb isotopic dataset for detrital zircon grains from sample 23-CCN-Geochron 3. Reported parameters include measured isotopic ratios, calculated 206Pb/238U, 207Pb/235U, and 207Pb/206Pb ages (Ma), analytical uncertainties (2σ), and concordance values.*